

# **Spins and Orbits**

## **in Semiconductor Quantum Dots**

**Inauguraldissertation**

zur

Erlangung der Würde eines Doktors der Philosophie

vorgelegt der

Philosophisch-Naturwissenschaftlichen Fakultät

der Universität Basel

von

**Leon Camenzind**

aus Gersau (SZ)

2019

Originaldokument gespeichert auf dem Dokumentenserver der Universität Basel

[edoc.unibas.ch](http://edoc.unibas.ch)

Genehmigt von der Philosophisch-Naturwissenschaftlichen Fakultät  
auf Antrag von

Prof. Dr. D. M. Zumbühl

Prof. Dr. S. Tarucha

Basel, den 26.3.2019

Prof. Dr. Martin Spiess

Dekan

# Abstract

Spins in semiconductor quantum dots are among the most promising candidates for the realization of a scalable quantum bit (qubit), the basic building block of a quantum computer [1, 2]. With this motivation, spin and orbital properties of quantum dots in three different semiconductor systems are investigated in this thesis: depletion mode quantum dots in GaAs/AlGaAs heterostructures as well as in silicon-germanium core-shell nanowires (GeSi NW), and accumulation mode quantum dots formed in a fin field-effect transistor (FinFET). The chronological order of this thesis reflects two major shifts of focus of the semiconductor spin qubit research in recent years: a transition from lateral GaAs quantum dots towards scalable, silicon-based systems and a change from electrons towards holes as the host of the spin qubit because of better prospects for spin manipulation and spin coherence.

In a lateral GaAs single electron quantum dot, a new in-plane magnetic-field-assisted spectroscopy is demonstrated, which allows one to deduce the three dimensional confinement potential landscape of the quantum dot orbitals, which gives insight into the alignment of the ellipsoidal quantum dot with respect to the crystal axes. With this full model of the confinement at hand, the dependence of the spin relaxation on the direction and strength of an in-plane magnetic field is investigated. To mitigate the spin relaxation anisotropy due to anisotropic in-plane confinement of the quantum dot, said confinement is symmetrized by tuning the gate voltages to obtain a circular quantum dot. Then, the experimentally observed spin relaxation anisotropy can be attributed to the interplay of Rashba and Dresselhaus spin-orbit interaction (SOI) present in GaAs. By using a theoretical model, the strength and the relative sign of the Rashba and Dresselhaus SOI was obtained for the first time in such a quantum dot. From the dependence of the spin relaxation on the magnetic field strength, hyperfine induced phonon mediated spin relaxation was demonstrated – a process predicted more than

15 years ago [3]. Here, the hyperfine interaction leads to a mixing of spin and orbital degrees of freedom and facilitates spin relaxation. Limited by this relaxation process, a spin relaxation time of  $57 \pm 15$  s was measured – setting the current record for spin lifetime in a nanostructure. Inspired by the unprecedented knowledge of the confinement and the SOI in the quantum dots used, a new theory to quantify the various corrections to the g-factor was developed [4]. Later, these theoretical predictions have been experimentally validated by measurements of the g-factor anisotropy using pulsed-gate spectroscopy.

Due to short spin qubit coherence time in GaAs, which is limited by the nuclear spins, a better approach is to build a spin qubit in a semiconductor vacuum with little or no nuclear spins. Because holes have minimal overlap with the nuclei of the semiconductor due to the p-type symmetry of their wave function, this type of decoherence is strongly suppressed when changing the host of the spin qubit from electrons to holes. The longer coherence times in combination with the predicted emergence of a direct type of Rashba SOI (DRSOI) – a particularly strong and electrically controllable SOI – motivated the investigation of hole quantum dots in GeSi NW [5]. In this system, anisotropic behavior of the leakage current through a double quantum dot in Pauli spin blockade was observed. This anisotropy is qualitatively explained by a phenomenological model, which involves an anisotropic g-factor and an effective spin-orbit field. While the dominant type of SOI could not be resolved conclusively, the obtained data is not inconsistent with the expectation of DRSOI.

Because each wire has to be placed manually, this NW based system lacks scalability. Hole and electron quantum dots in an industry-compatible silicon FinFET structure, conversely, are promising candidates for scalable spin qubits and, therefore, hold the potential to be used in a spin-based quantum computer. Recently, DRSOI was predicted to also emerge in narrow silicon channels such as FinFETs [6]. In this thesis, the formation of accumulation mode hole quantum dots in such a FinFET structure is

reported – an important first step towards the realization of a scalable, all-electrically controllable, DRSOI hole spin qubit.

# Contents

<b>Abstract</b>	<b>i</b>
<b>1 Introduction</b>	<b>1</b>
<b>2 Background</b>	<b>7</b>
2.1 Quantum dots . . . . .	8
2.1.1 Two-dimensional electron gas . . . . .	9
2.1.2 Lateral quantum dots . . . . .	13
2.1.3 Coulomb blockade . . . . .	14
2.1.4 Confinement potential . . . . .	19
2.1.5 Numerical simulations of the device potential . . . . .	23
2.2 Spin-orbit interaction . . . . .	26
2.2.1 SOI in the conduction band . . . . .	28
2.2.2 Direct Rashba spin orbit interaction . . . . .	31
<b>3 Spectroscopy of quantum-dot orbitals with in-plane magnetic fields</b>	<b>37</b>
3.1 Introduction . . . . .	38
3.2 Measurement scheme . . . . .	40
3.3 Model of the confinement potential and shape control . . . . .	42
3.4 Spectroscopy of quantum-dot orbitals . . . . .	44
3.5 Conclusions . . . . .	48
3.6 Acknowledgments . . . . .	48
3.7 Supplementary Information . . . . .	49

3.7.1	Calculated wave functions . . . . .	49
3.7.2	Total energy correction due to in-plane magnetic field and ground-state behavior . . . . .	49
3.7.3	Calculated energies of the ground- and excited orbital states . .	52
3.7.4	Shape invariance of leverarm $\alpha_P$ . . . . .	52
3.7.5	Measuring excited orbital states . . . . .	57
<b>4</b>	<b>Hyperfine-phonon spin relaxation in a single-electron GaAs quantum dots</b>	<b>61</b>
4.1	Introduction . . . . .	62
4.2	Results . . . . .	65
4.2.1	Quantum dot orbitals . . . . .	65
4.2.2	Spin-orbit induced spin relaxation anisotropy . . . . .	65
4.2.3	Hyperfine-phonon spin relaxation . . . . .	68
4.3	Methods . . . . .	71
4.3.1	Sample and measurement . . . . .	71
4.3.2	The numerical model . . . . .	73
4.3.3	Analytical results . . . . .	74
4.4	Acknowledgments . . . . .	75
4.5	Author Contributions . . . . .	75
4.6	Data availability . . . . .	75
4.7	Supplementary Information . . . . .	76
4.7.1	In-plane magnetic field alignment . . . . .	76
4.7.2	Level positioning algorithm and sensor stabilization . . . . .	76

4.7.3	Spin relaxation measurement scheme . . . . .	81
4.7.4	Spin-readout fidelity . . . . .	85
4.7.5	Definitions and notations for the electron, nuclear spins, and phonons . . . . .	88
4.7.6	The spin relaxation rate . . . . .	92
4.7.7	Anisotropy of the hyperfine relaxation rate . . . . .	94
4.7.8	Dipole matrix elements between the spin opposite states . . . . .	97
4.7.9	Numerical implementation . . . . .	100
4.7.10	Parameters and fitting of the spin-orbit constants . . . . .	100
<b>5</b>	<b>g-factor corrections in a GaAs single-electron quantum dot</b>	<b>104</b>
5.1	Introduction . . . . .	105
5.2	Sample and measurement scheme . . . . .	106
5.3	Tunnel rate into the spin states . . . . .	109
5.4	g-factor corrections . . . . .	111
5.5	Discussion . . . . .	114
5.6	Acknowledgments . . . . .	115
<b>6</b>	<b>Anisotropic Pauli spin blockade in a Ge/Si core-shell nanowire double quantum dot</b>	<b>116</b>
6.1	Introduction . . . . .	117
6.2	Device . . . . .	118
6.3	Pauli spin blockade . . . . .	119
6.4	Pauli spin blockade in presence of spin-orbit interaction . . . . .	121
6.5	Anisotropic Pauli spin blockade . . . . .	124



6.6	Discussion and conclusions . . . . .	127
<b>7</b>	<b>Ambipolar quantum dots in undoped silicon fin field-effect transistors</b>	<b>129</b>
7.1	Introduction . . . . .	130
7.2	Ambipolar fin field-effect transistor device . . . . .	132
7.3	Classical field-effect transistor . . . . .	133
7.4	Single electron field-effect transistor . . . . .	135
7.5	Discussion and Conclusions . . . . .	137
7.6	Acknowledgement . . . . .	137
<b>8</b>	<b>A spin qubit setup in a cryofree dilution refrigerator</b>	<b>138</b>
8.1	Introduction . . . . .	138
8.2	From room temperature to the mixing chamber . . . . .	142
8.3	Characterisation of the coaxial lines . . . . .	148
8.4	Filterboard and RF PCB . . . . .	149
8.5	Characterisation of tank circuits . . . . .	154
8.5.1	Parasitic capacitance with a Ge/Si core-shell nanowire sample . . . . .	157
8.6	Discussion and Outlook . . . . .	160
<b>9</b>	<b>Summary and Outlook</b>	<b>163</b>
9.1	Lateral GaAs quantum dots . . . . .	163
9.2	Ge/Si NW quantum dots and towards a direct Rashba spin-orbit interaction driven hole spin qubit . . . . .	165
9.3	Towards a scalable, all-electrically controllable hole spin-orbit qubit . . . . .	167

<b>Bibliography</b>	<b>170</b>
<b>Acknowledgments</b>	<b>195</b>
<b>Curriculum Vitae</b>	<b>197</b>



# 1 Introduction

Currently, the world witnesses its second quantum revolution. While the first quantum revolution was about understanding the basics of quantum mechanics and enabled the invention of technology, such as the laser and the semiconductor transistor, which lead to the digital revolution and the advancement into the information age, the ongoing second quantum revolution is about controlling and exploiting quantum systems in order to build quantum hardware and will, potentially, lead us into an age of quantum information. This new quantum hardware will be built to take advantage of the entanglement and superposition of coherent quantum states for practical applications. Presumably, this second revolution will lead to the development of quantum sensors, quantum cryptography hardware, and quantum computers.

The first revolution lead to the development of a 400 billion dollar semiconductor industry at an unprecedented pace. Since the start of mass production in 1971, Moore's law has been fulfilled and the number of transistors on a computer chip doubles about every two year [7]. To satisfy this law, the transistors had to become smaller and smaller. In 2018, the state of the art is a single transistor gate scale of 7 nm and the introduction of the 5 nm node is scheduled for 2020. With the downscaling of these objects, quantum effects become more significant. Therefore, if Moore's law holds in the future, computers will eventually have to deal with quantum effects in some way. In the 1980's, Richard Feynman [8], David Deutsch [9] and others initiated the idea of using quantum-mechanical phenomena like superposition and entanglement for computing. In analogue to the binary digit (bit) encoded in transistors of classical computers, the information of such a quantum computer was proposed to be stored in a quantum bit (qubit). While the classical bit is defined by 'on' (1) or 'off' (0) states, the quantum bit (qubit) allows the information to be in a superposition between (1) and (0) during a gate operation. At the end of the operation, the qubit collapses

into either state recovering its digital character. This superposition, combined with quantum mechanical entanglement of multiple qubits, allows one to perform operations on multiple quantum states simultaneously.

A qubit can be encoded in any quantum mechanical two-level system, whereas the two levels represent the (0) and (1) state. In a landmark work published in 2000, David DiVincenzo postulated five criteria necessary for physical qubits in order to build a quantum computer [10]: First, the qubit must be scalable, and second, it can be initialized into a known state. The third criteria states that the unavoidable decay of the quantum mechanical state – the qubit’s decoherence – is much slower than the operation time of the qubit. Further, there must be a universal set of quantum gates. These can be constructed out of a small set of 1 and 2 qubit gates. At last, the state of the qubit must be readable after the operation.

Nowadays, there are a number of physical implementations of qubits and all of them have some advantages and disadvantages in regards to one or more of the DiVincenzo criteria [11]. For example, qubits can be encoded into trapped ions [12, 13]. While this qubit show coherence times  $T_2$  and relaxation times  $T_1$  in the range of seconds, their manipulation time is rather slow and the scalability is not given. Non-abelian anyons like Majorana fermions were proposed as qubits and are under heavy investigation due to their topological protection, which is predicted to lead to very long coherence times [14, 15]. It is still controversial, however, if Majorana fermions have been experimentally observed [16–18]. Further, there is no universal set of gates for the Majorana qubit and the qubit has to be encoded into more complex systems like parafermions [19, 20], or leave the topologically protected space to provide a universal set of gates [21].

Currently, the most advanced family of qubits are encoded in superconducting circuits with two parallel Josephson junctions [22–24]. In 2018, IBM produced a device with 20 superconducting qubits available for the public to run, test and optimize quantum algorithms. The IBM devices have typical  $T_1$  and  $T_2$  times of tens of  $\mu s$ , make about

1 gate error per 1000 operations, and have a readout error of a few percent [25]. While this is exciting, superconducting qubits are objects on the scale of hundreds of micrometers coupled to resonators of several hundreds of micrometers, which have to be cooled down to millikelvin temperature with expensive machinery. Therefore it will be technologically challenging – if not impossible – to scale up these systems to processors with thousands or millions of qubits.

In 1998, Daniel Loss and David DiVincenzo proposed to encode the qubit into the spin of an electron confined in a semiconductor quantum dot [1]. In the same year, Kane proposed to use nuclear spins of phosphorus dopants embedded in silicon [26] as the base of a semiconductor spin qubit. Today, there are multiple implementations of such semiconductor spin qubits and all of them rely on trapping charge carriers in quantum dots and exploiting its spin degree of freedom in some way. The focus of this thesis is on Spin-1/2 or Loss-DiVincenzo spin qubits – an implementation very close to the original proposal.

Among the first technical realizations of spin qubits in semiconductor quantum dots were undertaken in III-V semiconductors: at the interface of a gallium arsenide (GaAs) and aluminium gallium arsenide (AlGaAs) heterostructure a high mobility two-dimensional electron gas (2DEG) is formed. By applying voltages to surface gates electrically separated from the 2DEG, the 2DEG is locally depleted such that a region with only a few electrons is formed. As these charge traps confine the electrons in a localized, quasi zero-dimensional region, they are called quantum dots. This approach was a huge success, and GaAs/AlGaAs systems became the workhorse of the spin qubit community for more than a decade, leading to milestone experiments: confinement of a single electron [27], charge sensing with a quantum point contact [28–30], single-shot spin read-out [31, 32] and, finally, demonstration of single [33] and two-qubit gates [34]. The first spin manipulations, performed with the magnetic component of an AC current through a stripline close to the electron, showed a

spin-flip rate of 100 ns due to electric spin resonance (ESR) and a coherence time  $T_2^*$  of only 37 ns [33]. In GaAs,  $T_2^*$  is limited by the nuclear spins of the gallium and arsenic atoms of the host material. The individual magnetic fields from nuclear spins add up and dynamically modulate the Larmor frequency of the electron leading to decoherence.

While the  $T_2^*$  was underwhelming, the spin relaxation time  $T_1$  was measured to be 1 s, strongly depending on the external magnetic field, and is limited by the spin-orbit interaction in the system [35]. For over a decade the picture was that hyperfine limits  $T_2$  while spin-orbit interaction defines  $T_1$ . We show in Chap. 4 that  $T_1$  is also limited by the hyperfine interaction at low magnetic fields and were able to achieve a maximal spin relaxation time of  $57 \pm 15$  s – setting a record for electron spin lifetime in a nano-structure [35, 36]. Spin-orbit interaction mediated spin relaxation shows a strong dependence on the shape of the quantum dot. Therefore, we developed a method to extract not only the ellipsoidal shape but also the orientation with respect to the crystal axis of a quantum dot imprinted into the 2DEG. This new spectroscopy method is described in Chap. 3.

While  $T_1$  is long and not limiting spin qubit performance, the third DiVincenzo criteria was not fulfilled in GaAs systems because of the short  $T_2$ . Three approaches were pursued to overcome this problem: decoupling the electron spin from the nuclear spin bath, changing to material with less spin-noise, and increasing the manipulation speed. The  $T_2$  can be increased by decoupling the electron spin from the nuclear bath with spin-echo [37] and CPMG<sup>1</sup> pulse schemes developed by the NMR community and, recently,  $T_2 \sim 0.87$  ms was achieved in a lateral GaAs quantum dot [38]. In another route, the community started to implement qubits in group IV semiconductor like silicon and germanium, in which the main isotopes are nuclear spin free. Since the large semiconductor industry is based upon it, shifting towards silicon was a natural

---

<sup>1</sup>Carr-Purcell-Meiboom-Gill sequence

choice. In an Si/SiGe heterostructure spin qubit a bare  $T_2 \sim 1 \mu\text{s}$  was measured [39], an enhancement of two orders of magnitude compared to GaAs. However, due to the large effective mass of electrons in silicon, the devices had to become smaller, which is challenging in regards to the nano-fabrication of these devices. In a third approach, the spin manipulation speed was increased. While the stripline technology is still used [40, 41], an increased coupling to the electron spin via electronic dipole spin resonance (EDSR) was proposed in 2006 [42] and demonstrated in 2007 in GaAs [43]. In this scheme, the quantum dot is coherently displaced, which leads to a coupling to the spin mediated by spin-orbit interaction (SOI). Because SOI is weak, and possibly due to the anisotropy (direction dependence) of SOI in GaAs, only relatively slow spin-flip or Rabi frequencies  $f_R \sim 5 \text{ MHz}$  were achieved. To achieve such a spin-orbit qubit, experiments were successfully performed in materials with stronger SOI such as indium arsenide (InAs) ( $f_R \sim 60 \text{ MHz}$ ) [44, 45] and indium antimonide (InSb)  $f_R \sim 100 \text{ MHz}$  [46, 47]. These qubits are problematic in terms of scalability because they are hosted in individually-placed nanowires. Qubits in these III-V systems also suffer from hyperfine induced decoherence ( $T_2 \sim 10 \text{ ns}$  [44]), as discussed above.

In bulk silicon and germanium, there is only very weak SOI in the conduction band and it has to be introduced artificially by placing micro-magnets close to the qubit. With this method a Rabi frequency  $f_R \sim 35 \text{ MHz}$  was achieved in a Ge/Si [48] quantum dot and  $f_R > 50 \text{ MHz}$  was predicted for GaAs/AlGaAs quantum dots [49]. Recently, Kloeffel *et al.*[5] proposed a new mechanism of strong SOI, which was named direct Rashba spin-orbit interaction (DRSOI) due to the mathematical similarity to the Rashba SOI. Under certain circumstances, holes confined in a Si or Ge nanowire coupling to an external electric field give rise to this artificial SOI. Due to the coupling to an external field, the DRSOI is electrically tunable and can be turned off on demand to protect the qubit from decoherence due to charge noise [50]. While this type of SOI has not yet been demonstrated conclusively [51–54], a qubit exploiting this effect is advanta-



geous because its hosting material is isotopically purifiable and unmatched spin-flip times as short as 100 ps are predicted due to the strong and electrically tunable SOI. Hence, such a qubit would contain the enhancements of the routes discussed above. In Chap. 6, anisotropic lifting of the Pauli spin blockade in a germanium-silicon core-shell nanowire (Ge/Si NW) is presented and discussed. DRSOI was first predicted in these nanowires before the concept was extended to silicon nanowires. In Chap. 7, we study the formation of quantum dots in a potentially scalable, semiconductor industry conform, ambipolar fin field-effect transistors (FinFet). This fin structure serves as a NW, for which the presence of strong DRSOI is predicted if the channel width is smaller than  $\sim 15$  nm [6].

In this thesis, quantum dots in three systems are studied: electrons in a GaAs heterostructure, holes in Ge/Si NW and electrons, as well as holes in silicon FinFETs. The sequence of these topics mirrors the shift of the spin qubit research trends in the recent years: from investigations of spin and orbital effects in a GaAs quantum dot in Chap. 3-5, to research in an isotopically purifiable Ge/Si NW predicted to show strong, direct Rashba type of SOI in Chap. 6, towards an industry-compatible, scalable potential DRSOI spin qubit in a FinFET structure in Chap. 7. Finally, as a promising outlook for future experiments, in Chap. 8 the design of a measurement setup capable of spin qubit operations is discussed.

## 2 Background

The physics discussed in the different chapters of this thesis, was studied in semiconductor quantum dots: In Chap. 3 to Chap. 5, a lateral GaAs depletion-mode quantum dot was formed by gating a two-dimensional electron gas (2DEG). In Chap. 6 a depletion-mode hole double quantum dot was formed by gating a Germanium-Silicon core-shell nanowire. In Chap. 7, finally, gate voltages were used to energize accumulation-mode quantum dots in a silicon Fin Field-effect transistor (FinFET).

This chapter is organized as follows: in the first section, the formation of a 2DEG in a GaAs/AlGaAs heterostructure is discussed, before lateral quantum dots are introduced. On this basis, the physics and implications of Coulomb blockade and the confinement of the quantum dot is described. In the second section, a physical background on spin-orbit interaction is given. First the consequences of spin-orbit interaction on the band-structure of a semiconductor is described on an atomic level. Using a simplified Kane Hamiltonian, it is then demonstrated that mixing of valence and conduction bands leads to corrections of the effective mass, the g-factor and the emergence of an indirect spin-orbit interaction term for conduction band electrons. This correlates with the different physics studied in GaAs quantum dots in Chap. 3 to Chap. 5. Motivated by the work on Germanium-Silicon core-shell nanowire spin qubits such as discussed in Chap. 6, the theory of the direct Rashba type of spin-orbit interaction for holes in such a nanowire is summarized. This strong type of SOI was recently also predicted to emerge in narrow silicon nanowires such as the fins on which the fin field-effect single electron transistor devices presented in Chap. 7 were produced [6]. This paves the way for investigating scalable, industrial-suited direct Rashba spin-orbit qubits.

## 2.1 Quantum dots

In this section, the background of quantum dots is discussed. Although most of the concepts discussed here are valid for all types of quantum dots, this section is focused on lateral GaAs quantum dots. For those systems, the main idea is to use electric fields from voltages applied to surface gates fabricated on top of a GaAs wafer to locally tune the electron density of a two dimensional electron gas (2DEG) located inside the structure.

The metal-semiconductor interface of the metallic surface gate electrodes and the GaAs bulk form a Schottky barrier which acts as a diode [55]. When a positive voltage is applied to these gate electrodes, this diode is operated in forward direction and electrons in the semiconductor are attracted to the interface. This bends the conduction band downwards in energy which leads to a reduction of the Schottky barrier height and width. Because the current through a Schottky barrier depends exponentially on the width and height of the barrier, this reduction leads to an exponential increase of the current with applied voltage. Applying a negative voltage to the metal electrodes results in a repulsion of the electrons from the interface and bends the conduction band upwards in energy and thus increasing the height of the barrier. In absence of inadvertent leakage, there is no current flowing and the diode is operated in reverse direction. But the additional charges on the metal results in a reduction of charges in the semiconductor.

The basic concept of a field-effect transistor (FET) is to exploit this diode effect by controlling the conductance of a channel between a source and a drain contact with a metallic gate electrode. According to their state at zero gate voltage, transistors are classified into two categories: depletion and enhancement mode transistors. An enhancement mode device is intrinsically highly resistive ('Off' state) and a gate voltage has to be used to open a conductance channel ('On' state). The Fin Field-effect transis-

tor device discussed in Chap. 7 is operated in such an enhancement or accumulation mode. A depletion mode transistor, on the other hand, shows an intrinsic conductance ('On' state) and the charge carriers are depleted by means of electric fields created by voltages applied to the metallic gate electrodes ('Off' state). An example of this type of transistor is the junction FET (JFET). There, the semiconductor between the source and drain contact is doped to contain an excess of either electrons (n-type) or holes (p-type). This leads to a conduction channel which can be pinched off by applying voltages to a pn-junction serving as a gate electrode located on top or on the side of the transistor. The setup of such a depletion mode transistor is conceptually very similar to the technology used to form quantum dots inside a 2DEG or inside a Silicon-Germanium nanowire. Here, the conductive channel is replaced by either a two-dimensional electron gas (2DEG) or a nanowire and nanofabricated gate electrodes with widths  $\sim 50$  nm are used for local control of the electrostatic potential to define the confinement of the quantum dot.

### 2.1.1 Two-dimensional electron gas

GaAs is a group III-V compound semiconductor with Zincblende crystal structure and a direct band gap with energy  $E_g = 1.44$  eV. When substituting Gallium atoms with Aluminum, this band gap energy can be artificially increased up to  $E_g = 2.16$  eV, the band gap of AlAs [55]. Such a semiconductor compound is written as  $\text{Al}_x\text{Ga}_{1-x}\text{As}$  for which  $x$  is the Aluminum concentration. For the structures used to perform the GaAs experiments presented in this thesis, a very common concentration of  $x = 0.3$  was used. In this case, the conduction band of  $\text{Al}_{0.3}\text{Ga}_{0.7}\text{As}$  is 300 meV above that of GaAs [55].

The interface of GaAs and  $\text{Al}_x\text{Ga}_{1-x}\text{As}$  builds a heterojunction<sup>2</sup>. At this heterojunction, a triangular quantum well in the conduction and valence band is formed.

---

<sup>2</sup>A heterojunction is a junction of two materials with different band gaps while in a homojunction the band gaps are similar.

This confinement leads to quantization of the energy states into sub-bands inside the quantum well. As a result, the electrons which occupy these sub-bands can only move freely in the plane parallel to the heterojunction. As shown in Chap. 3, for the lowest subband, the spatial extension of the wave function perpendicular to the interface is only  $\sim 7$  nm. This strong confinement leads to a large subband splitting such that only the lowest subband is occupied at temperatures below  $\sim 100$  K. Together with Graphene, AlGaAs/GaAs heterostructures are among the best experimental realizations of a two dimensional system at such low temperatures. In analogue to the Fermi gas, such systems are referred to as two dimensional electron gas. Because GaAs and AlAs have a very similar lattice constants with a mismatch of less than 0.5%, GaAs/ $\text{Al}_x\text{Ga}_{1-x}\text{As}$  interfaces do not disrupt the crystal periodicity across the interface. The lack of induced strain allows for a large mobility of the charge carriers when compared to interfaces with strain such as SiGe ( $\sim 5\%$  mismatch) or disordered interfaces like Si/SiO<sub>2</sub> in which SiO<sub>2</sub> crystallizes into a chaotic, glassy phase.

A schematic of the wafer profile used in the GaAs quantum dot experiments is shown in Fig. 2.1a . These structures are grown by molecular-beam epitaxy (MBE) on top of GaAs bulk crystal. On top of the bulk, first a super lattice structure is grown. This periodic sequence of 3 nm GaAs and 3 nm  $\text{Al}_{0.3}\text{Ga}_{0.7}\text{As}$  is implemented to release stress in the crystal which results in an increase of the charge carrier mobility in the 2DEG. After 800 nm GaAs serving as a buffer, the GaAs/ $\text{Al}_{0.3}\text{Ga}_{0.7}\text{As}$  interface which contains the 2DEG is grown. On top of the interface, 100 nm of  $\text{Al}_{0.3}\text{Ga}_{0.7}\text{As}$  is grown before a 10 nm GaAs cap layer is added to prevent oxidation of the aluminum in the AlGaAs compound. Semiconductors are intrinsic insulators at low temperature. Therefore, a layer of localized Silicon atoms with a concentration of  $4 \cdot 10^{12} \text{ cm}^{-2}$  serves as a remote doping of the 2DEG. This  $\delta$ -doping layer is setback by 40 nm from the 2DEG and is embedded into the AlGaAs during the MBE growth. When cooled down, some of these Silicon atoms provide electrons to the 2DEG and are left ionized. For the 2DEG under

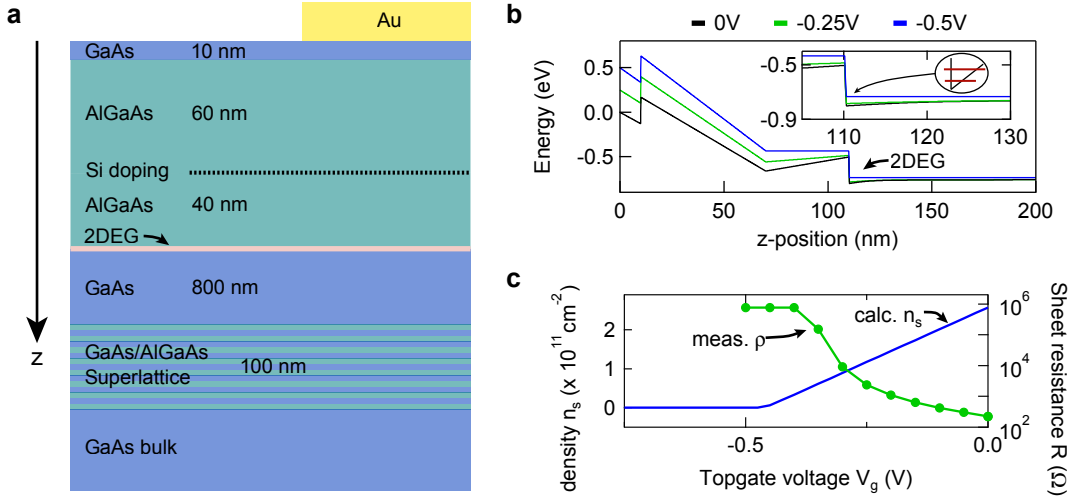


Figure 2.1: (a) Schematic representation of the GaAs/AlGaAs heterostructure used in the experiments. The two-dimensional electron gas (2DEG) is formed 110 nm below the surface at a GaAs/AlGaAs interface. Silicon atoms in a  $\delta$ -doping layer serve as a remote doping and provide electrons to the 2DEG. The gold (Au) implies the position of a top or surface gate. (b) Calculated valence band structure using the Schrödinger-Poisson solver AQUILA for different surface potentials imitating voltages applied to a top gate. In the inset, a schematic of the resulting triangular potential well with two subbands (red) is sketched. (c) Calculated sheet density  $n_s$  and measured sheet resistance  $\rho$  for different top gate voltages. In good agreement, both, the model as well as the experiment, indicate a complete depletion of the 2DEG for a top gate voltage of  $-0.45$  V.

consideration, the electron sheet density was determined to be  $n_s \sim 2.8 \cdot 10^{11} \text{ cm}^{-2}$  with a mobility of  $\mu \sim 4 \cdot 10^5 \text{ cm}^{-2}/\text{Vs}$ . Because the donors are spatially separated from the 2DEG, scattering at the Coulomb potentials of the ionized donors is mitigated. In comparison to conventionally doped structures, this remote doping technique allows for larger mobilities and scattering lengths of the charge carriers.

For practical reasons, e.g. to estimate the Rashba spin-orbit interaction [56], it is useful to calculate the band-structure of the heterostructure. Generally, it is not trivial to reproduce the band structure at a heterojunction: to achieve a steady state, electrons flow in between the materials to align the bands of both materials. This gives rise to electric fields which leads to a bending of the valence and conduction bands. Because the electron density and the electrostatic potential in such an interface are mutually

dependent, a self-consistent solution of the Schrödinger-Poisson has to be found. This is performed numerically until a convergence criterion is achieved: First the Schrödinger equation for an input electrostatic potential is solved which yields a set of wave functions for the electrons. From this wave functions, an electron density is calculated. Solving the Poisson equation for this electron density, leads to a new electrostatic potential, the output potential. A third potential, a mixture of the initial and the calculated potential, is then used to once more calculate a set of wave functions using the Schrödinger equation. A self-consistent solution is found, when the difference between the input and output potential is below a set threshold. As a result, the electron density and the electrostatic potential is obtained.

The black curve in Fig. 2.1b shows the calculated potential of the valence band for the structure of Fig. 2.1a using the MATLAB based Schrödinger-Poisson solver AQUILA for AlGaAs/GaAs heterostructures. The z-position correspond to the displacement from the surface of the crystal in the growth direction (see Fig. 2.1). Three distinguished local minima are recognized in the band structure: first at the interface between the GaAs cap and the AlGaAs (10 nm), then at the delta-doping layer (70 nm) and finally, the triangular potential well forming the 2DEG (110 nm). Note that the super lattice is not shown in this figure. Because the calculated sheet density was underestimated by the Schrödinger-Poisson solver, the doping concentration in the simulation had to be adjusted to match the experimentally found value. The validity of these calculation is reviewed by comparing the simulated and experimentally measured dependence of the the electron sheet density on an external electric field applied on a top gate. The calculated band structure for different electric fields is shown in Fig. 2.1b and in Fig. 2.1c the resulting, calculated sheet density  $n_s$  is presented by the blue curve. With more negative voltage, the 2DEG sheet density is reduced which leads to a reduction of the triangular potential well depth. At  $V_g \sim -0.45$  V the 2DEG is completely depleted.

To review these calculations, the dependence of  $n_s$  on the electric field obtained from

the Schrödinger-Poisson is compared to an experiment where the 2DEG is depleted with a metallic gate electrode. Therefore, a Ti/Au top gate was deposited on top of the Hall bar and serves as a global top gate. Note that the width and length of this top gate is very large ( $140\ \mu\text{m} \times 360\ \mu\text{m}$ ) compared to the nanometer-scale surface gates which are later used to energize the quantum dots. Thermally annealed GeAu/Pt ohmic contacts build a low-ohmic ( $< 50\ \Omega$ ) electronic connection to the 2DEG. With standard lock-in techniques, the sheet resistance of the 2DEG is determined as  $\sim 220\ \Omega$  in a four probe measurements. Then, the dependence of the sheet resistance on the voltage applied to the top gate is monitored. As shown in Fig. 2.1c, the resistance increases before it saturates at  $\sim 700\ \text{k}\Omega$ . This increase is understood as a field effect induced reduction of the sheet density  $n$  which leads to an increase of the electrical resistivity  $\rho$ . This is well represented by the Drude model where  $\rho = 1/(en\mu)$  with  $\mu$  being the electron mobility<sup>3</sup>. In good agreement with the simulation, the 2DEG depletes at around  $\sim -0.45\ \text{V}$ . From this agreement it is concluded, that the solutions of the Schrödinger-Poisson solver accurately represents the band-structure of the GaAs heterostructure used in the experiments.

### 2.1.2 Lateral quantum dots

By fabricating an appropriate gate pattern on top of the GaAs crystal with an embedded GaAs/AlGaAs 2DEG such as mentioned in Fig. 2.1, a nanometer scaled quantum dot connected to two reservoir can be formed by imprinting the gate pattern into the 2DEG. A schematic of such a device is shown in Fig. 2.2. In this gate design, the plunger gates labeled LP, CP and RP are used to deplete the 2DEG on the bottom part of the device, while the left (LW) and right (RW) wall gate electrodes are used to define the confinement in the horizontal direction of the device. Finally, the nose gate electrode (N) is used to define the confinement on the topside. The voltage between N

---

<sup>3</sup>Note that a reduction of  $n$  often leads to a reduction of the mobility  $\mu$  and these effects can not be distinguished in this simple measurement.



and LW defines a tunnel barrier to the left reservoir. Likewise, the right tunnel barrier is defined by N and RP. The two separation gate electrodes (SEP) are used to form a pointy reservoir which is electrostatically separated from the left respectively right side of the device. The reservoirs and gate electrodes are connected to the external electronics which allows to apply voltages. If the voltages at all the gate electrodes is adjusted properly, a quantum dot, tunnel coupled to the two reservoirs is energized. By applying a bias voltage to one of the reservoir, a current through the quantum dot is drained into the other reservoir. Following the terminology used for transistors, the reservoirs are denominated as source and drain (contact), whereas electrons always flow from source to drain. Because the quantum dot is laterally coupled to the source and drain, such systems as shown in Fig. 2.2 are referred to as lateral quantum dot devices. There are also vertical quantum dot devices, in which the quantum dot is defined in between the source and drain contact in a stacked structure [57, 58].

### 2.1.3 Coulomb blockade

As discussed in the previous section, a quantum dot is an object in which the energy of the available states is quantized due to spatial confinement. Therefore, it is often regarded as a physical representation of the famous particle in a box problem of quantum mechanics. These discrete levels can be filled with electrons according to the Pauli exclusion principle such that a well defined number of electrons  $N$  is confined in the dot<sup>4</sup>. Therefore, quantum dots are also often referred to as artificial atoms.

To understand quantum dots and to comprehend why they are interesting to investigate, it is inevitable to discuss the concept of Coulomb repulsion and its significance in these systems. For a disk shaped quantum dot with radius  $r$ , similar to the dot shown

---

<sup>4</sup>Quantum dots can also be filled with holes (see Chap. 6 and 7). In traditional GaAs heterostructures as discussed here, however, the charge carriers are electrons originating from Silicon atoms localized in the  $\delta$ -doping layer (see Sec. 2.1.1)

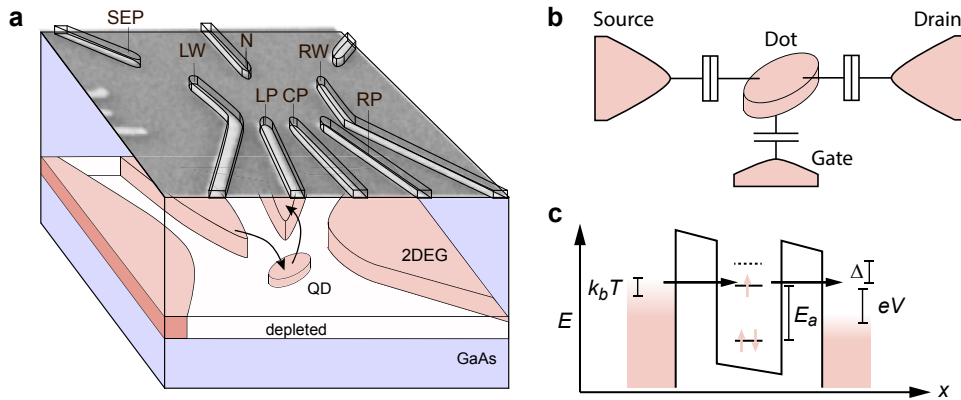


Figure 2.2: (a) Sketch of a lateral quantum dot formed by voltages applied to nanoscale gate electrodes locally depleting a GaAs two-dimensional electron gas (2DEG). The dot is tunnel coupled to two reservoirs such that electrons can be transported through the quantum dot upon applying a bias voltage. (b) Lumped element representation of a quantum dot, tunnel coupled to a source and a drain reservoir and capacitively coupled to a gate. The tunnel junctions can be represented as a tunnel resistance in parallel to a mutual capacitance between the respective reservoir to the quantum dot. (c) Energy representation of a quantum dot. On the left and right side are the reservoirs which are separated from the quantum dot by tunnel barrier potentials. Here, red color imply occupied states which follow a Fermi-Dirac distribution. Therefore, in a window of  $\sim k_B T$  around each chemical potential of the reservoirs, the states are only partially filled. The addition energy  $E_a$  to add an electron on the dot is the Coulomb energy  $E_C$  plus eventually the orbital energy  $\Delta$  if all degenerated states of the previous orbital are filled and a new orbital is started to become occupied.

in Fig. 2.2a, the capacitance is

$$C = 8\epsilon_0\epsilon_r r \quad (2.1)$$

where  $\epsilon_0\epsilon_r$  is the absolute permittivity [59]. Assuming a size of  $r = 25$  nm results in a capacitance of  $C = 22.8$  fA<sup>5</sup>. Because of this capacitance, an energy

$$E_C = e^2/2C \quad (2.2)$$

is required to add another electron with charge  $e$  to the quantum dot. This Coulomb repulsion energy or charging energy becomes substantial for small objects as  $E_C \propto r^{-1}$ . For the example used above  $E_C \approx 4$  meV which corresponds to a thermal energy  $k_B T$  of a temperature  $T \approx 46$  K where  $k_B$  is the Boltzmann constant. Therefore, if such a quantum dot device is cooled to low enough temperatures such that  $k_B T \ll E_C$ , single electron charging of the quantum dot is observed. It is this energy  $E_C$  which leads to the effect of Coulomb blockade and, therefore, makes quantum dots such an interesting system as a rather large energy is necessary to load an additional electron.

Up to here, only the concept of charging a model island was discussed. But in real devices, quantum dots are usually tunnel coupled to two reservoirs called source and drain contacts, and have a mutual capacitance to one or more gate electrode. A schematic is presented in Fig. 2.2b. Tunnel junctions are typically characterized by two elements: a capacitance and a tunnel resistance. Therefore, the total capacitance of the system  $C_{\text{tot}}$  is the sum of the capacitances

$$C_{\text{tot}} = C_S + C_D + C_g, \quad (2.3)$$

where  $C_S$ ,  $C_D$  and  $C_g$  are the mutual capacitance between the dot and source contact, drain contact and plunger gate, respectively. Using these capacitances, the total energy

---

<sup>5</sup>In GaAs, the relative permittivity is  $\epsilon_r = 12.9$ .

$U$  of a dot with  $N$  electrons is [60]

$$U(N) = \frac{(-|e|N + C_S V_S + C_D V_D + C_g V_g)^2}{2C_{\text{tot}}}. \quad (2.4)$$

Here,  $V_{S,D,g}$  denotes a voltage applied to the source, drain and gate electrode, respectively. It follows from Eq. (2.4) that the electrostatic potential on the dot can be continuously changed by applying voltage on the gate  $V_g$  as well as on the source and drain contacts. In a lateral quantum dot as discussed here (Fig. 2.2a), gating with  $V_g$  corresponds to a change of the confinement potential which leads to a shift of the quantum dot energy levels with respect to the chemical potential of the leads. Note that the model presented in Eq. (2.4), also referred to as the constant interaction model, is based on two assumptions: First, it is assumed that all Coulomb interactions involved in the system can be parametrized with capacitances. And secondly, the single-particle energy spectrum, or orbital spacing, is independent of the number of electron on the quantum dot [60].

The schematic presented in Fig. 2.2b resembles a transistor device: when a bias voltage  $V_{SD} = V_S - V_D$  is applied between the source and drain contact, a current is flowing from source to drain if a quantum dot level is in the bias window. For the discussion here, it is assumed that the source contact is negatively biased and the drain contact is on the ground potential which results in an energy diagram as presented in Fig. 2.2c. In this arrangement, the chemical potential for electrons in the source contact is larger by  $-|e|V_{SD}$  than for electrons in the drain such that electrons are generally transported from source to the drain. Applying a bias voltage of opposite polarity inverts the transport direction and results in a sign change of the measured current. In the low-bias regime ( $V_{SD} < E_C$ ) only one electron at the time is allowed pass the system because the charging energy  $E_C$  blocks the addition of a second electron to the quantum dot. This situation is depicted in Fig. 2.2c and a device operated in this limit is referred to as a single electron transistor (SET), again showing the close relation to the transistor.

To contribute to the transport signal, an electron has to tunnel two times in a sequential order: from the source contact into the quantum dot and then from the quantum dot into the drain contact. Because there are no free states available in the source contact at the energy of the quantum dot level (see Fig. 2.2), an electron which tunnels on the quantum dot is prohibited from tunneling back into the source contact. But given the bias voltage  $V_{SD}$ , there are free states available in the drain contact such that the electron can tunnel out of the quantum dot and thermalize with the electrons in the Fermi sea of the drain reservoir. In this process, the excessive energy is emitted e.g. by a phonon or a photon.

When the level through which the electrons are transported is brought below the chemical potential of the drain, no electrons can flow through the device due to lack of free states in the drain reservoir. The loaded electron will rest on the dot and will block further transport because the electrons in the source have not enough energy to overcome  $E_C$ . This effect is called Coulomb blockade and can be lifted by either gating the blocked or the next energetically higher level into the bias window or by increasing bias voltage until the next level is energetically accessible for transport. This leads to diamond-shaped regions of blocked transport when  $V_{SD}$  and  $V_g$  are scanned against each other. An example in which Coulomb diamonds are observed in the conductance  $G$  through a lateral quantum dot device similar to the one shown in Fig. 2.2a is presented in Fig. 2.3. For this measurement, the exact number of electrons on the quantum dot is not known. Therefore, the white labels in Fig. 2.3a only indicate the number of electrons relative to an arbitrarily chosen Coulomb diamond with occupation  $N$ .

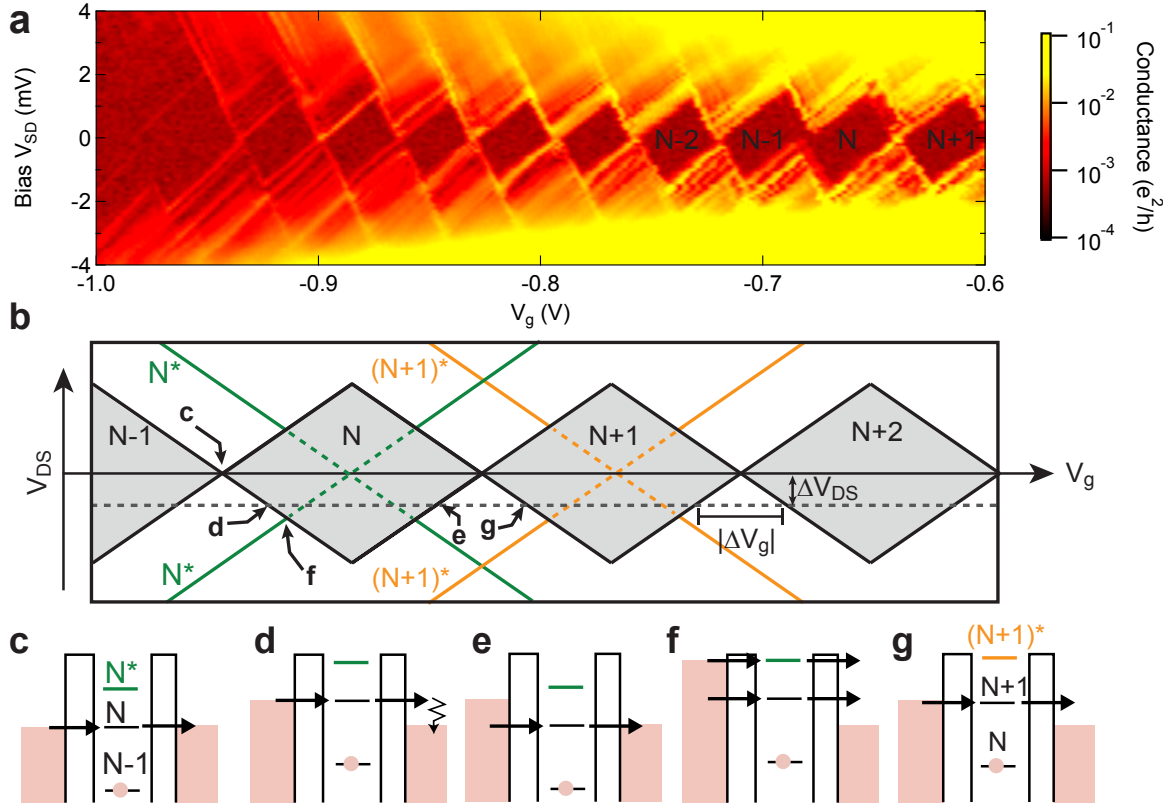


Figure 2.3: (a) Measurement of the conductance through a lateral quantum dot device as a function of source-drain voltage  $V_{SD}$  and gate voltage  $V_g$  features Coulomb diamonds, regions of blocked transport due to Coulomb blockade. Inside the Coulomb diamonds, the number of electrons in the quantum dot is fixed. The labels inside the diamonds indicate the number of electrons on the dot relative to an arbitrarily chosen Coulomb diamond with occupation  $N$ . With more negative  $V_g$ , the number of electrons on the quantum dot is successively decreased when the boundary of the next diamond is crossed. (b) Illustration of Coulomb diamonds with labels of different situations described in the energy diagrams given in (c)-(d). Transport is blocked in the gray regions. The green line represents an excited orbital state  $N^*$  of quantum dot level  $N$  and the orange line for the  $(N+1)$ -th level [61]. The extension of these lines into the blocked region (dashed line) merge to a single point at  $V_{SD} = 0$ . The black dashed line illustrates a cut in  $V_{SD}$  along which energy diagrams for different characteristic points in  $V_g$  are shown in (d), (e) and (g). The lever arm  $\alpha_g$  of the gate is  $\alpha_g = \Delta V_{DS}/|\delta V_g|$  and can be read directly from the Coulomb diamond measurement [62].

### 2.1.4 Confinement potential

Coulomb repulsion and therefore also Coulomb blockade, is a classical effect because it originates from the electrostatic energy of a loaded capacitor. The discrete energy levels

of a quantum dot, on the other hand, can only be described by quantum mechanics. The confinement of a lateral GaAs quantum dot can be separated into two parts: a very narrow confinement  $V_z$  along the growth direction  $\hat{z}$  (see Fig. 2.1, which results in the two dimensional electron gas, and a weaker, perpendicular confinement  $V_{2D}$  in the plane of the electron gas. As described in Sec. 2.1.1, the conduction band at a GaAs/AlGaAs heterojunction forms a triangular potential well. The subbands, the discrete energy levels due to this confinement, contribute, if occupied, to the 2DEG. The devices in our experiment were measured at cryogenic temperatures ( $T \ll 1$  K), and for the heterostructure used, only the lowest subband is occupied.

As we experimentally show in Chap. 3 for a lateral GaAs few-electron quantum dot, the in-plane confinement is well described by an anisotropic harmonic oscillator. Therefore

$$V_{2D}(x, y) = \frac{\hbar^2}{2m^*} \left( \frac{x^2}{l_x^4} + \frac{y^2}{l_y^4} \right) \quad (2.5)$$

$$\begin{aligned} V_z(z) &= V_0 && \text{if } z < 0 \\ V_z(z) &= eE_{\text{ext}}z && \text{if } z > 0, \end{aligned} \quad (2.6)$$

where  $l_{x,y}$  are the two confinement lengths along the  $x$  and  $y$  direction respectively,  $m^*$  is the effective mass of the electron,  $E_{\text{ext}}$  is the interface electric field, which typically arises from the remote doping layer, and  $V_0$  the band offset between GaAs and GaAs/Al<sub>0.3</sub>Ga<sub>0.7</sub>As (see Sec. 2.1.1). The anisotropic harmonic confinement potential described by Eq. (2.5) represents an ellipse with semi-axes of length  $l_x$  and  $l_y$ . An illustration of the confinement potentials is given in Fig. 2.4.

Solving the Schrödinger equation for linear quantum mechanical harmonic oscillator with angular frequency  $\omega$  leads to levels equidistant in energy and the energy of the  $n$ -th level is  $E_n = \hbar\omega(n + 1/2)$ . Analogue to the classical case, the spectrum of two independent linear quantum harmonic oscillators add up, such that in the case here  $E_{n_x, n_y} = \hbar\omega_x(n_x + 1/2) + \hbar\omega_y(n_y + 1/2)$ . The energy solutions for the triangular potential

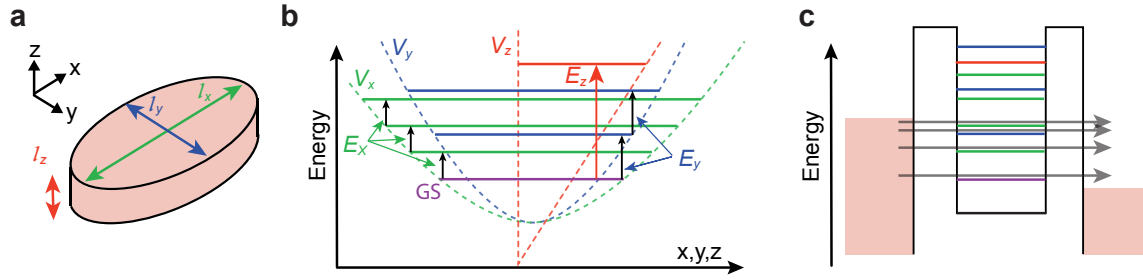


Figure 2.4: (a) Sketch of a quantum dot with strong confinement along  $z$  and an elliptic confinement in the  $x$ - $y$ -plane. (b) The dashed curves illustrate the confinement potentials  $V_{x,y,z}$  along  $x$ ,  $y$  and  $z$  and the solid lines show the energies of the quantum dot excited orbital states. A triangular potential well is formed along the  $z$  direction and defines a 2DEG in the  $x$ - $y$ -plane. In the 2DEG, the dot confinement is given as two independent harmonic potentials. The sketch is not true to scale – in reality  $E_z \sim 10 \cdot E_{x,y}$ . While the ground-state (GS) of the quantum dot is a mixture of the ground states of the individual confinement potentials, each direction contributes a separate set of energy eigenstates whereas the energy separations,  $E_x$ ,  $E_y$  and  $E_z$ , depend on the details of the corresponding confinement. (c) In a simple transport measurement, the excited states are opening up additional conductance channels. The single-particle energy ladder of the quantum dot with broken spherical symmetry, as shown here, leads to a complex transport signal and it is difficult to assign the observed excited state energies to the individual potentials.

also result in an energy ladder, namely  $E_{n_z} = - (e^2 E_{\text{ext}} \hbar^2 / (2m^*))^{1/3} a_{n_z}$  where  $a_n$  is the  $n$ -th zero of the Airy function. The potentials along the three coordinates  $x$ ,  $y$ , and  $z$  separate and can be treated individually such that the three individual state energies add up. For the confinement of the quantum dot described by Eq. (2.5) and Eq. (2.6), the Hamiltonian is  $H = H_{2\text{D}} + H_z$  and the three energy ladders sum up. As a consequence, the ground state of the quantum dot is a mixture of the ground states of the three individual confinements ( $n_x = n_y = n_z = 0$ ). From the ground-state each of the three confinements contributes with its own ladder of allowed energy states (see Fig. 2.4b). An external magnetic field couples these potentials such that they cannot be treated separately anymore. This effect is discussed in Chap. 3 for the coupling of the orbitals of a single-electron quantum dot.

For a discussion on which excited states will be filled first, it is useful to characterize



the potentials in terms of their length scales. For the potentials discussed here,

$$\hbar\omega_{x,y,z} = E_{x,y} = \hbar^2/m^*l_{x,y,z}^2 \quad (2.7)$$

and the  $E_{x,y}$  is the energy difference of harmonic oscillation ladder, and  $E_z$  the subband excitation energy<sup>6</sup>. In a typical GaAs lateral quantum dot and as presented in Chap. 3, we find  $l_x \sim l_y \sim 20$  nm while  $l_z \sim 6.5$  nm which results in a shape as represented by the schematic of Fig. 2.4a. Because the energy scales with the inverse of the length squared,  $E_{x,y} \ll E_z$  as implied in Fig. 2.4b and c. Note, that from the experiment  $E_{x,y} \sim 2.5$  meV and  $E_z \sim 30$  meV, such that in practice the difference of these energy scales even larger than shown in the Figure.

Qualitatively, the filling of a quantum dot was already discussed in Sec. 2.1.3 when only the classical Coulomb energy  $E_C$  is considered. Here, this discussion is extended for the realistic case that electrons with spins are loaded into the different orbitals defined by the confinement of the quantum dot. When filling the quantum dot of Fig. 2.4, the single-particle states are successively filled with electrons according to the Pauli principle: the first electron occupies a spin-up state<sup>7</sup>. To fill the next electron, the Coulomb repulsion energy  $E_C$  has to be paid<sup>8</sup> (see Fig. 2.2). The second electron will occupy the spin-down state of the orbital ground state. For the third electron, in addition to  $E_C$  also the orbital energy  $E_x$  is required to load it into the spin-up state of the first  $x$ -excited state (Fig. 2.4b). As presented in Fig. 2.3, the energies involved to add electrons to a quantum dot can be probed with transport measurements. In see Fig. 2.4c, the transport in the high bias regime through a quantum dot with a complicated orbital structure is schematically depicted. Such measurements allow to

<sup>6</sup>In contrast to  $E_{x,y}$ ,  $E_z$  is changing for higher subbands. Because the higher subbands are not occupied, only the first 2DEG subband is considered. Therefore, the length-scale  $l_z$  is associated only to the lowest subband excitation.

<sup>7</sup>In GaAs the g-factor is negative, therefore spin-up becomes the spin ground state.

<sup>8</sup>Additionally, also the Zeeman energy must be paid and therefore taken into account. But for the magnetic field scales of this thesis, this energy is very low  $\sim 25$   $\mu$ eV/T compared to the orbital energies  $\Delta$  or Coulomb repulsion energy  $E_C$  and therefore neglected for these considerations.

draw conclusions on the orbital degeneracies as well as on the involved confinement potentials and therefore on the quantum dot shape. In a symmetric quantum dot ( $E_x = E_y \ll E_z$ ), for example, the first excited orbital state is four-fold degenerate [57, 63] but if this symmetry is broken and the first excited orbital state is only spin, hence two-fold, degenerate (see Chap. 3).

In lateral quantum dots, the confinement in the plane of the 2DEG is defined by electric fields stemming from the gate electrodes of a fabricated gate layout. Therefore, this quantum dot confinement is electrically tunable. As a consequence, the shape of such quantum dots can be controlled *in situ* which allows to investigate shape dependent physics [35]. This shape manipulation is demonstrated in Chap. 3. This control also enabled the formation of a symmetric in-plane confinement of the quantum dot ( $E_x = E_y \gg E_z$ ) which simplified the interpretation of the experimental observations presented in Chap. 4.

### 2.1.5 Numerical simulations of the device potential

When dealing with GaAs/AlGaAs lateral quantum dots, a suitable layout of the surface gates is a major factor for the performance of the device. For the investigations presented in this thesis, it was essential to optimize a layout which allows to significantly tune the shape of a single-electron quantum dot. Because such a tunability was already achieved in the device used in Ref. [35], the layout was adapted from there. To reduce the amount of iterations by time-consuming experimental testing of small adjustments in the design of the gate layout, a finite element method was developed to simulate the electrostatic potential landscape expected from an input gate layout.

Therefore, an approximate solution of the Poisson-Schrödinger equation as proposed by Davies *et al.* [64] was used to calculate the contribution of each gate at every finite element of the 2DEG. In this approximate solution, the potential  $\phi$  at  $\mathbf{r}$  for a 2DEG

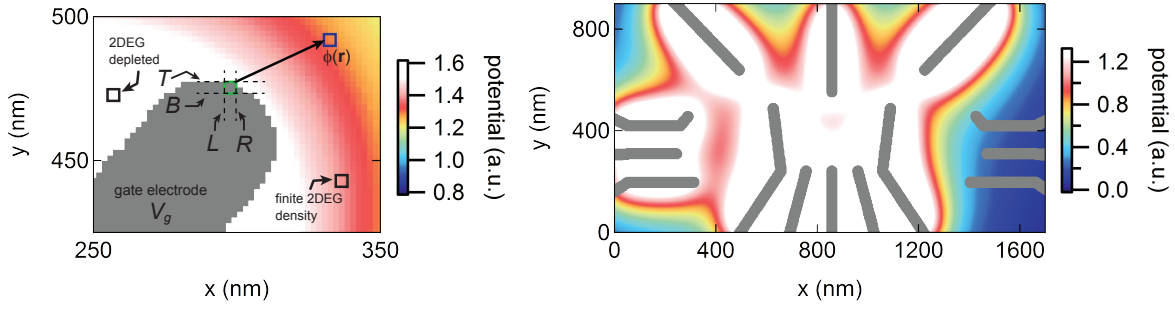


Figure 2.5: (a) Illustration of the finite element method to calculate the contribution of a rectangular gate segment with coordinates  $B$ ,  $T$ ,  $L$  and  $R$  to the electrostatic potential  $\phi$  at position  $\mathbf{r}$  of the 2DEG. (b) Calculated potential for an energized DALL v7 device. While the white regions correspond to a completely pinched 2DEG, blue sections show the intrinsic electron sheet density. In gray, an overlay of the gate design used for the calculations is shown. The quantum dot (middle) and the sensor quantum dot (left) are recognized. For this configuration, the left side of the device was not energized.

situated at a distance  $d$  underneath the surface is given by

$$\phi(\mathbf{r}, d)V_g = g(x - L, y - B) + g(x - L, T - y) + g(R - x, y - B) + g(R - x, T - y), \quad (2.8)$$

where  $V_g$  is the applied voltage while  $L$ ,  $R$ ,  $B$ ,  $T$  are the coordinates of the edges of the finite element gate electrode segment and

$$g(u, v) = \frac{1}{1\pi} \arctan \left( \frac{uv}{d\sqrt{u^2 + v^2 + d^2}} \right). \quad (2.9)$$

An illustration of the finite element method is shown in Fig. 2.5a. Because Eq. (2.8) only gives an approximate solution of the Poisson-Schrödinger equation and are therefore not self-consistent. Nevertheless, this simplified approach was very helpful to optimize the gate layout of the quantum dot devices. The total electrostatic potential at each 2DEG segment is obtained by summing up all individual gate contributions. Because in this model, the potential  $\phi$  is proportional to the gate voltage  $V_g$  (see Eq. (2.8)), the resulting potential of each gate is calculated individually such that it

can then be scaled by the applied voltage. When changing a voltage, the respective potential of the corresponding gate is scaled before all potentials are added together again. This is a fast operation because no electrostatic potentials have to be recalculated after the initial calculation. Therefore, it is also possible to tune the electrostatic potential of the simulated device in real-time to find a configuration of interest. This also simplified tuning of cooled down devices because the electrostatic potential landscape could be simulated and analyzed in parallel to the experiment. This tool was particularly helpful to effectively coordinate all involved gates to define quantum dot shape manipulations (see Chap. 3). A simulation of the total electrostatic potential resulting from the gate layout and individual gate voltages used for the device discussed in Chap. 3, 4 and 5, is presented in Fig. 2.5b.

## 2.2 Spin-orbit interaction

This section is motivated by the significance of spin-orbit interaction (SOI) in this thesis and covers the effect of SOI on the band-structure. In this process, it first motivates the use of holes rather than electrons in spin qubits. Then, the effect of inter-band mixing which gives rise to SOI in the conduction bands is discussed. The long spin relaxation times obtained in GaAs quantum dots such as shown in Chap. 4 are a consequence of this indirect SOI. Interestingly, it is the same higher-order physics which leads to corrections of the electron mass and spin g-factor. Motivated by the goal to achieve a spin-orbit spin qubit, subsequently, a simplified physical discussion on the emergence of direct Rashba type of SOI in confined hole systems is given.

SOI couples the spin and orbital degree of freedom of a charged particle. In an atom, this kind of coupling is a direct consequence of the Dirac equation. When the Dirac equation is non-relativistically approximated up to order  $(v/c)^2$ , the Pauli spin orbit (SO) term

$$H_{SO} = \frac{\hbar}{4m_0^2c^2} \boldsymbol{\sigma} \cdot (\mathbf{p} \times \nabla V) \quad (2.10)$$

is obtained [65]. Here,  $V$  is the potential of an electric field  $\mathcal{E} = (1/e)\nabla V$ ,  $\boldsymbol{\sigma}$  the Pauli spin vector,  $\mathbf{p}$  the momentum,  $m_0$  the bare mass of the particle and  $c$  the speed of light. If a central potential  $V_c(r)$  acts on the particle, the Pauli SO term becomes

$$H_{SO} = \frac{\hbar}{4m_0^2c^2} \left( -\frac{1}{r} \frac{dV}{dr} \right) \boldsymbol{\sigma} \cdot (\mathbf{x} \times \mathbf{p}) = \frac{1}{2m^2c^2} \frac{1}{r} \frac{dV}{dr} \mathbf{L} \cdot \mathbf{S}, \quad (2.11)$$

with the spin operator  $\mathbf{S} = \hbar\boldsymbol{\sigma}/2$  and the orbital angular momentum operator  $\mathbf{L} = \mathbf{x} \times \mathbf{p}$  [66]. For electrons in an atom, the central potential is a decent description of the electric field arising from the positive nuclei and  $H_{SO}$  leads to a splitting of the spectral lines known as *fine structure*. Because the electric field scales with atomic charge  $Z$ ,  $H_{SO}$  becomes stronger for heavier elements of the periodic table.

SOI is also present in solid state materials and has a profound effect on the band structure [67]. In Fig. 2.6a a schematic of a simplified semiconductor band structure close to  $k = 0$  is shown. It resembles the dispersion relation of the bands in GaAs close to  $\Gamma$  point, the center of the first Brillouin zone. At low energies, the dispersion  $E(k)$  of the individual bands is well approximated by the effective mass model where the kinetic energy of charge carrier in the semiconductor is the same as for a free particle but with a different mass. Then, the dispersion is  $E(k) = \hbar^2 k^2 / (2m^*)$  where  $m^*$  is the effective mass of the particle in the corresponding band.

In most semiconductors, the upper bands originate from s-type atomic orbitals and are called conduction bands. They are separated from the valence bands by the energy gap  $E_g$ . These valence bands arise from p-type atomic orbitals [68]. As a consequence, the states in the conduction bands (see Fig. 2.6a) have an orbital angular momentum quantum number of zero ( $L = 0$ ). In an envelope function approximation this corresponds to an s-symmetry in the lattice-periodic part of the Bloch wave function resulting in a particle wavefunction as schematically presented in in Fig. 2.6b [67, 69]. The Bloch wave function then has maximal amplitude at the position of the nuclei of the host material. The states in the valence band, on the other hand, have a lattice-periodic function with p-type symmetry ( $L = 1$ ) and the Bloch function has minima at the positions of the nuclei. Therefore, the contact hyperfine interaction is strongly suppressed for holes when compared to electrons. Therefore, changing spin qubit host to holes increases the coherence time for a system in which the electron spin decoherence is dominated by hyperfine interaction [69, 70].

From Eq. (2.11) it is recognized that SOI results in an additional energy  $H_{SO} \sim \mathbf{L} \cdot \mathbf{S}$ . Because  $L = 0$  for conduction band states, no correction is expected for the conduction bands but the valence bands are expected to split. For the valence bands the total angular momentum  $J = L + S$  must be considered as quantum number [71]. Because  $|L - S| < J < L + S$ , the valence bands splits into  $2 \times 2$  bands with  $J = 3/2$  and

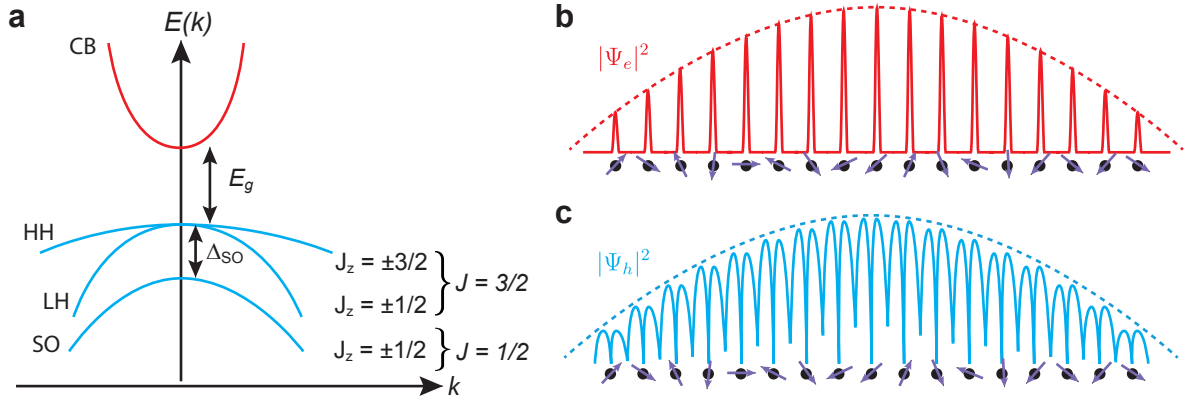


Figure 2.6: (a) Band structure around the  $\Gamma$ -point in the effective mass approximation for which the states are described by parabolic bands. While the conduction band (CB) is spin degenerate, the valence band which is separated by the fundamental gap  $E_g$ , is originally sixfold degenerate whereas at the  $\Gamma$ -point, the spin-orbit split off band (SO) is energetically lowered by the spin-orbit splitting  $\Delta_{SO}$  from the degenerate heavy hole (HH) and light hole (LH) bands. (b) Schematic illustration of the electron wave function (red curve) which is largely constructed from atomic s-orbitals. The dashed curve illustrates the envelope function. (c) Illustration of the hole wave function which is largely constructed from atomic p-orbitals. For holes, the probability density has minima at the location of the nuclei. (b) and (c) are adapted from Ref. [69].

$1 \times 2$  bands with  $J = 1/2$ . The spin-orbit split off band has  $J = 1/2$  and is twofold degenerated ( $J_z = \pm 1/2$ ). It is separated from the fourfold degenerate  $J = 3/2$ -bands with  $J_z = \pm 1/2$  and  $J_z \pm 3/2$  by the spin-orbit splitting  $\Delta_{SO}$  (see Fig. 2.6a). Like SOI in atomic physics (Eq. (2.11)),  $\Delta_{SO}$  is small in crystals with comparably light atoms such as silicon ( $\Delta_{SO} \approx 0.044eV$ ) and can become substantial in compounds with heavy atoms like InSb ( $\Delta_{SO} \approx 0.82eV$ ) or GaAs ( $\Delta_{SO} \approx 0.34eV$ ) [67, 72]. The difference in  $|J_z|$  leads to a distinct effective mass  $m^*$  which lifts the degeneracy of the  $J = 3/2$ -bands at finite momentum  $k \neq 0$  (see Fig. 2.6). According to their effective mass, the states with  $|J_z| = 1/2$  are named light hole (LH) respectively heavy hole (HH) states for  $|J_z| = 3/2$ .

### 2.2.1 SOI in the conduction band

According to the model described above, the electrons in the conduction band will not experience any SOI because their Bloch wave function has no orbital angular mo-

mentum ( $L = 0$ ). Interestingly, due to coupling with neighboring bands, the s-type conduction band states mix with the p-type valence band states. Therefore, a system with three valence bands (HH, LH and SO) and the lowest conduction band (CB) such as shown in Fig. 2.6a is considered in  $\mathbf{k} \cdot \mathbf{p}$  theory. The framework of the  $\mathbf{k} \cdot \mathbf{p}$  theory allows for a finite inter-band coupling.

This system is represented by an  $8 \times 8$  effective mass approximation or Kane Hamiltonian [67]. But, because only the spinor components of the conduction band are of interest in this section, the valence band components are eliminated from the Schrödinger equation but the inter-band coupling terms are kept. With this approach, the Schrödinger equation for the approximated envelope functions  $\Psi_c$  for electrons in the conduction band is [67]

$$\begin{aligned} \left( \frac{P^2}{3} \left[ \frac{2}{E_g} + \frac{1}{E_g + \Delta_{SO}} \right] k^2 + V - \frac{P^2}{3} \left[ \frac{1}{E_g} - \frac{1}{E_g + \Delta_{SO}} \right] \frac{e}{\hbar} \boldsymbol{\sigma} \cdot \mathbf{B} \right. \\ \left. + \frac{eP^2}{3} \left[ \frac{1}{E_g^2} + \frac{1}{(E_g + \Delta_{SO})^2} \right] \boldsymbol{\sigma} \cdot \mathbf{k} \times \boldsymbol{\mathcal{E}} \right. \\ \left. - \frac{3P^2}{6} \left[ \frac{2}{E_g^2} + \frac{1}{(E_g + \Delta_{SO})^2} \right] \nabla \boldsymbol{\mathcal{E}} \right) \Psi_c = E \Psi_c, \quad (2.12) \end{aligned}$$

where  $P$  is the matrix element of the coupling between the valence bands and the conduction band of the Kane model and  $\boldsymbol{\mathcal{E}}$  is the electric field. Note that this equation only contains the emerging corrections to the electron wave function due to inter band coupling.

In Eq. (2.12) the first term represents a correction to the kinetic energy such that the effective mass  $m^*$  is  $\frac{m_0}{m^*} = \frac{m_0}{m'} + \frac{2m_0}{\hbar^2} \frac{P^2}{3} \left( \frac{2}{E_g} + \frac{1}{E_g + \Delta_{SO}} \right)$  where  $m'$  is the unperturbed mass. The second term is the potential  $V$  and the third term is a correction to the Zeeman term  $H_Z = g^* \mu_B \boldsymbol{\sigma} \cdot \mathbf{B}$  in which  $\mu = e\hbar/(2m_0)$  is the Bohr magneton and  $g^*$  the effective g-factor. Similar to the effective mass, the effective g-factor is then  $\frac{g^*}{g_0} = \frac{g'}{g_0} - \frac{2m_0}{g_0 \hbar^2} \frac{P^2}{3} \left( \frac{1}{E_g} - \frac{1}{E_g + \Delta_{SO}} \right)$  where  $g_0 \approx 2$  is the bare g-factor of the free electron in vacuum and  $g'$  is the g-factor without inter band coupling. The fourth term is the



Rashba term  $H_R \sim \boldsymbol{\sigma} \cdot \mathbf{k} \times \boldsymbol{\mathcal{E}}$ .  $H_R$  represents spin-orbit coupling and is the solid-state equivalent to the Pauli SO term portrayed in Eq. (2.10). And last, the fifth term  $H_{Darw} \sim \nabla \boldsymbol{\mathcal{E}}$  is identified as the Darwin term.

Note that Eq. (2.12) is the solid state equivalent of the Pauli equation, the non-relativistic approximation of the Dirac equation which leads to the Pauli SO. Similar to the Pauli equation, Eq. 2.12 can also be derived using perturbation theory [67]. With this approach, the kinetic and the Zeeman term arise from second order perturbations theory but the Rashba and Darwin term require inclusion of third order perturbations. Because of their different order in perturbation theory, the mass and g-factor are  $\propto E_g^{-1}$  while the SO and Darwin term are suppressed with  $\sim E_g^{-2}$ . Note that Eq. 2.12 only includes terms up to  $E_g^{-2}$  and higher-order contributions are neglected.

In the conduction band, the electric fields needed for SOI arise from breaking symmetries of the bulk crystal. There are two distinguished types of symmetry breaking: bulk inversion asymmetry and structural inversion asymmetry. Bulk inversion asymmetry (BIA) arises if net electric fields due to the arrangement of the atoms in the unit cell are present. Silicon, for example, has a face-center diamond cubic unit cell symmetry with an inversion center and therefore electrons in silicon experience no BIA induced SOI. The compound semiconductor Gallium Arsenide (GaAs), on the other hand, has Zincblende structure with tetrahedral coordination and lacks an inversion center which gives rise to SOI. This BIA type of SOI is named after its inventor Gene Dresselhaus [73]. Structural inversion asymmetry (SIA) emerges from breaking the crystal bulk structure. While silicon has no BIA, the bulk symmetry is spatially broken at the surface of the crystal which leads to additional electric fields and thus SOI [74, 75]. Another example are AlGaAs/GaAs heterostructures or quantum wells where the interfaces between materials with different electronic band structures also results in electric fields[76, 77]. This type of SOI is called Bychkov-Rashba or Rashba SOI [76, 78].

The effects of SOI on electrons confined in a quantum dot which is energized in a two-dimensional electron gas (2DEG) is a very central topic of this thesis. It is an important ingredient to understand the behavior of the spin relaxation in a GaAs quantum dot discussed in Chap. 4. In this experiment, we were able to extract the Rashba and Dresselhaus spin-orbit interaction strengths in such a quantum dot. In Ref. [4] we analyze and reveal several SOI induced corrections to the g-factor tensor in a GaAs quantum dot and identify dominant isotropic and anisotropic terms. In Chap. 5, we present data on the g-factor which shows good agreement with the aforementioned model. The Rashba and Dresselhaus Hamiltonian which lead to the relevant SOI terms for electrons in a GaAs 2DEG are discussed in Sec. 4.7.5 of Chap. 4.

### 2.2.2 Direct Rashba spin orbit interaction

Like the  $\mathbf{k} \cdot \mathbf{p}$  approach discussed in Sec. 2.2.1, the Kane Hamiltonian takes the 8 most important bands (conduction, heavy-hole, light-holes and split-off with both spins) into account and is represented by an  $8 \times 8$  matrix [79]. The heavy and light holes in the valence bands are described by the Luttinger-Kohn (LK) Hamiltonian, a  $4 \times 4$  subspace of the Kane Hamiltonian [67, 79, 80].

Here, it is waived to reproduce the full Luttinger-Kohn Hamiltonian. But this Hamiltonian contains the dimensionless Luttinger parameters  $\gamma_{1,2,3}$  which are related to the inter-band coupling and therefore the effective masses of the holes in the involved valence bands.

In the spherical approximation  $\gamma_2 \approx \gamma_3 = \gamma_s$ , the Luttinger-Kohn Hamiltonian is simplified to [5, 79]

$$H_{LK} = \frac{\hbar^2}{2m_0} \left[ \left( \gamma_1 + \frac{5}{2}\gamma_s \right) k^2 - 2\gamma_s (\mathbf{k} \cdot \mathbf{J})^2 \right]. \quad (2.13)$$

Note that this spherical approximation is valid for Germanium ( $\gamma_2 = 4.27$ ,  $\gamma_3 = 5.61$ )

[81]) but not for silicon ( $\gamma_2 = 0.38$ ,  $\gamma_3 = 1.44$  [81]). In this notation, the effective masses of the heavy holes (HH) and light holes (LH) is

$$m_{HH,LH} = \frac{m_0}{\gamma_1 \mp 2\gamma_s}. \quad (2.14)$$

### Holes in two-dimensional systems

When confining the system in a hard-wall potential  $V_z$  along the z-direction with width  $L_z$ , the eigenstates of  $H_{LK} + V_z$  are different for the two types of holes because of the different masses  $E_n^{HH,LH} = \frac{n^2 \hbar^2 \pi^2}{2m_{HH,LH} L_z^2}$ . As a consequence, the HH-LH splitting  $\Delta_{HH-LH} \propto L_z^{-2}$  lifts the  $J = 3/2$  degeneracy at  $k = 0$  and the HH states  $|\pm 3/2\rangle$  become the ground state. For a strong confinement, the HH-LH splitting is large and that there is almost no mixing between the states. Remarkably, an electric field  $\mathcal{E} = \mathcal{E}_z \hat{\mathbf{z}}$  along the confinement axis which introduces a Rashba type of spin orbit interaction  $H_R \propto \mathcal{E}(\mathbf{k} \times \mathbf{J})$  is not able to couple the spin states ( $\langle 3/2 | H_R | -3/2 \rangle = 0$ ) because  $\langle 3/2 | J_\mu | -3/2 \rangle = 0$  for  $\mu \in \{x, y, z\}$  [6].

In the next section it will be shown that the  $(\mathbf{k} \cdot \mathbf{J})^2$  terms of the LK Hamiltonian (Eq. (2.13)) lead to the direct Rashba spin orbit interaction (DRSOI), a strong type of SOI. As a side note, the emergence of direct Rashba SOI is possible for a weak two-dimensional confinement which permits HH-LH mixing but it is strongly suppressed by  $\Delta_{HH-LH}$ .

### Holes in one-dimensional systems

If the system is confined in two directions, the bands are mixing and not purely of HH or LH character anymore. This becomes comprehensible when considering the LK Hamiltonian for a system confined in the  $x$  and  $y$  direction in the limit  $k_z = 0$ , then

$$H_{LK,0} = -\frac{\hbar^2}{2m_0} \left( \gamma_1 k_\perp^2 \mathbb{1}_{4 \times 4} + \gamma_s k_\perp^2 \left( J_z^2 - \frac{5}{4} \cdot \mathbb{1}_{4 \times 4} \right) - \gamma_s \left( k_-^2 J_+^2 + k_+^2 J_-^2 \right) \right) \quad (2.15)$$

where  $k_{\pm} = k_x \pm ik_y$ ,  $k_{\perp}^2 = k_x^2 + k_y^2$  and  $J_{\pm} = (J_x \pm iJ_y)/\sqrt{2}$  [82, 83]. The second term of Eq. (2.15) describes the HH-LH energy splitting. The operators  $J_{\pm}$  of the third term lead to a mixing of the HH and LH states where the admixture strength is proportional to  $\gamma_s$ . As a consequence, when  $k_{\perp} \neq 0$  and  $\gamma_s \neq 0$  the  $J_z$  component of these states is not  $\pm 3/2$  respectively  $\pm 1/2$  anymore. This mixing is the very foundation of DRSOI.

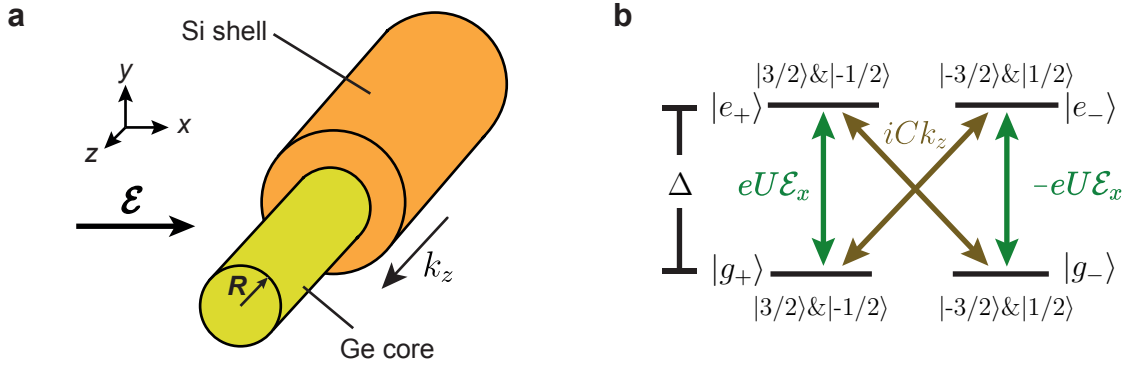


Figure 2.7: (a) Illustration of a Germanium-Silicon (Ge/Si) core-shell nanowire (NW) which is used to derive the direct Rashba spin orbit interaction (DRSOI). The wire is oriented along  $\hat{z}$  and an external electric field  $\mathcal{E} = \mathcal{E}_x \hat{x}$  is applied which gives rise to DRSOI. (b) The basis states of the Hamiltonian given in Eq. (2.16).  $|g_{\pm}\rangle$  and  $|e_{\pm}\rangle$  denote the two ground and excited states, respectively. The excited state energy  $\Delta$  is the sub band energy of the NW arising from the confinement and (if present) strain. While the couplings  $\sim eU\mathcal{E}_x$  arise from the external electric field, the terms  $\sim iCk_z$  result from the Luttinger-Kohn Hamiltonian. The combination of these two couplings lead to the emergence of strong DRSOI shown in Eq. (2.17).

To derive the DRSOI, a nanowire modeled as a cylinder with radius  $R$  and infinite dimension in  $z$ -direction is assumed (see Fig. 2.7a). A large band gap offset between the NW and the encapsulating material (e.g. Silicon in Ge/Si core-shell nanowires) is assumed such that the premise of a radial hard wall confinement potential  $V$  is valid. As described before, with this additional confinement,  $J_z$  is not a good quantum number anymore. But the total Hamiltonian  $H_{LK,0} + V$  commutes with  $F_z = L_z + J_z$  where  $L_z$  is the orbital angular momentum along the wire axis such that  $F_z$  is a good quantum number. The low-energy dispersion relation is then given by two degenerate bands with  $F_z = \pm 1/2$  each. At  $k_z = 0$ , the ground states of these bands  $|g_{\pm}\rangle$  have

$L_z \approx 0$  while the excited states  $|e_{\pm}\rangle$  have finite orbital angular momentum  $|L_z| = 1$ . Here, the subscript refer to a "spin block" which means that the states labeled with "+" contain the two  $J_z$  spin states  $|3/2\rangle$  and  $|-1/2\rangle$  and the ones with "-" have contributions of  $|-3/2\rangle$  and  $|1/2\rangle$ . The wave function of these four states can be derived analytically (see e.g. Refs. [5, 83]) and are of form  $|g_{\pm}\rangle = \Phi_{\pm}^{\mp 1/2}$  and  $|e_{\pm}\rangle = \Phi_{\pm}^{\pm 1/2}$  with  $\Phi_{\pm}^{F_z}(r, \phi) \sim a_{\pm}^{F_z} \Psi_{HH, \pm}^{F_z}(r, \phi) + b_{\pm}^{F_z} \Psi_{LH, \pm}^{F_z}(r, \phi)$  where  $a_{\pm}^{F_z}, b_{\pm}^{F_z}$  are normalization constants. Note that  $\Psi_{HH, \pm}$  and  $\Psi_{LH, \pm}$ , the HH and LH wave functions of the eigenstates in absence of a confinement, are linear combinations of  $|\pm 3/2\rangle$  and  $|\mp 1/2\rangle$ .

Next, an electric field along the  $x$ -direction is assumed  $\mathcal{E} = \mathcal{E}_x \hat{\mathbf{x}}$ . Then, the total Hamiltonian  $H_{LK} + V + e\mathcal{E}_x x$  can be projected onto the subspace spanned by  $|g_+\rangle, |g_-\rangle, |e_+\rangle$  and  $|e_-\rangle$ . In this base, the effective  $4 \times 4$  Hamiltonian is

$$H_{4 \times 4}^{eff} = \begin{pmatrix} \hbar^2 k_z^2 / (2m_g) & 0 & eU\mathcal{E}_x & -iCk_z \\ 0 & \hbar^2 k_z^2 / (2m_g) & -iCk_z & -eU\mathcal{E}_x \\ eU\mathcal{E}_x & iCk_z & \hbar^2 k_z^2 / (2m_e) + \Delta & 0 \\ iCk_z & -eU\mathcal{E}_x & 0 & \hbar^2 k_z^2 / (2m_e) + \Delta \end{pmatrix}, \quad (2.16)$$

where  $m_{e,g}$  are effective masses,  $C \propto 1/(m_0 R)$ ,  $U \propto R$  and  $\Delta \propto \Delta_{BP} + 1/(m_0 R^2)$  is the sub-band spacing resulting from the confinement of the wire and the shell-induced strain accounted by the Bir-Pikus energy term  $\Delta_{BP}$  [6]. Here, only the dependencies on the radius  $R$  are given, but these parameters can be calculated analytically. From Eq. 2.16 it is recognized that the terms involving  $|eU\mathcal{E}_x|$  couple the ground states to the excited state of the same type:  $|g_+\rangle$  to  $|e_+\rangle$  and  $|g_-\rangle$  to  $|e_-\rangle$ . The off-diagonal terms  $iCk_z$  on the other hand, couple the ground states to the excited states of opposite type:  $|g_+\rangle$  to  $|e_-\rangle$  and  $|g_-\rangle$  to  $|e_+\rangle$ . Note that these terms originate from the LK Hamiltonian  $H_{LK}$  and the coupling only occurs because the subspace states are a mixture of  $|J_z| = 3/2$  and  $|J_z| = 1/2$  states. A schematic of the couplings of the subspace states adapted from Ref. [6], is illustrated in Fig. 2.7b.

Although already present in Eq. 2.16, the DRSOI becomes apparent when applying a quasi-degenerate perturbation theory (Schrieffer-Wolff transformation) to Eq. 2.16 for which  $|eU\mathcal{E}_x/\Delta|$  and  $|Ck_z/\Delta|$  are assumed to be small perturbations  $\ll 1$ . According to Ref. [6], the effective Hamiltonian then becomes

$$H_{2\times 2}^{eff} = \left( \frac{\hbar^2}{2m_g} - \frac{C^2}{\Delta} \right) k_z^2 + \frac{2eCU}{\Delta} \mathcal{E}_x \sigma_y k_z. \quad (2.17)$$

Here, the second term resembles the standard Rashba SOI Hamiltonian  $H_R \sim \alpha_R (\boldsymbol{\sigma} \times \mathbf{k})$  and was therefore named direct Rashba SOI. In analogy to  $\alpha_R$  in  $H_R$ , a direct Rashba coupling strength coefficient can be defined as  $\alpha_{DR} = 2eCU/\Delta$ . But in contrast to the standard Rashba SOI (see Eq. (2.12)), the direct Rashba type of SOI is suppressed by the subband spacing  $\Delta$  defined by the confinement of the wire and not by the band gap  $E_g$ . In Ge/Si core-shell NWs,  $\Delta \approx 20$  meV while  $E_g \approx 740$  meV [5, 84]. Further,  $\alpha_{DR}$  depends directly on the electric field  $\mathcal{E}_x$ . While also standard SOI is electrically tunable to some extent [56, 85], the direct Rashba SOI is not only highly tunable but can also be turned off with a high on-off ratio. In a new type of spin qubits, DRSOI will be used for spin manipulation but it will inevitably lead to a fast spin relaxation. Therefore, an electrical control of this term is beneficial because the spin-orbit field acting on the spin qubit can be switched on demand.

According to Ref. [6], the predicted  $\alpha_{DR}$  in a Ge/Si NW is about 170 (1.6) times stronger than the SOI for electrons in GaAs (InSb). The emergence of direct Rashba type of SOI has not been shown conclusively in an experiment. But indications on the presence of DRSOI was found in an experiment on a Ge/Si NW in Ref. [51] where the spin-orbit coupling strength was found to be tunable with a back gate voltage. Further, in a quantum dot formed in a Ge/Si NW, a very short spin-orbit length of  $l_{SO} < 20$  nm was found which indicates a remarkably strong SOI [52]. Recent weak-antilocalization measurements in a dual gated Ge/Si NW also showed a very large SOI energy of between 1 and 6 meV and the SOI strength could be electrostatically

controlled in the device [53]. Additionally, QPC measurements in the same type of wires showed evidence of helical hole states and a SOI energy gap of  $\sim 2.1$  meV was reported. The results of these experiments point towards the presence of DRSOI in Ge/Si NWs.

In Ref. [4] and Chap. 5 we discuss SOI induced corrections to the g-tensor in a GaAs quantum dot. Due to the same kind of physics, the DRSOI gives rise to g-factor corrections for holes confined in a NW. But given the origin of DRSOI, these corrections are highly tunable with an external electric field. In Ref. [86] this was analyzed on a theoretical level in a Ge/Si NW and the g-factor was found to be controllable from 6 to almost 0 with experimentally achievable field strengths. In agreement with this theory, recently, an anisotropic g-factor for different magnetic field directions was experimentally observed [54] in a quantum dot formed in a Ge/Si NW. In Chap. 6 of this thesis, a model with an anisotropic g-factor in combination with the presence of a spin-orbit field was used to describe the experimentally observed anisotropy of the leakage current through a double dot in Pauli spin blockade. There, the direction of the resulting spin-orbit field does not disagree with the observation of a direct Rashba type of SOI.

### 3 Spectroscopy of quantum-dot orbitals with in-plane magnetic fields

Leon C. Camenzind, Liuqi Yu, Daniel Loss, Dominik M. Zumbühl,

*Department of Physics, University of Basel, Switzerland*

Jeremy D. Zimmerman, Arthur C. Gossard

*Materials Department, University of California, Santa Barbara, USA*

Peter Stano

*Center for Emergent Matter Science, RIKEN, Saitama, Japan*

*Department of Applied Physics, School of Engineering, University of Tokyo, Japan*

*Institute of Physics, Slovak Academy of Sciences, Bratislava, Slovakia*

#### Abstract

We show that in-plane-magnetic-field assisted spectroscopy allows extraction of the in-plane orientation and full 3D size parameters of the quantum mechanical orbitals of a single electron GaAs lateral quantum dot with sub-nm precision. The method is based on measuring of the orbital energies in a magnetic field with various strengths and orientations in the plane of the 2D electron gas. From such data, we deduce the microscopic confinement potential landscape, and quantify the degree by which it differs from a harmonic oscillator potential. The spectroscopy is used to validate shape manipulation with gate voltages, agreeing with expectations from the gate layout. Our measurements demonstrate a versatile tool for quantum dots with one dominant axis of strong confinement.

This chapter is published in *Phys. Rev. Lett.* [87].



### 3.1 Introduction

A spin in a magnetic field is one of the simplest canonical quantum two-level systems encoding a qubit [1]. To realize spin based quantum computing, the capability of addressing individual spin qubits is essential, as demonstrated in various semiconductor quantum dot devices [2]. Although significant progress has been made on the control of spin states, the challenge lies in the lack of means to adjust the confinement potential, particularly for dot systems formed in nanowires or by intrinsic defects. Lateral quantum dots, on the other hand, show excellent flexibility. Defined in a 2D electron gas (2DEG) by nanometer-scale surface gates, they allow, in principle, arbitrary and tunable dot shapes [35].

This tunability provides an additional knob important for stabilizing and manipulating the spin states [88]. The dot shape, impressed in its orbital energy spectrum, is directly associated with a variety of spin-electric related processes. These rely on mixing of spin and orbital degrees of freedom since the orbital shape determines the dipole moments connected with spin-flip transitions. For instance, such mixing presents the predominant channel for spin relaxation, in GaAs through both the spin-orbit [35, 89, 90], and hyperfine interactions (see Chap. 4) [3]. Both spin relaxation [35] and spin manipulation by electric-dipole spin resonance (EDSR) [43, 91] show a strong dependence on the dot shape and the orientation in the 2DEG plane and with respect to the magnetic field. The dependence can be exploited to control both the spin relaxation time and EDSR frequency [88].

The bottleneck in taking full advantage of this flexibility is that so far there is no direct method to adequately determine the quantum-dot confinement geometry. Many previous experiments probed low lying excited state energies [35, 60, 63, 87](see also Chap. 4). However, there are characteristics of the confinement which are difficult to disentangle from such measurements (the potential anharmonicity), which are energy-

tically not accessible (the subband spacing) and which are not present in such data at all (the dot orientation).

Looking for alternative ways to extract these characteristics is full of obstacles, too: Since the dot is imprinted into the 2DEG beneath the surface of the device, details of the dot shape are inaccessible for surface imaging tools, such as atomic force or scanning tunneling microscopy. Also, the electric fields from the surface gates will in return interfere with the probe aggravating such measurements [92, 93]. Further, these methods suffer from invasive back-action of the probe to the sample disturbing the quantum dot. In principle, nowadays software is capable of advanced simulations [63, 94]. However, the reliable input to such simulations is restricted to the design of the surface gates and the chemical composition used during the wafer growth. The details of the interfaces, strain distribution, and, most importantly, impurities and donors positions are unknown. At the moment, they can be at best guessed, and included into such simulations by hand. Formation of unintentional dots, and dots with positions and shapes differing from the one suggested by the gate layout, is more a rule than an exception. Finally, the fact that the dot details often change upon cool downs is a proof that even though simulations can serve as a rough guide, they are unable to provide sample-dependent details.

In this Letter, we present a non-invasive technique which is able to extract the 3D shape and orientation parameters of the quantum mechanical orbitals of a quantum dot with sub-nm precision. It is based on a response of the energy spectrum to an in-plane magnetic field of varying magnitude and direction. The theoretical principles of the method are explained in Ref. 95. Here, we demonstrate it experimentally. While our quantitative interpretation of the measurements is based on assuming an asymmetric (triangular) 2DEG confinement and a harmonic in-plane confinement, the method is directly applicable to any quasi two-dimensional system for which the unperturbed confinement can be reasonably guessed.

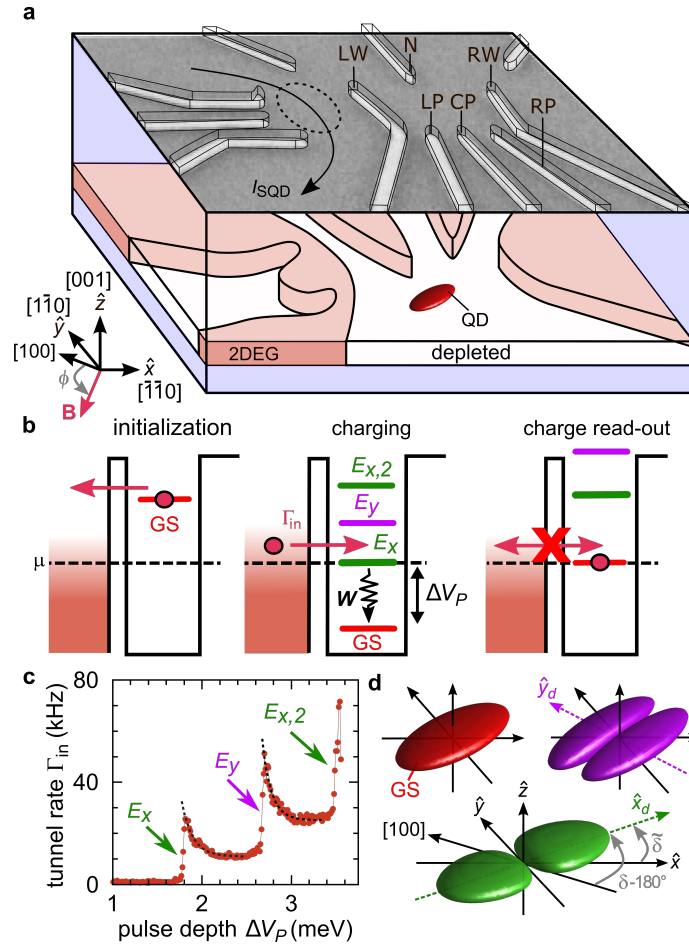


Figure 3.1: (a) Sketch with electron micrograph of the gate layout of a cofabricated device shown on top. The GaAs/  $\text{Al}_{0.3}\text{Ga}_{0.7}\text{As}$  heterostructure contains a 2DEG with density  $2.6 \times 10^{11} \text{ cm}^{-2}$  and mobility  $4 \times 10^5 \text{ cm}^2/\text{Vs}$  located 110 nm below the surface. The in-plane field angle  $\phi$  and wave function orientation  $\delta$  are defined with respect to  $[100]$ , while  $\tilde{\delta} = \delta - 225^\circ$  is the angle between  $\hat{x} = [\bar{1}\bar{1}0]$  and  $\hat{x}_d$ , the dot confinement x-axis. (b) Three-step pulse sequence described in the text. (c) Measurement of tunneling-in rate  $\Gamma_{in}$  as a function of  $\Delta V_P$  exhibiting three excited orbital states at energies  $E_x$ ,  $E_y$  and  $E_{x,2}$ . (d) Ground-state wave function (left) and the p-type orbitals for an elongated dot with exaggerated anisotropy, details are given in Supplementary Note 3.7.1.

### 3.2 Measurement scheme

The surface gate layout of the measured device, shown in Fig. 3.1a, is based on Ref. [35]. The device is biased into the single-electron quantum-dot regime, as indicated by the red ellipsoid. The dot is tuned to couple to the left reservoir only, with a tunnel

rate between 1 and 100 Hz. An additional quantum dot, located directly adjacent to the main dot, is serving as a charge sensor [28, 96], giving a change of sensor conductance of up to 100% per electron in the main dot. The sample can be oriented with essentially arbitrary angle with respect to an in-plane magnetic field up to 14 T using a piezoelectric rotator. Using standard van der Pauw measurements, the magnetic field is shown to deviate less than  $1.3^\circ$  out of the 2DEG plane, thus rendering the out-of-plane component negligible (see also Sec. 4.7.1 in Chap. 4). Measurements are done in a dilution refrigerator with an electron temperature of 60 mK [97–99].

The orbital energies are measured by pulsed gate spectroscopy using a three-step pulse sequence. Namely, an additional voltage  $\Delta V_P$  is applied to the center plunger gate  $CP$ , on top of the static gate voltage  $V_P$ , see Fig. 3.1a [35, 100, 101]. As illustrated in Fig. 3.1b, the sequence consists of initialization, charging and read-out steps, see also Supplementary Note 3.7.5. The elastic tunnel rate into the empty dot increases sharply when an orbital state becomes resonant with the chemical potential  $\mu$  of the reservoir. By measuring the dot-reservoir tunnel coupling for varying  $\Delta V_P$ , individual excited orbital states can be distinguished. An example is shown in Fig. 3.1c exhibiting three excited orbital states. The ground state, which calibrates  $\Delta V_P = 0$ , couples much weaker to the reservoir ( $\Gamma_{GS} \sim 10$  Hz) compared to the excited orbital states, attributed to the increased spatial extent of higher orbitals [102, 103].

The exponential decay in the tunnel rate of the excited states with increasing  $\Delta V_P$  [dashed curves in Fig. 3.1c] is due to an increasing tunnel barrier. [35, 104, 105]. Finally, we note that our method requires that the probe voltage does not change the confinement potential. We conclude that this assumption is well met, as the pulse  $\Delta V_P$  is much smaller (typically, tens of mV, applied only on one gate) than voltages required to change the dot shape substantially (typically hundreds of mV, applied on all gates), as deduced from Fig. 3.2 below.

### 3.3 Model of the confinement potential and shape control

We assume that the dot confinement separates into a 2D harmonic oscillator part for the in-plane coordinates and a much stronger confinement for the heterostructure growth direction ( $\hat{z}$ ) coordinate:

$$H = \frac{\mathbf{p}^2}{2m} + \frac{\hbar^2}{2m} \left( \frac{x_d^2}{l_x^4} + \frac{y_d^2}{l_y^4} \right) + v(z). \quad (3.1)$$

Here,  $\mathbf{p}$  is the momentum operator,  $\hbar$  the reduced Planck constant,  $m$  the effective mass, and  $l_{x,y}$  are the confinement lengths along the main axes  $\hat{x}_d$  and  $\hat{y}_d$  of the in-plane confinement. These axes are in general rotated from the crystal axes [100] and [010] by an angle  $\delta$ , see Fig. 3.1a,d. For simplicity, we introduce  $\tilde{\delta} = \delta - 225^\circ$  as the angle between potential axis  $\hat{x}_d$  and device axis  $\hat{x} = [\bar{1}\bar{1}0]$ . In the model described by Eq. (3.1), the excitation energies are  $E_{x,y} = \hbar^2/ml_{x,y}^2$  and the ground-state wave function can be represented by a disk-like ellipsoid. The two lowest excited states correspond to p-like orbitals aligned along two perpendicular axes  $\hat{x}_d, \hat{y}_d$ , as shown in Fig. 3.1d.

Within this model, the parameters  $E_x, E_y$ , and  $\delta$  characterize the dot shape, and vice versa, control of these parameters indicates dot-shape tunability. This is what we demonstrate next. Applying appropriate voltages on the surface gates, the dot can be elongated either in the  $\hat{x}$ - or alternatively in the  $\hat{y}$ -direction [35]. For instance, the dot can be squeezed in the  $\hat{y}$ -direction by applying more negative voltages on the plunger gates LP, CP and RP, see Fig. 3.1a. To keep the ground-state energy constant, these changes are compensated by applying less negative voltages on the other gates LW and RW, which leads to an expansion of the wave function in the  $\hat{x}$ -direction. We introduce a shape parameter  $V_{\text{shape}}$  to denote the full set of gate voltages corresponding to a particular configuration (see Fig. 3.2), with the numerical value of  $V_{\text{shape}}$  taken to be the voltage on gate CP.

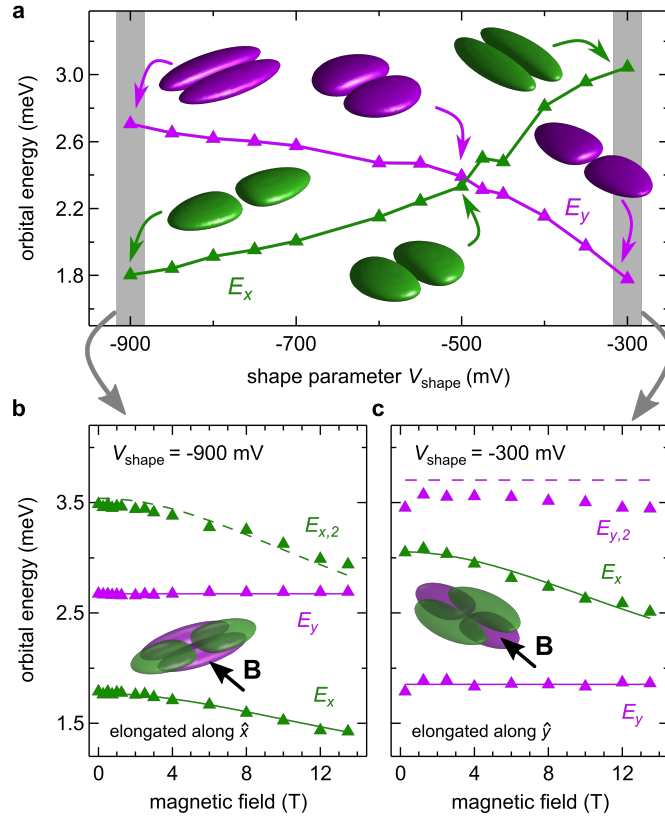


Figure 3.2: (a) Orbital excitation energies  $E_x$  (green) and  $E_y$  (purple) as a function of  $V_{\text{shape}}$ . The schematics give a qualitative picture of the excited orbital wave functions along the  $\hat{x}$ -direction (green) and  $\hat{y}$ -direction (purple) for the three shapes indicated by the arrows. Less exaggerated wave functions are shown in Supplementary Note 3.7.1. Orbital excitation energies for a magnetic field applied along the  $y$ -direction for two extreme dot shapes (b) elongated along  $\hat{x}$  and (c) elongated along  $\hat{y}$ , for  $V_{\text{shape}}$  as labeled. The data are fitted to Eq. (3.4), giving  $\lambda_z = 6.3 \pm 0.3$  nm and  $E_z = 28.6 \pm 3$  meV.

The two lowest orbital excitation energies are shown in Fig. 3.2a as a function of the dot shape  $V_{\text{shape}}$ . Upon making  $V_{\text{shape}}$  more negative, thus squeezing the dot in the  $\hat{y}$ -direction, one of the two energies increases, thus identified as the  $\hat{y}$  state. The other energy decreases, and thus has to be the  $\hat{x}$  state, as labeled in Fig. 3.2. Interestingly, at  $V_{\text{shape}} \sim -500$  mV, we find  $E_x \approx E_y$ , indicating a circular, isotropic wave function in the 2D plane. Such shape manipulation by gate voltages is limited on one hand by the minimum voltage needed to deplete the 2DEG underneath the surface gates, and on the other hand by the gate leakage threshold at more negative gate voltages. We emphasize that throughout the shape manipulation, the tunneling rate to the reservoir

is held approximately constant. For each dot shape, the relevant lever arm is measured, providing the gate voltage to energy conversion in order to obtain the excited state energies from pulsed gate spectroscopy, see Supplementary Note 3.7.4 for details.

### 3.4 Spectroscopy of quantum-dot orbitals

From such data, however, there is no estimate of the tilt angle  $\tilde{\delta}$  or how it depends on  $V_{\text{shape}}$  — other than that it is probably not too big. It is natural to expect that, as the dot is being squeezed, the wave function is also shifted and possibly somewhat rotated in space, depending on the detailed potential and disorder landscape present. In addition, we note that the subband excitations  $E_z \gg E_{x,y}$  are energetically out of reach of this pulsed-gate spectroscopy method, so that little can be said about the size of the dot orbitals along the growth axis. We are now going to show how this missing information can be revealed; this is the main advance that our work makes.

To this end, we exploit the effects of a strong in-plane magnetic field  $\mathbf{B}$  applied along an in-plane direction  $\hat{b}$ , which makes an angle  $\phi$  with the  $[100]$  crystallographic axis, see coordinate system in Fig. 3.1a. In Ref. [95], we show that the leading order effect can be expressed as a correction to Eq. (3.1) of the following form [106]

$$\delta H = -\frac{\Phi^2}{2m} \left[ \mathbf{p} \cdot (\hat{b} \times \hat{z}) \right]^2. \quad (3.2)$$

This interaction is the basis for our spectroscopy. Its strength scales with the magnetic flux  $\Phi$  penetrating the 2DEG due to its finite width. Explicitly,

$$\Phi = \frac{e}{\hbar} B \lambda_z^2, \quad (3.3)$$

where  $e > 0$  is the elementary charge and  $\lambda_z$  is the effective width of the wave function along the growth direction. We analyze the connection between a nominal width and the effective width of a 2DEG for several confinement profiles, namely triangular,

harmonic, and a square potential well [95]. Also, we note that flux threading was previously studied in open dots [107–109].

For typical 2DEGs and magnetic fields, the flux is small:  $\Phi \ll 1^8$ . Treating Eq. (3.2) as a perturbation to Eq. (3.1), the energies change by

$$\delta E_{x,y} = -\frac{\Phi^2}{2} \frac{\hbar^2}{ml_{x,y}^2} \sin^2(\delta_{x,y} - \phi). \quad (3.4)$$

Here, we denoted  $\delta_{x,y}$  as the corresponding excited orbital directions (with respect to [100]). They follow from Eq. (3.1) as  $\delta_x = \delta$  and  $\delta_y = \delta + \pi/2$ .

First, we apply a strong magnetic field along the  $y$ -direction for the two most elongated shapes available, see Fig. 3.2b and c. For sufficiently weak confinement along one direction, a second excited state  $E_{x,2}$  or  $E_{y,2}$  also becomes accessible. While  $E_{x,2} \sim 2E_x$  for the dot in Fig. 3.2b,  $E_{y,2}$  is slightly lower in energy than the second harmonic of  $E_y$ , as seen in Fig. 3.2c. For this configuration, the voltage on the nose N and all plunger gates are only barely sufficient to deplete the 2DEG, which could lead to a softening of the confinement potential along  $\hat{y}$ . Looking at the field dependence, we make the striking observation that  $E_y$  remains constant for both shapes while  $E_x$  clearly changes with magnetic field. This is consistent with the notion that the orbital effects of a magnetic field are given by a Lorentz force, which is a vector product of the velocity with the field, thus leaving motion along the direction of the applied field unaffected. This agrees with the prediction of Eq. (3.2), giving that  $\hat{x}_d \approx \hat{x}$ , meaning that the dot is oriented along the device axes. The invariance of  $E_y$  indicates that the corresponding orbital is rather well aligned with the magnetic field and therefore the  $y$ -axis of the device. Comparing the two cases in Fig. 3.2, we emphasize that, going from panel (b) to (c), the quantum dot was in fact rotated by  $90^\circ$ , thus demonstrating a gate-induced

<sup>8</sup>A generalization beyond this regime is given in Supplementary Note 3.7.2 and Ref. [95] and boils down to the replacement  $\Phi^2 \rightarrow 1 - 1/(1 + \Phi^2)$  in Eq. (3.2) and Eq. (3.4), which was used in fitting the data here, too. A more sophisticated fitting, beyond the perturbative regime, can be done straightforwardly [95], leading to only small changes in the values of extracted parameters.



quantum dot *rotation*. Indeed, this is expected from the gate voltage dependence  $V_{\text{shape}}$ , and is here validated in real space with the in-plane field spectroscopy.

By fitting the data to Eqs. (3.3) and (3.4), we can extract the effective width  $\lambda_z$ , and thus the size of the quantum dot along the growth direction. We can convert the latter, under a rather mild assumption that the heterostructure confinement is triangular, to the interface electric field  $E_{\text{ext}}$  and the subband energy splitting  $E_z$ . This in turn allows for the evaluation of the spin-orbit fields. Namely, from  $\lambda_z = 6.3 \pm 0.3$  nm we get the spin-orbit lengths  $l_r = 2.1 \pm 0.3$   $\mu\text{m}$  and  $l_d = 3.2 \pm 0.3$   $\mu\text{m}$  for Rashba and Dresselhaus interaction, respectively<sup>8</sup>. Using an independent fit from the directional variation of the spin-relaxation time discussed in Chap. 4, gave  $l_r = 2.5 \pm 0.2$   $\mu\text{m}$ , and  $l_d = 4.1 \pm 0.4$   $\mu\text{m}$  illustrating the agreement. We point out that, apart from determining the spin-orbit interactions strengths, the width of the 2DEG determines also the strength the electron Fermi-contact interaction with nuclear spins. Thus, knowledge on the quantum-dot size along the growth direction is essential for quantitative analysis of spin properties, such as the relaxation discussed in Chap. 4.

We now turn to a precise quantification of the dot orientation. It can be done by measuring the excitation energies at a magnetic field with fixed magnitude and varied orientation. Fig. 3.3 presents such data for  $B = 8$  T and a more symmetric dot. The energies show a sinusoidal behavior as expected from Eq. (3.4). The two states oscillate out of phase, proving that they represent orbitals oriented perpendicular to each other, see also Supplementary Note 3.7.3. For an elongated (quasi-1D) dot, the states would oscillate in phase [95]. Beyond confirming that our dot is indeed close to a symmetric one, we can specify its orientation in detail. By fitting the data of Fig. 3.3 to Eqs. (3.1) and (3.2), we obtain  $\tilde{\delta} = -8^\circ \pm 4^\circ$ , indicating the dot is slightly tilted away from the device coordinate system. We note that even such modest misalignment can have large

---

<sup>8</sup>The error intervals on the spin-orbit lengths given here are due to the uncertainty in  $\lambda_z$ . We do not reflect additional uncertainty, stemming from the conversion factors (basically, uncertainty in parameters of the  $\mathbf{k}\cdot\mathbf{p}$  theory).

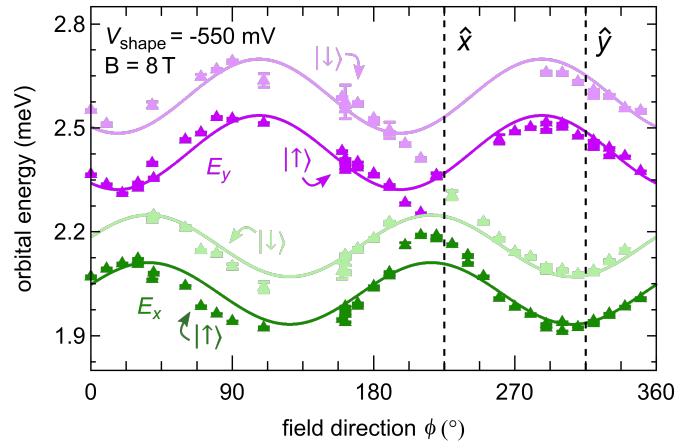


Figure 3.3: Spin-resolved excitation-energies measured at magnetic field of a fixed magnitude 8 T and varying direction in an almost circular quantum dot ( $V_{\text{shape}} \sim -550$  mV in Fig. 3.2). The solid curves show a fit according to Eq. (3.4) for each orbital state (separately for the green and purple data) assuming a direction independent Zeeman energy. Since the g-factor anisotropy is small [4], this is a very good approximation. The fit gives  $\tilde{\delta}_x = -8^\circ \pm 4^\circ$ ,  $\tilde{\delta}_y = 62^\circ \pm 4^\circ$  and  $\lambda_z = 6.1 \pm 0.3$  nm ( $E_z = 30.7 \pm 3$  meV).

impact on the qubit quality [88], and on characterization of the spin-orbit fields [89].

Before concluding, we look at the assumption that the in-plane confinement is a quadratic function of coordinates, adopted in Eq. (3.1). It has been used from the onset of quantum-dot investigations [63], as a practical choice for which analytical solutions are known [110–112]. Compared to its prevalent use, the evidence on such confinement shape is less abundant, and has been up to now restricted to checking the equidistant energy spacing of excited states of a harmonic oscillator. The data in Fig. 3.3 can provide additional information. Namely, fitting each of the accessible orbitals to Eq. (3.4) *individually*, we can extract the x,y orbital-specific angle  $\delta_{x,y}$ . In principle, one can map-out the dependence of  $\delta$  on the single-particle state energy, if more excited states are accessible. Here, we find  $\delta_y - \delta_x \approx 70 \pm 8^\circ$ . It is different from  $90^\circ$ , a value for a purely quadratic potential, and here we have quantified by how much.

### 3.5 Conclusions

In summary, we measure excitation energies in a single-electron lateral quantum dot with in-plane magnetic fields of varying orientation. We show that such measurement can determine the orientation of the dot, and extract its single-particle quantum-mechanical confinement parameters. In particular, this means that for a given orbital, one can assign a size and orientation within the 2DEG plane, as well as its extension along the growth direction with sub-nm resolution. The information on the quantum dot shape has an immediate use in correct quantification of the spin-orbit fields as well as the strength of the electron-nuclear Fermi contact hyperfine interaction. We note that the method is directly applicable to any quasi-2D dot, also in other materials, and more sophisticated structures, for example, triple-quantum-dot devices with non-collinear arrangement, as well as dots with higher electron occupations, where Hartree-Fock orbitals could be accessed in the same way.

### 3.6 Acknowledgments

We thank V. Golovach for valuable inputs and stimulating discussions, M. Steinacher and S. Martin for technical support and Basel Precision Instruments GmbH for specialized electronics such as preamplifiers and voltage sources. This work was supported by the Swiss Nanoscience Institute (SNI), NCCR QSIT, Swiss NSF, ERC starting grant (DMZ), and the European Microkelvin Platform (EMP). PS acknowledges support from CREST JST (JPMJCR1675), and JSPS Kakenhi Grant No. 16K05411.

## 3.7 Supplementary Information

### 3.7.1 Calculated wave functions

We calculate the wave functions using the solution of the three dimensional anisotropic oscillator with confinement frequencies  $\omega_{x,y,z} = E_{x,y,z}/\hbar$ . We do not account for the triangular confinement potential along the z-direction for which the solutions of the Schrödinger equation are Airy functions, since for  $n_z = 0$ , the difference of these confinements are found to be very small for the wave functions considered here[95]. Hence, we get

$$\Psi_{n_x, n_y, n_z} = \sqrt[4]{\frac{m^3 \omega_x \omega_y \omega_z}{\hbar^3}} \cdot \frac{\exp\left(-\frac{m(\omega_x x^2 + \omega_y y^2 + \omega_z z^2)}{2\hbar}\right)}{\sqrt{2^{n_x+n_y+n_z} n_x! n_y! n_z! \pi^{3/2}}} \cdot H_{n_x}\left(\sqrt{\frac{m\omega_x}{\hbar}}x\right) H_{n_y}\left(\sqrt{\frac{m\omega_y}{\hbar}}y\right) H_{n_z}\left(\sqrt{\frac{m\omega_z}{\hbar}}z\right) \quad (3.5)$$

where  $H_n$  is the n-th Hermite polynomial. Fig. 3.4 shows the solutions for the ground state and the first excited states along the excitation axes  $x$  and  $y$  for the three configurations discussed in the main text. In contrast to the exaggerated schematics in the main text, these realistic calculations only show subtle differences in real space between the configurations.

### 3.7.2 Total energy correction due to in-plane magnetic field and ground-state behavior

To avoid notation confusion, we defined the orbital energies  $E_{x,y}$  as the energy difference from the orbital ground state to the excited orbital states. All energies presented in the main text are defined with respect to the spin-ground state of the orbital ground state. The latter is a direct consequence of the measurement scheme which is explained in Supplementary Note 3.7.5 in more detail. In the zero-field case,  $E_{x,y}(B = 0)$

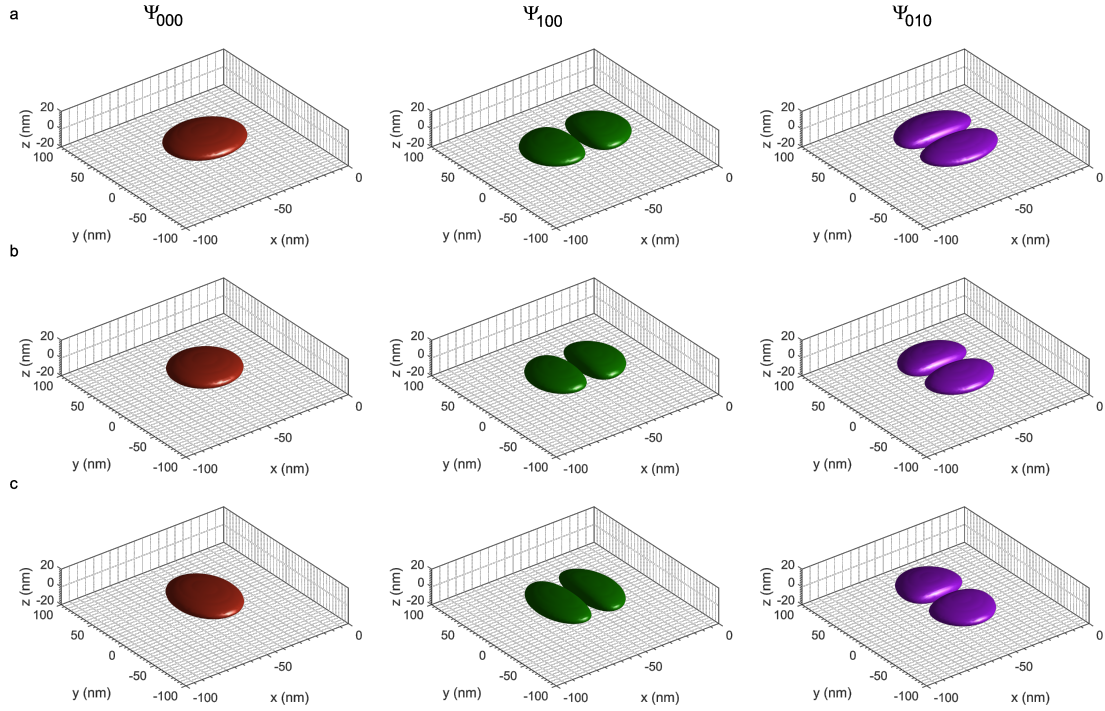


Figure 3.4: Spatial representation of the wavefunctions  $|\Psi_{n_x, n_y, n_z}|^2$  for a probability of presence larger than 90% for configurations (a)  $V_{\text{shape}} = -900$  mV ( $E_x = 1.8$  meV,  $E_y = 2.7$  meV), (b)  $V_{\text{shape}} = -550$  mV ( $E_x = 2.4$  meV,  $E_y = 2.6$  meV) and (c)  $V_{\text{shape}} = -300$  mV ( $E_x = 3$  meV,  $E_y = 1.8$  meV).

is the energy difference of the harmonic oscillator levels. When a field is applied,  $E_{x,y}$  becomes a more abstract energy scale conceivable as an increase of the particle mass of the harmonic oscillator. More precisely and as described in Ref. [95], for the particle mass in the direction perpendicular to the magnetic field  $m_{\perp}$ , we obtain a mass renormalization due to a magnetic flux  $\Phi = (e/\hbar)B\lambda_z^2$  given by

$$\frac{1}{m_{\perp}(\Phi^2 \ll 1)} \approx \frac{1}{m_{\perp}(\Phi = 0)} (1 - \Phi^2) \quad (3.6)$$

in the low field limit and

$$\frac{1}{m_{\perp}(\Phi^2 \gg 1)} \approx \frac{1}{m_{\perp}(\Phi = 0)} \left( \frac{1}{1 + \Phi^2} \right) \quad (3.7)$$

in the high field limit. Here  $\lambda_z$  is the effective width of the wave function along the growth direction penetrated by the magnetic field  $B$ .

As also derivated in Ref. [95], the magnetic field-induced energy correction to the total energy of the state  $(n_x, n_y)$  is

$$\delta E_{n_x, n_y} = -\frac{\Phi^2}{2} \left[ \hbar\omega_x \sin^2(\delta - \phi) (n_x + 1/2) + \hbar\omega_y \sin^2(\delta + \pi/2 - \phi) (n_y + 1/2) \right] \quad (3.8)$$

where  $\hbar\omega_{x,y}$  are the ladder spacings of the bi-harmonic oscillator at zero field and  $\delta$  defines the dot orientation (see Fig. 3.1). The energy  $\hbar\omega_{x,y}$  corresponds to  $E_{n_x, n_y}(B = 0)$  in our measurements because we can only measure orbital energies relative to the ground-state energy with spectroscopy method (see Supplementary Note 3.7.5). Therefore, the ground state dependence on the magnetic field has to be added to our data in order to obtain the energy correction of the harmonic oscillator. Note that Eq. (3.8) is a result for small fields ( $\Phi \ll 1$ ) when ignoring inter-subband corrections which is justified when only the lowest sub-band of the 2DEG is occupied ( $n_z = 0$ ). In Fig. 3.5, we show the two data sets of Fig. 3.2 as corrections of the total energy by including the ground state energy correction. Here it is recognized that in contrast to the spectroscopy measurements shown in Fig. 3.2, the effective energy modification of the orbital perpendicular to the field ( $E_x + E_{GS}$ ) is rather small compared to the orbital oriented parallel to field ( $E_y + E_{GS}$ ) because of increasing  $E_{GS}$ .

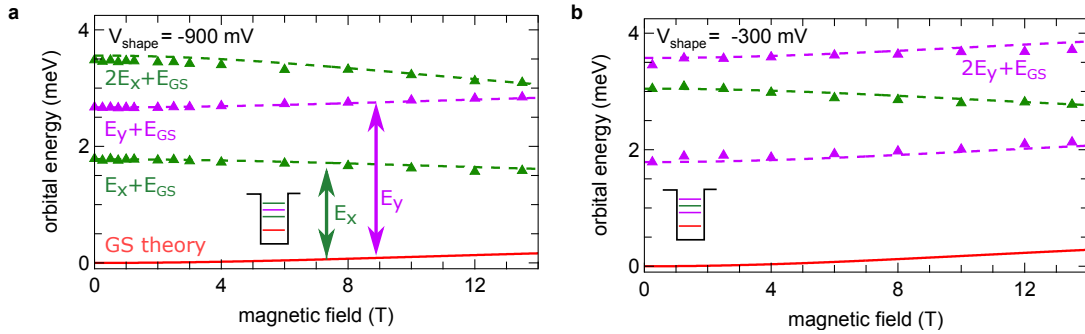


Figure 3.5: Magnetic field-induced energy corrections to the ground state (red) and excited orbital states (green, purple) for (a)  $V_{\text{shape}} = -900$  mV and (b)  $V_{\text{shape}} = -300$  mV. The data for the excited states (triangles) was obtained by adding the theoretically predicted ground state shift to data of Fig. 3.2.  $E_x$  and  $E_y$  indicate the energy measured in the experiment by the excited orbital state spectroscopy technique.

### 3.7.3 Calculated energies of the ground- and excited orbital states

From the experiment we are able to extract all parameters needed to calculate  $E_{n_x, n_y}(B, \phi, \delta, \hbar\omega_x, \omega_y, \omega_z)$  using Eq. (3.8). In Fig. 3.6, we present  $B - \phi$  diagrams of the induced energy corrections for the three configurations ( $V_{\text{shape}} = -900, -550$  and  $-300$  mV) discussed in the main text. Here, we use  $\delta \sim 225^\circ$  and assume that the quantum dot is aligned with the device coordinate system. Hence the small tilt ( $\delta \sim 215 \pm 1^\circ$ ) which is found for  $V_{\text{shape}} = -550$  mV is neglected for these calculations (see Fig. 3.2).

### 3.7.4 Shape invariance of leverarm $\alpha_P$

The leverarm for different shapes  $V_{\text{shape}}$  (Fig. 3.2) is obtained via charge sensing thermometry by probing the Fermi-Dirac occupation distribution of the electrons in the reservoir connected to the quantum dot (see Fig. 3.1) at an increased temperature of  $T = 300$  mK [98, 113]. Therefore, we open the tunnel barrier such that the ground state shows a coupling rate of a few hundreds Hz. This coupling is still well below the bandwidth of our charge sensor ( $\sim 30$  kHz measured using Low Noise/High Stability I

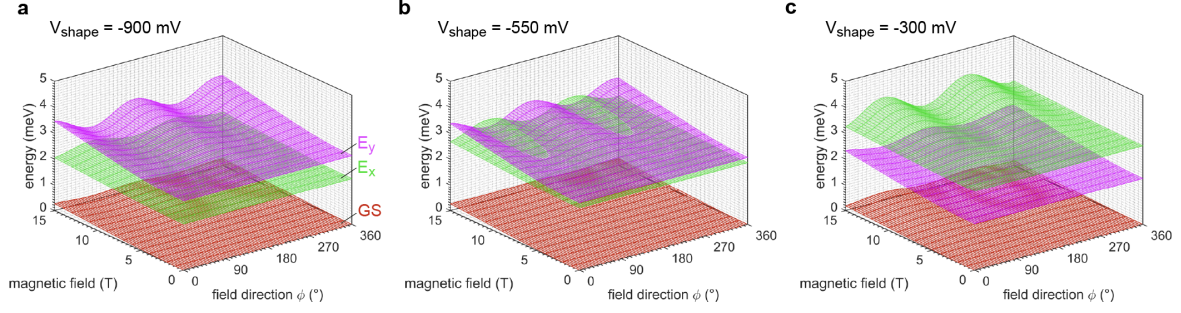


Figure 3.6: Calculated energy dependence of the ground state (red), x-like (green) and y-like (dark purple) orbital excited state for an in-plane magnetic field with angle  $\phi$  and field strength  $B$  for configurations (a)  $V_{\text{shape}} = -900$  mV ( $E_x = 1.8$  meV,  $E_y = 2.7$  meV), (b)  $V_{\text{shape}} = -550$  mV ( $E_x = 2.4$  meV,  $E_y = 2.6$  meV) and (c.)  $V_{\text{shape}} 300$  mV ( $E_x = 3$  meV,  $E_y = 1.8$  meV). Interestingly, for the situation in (b) a crossing of the excited orbital energies is predicted for certain magnetic field directions. The emerging of such a crossing is identified in the data in Fig. 3.2.

to V converter SP983 by Basel Electronics) which allows us to measure resonant tunneling in real time when the dot ground state level is placed within the temperature broadening  $\sim k_B T$  at the chemical potential  $\mu$  (Fig. 3.7a). Monitoring the conductance of the charge sensor  $G_{\text{sensor}}$  for certain waiting time  $t_w$  (about 5 s) allows us to calculate the dot occupation probability  $P_{\text{on}}$  by analyzing how long the dot was filled and respectively, empty during  $t_w$ . To do so we have to be able to discriminate the charge state during  $t_w$  (Fig. 3.7b). Therefore, a charge state separation threshold is determined retrospectively from  $G_{\text{sensor}}$  histograms (dashed line Fig. 3.7c). Using this threshold the real time trace is binarized (seen as green and blue curve in Fig. 3.7b). The total time the dot has been occupied is  $T_{\text{on}}$  and respectively, empty  $T_{\text{off}}$  during  $t_w$ . Then  $P_{\text{on}} = T_{\text{on}} / (T_{\text{on}} + T_{\text{off}})$  is calculated.



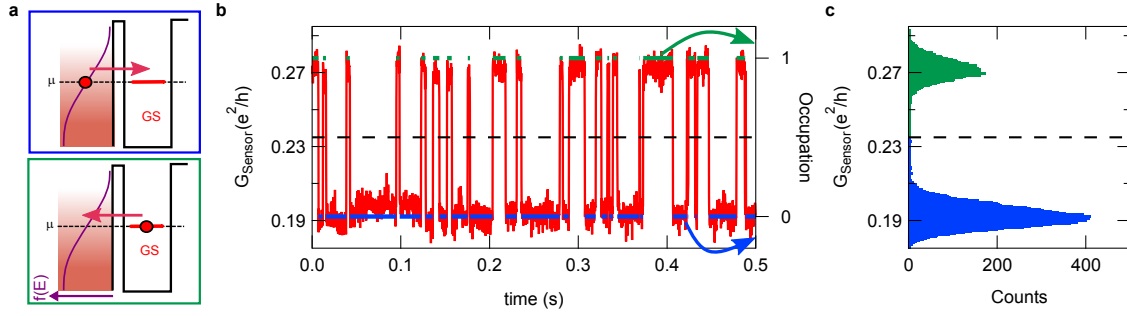


Figure 3.7: (a) Resonant tunneling occurs when the level of the quantum dot is aligned with the Fermi-Dirac temperature broadened occupation distribution  $f(E)$  around the chemical potential  $\mu$  of the reservoir. At this energies, occupied as well as unoccupied states are available in the reservoir (lower panel). Therefore, electrons can tunnel from filled state into the empty quantum dot (upper panel) or from the occupied quantum dot into an empty state of the reservoir. When the tunnel barrier is tuned accordingly, this leads to electrons tunneling in and out of the dot as a function of time. (b) In the sensor  $G_{\text{sensor}}$  the resonant tunneling is recognized as a fluctuating two-level system. (c) Histogram of  $G_{\text{sensor}}$  allows to reliably define a charge state separation threshold with which the charge states are assigned in measurements such as shown in (b), indicated with the green (charged dot) and blue (empty dot) traces. From this, the total charging probability  $P_{\text{on}}$  and also the tunnel-rate is calculated (see also Sec. 4.7.2 in Chap. 4).

Measuring  $P_{\text{on}}$  for various detuning  $\Delta V_{\text{P}}$  exhibits

$$P_{\text{on}}(\Delta V_{\text{P}}) = \left( 1 + \frac{1}{2} \exp \left( \frac{-e \cdot \alpha_{\text{P}} \cdot (\Delta V_{\text{P}} - V_{\text{P}})}{k_{\text{B}} T} \right) \right)^{-1} \quad (3.9)$$

with  $V_{\text{P}}$  being a voltage offset,  $\alpha_{\text{P}}$  the lever arm and  $k_{\text{B}}T$  the thermal energy of the electrons in the reservoir. In general, the temperature of the electronic system is larger than the mixing chamber temperature of the dilution refrigerator ( $\approx 25$  mK) [114]. Also a wider distribution is beneficial to later reduce the effective error on the extracted leverarm, we, therefore, heat up the system to 300 mK where the electronic temperature equals to the temperature of the mixing chamber. In Fig. 3.8, we show  $P_{\text{on}}(\Delta V_{\text{P}})$  for a dot shape configuration  $V_{\text{shape}} = -900$  mV (see Fig. 3.2). Because this technique is very sensitive to stochastic charge rearrangements in the semiconductor [98], we repeat this measurement between 3 and 10 times.

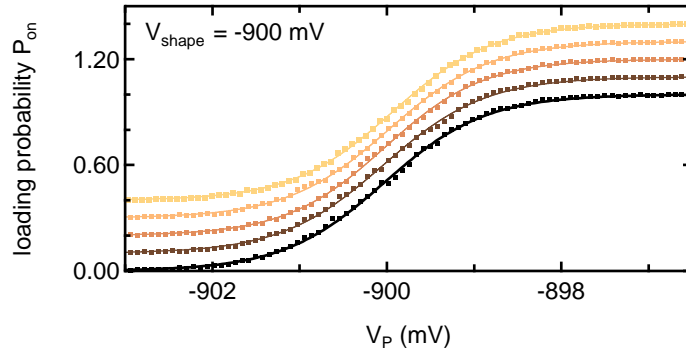


Figure 3.8: Dependence of the quantum dot occupation probability  $P_{\text{on}}$  as a function of detuning  $\Delta V_{\text{P}}$  obtained for a shape  $V_{\text{shape}} = -900$  mV at a temperature of 300 mK. Different traces correspond to various repetitions and are offset for clarity.

We fit each measurements individually to  $P_{\text{on}} \sim 1/(1 + 0.5 \cdot \exp(-(\Delta V_{\text{P}} - V_{\text{P}})/z))$  where  $1/z = \alpha_{\text{P}}/k_{\text{B}}T$ . Fig. 3.9 presents data for the configurations of  $V_{\text{shape}}$  showed in Fig. 3.2. The extracted fit-parameter  $z$  only shows a small deviation for different repetitions which indicates that this method gives consistent and reliable results. We also show data for  $V_{\text{shape}} = -200$  mV. At this configuration, the gate voltages at the plunger gates ( $V_{\text{LP}} = V_{\text{CP}} = V_{\text{RP}} = -200$  mV) are very small and are barely enough to deplete the 2DEG underneath. This leads to a very soft confinement potential at the bottom side of the device and the quantum dot is defined closer to gate CP leading to a sharp increase in the leverarm compared to the other configurations (see also Fig. 3.10b). Because of the soft confinement, charges can be trapped under these gates which significantly complicates gating of the system (e.g. by pulsing). Therefore the pulsed gate spectroscopy data for this configuration is unreliable and is not presented in the text.

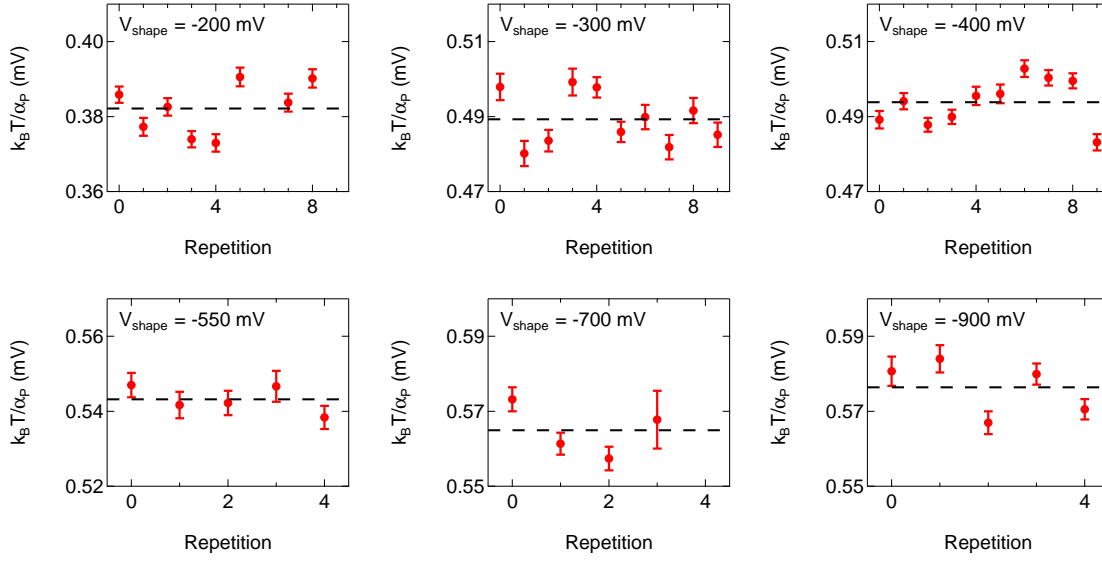


Figure 3.9: Extracted fit parameter  $z = k_B T / \alpha_P$  from measurements of the Fermi-Dirac distribution for different shape configurations.

In Fig. 3.10 we compare  $z$  as well as the resulting  $\alpha_P$  for different shape configurations. We apply similar voltages to the gates LW and RW and balance these changes with LP, CP and RP which share the nominal voltage. The voltage on the nose N is found by adjusting the tunnel barrier between LW and N such that the tunnel coupling to the reservoir is in the range of 10 to 100 Hz. Since the quantum dot shape manipulation is balanced to keep the dot in the center of the device, without  $V_{\text{shape}} = -200$  mV, the leverarm  $\alpha_P$  shows only a weak dependence on the shape configuration  $V_{\text{shape}}$ . The gate voltages for different configurations  $V_{\text{shape}}$  are found to be highly reproducible even for multiple cool-downs.

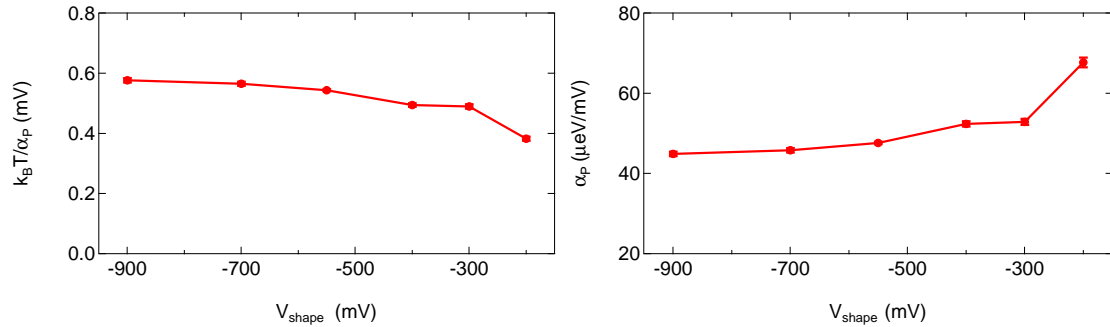


Figure 3.10: Different  $V_{\text{shape}}$  also leads to change in the capacity of the dot to plunger gate CP and therefore leverarm  $\alpha_P$ .  $\alpha_P$  is obtained by probing the Fermi-Dirac distribution of the reservoir by charge sensing thermometry at 300 mK[98].

### 3.7.5 Measuring excited orbital states

Our spectroscopy of quantum dot orbitals strongly relies on the ability to measure the coupling of the orbital excited states to the reservoir[35]. In this section we provide some additional experimental details on how this coupling is measured.

We obtain the orbital excitation energies, by measuring the coupling of the single-particle states in an empty quantum dot to the connected reservoir. For the situation in which an excited orbital state (EOS) is in resonant with the chemical potential of the reservoir  $\mu$  (see Fig. 3.1), it is energetically more favorable for the electrons to tunnel into the energetically lower orbital ground state. As soon as an electron has tunneled on the dot, the dot goes into Coulomb blockade which prevents additional electron tunneling into EOS. Therefore, the the EOS has to be brought into resonance with  $\mu$  on a timescale much faster than the GS is filled. Experimentally, this is achieved by pulsing the single particle energy states of the empty quantum dot faster than the tunnel rate into the GS. In this situation electrons prefer to tunnel into the energetically higher excited state because this states couples stronger to the reservoir than the orbital ground-state [115]. There are two reasons for this increased coupling. For a rectangular barrier, the transmission coefficient  $T(E) \sim \exp(-2\sqrt{2m^*/\hbar^2} \cdot |V_0 - E|)$  as found in WKB approximation is exponentially sensitive to energy detuning with

respect to the chemical potential of the reservoir. Therefore, the potential through which the electrons have to tunnel is much larger for the energetically more detuned GS (see Fig. 3.1b). For the same reason, coupling of the EOS becomes exponentially suppressed once detuned from  $\mu$  as indicated with the black dotted curves in Fig. 3.1c. Also, the spatial span of the excited orbital states is increased compared to the ground state (see Fig. 3.4). This leads to a larger overlap of the quantum dot wave function with the wave functions of the electrons in reservoir and results in an increased tunnel coupling.

In the experiment the coupling of the first excited states is found to be orders of magnitudes stronger. The device is tuned such that the tunnel coupling of the GS is between 10-100 Hz which leads to EOS couplings of tens of kHz. We note that different coupling of the individual EOS has been observed when manipulating the shape of the quantum dot because of accompanied changes in orientation and extent of the wave function. The EOS coupling rates often exceed the bandwidth of our charge sensor ( $\sim 30$  kHz) and are therefore not directly resolvable. We overcome this limitation by exploiting the fact that the pulse bandwidth of our gates ( $\sim 1$  MHz) exceeds the sensor bandwidth by orders of magnitudes. Therefore, this fast couplings can be resolved by having the EOS resonant with  $\mu$  for a pulse duration  $t_w$  when applying pulses to the plunger gate CP (see Fig. 3.11a). An electron tunneling into an EOS will decay into the orbital ground state under the emission of a phonon [116] (Fig. 3.1b). This process happens on GHz timescale and leads to the electron being trapped in the orbital GS. After  $t_w$ , the dot is pulsed such that the GS is resonant with  $\mu$  and the charge sensor conductance  $G_{\text{sensor}}$  is monitored for  $500 \mu\text{s}$  which allows to discriminate if the pulse lead to a charging of the dot. Because of the finite tunnel coupling of the GS to the reservoir, four different events are distinguishable in the read-out time: either the dot is empty or charged or an electron tunnels out respectively in to the dot. These events are detected and taken into account for the statistics of the charging probability  $P_{\text{on}}$ .

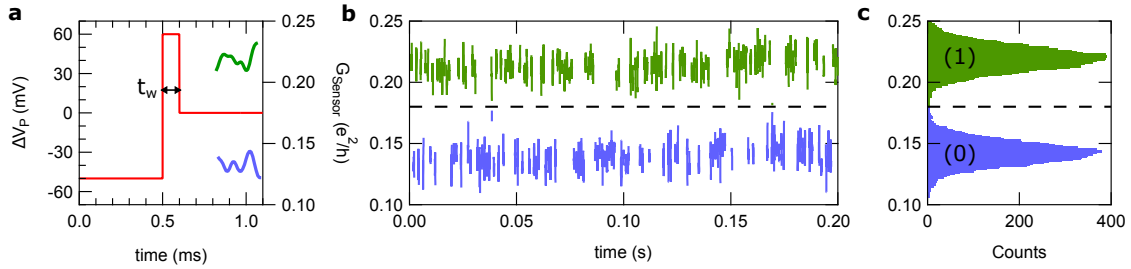


Figure 3.11: (a) Exemplary shape of a three step pulse applied to gate CP for  $\Delta V_p = 60$  mV (red trace): in the first 0.5 ms the dot is depleted at a negative energy detuning. The dot is then pulsed into the charging state for  $t_w = 0.1$  ms in this case. To read-out the dot is pulsed such that the orbital ground state is resonant with the chemical potential  $\mu$ . Here the charge sensor is monitored for about  $200 \mu\text{s}$ . Because the specific sensor conductance  $G_{\text{sensor}}$  for the charge states are known, this allows to determine if the dot is empty (blue trace) or if it has been charged during the charging step (green trace). The first  $300 \mu\text{s}$  during the read-out state are cut because the sensor has to relax from the capacitive cross-talk from the large pulse amplitudes applied here. (b) An assembled segment of 180 read-out traces out of a 2000 pulse sequence used to resolve the charging probability  $P_{\text{on}}$ . (c) Histogram of the values of the charge sensor during read-out confirms the capability to distinguish the charge states in a single shot measurement. Here, the total counts for both charge states are very comparable which indicates  $P_{\text{on}} \sim 0.5$ .

For the tunnel rates and read out times chosen, only a few percent of the read out traces actually show a tunneling event which reduces the amount of misinterpreted read out outcomes due to missed events. To illustrate the measurement outcome, we present the dependence of  $P_{\text{on}}$  on different amplitudes  $\Delta V_p$  and waiting times  $t_w$  in Fig. 3.12. Here, the EOS are observed as sharp increases of  $P_{\text{on}}$  for different  $t_w$  given by their individual coupling. The loading probability is  $P_{\text{on}} = 1 - e^{-\Gamma_{\text{in}} \cdot t_w}$  which allows us to obtain  $\Gamma_{\text{in}}$  by fitting to  $P_{\text{on}}(t_w)$ . Because the general scaling of the coupling (e.g. coupling of GS) is different, it is not useful to compare values of the coupling  $\Gamma_{\text{in}}$  of particular measurements. In interest of time, we therefore often conduct the excited orbital spectroscopy for one carefully chosen  $t_w$  and only extract the energies of the EOS.

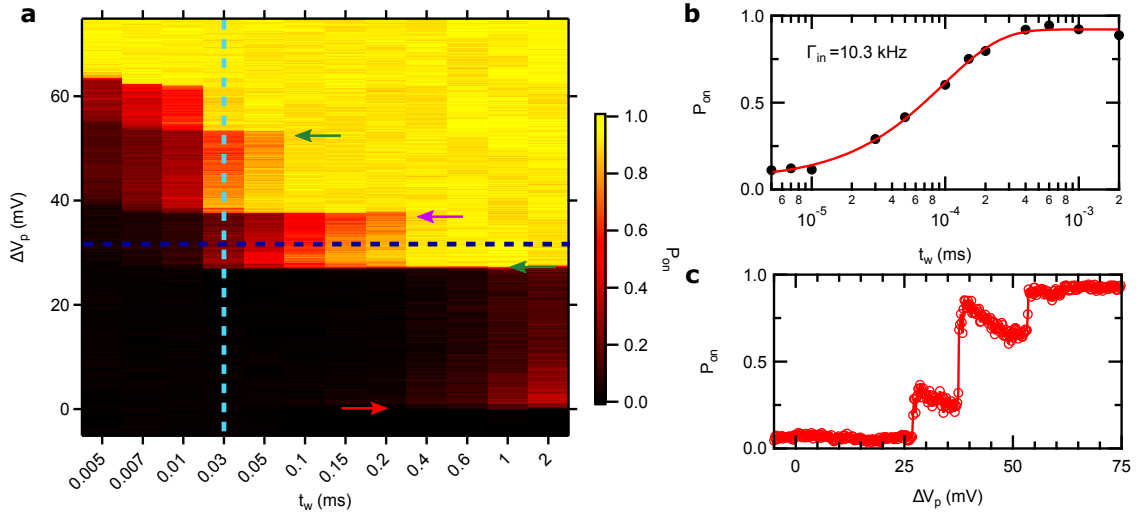


Figure 3.12: (a) Probability for the dot being loaded after charge pulse with depth  $\Delta V_P$  and waiting time  $t_w$  for a configuration  $V_{\text{shape}} = -700$  mV. The arrows depict the ground state (red) as well as the x-like (green) and y-like (purple) excited orbital states. Note that the x-axis is not linear. (b) Cut along  $t_w$  as indicated with the bright blue line in (a). By fitting an exponential function, the total coupling of the quantum dot  $\Gamma_{in}(\Delta V_P)$  is obtained. (c) Cut along the dark blue line in (a) shows all states. For most of the measurements, spectroscopy with a single  $t_w$  was performed whereas  $t_w$  was chosen such that all relevant states are resolved.

## 4 Hyperfine-phonon spin relaxation in a single-electron GaAs quantum dots

Leon C. Camenzind<sup>†</sup>, Liuqi Yu<sup>†</sup>, Daniel Loss, Dominik M. Zumbühl,

*Department of Physics, University of Basel, Switzerland*

Jeremy D. Zimmerman, Arthur C. Gossard

*Materials Department, University of California, Santa Barbara, USA*

Peter Stano

*Center for Emergent Matter Science, RIKEN, Saitama, Japan*

*Department of Applied Physics, School of Engineering, University of Tokyo, Japan*

*Institute of Physics, Slovak Academy of Sciences, Bratislava, Slovakia*

### Abstract

Understanding and control of the spin relaxation time  $T_1$  is among the key challenges for spin based qubits. A larger  $T_1$  is generally favored, setting the fundamental upper limit to the qubit coherence and spin readout fidelity. In GaAs quantum dots at low temperatures and high in-plane magnetic fields  $\mathbf{B}$ , the spin relaxation relies on phonon emission and spin-orbit coupling. The characteristic dependence  $T_1 \propto B^{-5}$  and pronounced  $B$ -field anisotropy were already confirmed experimentally. However, it has also been predicted 15 years ago that at low enough fields, the spin-orbit interaction is replaced by the coupling to the nuclear spins, where the relaxation becomes isotropic, and the scaling changes to  $T_1 \propto B^{-3}$ . Here, we establish these predictions experimentally, by measuring  $T_1$  over an unprecedented range of magnetic fields – made possible by lower temperature – and report a maximum  $T_1 = 57 \pm 15$  s at the lowest fields, setting a record electron spin lifetime in a nanostructure.

This chapter is published in *Nat. Commun.* [117]

<sup>†</sup>*These authors contributed equally to this work.*



## 4.1 Introduction

The decay of the energy stored in the qubit defines the relaxation time  $T_1$ . In qubits based on electronic spins, it corresponds to the relaxation of spin – a longstanding topic of research in semiconductors. The suppression of this process in a confined system compared to the bulk [118] makes quantum dot spin qubits a serious candidate for a quantum technology platform [1, 2, 60]. For spin qubits, the energy splitting is due to the Zeeman term of an applied magnetic field  $B$ . The requirement for a sizable splitting, necessary for many of the protocols to initialize, measure, or manipulate spin qubits [33, 34, 43, 91], then imposes limitations on  $T_1$ , which in turn might influence these protocols in a profound way [36, 119, 120]. This further motivates investigations of mechanisms and fundamental limits of the spin relaxation in quantum dots.

To understand this process in a GaAs quantum dot spin qubit, one needs to consider that it involves the dissipation of both energy and angular momentum, i.e. spin. The former proceeds by emission of a phonon. Considering, for simplicity, long-wavelength three-dimensional bulk phonons, one gets the spin relaxation rate  $W \equiv T_1^{-1} \propto B^3 d^2$  for piezoelectric and  $W \propto B^5 d^2$  for deformation potential phonons, where  $d$  is the dipole moment matrix element between the initial and final state of the transition. For typical Zeeman energies, piezoelectric phonons dominate. Since the initial and final states are opposite in spin, a nonzero dipole element can only arise due to some spin-dependent interaction. In GaAs, the two most relevant ones are the spin-orbit and hyperfine interactions. Their essential difference here is the time-reversal symmetry of the SOI, which also implies  $T_2 = 2T_1$  [90]; there is no such relation for the HF effects. While the hyperfine (HF) interaction induces a  $B$ -independent moment, the time reversal symmetry of the spin-orbit interaction (SOI) results, through the Van-Vleck cancellation, in an additional magnetic field proportionality,  $d^2 \propto B^2$ . Putting these pieces together, the SOI, with  $W \propto B^5$ , will dominate at high fields, and HF, with  $W \propto B^3$ , at low fields. For the parameters of typical surface gate defined GaAs

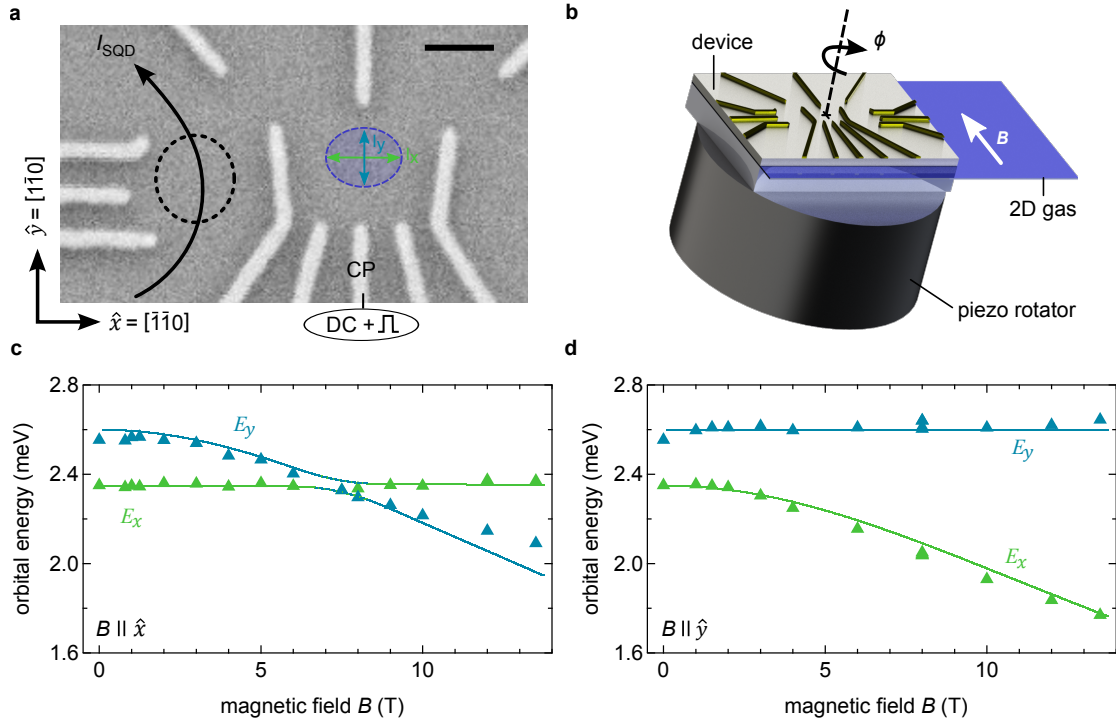


Figure 4.1: **Quantum dot setup and orbital spectroscopy.** **a** Scanning electron microscope image of a co-fabricated lateral, surface gate defined quantum dot. The single electron wave function is indicated by the blue ellipse (not to scale) and is tunnel coupled to the left reservoir only (no tunneling to right lead). An adjacent dot (black circle) serves as a real-time charge sensor, operated in Coulomb blockade for better sensitivity. Sub-microsecond pulses are applied on the center plunger CP. The scale bar corresponds to 200 nm. **b** Measurement setup with sample on a piezo-electric rotator allowing change of the direction of the in-plane magnetic field (up to 14 T) with respect to the crystal axis  $[100]$ , specified by the angle  $\phi$ . **c,d** Energies of the two lowest orbital excited states,  $E_x$  and  $E_y$ , measured with respect to the ground state, as a function of the magnetic field applied along  $\hat{x}$ - (**c**) and  $\hat{y}$ -direction (**d**). Triangles are measured data, solid curves are numerics (see text).

dots, the crossover is predicted at around 1 – 2 Tesla. We estimate that in natural silicon the crossover would happen at magnetic fields roughly hundred times smaller.

Beyond field scaling, the SOI with competing Rashba and Dresselhaus terms results in a strong dependence of spin relaxation on the direction of the applied magnetic field in the plane of the 2D gas—the spin relaxation anisotropy [89, 90, 121]. The HF mechanism, on the other hand, is isotropic [3], even for a dot shape which breaks circular symmetry. These two hallmark features together—*isotropic behavior and  $B^3$  scaling*—constitute a unique fingerprint of the HF relaxation mechanism. Note that the

phonon-assisted inelastic transition is fundamentally different from the elastic electron–nuclear spin flip-flop, which is strongly suppressed due to the pronounced mismatch of the electron and nuclear Zeeman energy for fields above a few mT [122].

Even though the HF assisted mechanism of spin relaxation was predicted early on [3], experimental observation has remained elusive so far for a number of reasons: rather low fields below 1 Tesla are required to reach the HF limit. For a spin doublet, only energy selective spin-readout is available, thus requiring rather low electron temperatures below 100 mK to keep the Zeeman splitting well above the thermal broadening. To check for the direction dependence of relaxation, suitable piezo rotator control over the applied field direction is required, but this has only relatively recently become available. Finally, very long  $T_1$ -times far exceeding 1 s are predicted at such low fields, posing a formidable challenge on the long-term stability and control of a semiconductor nanostructure. Here, we overcome these difficulties by employing a very stable 2D gas and implementing active feedback procedures to keep the energy levels aligned with sub-microvolt precision over days (see Supplementary Note 4.7.2). Specially developed Ag-epoxy filters [97] provide an electron temperature of  $\sim 60$  mK – more than a factor of two lower than before [35]. Using these advances, we show isotropic relaxation combined with a  $T_1 \propto B^{-3}$  scaling at low magnetic fields, thus demonstrating the hallmark signatures of hyperfine-phonon spin relaxation. At the lowest fields, we find  $T_1 = 57 \pm 15$  s – a new record spin lifetime in a nanostructure. The error range specified here and elsewhere in this work is one standard deviation, as obtained from fitting.

## 4.2 Results

### 4.2.1 Quantum dot orbitals

We use a flexible gate layout (see Fig. 4.1a) to shape a nearly circularly symmetric dot and set up a cryogenic piezo-rotator to apply almost perfectly aligned in-plane fields (see Supplementary Note 4.7.1) up to 14 T with arbitrary angle  $\phi$  with respect to the [100] crystal direction (see Fig. 4.1b). The rotator capability allows us to probe the dot orbitals and their shape in large magnetic fields using the established technique of pulsed-gate orbital excited state spectroscopy [35]. Figure 4.1c displays two excited states, shown in green and blue, for field applied along the  $\hat{x}$ -direction. While one state clearly moves down in energy (blue) with increasing field, the other one remains unaffected (green). Since only electron motion perpendicular to the applied field is affected by it, the  $B$ -invariant energy thus corresponds to the excitation along the  $\hat{x}$ -direction, justifying labels as shown on Fig. 4.1c [87, 95]. When the sample is rotated by  $90^\circ$ , the excitations' roles swap and the blue line becomes invariant, see Fig. 4.1d. Such striking behavior, including further  $B$ -directions, is reproduced by an anisotropic harmonic oscillator model [110, 123], which confirms that the quantum dot main axes are well aligned with the  $\hat{x}$ - and  $\hat{y}$ -directions. This essential information about the dot orbitals makes possible a detailed understanding of all measurements, reproducing the measured  $T_1$  quantitatively by numerics using a single set of parameters without phenomenological constants (see Methods for details).

### 4.2.2 Spin-orbit induced spin relaxation anisotropy

With a full orbital model at hand, we now turn to spin relaxation measurements, done by cycling the dot through ionization, charge and relax, and read-out configuration, as depicted in Fig. 4.2a. Averaging over many thousand cycles, we obtain the spin excited

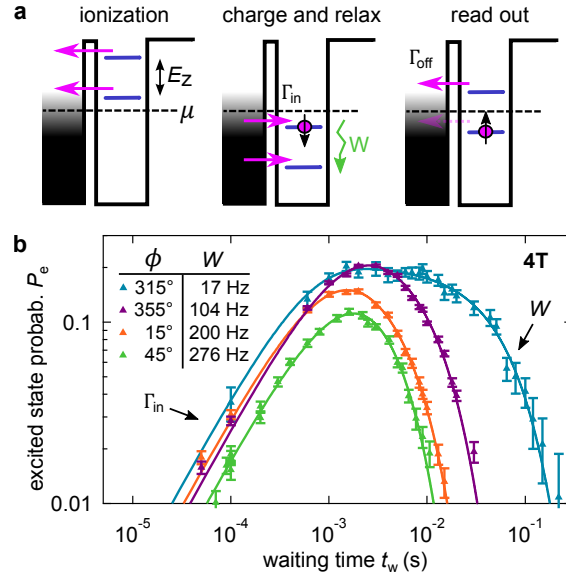


Figure 4.2: **Spin relaxation measurement.** **a** Three step pulse scheme, shifting dot levels with gate-voltage pulses: First, during “ionization”, the dot is emptied. Second, in “charge and relax”, an electron is loaded and if the spin is down, i.e. in the excited spin state, it relaxes with rate  $W$  during the waiting time  $t_w$ . Third, spin-charge conversion is used in “read-out” to detect the spin state: the spin-down electron only will tunnel off the dot, which is detected by the charge sensor. The spin relaxation rate  $W$  is extracted from the dependence of the probability  $P_e$  to find the spin in the excited (down) state as a function of  $t_w$ , shown in **b** for a magnetic field of 4 T applied along different angles  $\phi$  as indicated. Markers show measurements with statistical error bars, curves are fits to the formula  $P_e(t_w) \propto (\exp(-Wt_w) - \exp(-\Gamma_{\text{in}}t_w))/(\Gamma_{\text{in}} - W)$ , where the tunneling-in rate  $\Gamma_{\text{in}}$  is determined independently (see Supplementary Note 4.7.3).  $W$  is thus extracted as the only fit parameter. Error bars are standard deviations from fitting to counts.

state probability  $P_e$  as a function of the waiting time  $t_w$  – the time the electron was given to relax into the spin ground state. A few examples are plotted over four orders of magnitude in  $t_w$  on Fig. 4.2b at a magnetic field of 4 T. All such curves fit very well to the sum of two exponentials, from which we reliably extract the spin relaxation rate  $W \equiv T_1^{-1}$  (see Supplementary Note 4.7.3 for more details). A pronounced dependence of  $W$  on the direction of the magnetic field is observed, as displayed in Fig. 4.3a as a function of the field angle  $\phi$ . A modulation of  $W$  by a factor of  $\sim 16$  is found, with minimal relaxation rate along the  $\hat{x}$ -direction.

This pronounced anisotropy is rooted in a combination of the dot shape asymmetry and the interference of the Rashba and Dresselhaus SOI terms. The latter can quali-

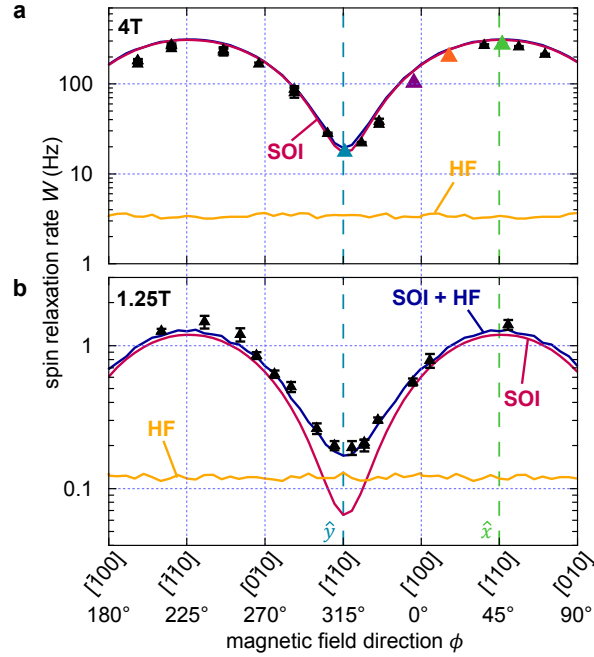


Figure 4.3: **Spin relaxation anisotropy.** Spin relaxation rate  $W$  (triangles with error bars) for in-plane magnetic fields of **a** 4 T and **b** 1.25 T, as a function the field direction. The solid curves show the results from numerics taken into account only the SOI (red), only the HF interaction (orange), and both (dark blue). The ripples in curves from numerics are fluctuations due to finite statistics over random nuclear spin configurations. Error bars are standard deviations from fits to data as introduced in Fig. 4.2b.

tatively be understood from the dependence of the total effective spin-orbit magnetic field on the direction of the electron momentum (Supplementary Note 4.7.5). First derived for symmetric quantum dots [90], the spin relaxation anisotropy due to the dot shape asymmetry was also soon included in a theoretical generalization [121]. The shape-induced contribution to the anisotropy of  $W$  is well known here from the orbital spectroscopy and found to be small. Thus, the anisotropy here is largely due to the SOI, and given the precisely measured orbital energies, it is possible to extract the SOI coupling strengths by fitting the model (see Methods for details). The best fit delivers a ratio  $\alpha/\beta \sim 1.6$  and a spin-orbit length  $l_{so} \approx 2.1 \mu\text{m}$  setting the overall strength of the SOI. These values are well in-line with previous reports for GaAs structures [35, 56, 124]. We note that  $\alpha$  and  $\beta$  are found to have the same sign for the 2D material used. Without knowledge of the orbital energies, the SOI parameters cannot be

directly determined from  $T_1$  [89, 125, 126].

### 4.2.3 Hyperfine-phonon spin relaxation

A very long  $T_1$  time can be achieved by reducing the magnetic field strength and orienting the magnetic field along the crystalline axis with minimal SOI field. Therefore, we carried out the same anisotropy measurements at 1.25 T. Indeed,  $T_1$  times longer than 1 s are obtained. Interestingly, in contrast to the measurements at 4 T, around the  $\hat{x}$ -direction with minimal  $W$ , the measured spin relaxation rate  $W$  (black markers) is seen to be almost a factor of three larger than the calculated SOI rate (red curve, Fig. 4.3b). This is far beyond the error bars, and indicates an additional spin relaxation channel beyond SOI-mediated phonon emission.

Because the dot orbitals are characterized, the HF contribution can be quantified by numerics (see Methods). As shown in Fig. 4.3a, at  $B = 4$  T the microscopic model predicts that the HF contribution (orange curve) is 1 to 2 orders of magnitude smaller than the one due to the SOI (red curve), and is therefore not observable experimentally. In comparison, at  $B = 1.25$  T, as shown in Fig. 4.3b, the SOI model alone is unable to explain the data, but fits very well when the nuclei are included (purple curve), particularly now capturing the minimum close to the  $\hat{x}$ -direction very well. Backed by numerics, we thus conclude that this seemingly subtle feature in the angular modulation of  $W$  actually constitutes the first evidence of the HF relaxation mechanism.

To substantiate this claim, we measure the field magnitude dependence of  $W$ . In Fig. 4.4a we compare two sets, for the magnetic field along the  $\hat{x}$  and  $\hat{y}$ -direction, where the effects of the nuclei with respect to SOI are, respectively, maximal and minimal. The two curves indeed show pronounced differences. With the field along the  $\hat{x}$ -direction, the relaxation follows the  $B^5$  scaling quite well over the entire range of the measured magnetic fields. Thus, for the  $\hat{x}$ -direction, the relaxation is dominated by the SOI for the full field range. In contrast, for fields along  $\hat{y}$ , there is a crossover

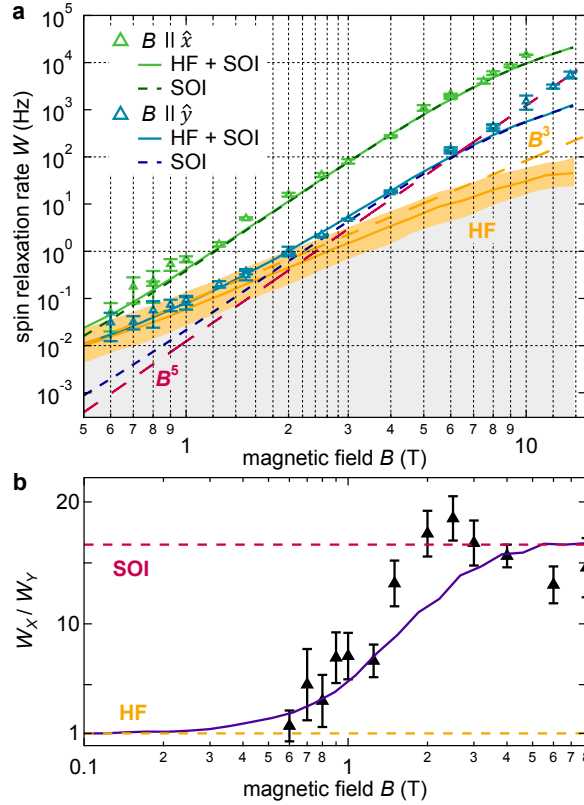


Figure 4.4: **Hyperfine induced spin relaxation.** **a** Spin relaxation rate  $W$  for an in-plane magnetic field along the  $\hat{x}$ -direction (green, along  $[110]$ ) and the  $\hat{y}$ -direction (blue, along  $[1\bar{1}0]$ ) as a function of the field magnitude. The data are shown as triangles with error bars. Numerics considering various terms are shown as labeled. The pure  $B^5$  scaling (red dash) and  $B^3$  scaling (orange dash) are also given as a guide to the eye. The orange band around the HF curve indicates the statistical uncertainty due to a finite number of nuclear spin configurations used in the simulation. **b** The relaxation anisotropy  $W_X/W_Y$  as a function of field magnitude. Experiment is shown as triangles with error bars, numerics with both SOI and HF as a solid curve, showing the transition to isotropic relaxation at low fields. Red dashed line is SOI theory only, orange dash at  $W_X/W_Y = 1$  is the isotropic HF theory. A possible dip below the theory above  $\gtrsim 6$  T could be due to the only remaining discrepancy between theory and experiment, occurring at high fields (see main text). Error bars are fit errors.

around 2 T with a change of the power law scaling from roughly  $B^5$  at high fields to  $B^3$  at low fields, corresponding to a crossover from SOI to HF dominated relaxation.

Some comments are in place. First, dynamic nuclear spin polarization would distort the power laws. The absence of nuclear spin polarization in our measurements is guaranteed by the slowness of electron spin transitions at low fields and is an important advantage over experiments exploiting Pauli spin blockade in double dots. Second, the



only remaining discrepancy of data and model is seen at high fields (see the blue data points and theory curve in Fig. 4.4a for  $B \gtrsim 6$  T). This saturation is predicted in perturbative calculations [90, 116, 127] and exact numerics [121, 128], including our model here, but it is not observed in our data. The explanation needs further investigations. Nevertheless, the issue is irrelevant for the nuclear-induced relaxation taking place at much smaller fields and longer times. Finally, we note a  $T_1$  time of  $57 \pm 15$  s for a magnetic field of 0.6-0.7 T along  $\hat{x}$ , where the range represents the error from fitting (see Supplementary Note 4.7.3). To our knowledge, this is the longest  $T_1$  time reported to date in a nanoelectronic device [35, 36, 126].

This all being said, we stress that the simple observation of a change in the power law scaling of  $W \propto B^3$  is not sufficient as a proof of its HF origin. It could be that the phonons as an energy dissipation channel are replaced by another bath, e.g. charge noise or an ohmic bath also leads to a  $B^3$  dependence [129–131]. The absence of deviations in the scaling of the  $B||\hat{x}$  data indicates that phonons are responsible for the energy dissipation *throughout* and the crossover in the  $\hat{x}$  data is not related to a specific value of  $W$ , or transition energy. Also, if the SOI remained as the mixing mechanism and the energy dissipation channel instead were to change, then the spin relaxation anisotropy, quantified by the ratio  $W_X/W_Y$ , would remain large at low fields. However, as shown in Fig. 4.4b, the anisotropy is seen to decrease from about 16 at high fields towards one at fields below 1 T. This behavior displays spin relaxation with equal speed in both principal directions, thus indicating *isotropic* relaxation at low fields. Together with the  $W \propto B^3$  scaling, these observations constitute unequivocal demonstration of HF-mediated spin relaxation.

In conclusion, we have demonstrated a spin relaxation time of up to  $57 \pm 15$  s limited by HF-phonon spin relaxation in a single electron lateral GaAs quantum dot, exhibiting a  $\propto B^3$  field scaling together with isotropic relaxation at fields below 1 T. At larger fields, the spin relaxation becomes strongly anisotropic, with  $W_X/W_Y \sim 16$ , and the B-field

scaling follows a  $W \propto B^5$  law. Using excited state spectroscopy, we determine the dot orbital energies, can extract the Rashba and linear Dresselhaus parameters from the B-field anisotropy of  $W$ , and simulate the HF induced spin relaxation  $W$ , in very good agreement with the experiment. While ramping the magnetic field from 0.6 T to about 10 T, the spin relaxation rate changes by a striking 6 orders of magnitude. Yet this is captured by the theory throughout the entire range — putting the model using a single set of parameters to a very stringent test. With the SOI parameters at hand, one can maximize the electric dipole spin resonance Rabi frequencies [42, 43] in future experiments by optimizing geometry, with potentially large gains in qubit quality [88].

## 4.3 Methods

### 4.3.1 Sample and measurement

The measurement was performed on a surface gate defined single electron quantum dot formed in a GaAs 2D electron gas. The device was fabricated on a GaAs crystal, grown along the [001] crystal direction, with a GaAs/AlGaAs single heterojunction located 110 nm below the surface with density  $2.6 \times 10^{11} \text{ cm}^{-2}$  and mobility  $4 \times 10^5 \text{ cm}^2 \text{ V}^{-1} \text{ s}^{-1}$ . The layout of the surface gates (see Fig. 4.1a) is modified from that in [35], and allows effective control of the dot shape. Negative gate voltages were applied on the gates to locally deplete the 2D gas and form a quantum dot in the center of the device (blue ellipse in Fig. 4.1a) and the adjacent charge sensor quantum dot (black dashed circle). The main dot is tuned to the single electron regime and tunnel coupled only to its left lead.

The single electron quantum dot is capacitively coupled to the charge sensor, the conductance through which changes by 50-100% when adding or removing an electron to the main dot. Real time detection of the dot charge state was realized by monitoring sensor dot current with a measurement bandwidth of 30 kHz obtained with a specially designed current pre-amplifier (Low-noise high-stability current preamp IF3602, Basel Electronics Lab) capable of handling capacitive input loads as appearing from the microwave filtering. The charge

sensor bandwidth is limited by the low-pass filter of the preamp. For data acquisition as well as gate pulses, a National Instruments USB-6366 DAQ is used. The rectangular pulses are resistively coupled to a DC voltage offset with carefully matched impedance. Our lines show a resistance of about  $40 \Omega$  with a capacitance of about  $5 \text{ nF}$  dominated by the microwave filters [97], which leads to a technical bandwidth of about  $1 \text{ MHz}$ . To reduce the input capacitance induced noise on the IV-converter, microwave filters with a lower capacitance of  $2 \text{ nF}$  were used on those lines.

The main dot is electrically extremely stable due to excellent 2D gas material quality and allows control of the dot energy levels using a level positioning algorithm (Supplementary Note 4.7.2) for an extended period of time, which is crucial for long spin relaxation measurements. This feedback technique was regularly carried out throughout the measurements to compensate drift of the dot energy level with respect to chemical potential of the lead. Additionally, a feedback to compensate the drift of the sensor dot conductance was also performed regularly. Electron exchange processes with the reservoir [99] occurring during the charge and relax pulse step for long waiting times  $t_w$  are detected by continuously monitoring the dot charge state and are removed from the data sets. This becomes an important factor particularly at low fields.

Lots of efforts have gone into operating at low electron temperatures [97–99, 114, 132–141], see [98] for a recent review. The base temperature of the dilution refrigerator is  $T_{\text{base}} \approx 25 \text{ mK}$  and the electron temperature is  $T_{\text{el}} \approx 60 \text{ mK}$ , measured by probing the Fermi-Dirac distribution of the coupled lead. By heating to  $300 \text{ mK}$  where  $T_{\text{el}} \approx T_{\text{base}}$ , the Fermi-Dirac distribution method was also used to quantify the gate lever-arm. The sample was rotated (Attocube ANRv51/RES/LT/HV piezoelectric rotator) in a magnetic field up to  $14 \text{ T}$  applied in the plane of the 2D gas [142]. The out-of-plane magnetic field is determined by standard Hall effect measurements using van der Pauw configurations (Supplementary Note 4.7.1). The maximal misalignment of the in-plane magnetic field is  $1.3^\circ$ , thus the effect of the out-of-plane component is negligible [108]. With all these precautions, we achieve spin-state read-out fidelity of  $\sim 81\%$  at low fields, and as high as  $99\%$  at higher fields. See Supplementary Note 4.7.4 for more details.

### 4.3.2 The numerical model

A microscopic model is used to describe the dot orbital spectroscopy and spin relaxation data. The implementation is based on an exact diagonalization of the electronic Hamiltonian which includes the kinetic energy with an anisotropic mass, a bi-quadratic (harmonic) confinement potential in the 2D plane, the Zeeman term, the linear and cubic spin-orbit terms, and the Fermi contact HF interaction with nuclear spins. This Hamiltonian is discretized in real space, typically on a grid of 100 by 100 points, with Dirichlet boundary conditions for the wavefunction. The resulting hermitian Hamiltonian matrix is diagonalized by the Arnoldi method using the ARPACK library, to obtain a few lowest eigenstates and the corresponding energies [143]. As an example, Fig. 4.1c,d (solid curves) shows the excitation energies calculated from such an exact spectrum as a function of the field. The spin relaxation rates are calculated by Fermi's gold rule using the exact spectrum, and bulk phonons coupled to electrons by deformation and piezoelectric potentials. The rates denoted as "SOI" in the figures were obtained in the same way, but with the HF interaction excluded from the Hamiltonian. Similarly, the tag "HF" means that the spin-orbit terms were excluded.

The results from such a numerical procedure are expected to have a very high precision [144, 145], in the sense of convergence (numerical stability), and also compared to analytical results in cases where the latter are known. As an example, the energies of the Fock-Darwin spectrum for our parameters match the analytical formulas up to errors well below  $1 \mu\text{eV}$ . The errors stemming from the numerical procedures themselves are therefore expected to be completely negligible compared to errors induced by uncertainties of the used parameters, the true confinement shape, or the departures from the assumed simple forms of the spin-orbit, electron-phonon and HF interactions. Whenever the Hamiltonian includes the HF interaction, the given relaxation rate is a geometric average of rates for 1000 configurations of static nuclear spins with random orientations (the approximation of unpolarized nuclei at infinite temperature). More details on the Hamiltonian and the numerical methods used to solve it are given in the Supplementary Notes 4.7.5 to 4.7.10.

### 4.3.3 Analytical results

The following formulas reflect the main features of the relaxation rate important in our experiments. The relaxation rate due to transverse piezoelectric phonons and nuclear spins is

$$\Gamma_{\text{HF}} \approx \frac{8(eh_{14})^2 I(I+1)A^2}{315\pi\hbar^2 m \rho c_t^5 N} \left( \frac{1}{E_x^3} + \frac{1}{E_y^3} \right) (g\mu_B B)^3. \quad (4.1)$$

It is isotropic and proportional to  $B^3$ . Replacing HF with spin-orbit effects leads to

$$\Gamma_{\text{SOI}} \approx \frac{(eh_{14})^2}{210\pi m^2 \rho c_t^5 l_{\text{so}}^2} \left( \frac{1}{E_x^4} + \frac{1}{E_y^4} \right) (g\mu_B B)^5 \times [\cos^2 \xi (f_1 + \epsilon f_2) + \sin^2 \xi (f_3 + \epsilon f_4)]. \quad (4.2)$$

The rate grows as  $B^5$  and is anisotropic, with the angular dependence described by

$$f_1 = 1 + \sin 2\vartheta \sin 2\phi,$$

$$f_2 = \sin 2\delta \sin 2\vartheta + \sin 2\delta \sin 2\phi + \cos 2\delta \cos 2\vartheta \cos 2\phi,$$

$$f_3 = 2,$$

$$f_4 = 2 \sin 2\delta \sin 2\vartheta,$$

$$\epsilon = (E_x^{-4} - E_y^{-4}) / (E_x^{-4} + E_y^{-4}).$$

These formulas are derived in the Supplementary Notes 4.7.5 and 4.7.6, where their generalized forms, including the effects of finite temperature, longitudinal phonons, and deformation electron-phonon potential, are also given.

The parameters in these equations are (values given for GaAs): piezoelectric potential  $h_{14} = 1.4 \times 10^9 \text{ V m}^{-1}$ , nuclear spin  $I = 3/2$ , Fermi-contact interaction constant  $A = 45 \mu\text{eV}$ , effective mass  $m = 0.067 m_e$  with  $m_e$  the electron mass in vacuum, material density  $\rho = 5300 \text{ kg m}^{-3}$ , transverse acoustic phonon velocity  $c_t = 3350 \text{ m s}^{-1}$ , Bohr magneton  $\mu_B = e\hbar/2m_e$ . The number of nuclei in the dot  $N \approx 8.3 \times 10^5$ , the excitation energies  $E_x = 2.33 \text{ meV}$ ,  $E_y = 2.61 \text{ meV}$ , the g-factor  $g = -0.36$ , and the angle of the dot potential axis with the [100] direction  $\delta \approx 50.6^\circ$ , were fitted from spectral data such as in Fig. 4.1. The spin-

orbit parameters  $l_{\text{so}} = 2.1 \mu\text{m}$  and  $\vartheta = 31^\circ$ , defined by writing the Rashba and Dresselhaus interaction strengths (see Eq. (4.17) in Supplementary Note 4.7.5) as  $\alpha = (\hbar/2ml_{\text{so}}) \cos \vartheta$ , and  $\beta = (\hbar/2ml_{\text{so}}) \sin \vartheta$ , were fitted from the  $T_1$  data shown in Figs. 4.3 and 4.4. Finally, the magnetic field orientation is parameterized by writing  $\mathbf{B} = B[\cos \xi \cos \phi, \cos \xi \sin \phi, \sin \xi]$ , referring to crystallographic coordinates.

## 4.4 Acknowledgments

We would like to thank V. Golovach and P. Scarlino for valuable inputs and stimulating discussions and M. Steinacher and S. Martin for technical support. This work was supported by the Swiss Nanoscience Institute (SNI), NCCR QSIT, Swiss NSF, ERC starting grant (DMZ), the European Microkelvin Platform (EMP). PS acknowledges support from CREST JST (JPMJCR1675), and JSPS Kakenhi Grant No. 16K05411.

## 4.5 Author Contributions

L.C.C., L.Y., P.S. and D.M.Z. designed the experiments, analysed the data and wrote the paper. L.C.C. and L.Y. processed the samples and performed the experiments. J.D.Z. and A.C.G. carried out the molecular beam epitaxy growth of the heterostructure. P.S. and D.L. developed and carried out the theoretical work and numerical modeling. All authors discussed the results and commented on the manuscript.

## 4.6 Data availability

The data that support the findings of this study are available in a Zenodo repository at <http://doi.org/10.5281/zenodo.1241104> [146].

## 4.7 Supplementary Information

### 4.7.1 In-plane magnetic field alignment

For the measurements shown, it is crucial to have a good alignment of the external magnetic field  $\mathbf{B}$  with the plane of the 2DEG. Large enough in-plane magnetic field needs to be applied to induce sufficient Zeeman splitting for energy readout. On the other hand, formation of Landau levels due to the perpendicular magnetic fields must be avoided. We extract the out-of-plane angle  $\xi$  via Hall measurements using the standard van der Pauw geometry. The Hall coefficient  $R_{H,\perp}$  for a perpendicular magnetic field was determined in a separate cool-down. In a parallel field configuration, the finite Hall slope from the out-of-plane field component is  $R_{H,\parallel} = R_{H,\perp} \sin(\xi)$  and depends on the tilt of the device. No quantum oscillations were observed up to 10 T, which indicates that the out-of-plane component of the applied magnetic field is very small. We use a piezo-electric rotator (Fig. 4.1b) to rotate the device in a 4 T magnetic field. In Fig. 4.5b,  $\xi$  is plotted as a function of  $\phi$ , the angle with respect to [100] (Fig. 4.5a). As expected,  $\xi$  shows a sinusoidal behavior in  $\phi$  with periodicity of  $360^\circ$ . We find a maximal misalignment of  $1.3^\circ$  close to the crystalline direction [110]. Therefore, we conclude that the effect on our measurements due to the field misalignment is negligible (see Sec. 4.7.7).

### 4.7.2 Level positioning algorithm and sensor stabilization

The spin relaxation measurement scheme strongly depends on the associated tunneling rates (see Sec. 4.7.3) which themselves strongly depend on the energy detuning of ground-state and the chemical potential  $\mu$  of the lead [147]. The dot energy levels drift over time, and to compensate for changes in the tunnel rates, we integrate active stabilization protocols. In this section we first give a brief introduction to resonant tunneling before explaining how we exploit this energy dependence for our active level positioning algorithm (LPA) [147]. We then focus on our protocol to maintain the sensitivity of our sensor quantum dot which is also susceptible to fluctuations.

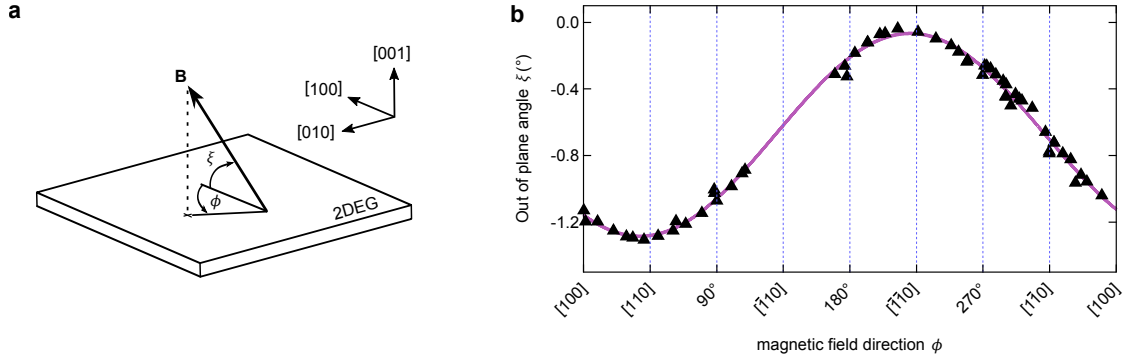


Figure 4.5: **In-plane field alignment with 2DEG.** **a** The angles parametrizing the external magnetic field orientation. The small misalignment of the external magnetic field  $B$  with the plane of the 2DEG is described by the out of plane angle  $\xi$ . The in-plane angle  $\phi$  is defined as the angle with respect to crystal direction  $[100]$ . **b** The out-of-plane angle  $\xi$  alters as the sample is rotated by the piezoelectric rotator. The data set is very well fitted with a sine of  $2\pi$  periodicity (purple solid). Between  $\phi = 115^\circ$  and  $165^\circ$  the sensor of the piezo-rotator does not encode angles.

Resonant tunneling of an electron occurs if the occupation probability of the quantum dot is between 0 and 1. In our system, this is observed when the orbital ground-state level of the quantum dot is energetically within the temperature broadening of the 2DEG reservoir (a few  $k_B T$ ) around the lead chemical potential  $\mu$ . An example is presented in Fig. 4.6a where the dot ground state is aligned with  $\mu$ . Then the occupation probability of the dot is  $1/2$  and electrons resonantly tunnel from the reservoir to the dot and vice versa. The timescale for this tunneling events is given by the details of the tunnel-barrier and is tunable by the surface gates. Quantitatively the tunneling rate at energy  $E$  is  $\Gamma(E) = (2\pi/\hbar)T(E)\rho(E)$  with  $T$  the transmission coefficient and  $\rho$  the density of states in the reservoir [148]. Here, we assume that the tunnel-barrier and the corresponding transmission coefficient  $T$  are energy independent for small detuning from  $\mu$  by a few  $k_B T$ .

In Fig. 4.6b we show an example of resonant tunneling reflected in  $I_{SQD}$ , the current through the sensor quantum dot. We use histograms of  $I_{SQD}$  (Fig. 4.6c) to distinguish the charge states. For a given waiting time  $t_w$ , we define the total time of the dot being occupied as  $T_{on}$ , and being empty as  $T_{off}$  respectively. The tunnel rates in and out of the quantum dot are then given by  $\Gamma_{in} = N_{total}/(2T_{off})$  and  $\Gamma_{off} = N_{total}/(2T_{on})$  with  $N_{total} = N_{on} + N_{off}$  the total number of tunneling events during  $t_w$ . Another method is to histogram the time



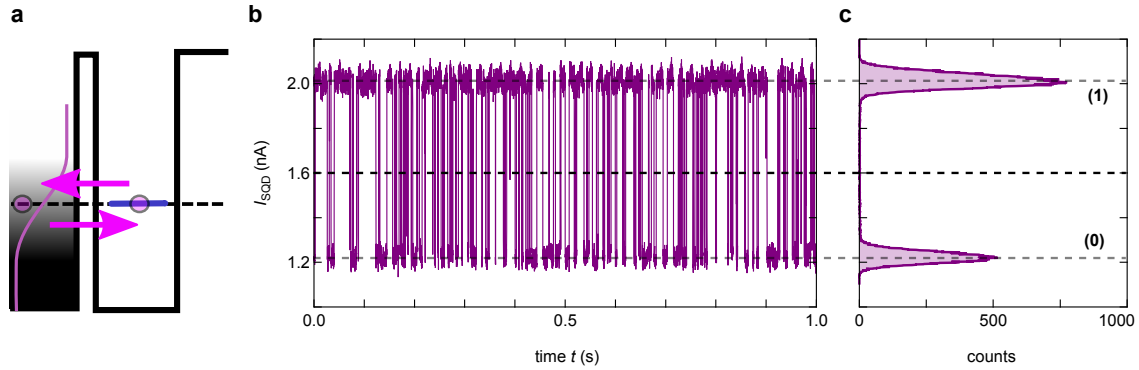


Figure 4.6: **Level positioning algorithm (LPA)**. **a-e** Schematics of tunnel rates (purple arrows) for different positions of the ground state with respect to  $\mu$ . The purple curve in the reservoir (left) depicts the probability of finding an electron in the reservoir as a function of energy. **f** Energy dependence of resonant tunnel rate out of the dot  $\Gamma_{\text{off}}$  (red square).  $\Gamma_{\text{in}}$  exhibits Fermi-Dirac statistics around the regime of resonant tunneling. The electron temperature is around 200 mK. The ground state of the dot drifts over time.  $\Gamma_{\text{tol}}$  of  $\Gamma_{\text{set}}$  is the tolerance interval, which, in practice, is usually set to be 10% of  $\Gamma_{\text{set}}$ , as shown by the green shaded region. For illustration, an example for a correction is shown: if the measured tunnel off rate  $\Gamma_{\text{now}}$  is beyond the tolerance interval, the corresponding plunger gate is corrected by  $\Delta E$  to reset the initial position the ground state. This process is repeated in a closed-loop until  $\Gamma_{\text{set}}$  is restored. **g** The stability of the quantum dot is represented by the correction  $\Delta E$  for one spin relaxation measurement whereas the LPA is performed about every three minutes. A histogram of  $\Delta E$  is shown on the right side of the panel. The data exhibits a Gaussian distribution centered at 0 with standard deviation of  $1.4 \mu\text{eV}$ . It demonstrates that the dot is very stable.

intervals where the dot is empty ( $t_{\text{off}}$ ) or occupied ( $t_{\text{on}}$ ). These times show an exponential distribution, for example,  $\rho_{\text{off}}(t_{\text{off}}) \propto \exp(-\Gamma_{\text{in}}t_{\text{off}})$ , from where the rates are fitted. In our experiment, the tunnel rates using these methods are in very good agreement. However, the first method avoids errors induced by binning or fitting, thus is preferred for automatized control. In Fig. 4.7a-e, the energy diagrams illustrate  $\mu$ , the ground-state energy of the dot and resonant tunnel rates in ( $\Gamma_{\text{in}}$ ) and out ( $\Gamma_{\text{out}}$ ) of the dot for five exemplary situations [104, 113]. Here the dot level is controlled by adjusting the voltage on the center plunger gate CP (see Fig. 4.1a in the main text). In Fig. 4.7a, the ground state is well above  $\mu$  such that an electron on the dot would tunnel out immediately. When the detuning to  $\mu$  is made smaller, occupied states in the reservoir become resonant with the dot level and elastic tunneling could occur (Fig. 4.7b). Because there are more empty than occupied states in the

reservoir, the dot is predominantly empty and  $\Gamma_{\text{off}} > \Gamma_{\text{on}}$ . When the ground state is aligned with  $\mu$  (Fig. 4.7c),  $\Gamma_{\text{off}} = \Gamma_{\text{on}}$  and the dot occupation probability is 1/2. Further lowering the dot level reverses the behavior and  $\Gamma_{\text{off}} < \Gamma_{\text{on}}$  (Fig. 4.7d) until there is no available empty state in the reservoir for the electron to elastically tunnel out of the dot (Fig. 4.7e). In our system, we find that inelastic tunneling is strongly suppressed and the electrons are usually trapped for tens of seconds.

Figure 4.7f shows the quantitative dependence of  $\Gamma_{\text{in}}$  and  $\Gamma_{\text{off}}$  on the detuning from  $\mu$ . To illustrate that this behavior is explained by the occupation statistics of the lead, the data is fit to a Fermi-Dirac distribution. The knowledge that the rates are distributed accordingly is used for positioning the ground state relative to  $\mu$  by establishing a closed-loop feedback either on the tunnel rates or on the dot occupation probability.

The feedback protocol is illustrated in Fig. 4.7f. As shown in the example, the measured tunnel rate off the dot  $\Gamma_{\text{now}}$  is feedbacked to adjust the dot level. Therefore, a correction  $\Delta E$  is calculated and applied to the plunger gate CP (see in Fig. 4.1a) to restore the set tunnel rate  $\Gamma_{\text{set}}$ . This process is repeated until  $\Gamma_{\text{now}}$  is within the tolerance  $\Gamma_{\text{tol}}$  around  $\Gamma_{\text{set}}$ . During the spin relaxation measurements, this feedback is performed about every three minutes. As will be discussed in Sec. 4.7.3, it is of great significance to have a small, well known and constant  $\Gamma_{\text{off}}$  of the spin ground state to guarantee a reliable spin-to-charge conversion. The dot is usually loaded and in Coulomb blockade when the spin excited state becomes resonant, so that only resonant tunneling with the spin ground state is visible. In reality, due to the thermal broadening, the spin excited state at the smallest fields also contributes to the total resonant tunneling which distorts the measured rates. However, even if the rates are distorted the tunnel off rates of the spin excited state is much larger than for the spin ground state which is needed for the spin-to-charge conversion (see Sec. 4.7.3).

In Fig. 4.7g, a series of 5000 corrections ( $\Delta E$ ) are shown for a single spin relaxation measurement at 0.7 T over a continuous measuring time of almost 10 days. For this measurement, the spin ground state is maintained at  $\Gamma_{\text{off}} = 10$  Hz. We record resonant tunneling (Fig. 4.6) for 14 s and extract the rates  $\Gamma_{\text{in,off}}$ . Note that  $\Gamma_{\text{off}}$  is equivalent to the background rate  $\Gamma_b$  described in the spin-to-charge conversion in Sec. 4.7.3. The LPA allows measurements

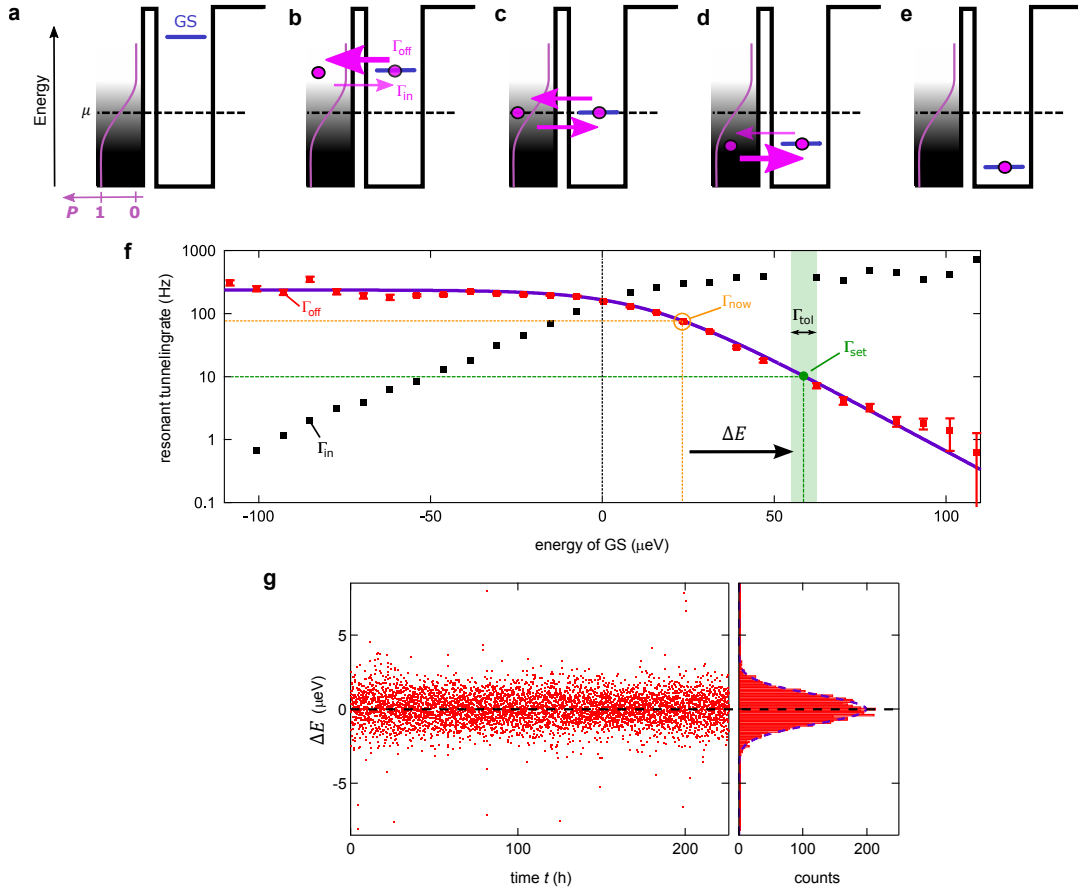


Figure 4.7: **Resonant tunneling and discrimination of charge states.** **a** Schematics of resonant tunneling of electrons between the quantum dot and the reservoir. The purple curve indicates the thermal broadening of occupation statistics. This Fermi-Dirac distribution represents the probability of finding an electron in the reservoir as a function of energy. Due to Coulomb blockade we assume no other level is available and the dot is either empty (0) or loaded (1). **b** An exemplary time trace of the resonant tunneling reflected as jumps between two distinguished values of  $I_{\text{SQD}}$ . As described in the main text, the tunnel rates  $\Gamma_{\text{on,off}}$  are calculated by analyzing such resonant tunneling traces. **c** Histogram of the trace shown in **b** exhibits two-level statistics. Due to the large signal-to-noise ratio the charge states (0) and (1) are distinguished with high fidelity. Also, we measure with tunnel rates well below the bandwidth of the charge sensor what minimizes errors due to missed events.

relying on precise alignment of the dot energy levels for an extended period of time, which is crucial to acquire enough data to provide statistics for extractions of long spin relaxation times. Next, we turn to corrections of the sensor quantum dot. The best sensitivity is achieved when the sensor is positioned on the steepest point of a Coulomb peak (see Fig. 4.8a). To preserve this operation point, a feedback is regularly carried out to compensate for sensor

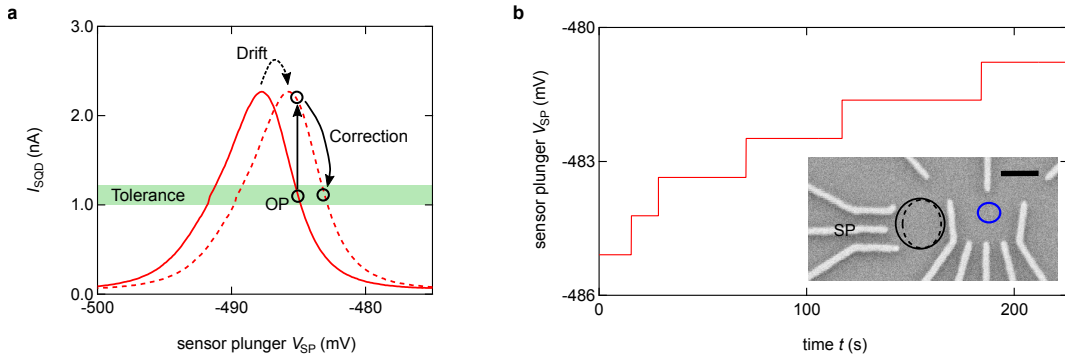


Figure 4.8: **Sensor feedback.** **a**  $I_{\text{SQD}}$  of a sensor Coulomb peak (red solid curve) with the sensor operation point (OP, black circle). With time, the Coulomb peak shifts in energy and hence in plunger voltage  $V_{\text{SP}}$  (red dashed curve). This changes the sensor signal as well as the sensitivity indicated by the vertical arrow. To restore the original operation point,  $V_{\text{SP}}$  is adjusted until  $I_{\text{SQD}}$  is once more within a tolerance. **b** The effective voltage on  $SP$  for a long measurement showing corrections to compensate drift. The carried-out corrections are of similar magnitude because the feedback is applied as soon as  $I_{\text{SQD}}$  is out of the tolerance. The inset schematically shows the sensor dot becoming more confined (dashed circle) due to the drift. Scale bar is 200 nm.

drifts. Before the sensor feedback was carried out, the main dot is slightly detuned from  $\mu$  to avoid resonant tunneling and a stable  $I_{\text{SQD}}$  is read. Drift results in changes of the sensor dot energy spectrum indicated in Fig. 4.8a. This leads to a change of  $I_{\text{SQD}}$  and, more importantly, to a reduction in sensitivity ( $dI_{\text{SQD}}/dV_{\text{SP}}$ ). By applying corrections to the sensor plunger  $SP$  (Fig. 4.8b) in a closed loop, the original sensor operation point is restored. These corrections are calculated with the flank of the Coulomb peak being linearly approximated in  $V_{\text{SP}}$ . In Fig. 4.8b, the evolution of applied voltage on  $SP$ ,  $V_{\text{SP}}$ , is shown for the same spin relaxation measurement discussed in Fig. 4.7. In contrast to Fig. 4.7g, only a few and solely positive corrections were carried out. This unidirectional behavior is often seen but its origin is not clear.

### 4.7.3 Spin relaxation measurement scheme

In this section, we present the rate equations describing the three-step pulse measurement scheme used to extract the spin relaxation rate  $W$ . This section gives a brief summary of the rate equations solved in Ref. [147].

## Ionization

Both spin-up and spin-down states are pulsed well above  $\mu$  for several ms. If the dot is occupied, the electron will tunnel off so that the dot will be empty or ionized. We choose the duration and the ground state energy detuning such that the ionization probability is more than 99%.

## Charge and Relax

In the charge and relax pulse step, both spin states are pulsed below  $\mu$  (see Fig. 4.9a). During the waiting time  $t_w$ , four pathways are possible: (1) the dot stays empty; (2) an electron tunnels into the spin ground state; (3) an electron tunnels into and stays in the spin excited state; (4) an electron tunnels into the spin excited state and relaxes into the spin ground state. There are other suppressed paths like exchange with the reservoir after loading. Such alternative events are found not to influence the statistics and therefore are neglected. Put simply, the measurement scheme relies on counting electrons taking path (3), which are identified by observing a tunneling out of the spin-excited state during the spin-to-charge conversion.

Under the assumption that the dot is ionized in the beginning of the charge and relax step (see Fig. 4.9a), the rate equation for the probability for the dot being empty is

$$\dot{P}_{\text{empty}}(t) = -\Gamma_{\text{in}}P_{\text{empty}} \rightarrow P_{\text{empty}}(t) = e^{-\Gamma_{\text{in}}t}. \quad (4.3)$$

$$\Gamma_{\text{in}} = (\Gamma_e + \Gamma_g) \quad (4.4)$$

Note that  $P_{\text{empty}}(t) = 1 - P_L(t)$  with  $P_L$  the loading probability during the charge and relax step. Although the individual coupling of the spin excited and ground states to the reservoir,  $\Gamma_e$  and  $\Gamma_g$ , is unknown [105, 149–151], the total coupling  $\Gamma_{\text{in}}$  can be obtained by two different methods. Fig. 4.9b shows  $P_{\text{empty}}(t_w)$ , the probability distribution of the dot being empty when entering the read-out stage (3c) after waiting time  $t_w$  in the charge-and-relax stage. This probability is fitted to an exponential function to find  $\Gamma_{\text{in}}$ . In the second method,  $\Gamma_{\text{in}}$  is obtained by a fit to the histogram of  $t_{\text{on}}$ 's, the times for an electron to tunnel into the empty

dot (Fig. 4.9c). The drawback of this method is that in addition to the readout the sensor must also be sensitive during the charge and relax stage to detect  $t_{\text{on}}$ . We therefore apply a compensation pulse to sensor plunger gate SP (see the inset of Fig. 4.8b) to retain sensitivity. This method also allows to obtain  $\Gamma_{\text{in}}$  for each waiting time  $t_w$  individually. As shown in Fig. 4.9d,  $\Gamma_{\text{in}}$  is independent of  $t_w$  as expected.

Without considering the contribution due to the thermal excitation from the spin ground state, the rate equation of the probability for an electron being in the spin excited state is  $\dot{P}_e = \Gamma_e P_{\text{empty}} - W P_e$ . By solving this equation, we find the probability

$$P_e(t) = \frac{\Gamma_e}{\Gamma_{\text{in}}} \cdot \frac{\Gamma_{\text{in}}}{\Gamma_{\text{in}} - W} \cdot (e^{-Wt} - e^{-\Gamma_{\text{in}}t}). \quad (4.5)$$

Note that  $\frac{\Gamma_e}{\Gamma_{\text{in}}}$ , which is not known, is only a scaling factor.

### Read out

When entering the read-out (RO) stage, the probability of the electron still being in the spin excited state after the charge and relax stage is  $P_e(t_w)$ . In the read-out stage, an electron can leave the spin excited state by either tunneling off the dot with a rate  $\Gamma_{\text{off},e}^{\text{RO}}$  or by relaxing into the spin ground state with spin relaxation rate  $W$ . Thus, the rate equation for an electron tunneling out of the spin excited state is  $\dot{P}_e^{\text{RO}} = -\Gamma_{\text{off},e}^{\text{RO}} P_e^{\text{RO}} - W P_e^{\text{RO}}$ , which leads to

$$P_e^{\text{RO}}(t) = P_e(t_w) \cdot e^{-(\Gamma_{\text{off},e}^{\text{RO}} + W)t}. \quad (4.6)$$

For the spin ground state, either an electron in the spin excited state can relax with rate  $W$  or an electron can tunnel into the reservoir with background rate  $\Gamma_b$ . The rate equation is  $\dot{P}_g^{\text{RO}} = -\Gamma_b P_g^{\text{RO}} + W P_e^{\text{RO}}$ , whereas the spin excited state is involved due to spin relaxation. The solution for this equation is

$$P_g^{\text{RO}}(t) = P_g(t_w) e^{-\Gamma_b t} + P_e(t_w) \cdot \frac{W}{\Gamma_{\text{off},e}^{\text{RO}} + W - \Gamma_b} (e^{-\Gamma_b t} - e^{-(\Gamma_{\text{off},e}^{\text{RO}} + W)t}), \quad (4.7)$$

where  $P_g(t_w) = 1 - P_e(t_w) - P_{\text{empty}}(t_w)$  is the probability for an electron to be in the spin ground state when entering the read-out configuration.  $P_g^{\text{RO}}(t)$  and  $P_e^{\text{RO}}(t)$  are not directly

observable in the experiment. But we can detect the timing of tunnel events out of the quantum dot during the readout stage. The probability for an electron tunneling off at time  $t_{\text{off}}$  in the readout stage is  $P_{\text{off}}^{\text{RO}} = \Gamma_{\text{off},e}^{\text{RO}} P_e^{\text{RO}}(t_{\text{off}}) + \Gamma_b P_g^{\text{RO}}(t_{\text{off}})$  which is equivalent to

$$P_{\text{off}}^{\text{RO}} = \eta \cdot P_e(t_w) \left( \Gamma_{\text{off},e}^{\text{RO}} + W \right) e^{-(\Gamma_{\text{off},e}^{\text{RO}} + W)t_{\text{off}}} + \left( P_g(t_w) + \frac{W}{\Gamma_{\text{off},e}^{\text{RO}} + W - \Gamma_b} P_e(t_w) \right) \Gamma_b e^{-\Gamma_b t_{\text{off}}} \quad (4.8)$$

with  $\eta = \left( 1 - \frac{W\Gamma_b}{\Gamma_{\text{off},e}^{\text{RO}}(\Gamma_{\text{off},e}^{\text{RO}} + W - \Gamma_b)} \right) \frac{\Gamma_{\text{off},e}^{\text{RO}}}{\Gamma_{\text{off},e}^{\text{RO}} + W}$ , the fraction of electrons in the spin excited state which tunnel out before they relax into the spin ground state. For low fields,  $\Gamma_{\text{off},e}^{\text{RO}} \gg W, \Gamma_b$  such that  $\eta \approx 1$  while at high fields  $W \sim \Gamma_{\text{off},e}^{\text{RO}}$  and  $\eta$  is reduced to  $\Gamma_{\text{off},e}^{\text{RO}}/(\Gamma_{\text{off},e}^{\text{RO}} + W)$ . Note that for the measurements presented in Fig. 4.2 of the main text,  $\eta \approx 1$ , and it thus has not been involved in the discussion for better readability.

### Extraction of W

Figure 4.9e shows exemplary histograms of  $t_{\text{off}}$  for three waiting times  $t_w$  in the charge and relax stage. The counts out of the dot depend on the loading probability  $P_L(t_w)$  and the probability to relax into the spin ground state during  $t_w$ ,  $W$ . In first panel of Fig. 4.9e,  $t_w$  is short compared to  $1/\Gamma_{\text{in}} \sim 1\text{kHz}$  and the dot is mostly empty when entering the read-out stage. For the next panel,  $t_w > 1/\Gamma_{\text{in}}$  so that  $P_L$  is increased. But  $t_w < 1/W$  and there is an increased number of electrons in the spin excited state which have not yet relaxed when entering the read out stage. For the third panel,  $P_L \sim 1$  but also  $t_w > 1/W$  such that almost all electrons have relaxed into the spin ground state when entering the read-out stage. The total rate out of the excited state  $R = \Gamma_{\text{off},e}^{\text{RO}} + W$  is independent of  $t_w$ , as shown in Fig. 4.9f. This allows us to extract  $\eta P_e$  by fitting Eq. (4.8) to our  $t_{\text{off}}$  histograms for  $t_w$ 's.  $\Gamma_b$  is set and fixed by the LPA as mentioned above. For low fields, where  $\Gamma_{\text{off},e}^{\text{RO}} \sim \Gamma_b$ , we also explicitly fit  $\Gamma_b$  giving excellent agreement with the values chosen for the LPA.

$\eta P_e$  is then plotted as a function of  $t_w$ . The spin relaxation rate  $W$  can be explicitly found out by fitting  $\eta P_e(t_w)$  to Eq. (4.5). As mentioned above,  $\Gamma_{\text{in}}$  is independently obtained from histograms of  $t_{\text{on}}$  or  $P_{\text{empty}}(t_w)$ . Note that  $\eta$  is only a scaling factor for Eq. (4.5) and does

not affect our ability to extract  $W$ . Figure 4.9g shows  $\eta P_e(t_w)$  for selected applied magnetic fields with the respective fits. For the first three panels  $W < \Gamma_{\text{in}}$  and the exponential increase in  $\eta P_e(t_w)$  is represented by  $\Gamma_{\text{in}}$  while the decay is characterized by  $W$ . For the last panel,  $W > \Gamma_{\text{in}}$  and the exponential increase is actually given by  $W$  and the loading rate  $\Gamma_{\text{in}}$  is seen in the decay.

#### 4.7.4 Spin-readout fidelity

In this section, we describe a method to calculate the single-shot read-out fidelity. This method is different from the technical read-out fidelity often adopted in systems where detection of tunneling events is difficult [31, 152] or re-tunneling into the spin ground state during read-out occurs with speed in the order of the detection bandwidth. For the experiment here, the bandwidth of the sensor exceeds all relevant tunneling rates. Rather, the fidelity here is limited by our capability to distinguish the "blind counts" from electrons either tunneling out of the spin excited state or the spin ground state.

As described in Sec. 4.7.3, we do not assign each tunnel-event in the read-out stage as a spin excited event. Our method takes events from the spin-ground state into account which makes the analysis more generic. Obviously it is beneficial if the tunneling rate out of the spin excited state  $\Gamma_e^{\text{RO}} = \Gamma_{\text{off}}$  dominates over the rate out of the spin ground state  $\Gamma_g^{\text{RO}} = \Gamma_b$  which is best fulfilled at large Zeeman splittings  $E_z$  (see Fig. 4.9(e) for an example). At low fields, these rates become closer and the spin read-out fidelity drops.

Using the input from our experimental data, we do excessive simulations of the complete spin relaxation measurement (load and read-out stage) which allows us to track the spin information of a single-shot measurement at any given time (see Fig. 4.10). With these simulations, we generate a complete data set of sensor-current of the pulse-sequences which we run against our analysis algorithms. The fidelity is then based on simulations describing how well the experimental data agree with the rate-equation model (see Sec. 4.7.3). We obtain the spin read-out fidelity by assigning all (simulated) tunnel events counted in the read-out stage before time  $t_{\text{off}}^*$  as spin excited events and all events afterward as spin-ground state and determine our success rate. The contribution of the ground and excited state during



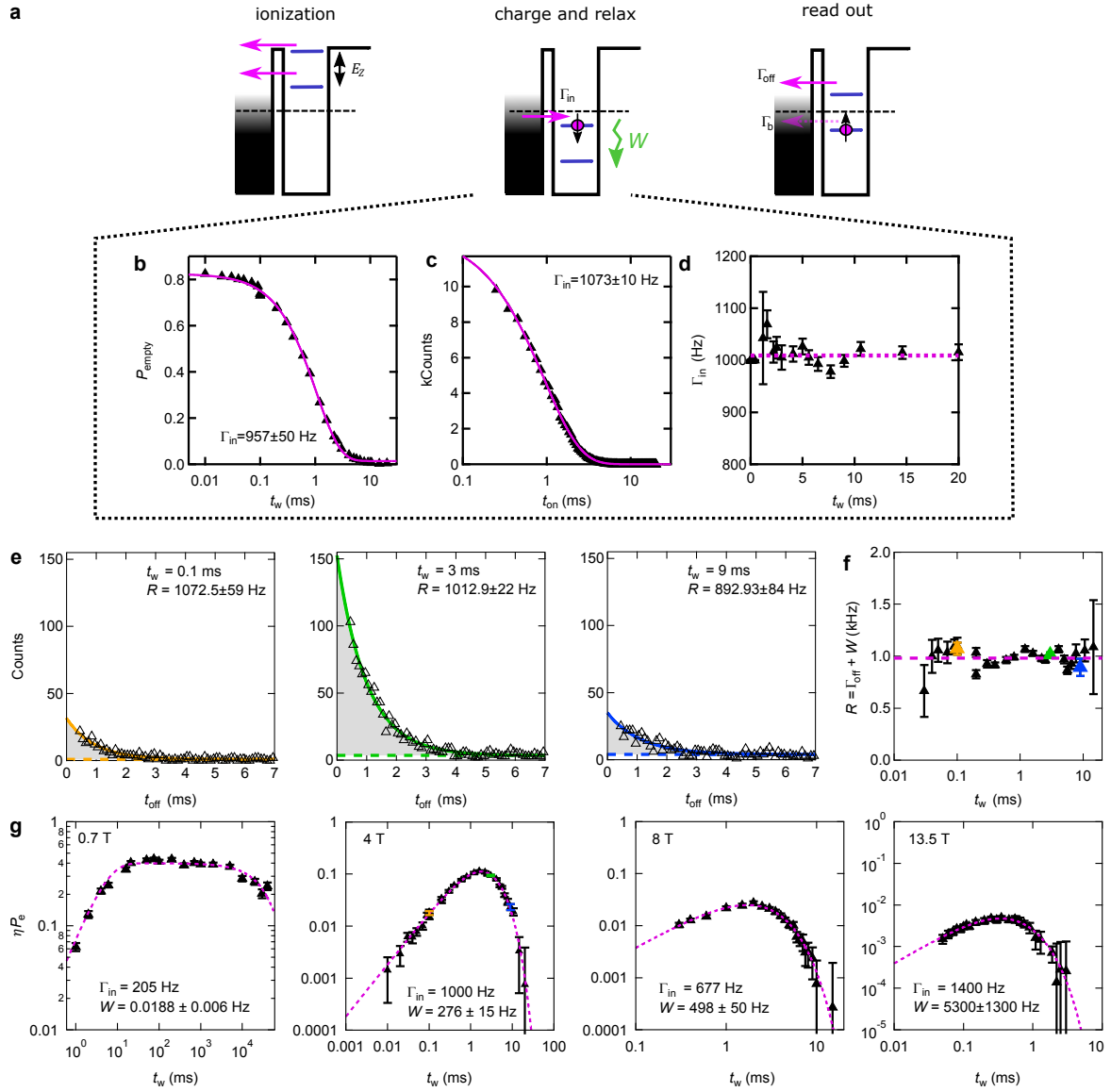


Figure 4.9:  **$T_1$  measurement scheme.** **a** Schematics of the three-step pulse sequence used for the  $T_1$  measurement for Zeeman energy  $E_z = g\mu_B B$  and spin relaxation rate  $W$ . Methods to extract  $\Gamma_{\text{in}}$  by fitting ionization probability  $P_{\text{empty}}$  for different waiting times  $t_w$  (**b**) or by fitting the histogram of  $t_{\text{on}}$  for all data (**c**). **d** shows  $\Gamma_{\text{in}}$  at various waiting times  $t_w$  using the second extraction method. It shows that  $\Gamma_{\text{in}}$  is independent of  $t_w$ . **e** Histograms of tunnel off times  $t_{\text{off}}$  in the read-out stage for three different waiting times  $t_w$  exhibit a double exponential distribution with rates  $R = \Gamma_{\text{off}}^{\text{RO}} + W$  (solid line) and  $\Gamma_b$  (dashed) as described in the text. **f**  $R$  as a function of  $t_w$ . Colored datapoints correspond to colors adopted in **e**. **g**  $P_e$  for different  $t_w$  with fits to Eq. (4.5) as described in the text for four different fields.  $W$  can be then extracted accordingly. Error bars are fit errors.

read out are described in Eq. (4.8) of Sec. 4.7.3 in great detail. We rewrite this formula as

$$P_{\text{off}}^{\text{RO}} = P_{\text{off,e}}^{\text{RO}} + P_{\text{off,g}}^{\text{RO}} = A_e \cdot e^{-(\Gamma_{\text{off}}^{\text{RO}}+W)t_{\text{off}}} + A_g \cdot e^{-(\Gamma_b^{\text{RO}})t_{\text{off}}} \quad (4.9)$$

and describe the fidelity as the ratio of the correctly assigned events to the total counted events

$$F(t_{\text{off}}^*) = \frac{\int_0^{t_{\text{off}}^*} P_{\text{off,e}}^{\text{RO}} dt_{\text{off}} + \int_{t_{\text{off}}^*}^{\infty} P_{\text{off,g}}^{\text{RO}} dt_{\text{off}}}{\int_0^{\infty} (P_{\text{off,e}}^{\text{RO}} + P_{\text{off,g}}^{\text{RO}}) dt_{\text{off}}}. \quad (4.10)$$

Note that  $\int_0^{\infty} (P_{\text{off,e}}^{\text{RO}} + P_{\text{off,g}}^{\text{RO}}) dt_{\text{off}}$  does not necessarily equal 1 because of the possibility to enter the read-out stage with an empty quantum dot. Next, we give the explicit expression for the fidelity

$$F(t_{\text{off}}) = \frac{R \left( \frac{e^{-\Gamma_b t_{\text{off}}}(P_g(t_w)(-R+\Gamma_b)-P_e(t_w)W)}{-R+\Gamma_b} + \frac{(1-e^{-R t_{\text{off}}})P_e(t_w)(R\Gamma_{\text{off}}-\Gamma_b(\Gamma_{\text{off}}+W))}{R(R-\Gamma_b)} \right)}{(P_g(t_w)R + P_e(t_w)(\Gamma_{\text{off}} + W))} \quad (4.11)$$

and the optimal time for the spin state discrimination

$$t_{\text{off}}^* = -\frac{\log \left( \frac{P_g(t_w)R\Gamma_b - P_g(t_w)\Gamma_b^2 + P_e(t_w)\Gamma_b W}{P_e(t_w)(R\Gamma_{\text{off}} - \Gamma_b(\Gamma_{\text{off}} + W))} \right)}{R - \Gamma_b}. \quad (4.12)$$

To prove the validity of our method, we compare the histogram of the total events from the simulations with the histogram obtained from the experiment and find excellent agreement. Fig. 4.10a shows an exemplary data set for an intermediate field of 4 T. Because of decent Zeeman splitting,  $\Gamma_{\text{off}} \ll \Gamma_b$  and the error of assigning spin ground state events as the spin excited events is small. A maximal fidelity of 99% is found for  $t_{\text{off}}^* = 3.7$  ms. Note that even for  $t_{\text{off}}^* = 0$  the fidelity is larger than 50% because as the measurement-scheme enters the read-out stage, the majority of electrons loaded into the spin excited state already relaxed into the spin ground state and will tunnel out with very small rate  $\Gamma_b$ . For lower magnetic fields, the fidelity drops as the ground state contribution significantly affects the read out statistics [see Fig. 4.10b]. For the low field measurement presented (0.7 T) we found a maximal fidelity of 81.5%.

Because of spin relaxation, the count of spin excited electrons is always smaller than the

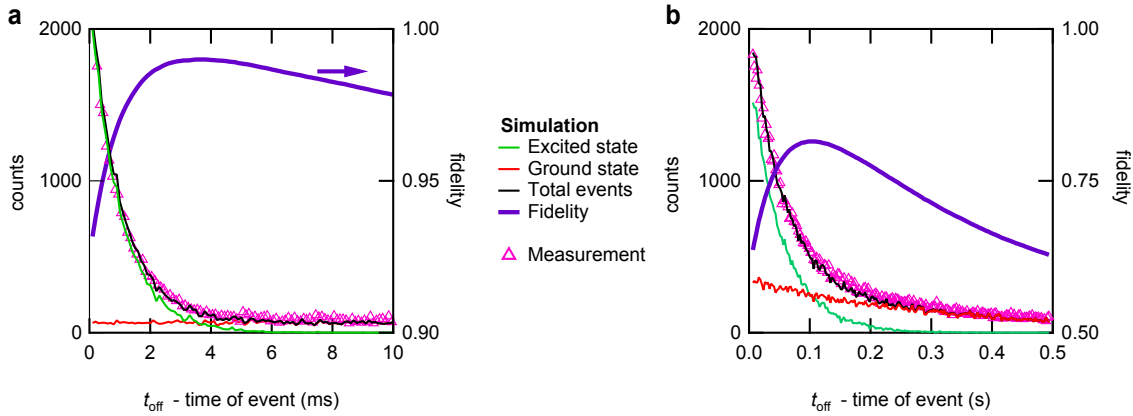


Figure 4.10:  **$T_1$  Spin-readout fidelity.** Simulated distribution of tunneling events in the read out stage for electrons tunneling out of the spin excited (green) and spin ground state (red) using the parameters extracted from the experiment for a dataset of **a** 4 T and **b** 0.7T. The simulated total count (black curve) agrees well with the experimental data (purple triangles). The fidelity (blue curve) is calculated by assigning all events tunneling out of the quantum dot before a certain  $t_{\text{off}}$  as excited state events and all other as spin ground state events and extracting the number of positive classified events from the simulated data set.

spin ground state electrons, which leads to an increased spin readout fidelity. The formalism presented allows to calculate the fidelity with  $P_g(t_w) = P_e(t_w) = 0.5$ . This corresponds to the limit of  $\Gamma_{\text{on}} \rightarrow \infty$  and  $t_w \rightarrow 0$ . In this scenario, the fidelity reduces to 98.1% at 4 T and 79% at 0.7 T, respectively.

#### 4.7.5 Definitions and notations for the electron, nuclear spins, and phonons

We describe the quantum dot and the spin relaxation by the following model. The total electronic Hamiltonian is

$$H = T + V + H_Z + H_{\text{SOI}} + H_{\text{HF}}, \quad (4.13)$$

the components of which we now discuss. To this end, we define the coordinate system along the crystallographic directions by defining unit vectors  $\mathbf{x} \equiv [100]$ ,  $\mathbf{y} \equiv [010]$ , and  $\mathbf{z} \equiv [001]$  and the corresponding coordinates  $x$ ,  $y$ , and  $z$ . The heterostructure is grown along  $\mathbf{z}$ , and the wavefunction corresponding to the lowest 2DEG subband is  $\psi_0(z)$ . In the  $xy$ -plane, the

electronic states are defined by the kinetic energy with the electron effective mass  $m$ , the anisotropy tensor  $\mathcal{M}$ , and a bi-quadratic confinement potential,

$$T + V = \frac{1}{2m} \mathbf{p} \cdot \mathcal{M} \cdot \mathbf{p} + \frac{\hbar^2}{2m} \left( \frac{(\mathbf{r} \cdot \mathbf{n}_1)^2}{l_1^4} + \frac{(\mathbf{r} \cdot \mathbf{n}_2)^2}{l_2^4} \right). \quad (4.14)$$

The tensor  $\mathcal{M}$  reflects the orbital effects of strong in-plane magnetic fields. It is diagonal in coordinate system with the first axis along the in-plane component of the magnetic field and the second perpendicular to it. In these coordinates  $\mathcal{M}^{-1} = \text{diag}(1, 1 + \Phi^2)$ , so that the mass along the in-plane field is unchanged, and perpendicular to it is enhanced. The enhancement grows with  $\Phi$ , the flux penetrating the 2DEG due to the field (see below). The confinement soft and hard potential axes,  $\mathbf{n}_1$  and  $\mathbf{n}_2$ , respectively, are slightly rotated, by angle  $\delta \approx 6^\circ$ , with respect to the device axes  $[110]$ , and  $[\bar{1}10]$ . The confinement lengths  $l_1$  and  $l_2$  are related to the excitation energies by

$$E_1 = \hbar^2 / ml_1^2, \quad (4.15)$$

and an analogous equation for index 2.

The electron is subject to spin-dependent interactions. These comprise, first, the Zeeman term,

$$H_Z = \mu_F \boldsymbol{\sigma} \cdot \mathbf{B}, \quad (4.16)$$

where  $(\sigma_x, \sigma_y, \sigma_z) = \boldsymbol{\sigma}$  is the vector of sigma matrices,  $\mathbf{B} = B(\cos \xi \cos \phi, \cos \xi \sin \phi, \sin \xi)$  is the magnetic field, and  $\mu_F = (g/2)\mu_B$  is the reduced electron magnetic moment, with the g-factor  $g$ , and the Bohr magneton  $\mu_B$ . The associated Zeeman energy is  $\epsilon_z = g\mu_B B = 2\mu_F B$ . Second, the spin-orbit interactions. We split them to the linear Rashba and Dresselhaus terms,

$$H_{\text{SOI}}^{(1)} = \alpha (\sigma_y p_x - \sigma_x p_y) + \beta (-\sigma_x p_x + \sigma_y p_y), \quad (4.17)$$

and the cubic Dresselhaus term,

$$H_{\text{SOI}}^{(3)} = \frac{\gamma_c}{\hbar^3} (\sigma_x p_x p_y^2 - \sigma_y p_y p_x^2). \quad (4.18)$$

The linear interactions' strengths are parameterized by spin-orbit length  $l_{\text{so}}$ , and angle  $\vartheta$  by

writing  $\alpha = (\hbar/2ml_{\text{so}}) \cos \vartheta$ , and  $\beta = (\hbar/2ml_{\text{so}}) \sin \vartheta$ . The linear spin-orbit terms can be recast, by a unitary transformation of the Hamiltonian, into the effective interaction [145],

$$H_{\text{SOI}}^{\text{eff}} = \mu_F (\mathbf{n}_{\text{so}} \times \mathbf{B}) \cdot \boldsymbol{\sigma}, \quad (4.19)$$

which will be convenient below. The dimensionless spin-orbit vector

$$\mathbf{n}_{\text{so}}(\mathbf{r}) = \frac{x}{l_{\text{so}}} [\sin \vartheta, -\cos \vartheta, 0] + \frac{y}{l_{\text{so}}} [\cos \vartheta, -\sin \vartheta, 0]. \quad (4.20)$$

We write it using the dot coordinates as

$$\mathbf{n}_{\text{so}}(\mathbf{r}) = \mathbf{n}_{\text{so}}^{(1)}(\mathbf{n}_1 \cdot \mathbf{r}) + \mathbf{n}_{\text{so}}^{(2)}(\mathbf{n}_2 \cdot \mathbf{r}), \quad (4.21)$$

by defining the following vectors

$$\mathbf{n}_{\text{so}}^{(1)} = \frac{1}{l_{\text{so}}} [\sin(\delta + \vartheta), -\cos(\delta - \vartheta), 0], \quad (4.22a)$$

$$\mathbf{n}_{\text{so}}^{(2)} = \frac{1}{l_{\text{so}}} [\cos(\delta + \vartheta), \sin(\delta - \vartheta), 0]. \quad (4.22b)$$

For later convenience the following expressions are noted,

$$\begin{aligned} |\mathbf{n}_{\text{so}}^{(1)} \times \mu_F \mathbf{B}|^2 &= \left( \frac{\mu_F B}{l_{\text{so}}} \right)^2 \cdot \\ &\quad \left\{ \cos^2 \xi \cdot [\cos \phi \cos(\delta - \vartheta) + \sin \phi \sin(\delta + \vartheta)]^2 + \sin^2 \xi \cdot (1 + \sin 2\delta \sin 2\vartheta) \right\}, \\ |\mathbf{n}_{\text{so}}^{(2)} \times \mu_F \mathbf{B}|^2 &= \left( \frac{\mu_F B}{l_{\text{so}}} \right)^2 \cdot \\ &\quad \left\{ \cos^2 \xi \cdot [\cos \phi \sin(\delta - \vartheta) - \sin \phi \cos(\delta + \vartheta)]^2 + \sin^2 \xi \cdot (1 - \sin 2\delta \sin 2\vartheta) \right\}. \end{aligned} \quad (4.23)$$

These expressions are anisotropic, due to the anisotropy of the spin-orbit interactions, Eq. (4.17), illustrated in Fig. 4.11.

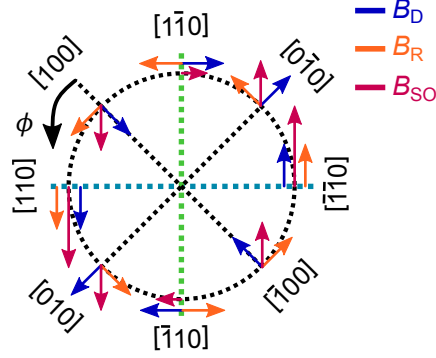


Figure 4.11: **Angular spin-orbit interaction.** The total SOI field  $B_{\text{SOI}} = B_R + B_D$  (red) along various crystal axes from the interplay of the Rashba  $B_R$  (orange) and linear Dresselhaus  $B_D$  (dark blue) SOI components. The interplay of  $B_R$  and  $B_D$  leads to an anisotropic  $B_{\text{SO}}$ . A maximal  $B_{\text{SO}} \sim |\alpha + \beta|$  is expected along  $[110]$  and minimal  $B_{\text{SO}} \sim |\alpha - \beta|$  along  $[1\bar{1}0]$ .  $\phi$  is defined as the angle with respect to  $[100]$ .

Third, there is Fermi's contact interaction,

$$H_{\text{HF}} = Av_0 \sum_n \delta(z - z_n) \delta(\mathbf{r} - \mathbf{r}_n) \boldsymbol{\sigma} \cdot \mathbf{I}_n. \quad (4.24)$$

Here,  $n$  labels the nuclei with spin  $\mathbf{I}_n$  and position  $\mathbf{R}_n \equiv (\mathbf{r}_n, z_n)$ , and similarly  $\mathbf{R} = (\mathbf{r}, z)$  is the three dimensional electron position operator. Further,  $A$  is a material constant, and  $v_0 = a_0^3/8$  is the volume per atom, with  $a_0$  the lattice constant. To evaluate the matrix elements  $H_{\text{HF}}$ , one has to consider also the extension of the electronic state along the  $\mathbf{z}$  axis. We define the length scale  $l_h$  by [153]

$$l_h^{-1} = \int dz |\psi_0(z)|^4, \quad (4.25)$$

which therefore depends on the 2DEG width along the growth direction. The flux due to the in-plane field is also related to the 2DEG width, by

$$\Phi = \frac{e}{\hbar} \lambda_z^2 B \cos \xi, \quad (4.26)$$

through another effective length  $\lambda_z$ . Both  $l_h$  and  $\lambda_z$  are of the order of the nominal width of the 2DEG,  $l_z$ , with the precise relation dependent on the heterostructure confinement profile.

For  $\psi_0(z)$ , we use the ground state of a triangular potential (the Airy function), as described in detail in Ref. [95].

The electron-phonon interaction is described by

$$H_{\text{ph}} = \sum_{\lambda\kappa} (b_{\lambda\kappa} + b_{\lambda-\kappa}^\dagger) H_{\text{ph}}^{\lambda\kappa}, \quad (4.27)$$

where  $\lambda \in \{l, t_1, t_2\}$  is the acoustic phonon branch index, with  $l$  the longitudinal and  $t_1, t_2$  the two transversal branches of acoustic phonons,  $\kappa$  is the three dimensional phonon wavevector, and the coupling

$$H_{\text{ph}}^{\lambda\kappa} = \sum_{\eta} \sqrt{\frac{\hbar\kappa}{2\rho V c_{\lambda}}} \sigma_{\eta} M_{\lambda\kappa}^{\eta} e^{i\kappa \cdot \mathbf{R}}. \quad (4.28)$$

For later notational convenience the index  $\eta \in \{\text{df}, \text{pz}\}$  labels here the electron-phonon interactions, deformation and piezoelectric. Further,  $\rho$  is the material density,  $V$  is the crystal volume,  $c_{\lambda}$  is the sound velocity,  $M_{\lambda\kappa}^{\text{df}} = \delta_{\lambda l}$  with the latter being the Kronecker delta symbol,  $\sigma_{\text{df}} = \sigma_e$  is the deformation potential,  $\sigma_{\text{pz}} = -ieh_{14}/\kappa$ , with  $h_{14}$  being the piezoelectric constant, and

$$M_{\lambda\kappa}^{\text{pz}} = \frac{2}{\kappa^2} (\kappa_x \kappa_y e_{\lambda}^z + \kappa_z \kappa_x e_{\lambda}^y + \kappa_y \kappa_z e_{\lambda}^x), \quad (4.29)$$

is a dimensionless factor defined by the components of  $\mathbf{e}_{\lambda}$ , the three mutually perpendicular polarization vectors of unit length.

#### 4.7.6 The spin relaxation rate

The relaxation rate between an initial electronic state  $i$  and the final state  $f$ , with the corresponding energies  $E_i, E_f$ , corresponding to a single phonon emission, is given by the Fermi's Golden rule

$$\Gamma = \frac{2\pi}{\hbar} \sum_{\lambda\kappa} |\langle f | H_{\text{ph}}^{\lambda\kappa} | i \rangle|^2 \delta(E_{if} - \hbar c_{\lambda} \kappa) [n(E_{if}) + 1], \quad (4.30)$$

where we assumed  $E_{if} = E_i - E_f > 0$ , and  $n$  is the phonon thermal occupation factor

$$n(\epsilon) = \frac{1}{\exp(\epsilon/k_B T) - 1}, \quad (4.31)$$

with  $k_B$  the Boltzmann constant and  $T$  the temperature.

For the spin relaxation, the initial state is  $|i\rangle = |\Psi_{0\downarrow}\rangle$ , the orbital ground state with spin down, the final state is  $|f\rangle = |\Psi_{0\uparrow}\rangle$ , the orbital ground state with spin up, and the transition energy equals to the Zeeman energy,  $E_{if} = \epsilon_z$ . In the continuum limit for phonons,  $\sum_{\boldsymbol{\kappa}} \rightarrow [V/(2\pi)^3] \int d\boldsymbol{\kappa}$ , we get Eq. (4.30) in the following form

$$\Gamma = [n(\epsilon_z) + 1] \sum_{\eta\lambda} \int d\boldsymbol{\kappa} \frac{\kappa}{8\pi^2 \rho c_\lambda} |\sigma_\eta|^2 |M_{\lambda\boldsymbol{\kappa}}^\eta|^2 |\tau(\boldsymbol{\kappa})|^2 \delta(\epsilon_z - \hbar c_\lambda \kappa), \quad (4.32)$$

where we introduced

$$\tau(\boldsymbol{\kappa}) = \langle \Psi_{0\downarrow} | e^{i\boldsymbol{\kappa} \cdot \mathbf{R}} | \Psi_{0\uparrow} \rangle, \quad (4.33)$$

as the matrix element of the electron-phonon interaction between the initial and final state. Even though our numerics implements the evaluation of these formulas exactly, to substantiate the discussion in the main text introduction, we also provide analytical results. To this end, we adopt some approximations, most importantly the dipole approximation, expanding the exponential in Eq. (4.33) to the lowest order. The quantity  $|\tau|^2$  is then given by the dipole matrix element between the lowest spin opposite quantum dot states and is bilinear in the components of vector  $\boldsymbol{\kappa}$  (see Fig. 4.7.8). To proceed with such an expression, we define the following average

$$\langle f(\boldsymbol{\kappa}) \rangle = \int d\boldsymbol{\kappa} |M_{\lambda\boldsymbol{\kappa}}^\eta|^2 f(\boldsymbol{\kappa}) \delta(\epsilon_z - \hbar c_\lambda \kappa), \quad (4.34)$$

as the integral over phonon wavevectors with the weights from Eq. (4.32). The zinc-blend crystal symmetry gives the following result

$$\langle (\boldsymbol{\kappa} \cdot \mathbf{n})(\boldsymbol{\kappa} \cdot \mathbf{m}) \rangle = C_\lambda^\eta \frac{\kappa_\lambda^4}{\hbar c_\lambda} (\mathbf{n} \cdot \mathbf{m}), \quad (4.35)$$

for  $\mathbf{n}$  and  $\mathbf{m}$  being in-plane unit vectors,  $\kappa_\lambda = \epsilon_z / \hbar c_\lambda$ , and the numerical constants  $C_l^{\text{df}} =$



$2\pi/3$ ,  $C_l^{\text{pz}} = 8\pi/35$ , and  $C_{t_1}^{\text{pz}} = C_{t_2}^{\text{pz}} = 2/3 \times C_l^{\text{pz}}$ . We now write the rate as

$$\Gamma = \gamma \langle d^2 \rangle, \quad (4.36)$$

splitting it to the phonon part and the (averaged) dipole moment between the spin opposite states. The first is

$$\gamma = [n(\epsilon_z) + 1] \sum_{\eta\lambda} C_\lambda^\eta \frac{\kappa_\lambda^5}{8\pi^2 \hbar \rho c_\lambda^2} |\sigma_\eta|^2 = \frac{n(\epsilon_z) + 1}{15\pi \hbar \rho} \left( \frac{5}{4} \frac{\sigma_e^2}{\hbar^5 c_l^7} \epsilon_z^5 + \frac{(eh_{14})^2}{\hbar^3 \bar{c}^5} \epsilon_z^3 \right), \quad (4.37)$$

where we defined a weighted phonon velocity

$$\frac{1}{\bar{c}^5} = \left( \frac{3}{7} \frac{1}{c_l^5} + \frac{4}{7} \frac{1}{c_t^5} \right). \quad (4.38)$$

The second, derived in Sec. 4.7.8, is

$$|d_{\text{SOI}}|^2 \approx |\mu_F \mathbf{B} \times \mathbf{n}_{\text{so}}^{(1)}|^2 l_1^4 \frac{E_1^2}{(E_1^2 - \epsilon_z^2)^2} + |\mu_F \mathbf{B} \times \mathbf{n}_{\text{so}}^{(2)}|^2 l_2^4 \frac{E_2^2}{(E_2^2 - \epsilon_z^2)^2}, \quad (4.39a)$$

$$|d_{\text{HF}}|^2 \approx \frac{2I(I+1)A^2}{3N} \left( l_1^2 \frac{E_1^2}{(E_1^2 - \epsilon_z^2)^2} + l_2^2 \frac{E_2^2}{(E_2^2 - \epsilon_z^2)^2} \right). \quad (4.39b)$$

Equations Eq. (4.37) and Eq. (4.39) make the power dependence on the magnetic field explicit for any combination of the phonon interaction, with  $\gamma^{\text{df}} \propto B^5$  and  $\gamma^{\text{pz}} \propto B^3$  and the spin-dependent electron interaction, with  $|d_{\text{SOI}}|^2 \propto B^2$ , and  $|d_{\text{HF}}|^2 \propto B^0$  (up to the small magnetic field orbital effects; see below). The expressions for the relaxation rates given in the Methods, Eq. 4.1 and Eq. 4.2, can be obtained by restricting to the dominant piezoelectric phonons in Eq. (4.37), neglecting the Zeeman term with respect to the orbital energies, and using Eq. (4.15), and for the spin-orbit interaction case also Eq. (4.23).

#### 4.7.7 Anisotropy of the hyperfine relaxation rate

The strong anisotropy of the relaxation induced by the spin-orbit interactions played a major role in our experiment and allowed to distinguish it from the hyperfine effects. Indeed, compared to the explicitly anisotropic Eq. (4.39a), the expression in Eq. (4.39b) stays unchanged,

as long as the dot shape is fixed. Neglecting the orbital effects of the magnetic field, this is indeed the case. In this section we estimate the small anisotropy induced by going beyond this approximation (of a purely in-plane field, and a 2DEG with zero width). We first consider the orbital effects of a purely in-plane field, and then an out-of-plane field. For both of these it is useful to consider a change of the mass in the kinetic term of a linear harmonic oscillator,  $m \rightarrow m^*$ . With the Hamiltonian written in the form of Eq. (4.14),

$$\frac{p^2}{2m} + \frac{\hbar^2 r^2}{2m l^4} \rightarrow \frac{p^2}{2m^*} + \frac{\hbar^2 r^2}{2m l^4} \equiv \frac{p^2}{2m^*} + \frac{\hbar^2 r^2}{2m^* l^{*4}}, \quad (4.40)$$

Upon such a change the oscillator energy and dipole elements rescale to

$$E^* = E \left( \frac{m}{m^*} \right)^{1/2}, \text{ and } l^* = l \left( \frac{m}{m^*} \right)^{1/4}. \quad (4.41)$$

the latter following from  $E^* = \hbar/m^*l^{*2}$ , the standard relation for the LHO energy. The in-plane field orbital effects will lead to such changes along the axis perpendicular to the magnetic field. If the dot is anisotropic, this will lead to anisotropic change of the dipole moment  $|d_{\text{HF}}|^2$ . We quantify the magnitude of such anisotropy by the ratio of the difference and sum, of the dipole moment extrema (as a function of the magnetic field direction), which are achieved with the magnetic field along the potential axes,

$$\Delta_{|d|^2}^{\text{in}} \equiv \frac{|d(\mathbf{B} \parallel \mathbf{n}_1)|^2 - |d(\mathbf{B} \parallel \mathbf{n}_2)|^2}{|d(\mathbf{B} \parallel \mathbf{n}_1)|^2 + |d(\mathbf{B} \parallel \mathbf{n}_2)|^2} = \frac{1 - (1 + \Phi^2)^{3/2} E_1^{-3} - E_2^{-3}}{1 + (1 + \Phi^2)^{3/2} E_1^{-3} + E_2^{-3}}. \quad (4.42)$$

The left hand equality sign is a definition, and the right hand side was obtained by neglecting the Zeeman energy in Eq. (4.39b), and using that that the in-plane field renormalizes the mass according to  $m^*/m = 1 + \Phi^2$ , with the flux given in Eq. (4.26). The expression in Eq. (4.42) is plotted for our parameters in Fig. 4.12.

We now turn to the case of a magnetic field with an out-of-plane magnetic component,  $B \sin \xi \neq 0$ . We will consider an isotropic quantum dot, for simplicity, and define the anisotropy of the rate by comparing its value for a purely in-plane field, and a value for a finite out-of-plane component. With these two values, we define  $\Delta$  for this case analogously to

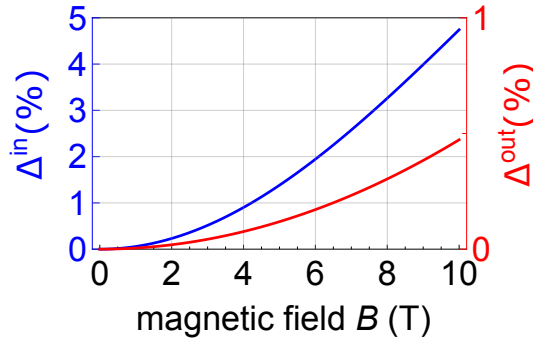


Figure 4.12: **Anisotropy of the hyperfine induced relaxation rate.** The blue curve shows  $\Delta^{\text{in}}$ , Eq. (4.42), the in-plane anisotropy of the relaxation rate. It equals the ratio of the maximal deviation of the rate from its average, and the average, upon varying the magnetic field within the 2DEG plane. The red curve shows  $\Delta^{\text{out}}$ , Eq. (4.44), the out-of-plane anisotropy of the rate (the full expression and its approximation discussed in the text are indistinguishable on the figure resolution). It shows, again on relative scale, the change of the rate upon misaligning the field out of the 2DEG plane. We adopted the parameters of the dot, and for the second quantity we set  $\xi = 1.3^\circ$ , the maximal misalignment angle found in Fig. 4.5b.

Eq. (4.42). The orbital effects of an out-of-plane field are described by a renormalization of the confinement length, and splitting the excited states energies according to their orbital moment  $L$ . These two effects are for the two excited lowest states,  $L = \pm 1$ , given by

$$l^{*-4} = l^{-4} + \left( \frac{eB \sin \xi}{2\hbar} \right)^2, \text{ and } E^* = \frac{\hbar^2}{ml^{*2}} \pm \frac{\hbar e}{2m} B \sin \xi. \quad (4.43)$$

Calculating  $\Delta$  becomes a straightforward algebra, using the previous equation, and Eq. (4.39b), and we plot the result in Fig. 4.12. We note that for the case of a slightly asymmetric dot, the energy effect is quenched as long as  $(\hbar e/2m)B_z \ll |E_1 - E_2|$ , which is the case in our experiment. Keeping only the orbital squeezing effect (the renormalization of the confinement length), we then get

$$\Delta_{|d|^2}^{\text{out}} \equiv \frac{|d(\xi)|^2 - |d(\xi = 0)|^2}{|d(\xi)|^2 + |d(\xi = 0)|^2} \approx 3 \frac{e^2 B^2}{8\hbar^2} \sin^2 \xi. \quad (4.44)$$

Looking at the figure, we conclude that the expected anisotropies of the hyperfine relaxation rates due to the orbital effects of the magnetic field are indeed very small, and the hyperfine induced relaxation is therefore expected to be isotropic within the experimental resolution.

#### 4.7.8 Dipole matrix elements between the spin opposite states

We now derive Eq. (4.39), considering the spin-dependent effects (other than the Zeeman energy) in the Hamiltonian of Eq. (4.13) perturbatively. To this end, we define the unperturbed Hamiltonian  $H_0 = T + V + H_Z$  and consider the effects of the remaining terms,  $H' = H_{\text{SOI}} + H_{\text{HF}}$ , in the basis of the unperturbed eigenstates, denoted  $|\Phi\rangle$ , while the exact eigenstates are denoted by  $|\Psi\rangle$ . Both are labelled by the orbital and spin index of the electronic wavefunction,  $j = 0, 1, \dots$ , and  $\sigma = \uparrow, \downarrow$ , respectively, and the many-particle state of the nuclear spins in the quantum dot, denoted as a multi-index  $\mu$ .

With this notation, we calculate the matrix element in Eq. (4.33) in the lowest order perturbation in  $H'$ . Expanding the indexes by the one corresponding to the nuclear spins, the initial state is

$$|\Psi_{0\bar{\sigma}\mu}\rangle \approx |\Phi_{0\bar{\sigma}\mu}\rangle + \sum_{j\sigma'\mu' \neq 0\bar{\sigma}\mu} \frac{\langle \Phi_{j\sigma'\mu'} | H' | \Phi_{0\bar{\sigma}\mu} \rangle}{E_{0\bar{\sigma}\mu} - E_{j\sigma'\mu'}} |\Phi_{j\sigma'\mu'}\rangle, \quad (4.45)$$

where the phonon emission (absorption) corresponds to  $\sigma = \uparrow (\downarrow)$ , while the final state is

$$|\Psi_{0\sigma\mu^*}\rangle \approx |\Phi_{0\sigma\mu^*}\rangle + \sum_{j\sigma'\mu' \neq 0\sigma\mu^*} \frac{\langle \Phi_{j\sigma'\mu'} | H' | \Phi_{0\sigma\mu^*} \rangle}{E_{0\sigma\mu^*} - E_{j\sigma'\mu'}} |\Phi_{j\sigma'\mu'}\rangle. \quad (4.46)$$

We assume that the unperturbed basis can be factorized

$$|\Phi_{j\sigma\mu}\rangle = |\Phi_j\rangle \otimes |\sigma\rangle \otimes |\mu\rangle, \quad (4.47)$$

so that the orbital part does not depend on the spin indexes, and that the electron-phonon interaction, the matrix element of which we are calculating, is diagonal in both spin indexes.

This gives

$$\tau(\boldsymbol{\kappa}) = \sum_j \langle \bar{\sigma}\mu | \frac{e^{i\boldsymbol{\kappa}\cdot\mathbf{R}_{0j}} H'_{j0}}{E_{0j} + (E_{\sigma\bar{\sigma}} + E_{\mu^*\mu})} + \frac{e^{i\boldsymbol{\kappa}\cdot\mathbf{R}_{j0}} H'_{0j}}{E_{0j} - (E_{\sigma\bar{\sigma}} + E_{\mu^*\mu})} | \sigma\mu^* \rangle, \quad (4.48)$$

where we have introduced the notation for orbital matrix elements as

$$O_{ij} = \langle \Phi_i | O | \Phi_j \rangle, \quad (4.49)$$

for energies as  $E_{ij} = E_i - E_j$ , and similarly for the spin indexes. Note also that the  $j = 0$  term cancels exactly from the sum in Eq. (4.48).

We now adopt the dipole approximation, by expanding the electron-phonon interaction to the lowest order

$$e^{i\boldsymbol{\kappa}\cdot\mathbf{R}} \approx 1 + i\boldsymbol{\kappa}\cdot\mathbf{R}, \quad (4.50)$$

which leads to

$$\tau(\boldsymbol{\kappa}) = i\boldsymbol{\kappa}\cdot\sum_{j\neq 0}\langle\bar{\sigma}\mu|\frac{\mathbf{R}_{0j}H'_{j0}}{E_{0j}+(E_{\sigma\bar{\sigma}}+E_{\mu^*\mu})}+\frac{\mathbf{R}_{j0}H'_{0j}}{E_{0j}-(E_{\sigma\bar{\sigma}}+E_{\mu^*\mu})}|\sigma\mu^*\rangle, \quad (4.51)$$

This leads to substantial simplification for a bi-harmonic confinement. Indeed, in such case, only the lowest two excited states have non-zero dipole matrix element with the ground state, which are mutually orthogonal (even if they are complex, which is, however, not considered here). In this case, the integration over the phonon wavevectors  $\boldsymbol{\kappa}$  makes the mixed terms in  $|\tau|^2$  zero, see Eq. (4.35). We therefore get

$$\langle|\tau(\boldsymbol{\kappa})|^2\rangle = \langle|\boldsymbol{\kappa}\cdot\mathbf{d}_1|^2\rangle + \langle|\boldsymbol{\kappa}\cdot\mathbf{d}_2|^2\rangle, \quad (4.52)$$

where the dipole moments for the excited states are given by

$$\mathbf{d}_j = \langle\bar{\sigma}\mu|\frac{\mathbf{R}_{0j}H'_{j0}}{E_{0j}+(E_{\sigma\bar{\sigma}}+E_{\mu^*\mu})}+\frac{\mathbf{R}_{j0}H'_{0j}}{E_{0j}-(E_{\sigma\bar{\sigma}}+E_{\mu^*\mu})}|\sigma\mu^*\rangle. \quad (4.53)$$

Next we evaluate these dipole elements separately for the spin-orbit, and hyperfine interactions. We will also neglect the nuclear Zeeman energies  $E_{\mu^*\mu}$  as negligible compared to the electron Zeeman energy  $E_{\sigma\bar{\sigma}} = \bar{\sigma}\epsilon_z$ , and notice that we can put  $\mathbf{R}_{ij} = \mathbf{r}_{ij}$ , if all considered states are from the lowest 2DEG subband, what is the case here.

Let us take first the spin-orbit interactions. We take into account only the linear terms in their effective form,  $H' = H_{\text{SO1}}^{\text{eff}}$ , and neglect the cubic term, and ignore nuclear effects, by putting  $\mu^* = \mu$ . Since the effective spin-orbit interaction is also of the dipole operator form,

we easily get

$$|\mathbf{d}_j|_{\text{SOI}}^2 = |\mathbf{r}_{0j}|^4 |\mathbf{n}_{\text{so}}^{(j)} \times \mu_F \mathbf{B}|^2 \frac{4E_{0j}^2}{(E_{0j}^2 - \epsilon_z^2)^2}. \quad (4.54)$$

Using here the results for the Fock-Darwin eigenfunctions,  $\mathbf{r}_{01} = (l_1/\sqrt{2})\mathbf{n}_1$ , and  $\mathbf{r}_{02} = (l_2/\sqrt{2})\mathbf{n}_2$ , and Eq. (4.52) gives Eq. (4.39a).

The calculation for the hyperfine interaction proceeds analogously, and we get

$$|\mathbf{d}_j|_{\text{HF}}^2 = (Av_0)^2 \sum_{mn} \left( \frac{\mathbf{r}_{0j} \delta_{j0}^n}{E_{0j} + E_{\sigma\bar{\sigma}}} + \frac{\mathbf{r}_{j0} \delta_{0j}^n}{E_{0j} - E_{\sigma\bar{\sigma}}} \right) \cdot \left( \frac{\mathbf{r}_{j0} \delta_{0j}^m}{E_{0j} + E_{\sigma\bar{\sigma}}} + \frac{\mathbf{r}_{0j} \delta_{j0}^m}{E_{0j} - E_{\sigma\bar{\sigma}}} \right) \langle \bar{\sigma}\mu | \mathbf{I}_n \cdot \boldsymbol{\sigma} | \sigma\mu^* \rangle \langle \sigma\mu^* | \mathbf{I}_m \cdot \boldsymbol{\sigma} | \bar{\sigma}\mu \rangle, \quad (4.55)$$

where we denoted  $\delta_{ij}^n = [\delta(\mathbf{R} - \mathbf{R}_n)]_{ij}$ . The expression in Eq. (4.55) depends on the initial and final state of the nuclear subsystem. The experimentally relevant situation is that these two states are not restricted in any way, which corresponds to a rate being summed over all possible final states and averaged, with the proper statistical weights, over the possible initial states,

$$\overline{|\mathbf{d}|^2} = \sum_{\mu\nu} p(\mu) |\mathbf{d}(\mu, \nu)|^2. \quad (4.56)$$

A straightforward calculation for an unpolarized nuclear ensemble,  $p(\mu) = \text{const}$ , gives

$$\overline{\langle \sigma\mu | \mathbf{I}_m \cdot \boldsymbol{\sigma} | \bar{\sigma}\nu \rangle \langle \bar{\sigma}\nu | \mathbf{I}_n \cdot \boldsymbol{\sigma} | \sigma\mu \rangle} = \frac{2}{3} I(I+1) \delta_{nm}, \quad (4.57)$$

with  $\delta$  the Kronecker delta. Using this in Eq. (4.55) we get

$$\overline{|\mathbf{d}_j|_{\text{HF}}^2} = A^2 \frac{2}{3} I(I+1) |\mathbf{r}_{0j}|^2 \frac{4E_{0j}^2}{(E_{0j}^2 - \epsilon_z^2)^2} v_0^2 \sum_m |\Phi_0(\mathbf{R}_m)|^2 |\Phi_j(\mathbf{R}_m)|^2. \quad (4.58)$$

As the linear density of the nuclear spins,  $2/a_0$ , is very high compared to the lengthscales of the electronic wavefunctions,  $l_1, l_2, l_z$ , the sum over nuclei can be well approximated by an integral,  $v_0 \sum_m \rightarrow \int d\mathbf{R}$ . Defining inverse volumes as the following wavefunction overlaps

$$V_{0j}^{-1} = \int d\mathbf{R} |\Phi_0(\mathbf{R})|^2 |\Phi_j(\mathbf{R})|^2, \quad (4.59)$$

the harmonic model gives  $V_{00} = 2\pi l_1 l_2 l_h$ , and  $V_{01} = V_{02} = 4\pi l_1 l_2 l_h$ . Putting  $N = V_{00}/v_0$  as the number of the nuclei "within" the quantum dot volume, leads to Eq. (4.39b) by using Eq. (4.58) in Eq. (4.52).

#### 4.7.9 Numerical implementation

The spin relaxation rates are obtained inserting the numerically exact eigenstates into Eq. (4.30) and performing the integration over the phonon momenta numerically, by standard methods [143]. Whenever the Hamiltonian includes the hyperfine interaction, the given relaxation rate is a geometric average of rates for 1000 configurations of static nuclear spins with random orientations (the approximation of unpolarized nuclei at infinite temperature). Specifically, the rate obtained at run  $i$  is written as  $\Gamma_i = \exp(\gamma_i)$ , and the average rate is defined as  $\Gamma_{\text{mean}} \equiv \exp(\bar{\gamma})$ , while the "error bar" given on such a value is defined by the maximal and minimal rates being  $\Gamma_{\text{max/min}} = \exp(\bar{\gamma} \pm \delta\gamma)$ , with  $\delta\gamma^2$  the dispersion of the exponents  $\gamma_i$ . This definition is chosen for convenience of resulting in a symmetric "error" interval on a logarithmic plot, so that the minimal rate stays non-zero, irrespective of the degree of the fluctuations among the individual rates. It should be taken only as a way to compare the degree of fluctuations among two values from numerics, rather than an assessment of fluctuations possibly observed in the experiment, since the latter depend in a non-trivial way on the relation between the measurement total time and the nuclear ensemble ergodic time [154].

#### 4.7.10 Parameters and fitting of the spin-orbit constants

In the evaluation of the rates according to the above described model, we use the parameters of GaAs,  $\rho = 5300 \text{ kg m}^{-3}$ ,  $c_l = 4784 \text{ m s}^{-1}$ ,  $c_t = 3350 \text{ m s}^{-1}$ ,  $\sigma_e = 7 \text{ eV}$ ,  $h_{14} = 1.4 \times 10^9 \text{ V m}^{-1}$ ,  $m = 0.067 m_e$ ,  $\gamma_c = 11 \text{ eV \AA}^3$ ,  $I = 3/2$ ,  $A = 45 \mu\text{eV nm}$ ,  $a_0 = 5.65 \text{ \AA}$ . We also estimate the electron temperature  $T = 60 \text{ mK}$ , though the corresponding thermal factor in Eq. (4.31) is negligible even for highest magnetic fields, so that the temperature plays little role for the value of the spin relaxation (it can be set to zero in Eq. (4.30) leading to no visible

changes). In addition to these parameters, we extract the excitation energies  $E_x = 2.3$  meV and  $E_y = 2.6$  meV, corresponding to  $l_x \approx 22$  nm, and  $l_y \approx 21$  nm, and the g-factor  $g = -0.36$ , from the spectral data such as those shown on Fig. 4.1c,d of the main text, and their spin-resolved analogues. As noted in the above and in the main text, to match the experimental relaxation rates quantitatively, one needs further details on the dot shape. As explained in detail in Ref. [95], we fit  $l_z = 6.5$  nm, and  $\delta = 5.6 \pm 1^\circ$ , which gives  $l_h/l_z = 2.4$ ,  $\lambda_z/l_z = 1.009$  upon assuming a triangular confinement potential along the heterostructure growth direction. With all these values fixed, we fit the linear spin-orbit lengths by minimizing the following chi-square sum

$$\chi^2 = \sum_i \left( \ln \Gamma_{\text{theory}}^{(i)} - \ln \Gamma_{\text{exp}}^{(i)} \right)^2 w_i, \quad (4.60)$$

with respect to the fitting parameters  $l_{\text{so}}$  and  $\vartheta$ . In the sum the index  $i$  runs through the whole measured dataset of the relaxation rates  $\Gamma = 1/T_1$  and we take the logarithm of the rate as it spans a range of many orders of magnitude. The weights are chosen as  $w_i = \ln(1.05 + \delta\Gamma_{\text{exp}}^{(i)}/\Gamma_{\text{exp}}^{(i)})$ , with  $\delta\Gamma$  the error estimated when fitting the value of  $\Gamma$ , as explained in Fig. 4.9, and 1.05 is an arbitrarily chosen factor. However, we find that the extracted values of  $l_{\text{so}}$  and  $\vartheta$  are rather robust to many other choices (including ignoring the errors altogether). We find that the minimization converges into the following two local minima

$$l_{\text{so}} = 2.1(1) \mu\text{m}, \vartheta = 31(1)^\circ, \quad (4.61a)$$

$$l_{\text{so}} = 2.1(1) \mu\text{m}, \vartheta = 61(1)^\circ. \quad (4.61b)$$

where the values in the brackets give the typical error on the last given digit. These errors are estimated from the spread of the converged values upon running the minimization algorithm many times. The reason that we are not able to quantify these errors more precisely, is due to several uncertainties pertaining to the experimental as well as numerical inputs to the chi square sum. For example, the numerical value  $\Gamma_{\text{theory}}^{(i)}$  is a random variable, due to the randomness in the nuclear configuration. For the minimization, which is very computationally demanding, we are able to perform an average over typically only tens of random nuclear



configurations for each  $i$ , which makes these statistical fluctuations quite large. For the same reasons, we are not able to quantify the likelihood ratio for the two local minima given in Eq. (4.61). However, using again multiple runs, we conclude that the difference between the two possibilities is, within our model, statistically significant, and the value  $\vartheta = 31^\circ$  fits the measured data better. Figure 4.13 illustrates the amount of data used to calculate  $\chi^2$  in the described minimization procedure.

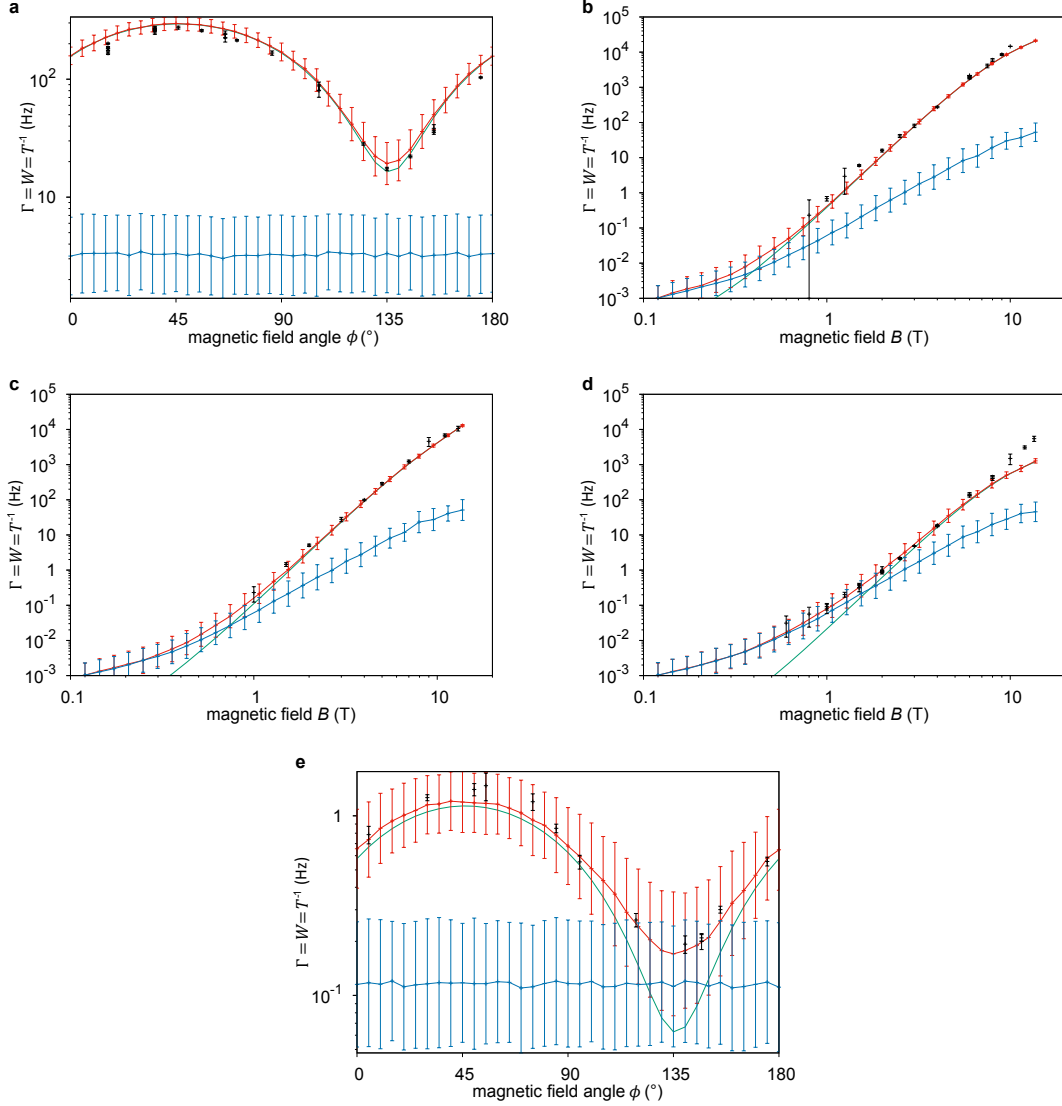


Figure 4.13: **The total set of  $T_1$  data used to fit the spin-orbit parameters.** In all panels, we show the measured spin relaxation rates (black points with error bars) versus the theoretical values (lines) for the full model (red), the model excluding the hyperfine interactions (green) and the model excluding the spin-orbit effects (blue). The plotted values were obtained for  $\vartheta = 31.3^\circ$  and  $l_{\text{so}} = 2.08 \mu\text{m}$  and illustrate a single step in the minimization routine. Typically less than hundred steps are needed for convergence. In panel **a–e**, the following parameters are fixed: **a**  $B = 4$  T, **b**  $\phi = 45^\circ$ , **c**  $\phi = 356^\circ$ , **d**  $\phi = 315^\circ$ , **e**  $B = 1.25$  T. Error bars in the calculated data is from geometric average of rates for 1000 configurations of static nuclear spins with random orientations (see Sec. 4.7.9). Error bars on experimental data are fitting errors.

# 5 g-factor corrections in a GaAs single-electron quantum dot

Leon C. Camenzind, Liuqi Yu, Daniel Loss, Dominik M. Zumbühl,

*Department of Physics, University of Basel, Switzerland*

Jeremy D. Zimmerman, Arthur C. Gossard

*Materials Department, University of California, Santa Barbara, USA*

Peter Stano

*Center for Emergent Matter Science, RIKEN, Saitama, Japan*

*Department of Applied Physics, School of Engineering, University of Tokyo, Japan Institute of Physics, Slovak Academy of Sciences, Bratislava, Slovakia*

## Abstract

We identify isotropic and anisotropic g-factor corrections in a lateral GaAs single-electron quantum dot. We extract the Zeeman splitting by measuring the tunnel rates into the individual spin states of an empty quantum dot for an in-plane magnetic field with various strengths and directions. By using a phenomenological model, we quantify the Zeeman energy and find a linear dependence on the magnetic field strength which allows us to extract the g-factor. Using a recent theoretical model, the magnitude of the directional dependent g-factor is understood in terms of spin-orbit interaction induced isotropic and anisotropic corrections to the GaAs bulk g-factor. Because this implies a dependence of the spin splitting on the magnetic field direction, these findings are of significance for spin qubits in GaAs quantum dots.

This chapter is in preparation for publication.

## 5.1 Introduction

Spins in semiconductor quantum dots are among the most promising candidates for the realization of a scalable quantum bit (qubit) [1, 2]. For such spin qubits, the qubit energy is the Zeeman energy  $\Delta = g\mu_B B$ , where  $\mu_B$  is the Bohr magneton and  $B$  is the magnetic field and  $g$  is the *g*-factor. It is generally a major challenge to keep the quantum state of a qubit coherent for the duration of a qubit operation. For spin qubits, decoherence is a consequence of fluctuations of  $\Delta$ . In GaAs, fluctuations in  $B$  dominate this decoherence. These fluctuations are due to hyperfine coupling between the electron spin and the nuclear spin bath of the host material [34, 37, 155, 156]. With procedures to actively decouple the electron spin from the nuclear spin bath, the the coherence time can be increased from tens ns [33, 34] to almost 1 ms [38]. Another source of decoherence are fluctuations in  $g$ . Such fluctuations originate from charge noise, because  $g$  is sensitive to the electric field which gives rise to an inhomogenous *g*-factor [40, 74, 75]. In group-IV semiconductors with little or no nuclear spins, like silicon [75] or Si/SiGe heterostructures [157], this type of decoherence dominates. To understand these decoherence processes, it is essential to understand the *g*-factor corrections of a spin qubit.

In semiconductors, these *g*-factor corrections arise from the spin-orbit interaction (SOI) [4, 67] and spatial variations of  $g$  might occur due to local electric fields which modulate this interaction [4, 74, 75]. Recently, measurements in a SiMOS spin qubit [75] showed that these corrections are small for electrons in silicon due to comparably weak SOI. For holes, experiments in silicon MOSFETs [158, 159], in a GaAs heterostructure [160] and in a silicon-germanium core-shell nanowire [161] show that these corrections are more pronounced due to stronger SOI [2].

Here, we achieve to separate the *g*-factor corrections in a GaAs single-electron spin qubit device. A recent theoretical model by *Stano et al.* predicts that the Rashba SOI together with a bulk structure SOI term which is generated at finite magnetic field, lead to an isotropic correction of  $g$  from the GaAs bulk value, while the Dresselhaus SOI is anticipated to give rise to an anisotropic correction [4]. We extract the isotropic and anisotropic *g*-factor corrections

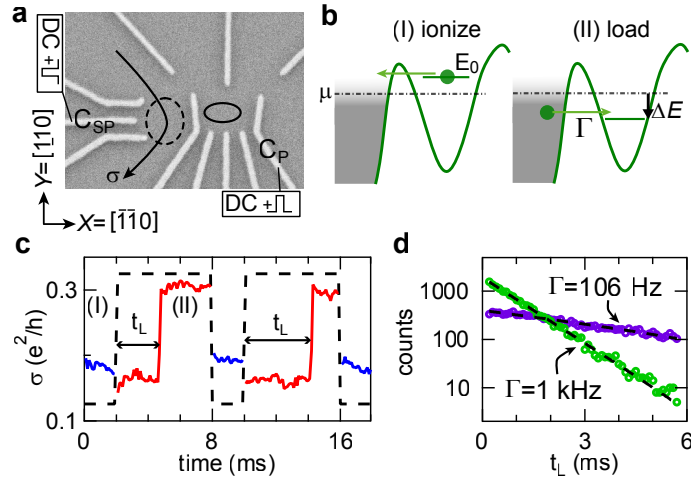


Figure 5.1: (a) Scanning electron micrograph picture of the device with indications of the position of the quantum dot (black ellipse) and adjacent sensor quantum dot (dashed ellipse). Monitoring the conductance  $\sigma$  through the sensor allows real-time detection of the quantum dot charge state. To measure the tunnel coupling into the empty quantum dot, pulses are applied to the most right wall gate. To keep the sensor sensitive, a weaker compensation pulse is applied to the sensor plunger gate. (b) Two-step pulse scheme to measure tunnel-in rate  $\Gamma$  for detuning  $\Delta E$  from  $\mu$ . The confinement landscape with the barrier potential is a modulation of the conduction band due to voltages applied on the gate electrodes shown in (a).  $E_0$  depicts the ground state energy of the quantum dot. (c) Time trace of sensor conductance  $\sigma$  for two pulses cycles (dashed curve). Low conductance indicates an empty dot. The ionization rate during (I) is faster than the bandwidth of the charge sensor. In the load stage (II), the times for electrons to tunnel into the empty dot  $t_L$  were recorded. These tunnel events are detected by jumps of the charge sensor upon charging of the dot. (d) Fitting histogram of  $t_L$  by an exponential gives the tunnel rate  $\Gamma$ . For the examples shown,  $\Gamma = 106$  Hz (purple) and  $\Gamma = 1000$  Hz (green).

experimentally, and find a reasonable agreement with the theory. This agreement is evidence for the profound theoretical understanding of the different corrections, as a key characteristic of a spin qubit realized in a GaAs few-electron quantum dot.

## 5.2 Sample and measurement scheme

This experiment was performed in a single-electron quantum-dot which was energized in a GaAs/AlGaAs heterostructure forming a two dimensional electron gas (2DEG) by applying voltages to surface gate electrodes. A scanning electron micrograph picture of a co-fabricated device is shown in Fig. 5.1a and illustrates the layout of the surface gate electrodes. By

applying negative voltages to these electrodes, the 2DEG is locally depleted which results in a single electron quantum dot in the middle and a larger, few-electron sensor quantum dot on the left side of the device (solid and dashed ellipse in Fig. 5.1a, respectively). Here, the quantum dot is tunnel coupled only to the left reservoir. Measuring the conductance through the sensor quantum dot, allows for non-invasive real-time monitoring of the charge state of the capacitively coupled single electron quantum dot with a bandwidth of  $\sim 30$  kHz [28, 96]. The device is mounted on a piezo rotator stage (Attocube ANRv51) such that a magnetic field of up to 14 T can be applied in an arbitrary direction in the plane of the 2DEG. By performing van der Pauw measurements, the out of plane angle has been determined to be less than  $2^\circ$ .

To calculate the Zeeman energy  $\Delta$ , it is necessary to convert changes of the voltage applied to the plunger gate  $C_p$  to changes in energy of the quantum dot ground state level  $E_0$  (see Fig. 5.1b). We therefore calibrate the lever arm by probing the Fermi-Dirac distribution of the reservoir at an increased base temperature ( $\sim 550$  mK) where we assume that the electronic temperature is equivalent to the temperature of the mixing chamber [98]. We checked that the lever arm shows no significant dependence on the strength or direction of the external magnetic field.

Because the *g*-factor corrections depend on the shape of the quantum dot, we performed a recently developed spectroscopy of the quantum dot orbitals with in-plane magnetic fields and found orbital energies at  $E_x = 1.9$  meV,  $E_y = 2.6$  meV and  $E_z = 28$  meV (see Chap. 3). This suggests an ellipsoidal quantum dot which is elongated along the x-axis of the device such as depicted in Fig. 5.1a.

We obtain *g* by measuring the tunnel rates into the spin states of an empty quantum dot. From these rates we extract the Zeeman splitting  $\Delta$  and from the dependence of  $\Delta$  on the magnetic field strength we fit *g*. We measure the tunnel rates by applying a rectangular two-step pulse to the plunger gate  $C_p$  (see Fig. 5.1a) to repeatedly ionize and load the quantum dot as shown by the energy diagrams in Fig 5.1b: to ionize the dot, the ground state  $E_0$  is pulsed above  $\mu$ , the chemical potential of the reservoir. Because there are empty states available at this energy, an electron in the dot will tunnel into the reservoir and thermalize.

We tune this ionization pulse such that the ionization efficiency is close to unity. To load the empty dot, we pulse  $E_0$  to an energy  $\Delta E$  below  $\mu$ . As there are filled states in the reservoir at this energy, an electron can elastically tunnel through the potential barrier and load the quantum dot. The timing of this loading process is given by tunnel rate  $\Gamma$ .

The tunnel rate  $\Gamma$  is obtained by extracting the times of the loading events  $t_L$  by monitoring the conductance  $\sigma$  of the charge sensor as shown in Fig 5.1c. Here, the tunneling of an electron leads to a change of the charge state from empty to loaded which results in a conductance increase. We cycle through this pulse scheme between 2k and 20k times and extract the tunnel rate  $\Gamma$  by fitting an exponential function to histograms of  $t_L$  (see Fig 5.1d). When changing the pulse amplitudes, we obtain  $\Gamma$  as a function of detuning  $\Delta E$ .

In regard to the measurement scheme, we want to point out two experimental particularities. First, to stay in the sweet spot of the sensor during the pulse sequence, we have to compensate the crosstalk between the pulses applied to  $C_p$  and the sensor quantum dot by applying pulses of opposite polarity to the sensor plunger gate  $C_{SP}$  (see Fig 5.1a). Second, we divide the total number of pulse cycles in rounds to mitigate drift-related effects: In every round, 100 pulses are applied at each selected detuning  $\Delta E$  before an automated feed-back loop is used to compensate for time-dependent drifts of  $E_0$  by retrieving the position of  $\Delta E = 0$  [149]. We exclude hysteresis effects by selecting the sequence of detunings  $\Delta E$  to which we pulse randomly for each round.

In Fig. 5.2a we show data of  $\Gamma(\Delta E)$  for different magnetic field-strengths. Because the tunnel barrier is slightly readjusted for each magnetic field, the magnitudes of  $\Gamma(\Delta E)$  of the different traces are not comparable. Therefore, these traces were normalized to their respective maximal value of the tunnel rate. From their magnetic field behavior, the two steps in the traces of  $\Gamma(\Delta E)$  (orange arrows in Fig. 5.2a) are identified as the two spin states, separated by the Zeeman splitting  $\Delta$ .

### 5.3 Tunnel rate into the spin states

Next, we propose a qualitative model for  $\Gamma(\Delta E)$  to find the Zeeman energy  $\Delta$  by fitting to pulse spectroscopy data such as the traces presented in Fig. 5.2a. We show the energy diagrams of three characteristic detunings  $\Delta E$  in Fig. 5.2b. The spin degeneracy of the ground state is lifted in an external magnetic field such that the ground ( $|\uparrow\rangle$ ) and the excited spin state ( $|\downarrow\rangle$ ) become energetically separated by the Zeeman energy  $\Delta$ .

When occupied states in the reservoir are aligned with empty levels of the quantum dot, an electron can elastically tunnel into the empty quantum dot [104]. In this situation, which is also depicted in Fig. 5.2b, the tunnel rate  $\Gamma$  is defined by a combination of three factors: the density of electrons capable of tunneling into the quantum dot, the number of quantum dot levels in which these electrons could tunnel and the details of the tunnel barrier. At zero temperature and when ignoring any energy dependence of the the tunnel barrier,  $\Gamma(\Delta E)$  rises to the ground state tunnel rate  $\Gamma_g$  when the  $E_0$  is aligned with  $\mu$  at  $\Delta E = 0$ . Upon increasing  $\Delta E$  further,  $\Gamma(\Delta E) = \Gamma_g$  until tunneling into the spin excited state becomes energetically allowed at  $\Delta E = \Delta$  such that  $\Gamma(\Delta E) = \Gamma_g + \Gamma_e$  where  $\Gamma_e$  is the tunnel rate into the spin excited state.

At a finite temperature, the states in the reservoir are occupied according to the Fermi-Dirac distribution  $f(E, k_B T) = 1 / (\exp(\Delta E / (k_B T)) + 1)$  where  $k_B$  is the Boltzmann constant and  $T$  is the temperature. This thermal occupation factor,  $f(E, k_B T)$ , is identified in the data of Fig. 5.2a close to zero detuning  $\Delta E = 0$  and at the Zeeman splitting  $\Delta E = \Delta$ , as a broadening of the resonance condition of  $\mu$  being aligned with  $|\uparrow\rangle$  and  $|\downarrow\rangle$ , respectively.

Further, the tunnel barrier potential leads to a suppression of  $\Gamma$  with increasing  $\Delta E$  because the electrons have to tunnel through a larger potential [35, 104, 105, 162]. This effect is prominent in the traces shown in Fig. 5.2a and is schematically illustrated in Fig. 5.2b as an increase of the green (blue) area of the potential for electrons tunneling into the spin ground (excited) state with increasing  $\Delta E$ . This energy dependence is reflected in the WKB expression for the tunnel rate of a particle with energy  $E$  through a rectangular potential barrier of height  $V_0$  and length  $l$  such that  $\Gamma \sim \tilde{\Gamma}_0 e^{-\sqrt{\tilde{\beta}(V_0 - E)}}$  where  $\tilde{\beta} = 8ml^2/\hbar^2$  and  $\tilde{\Gamma}_0$



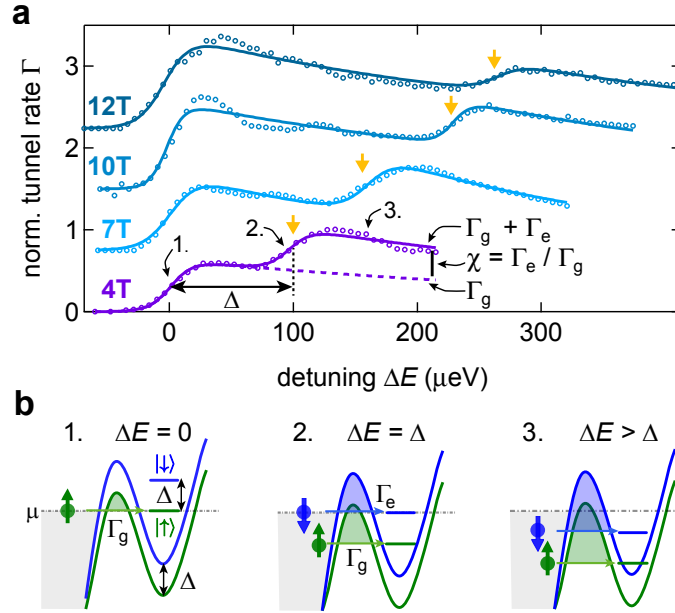


Figure 5.2: (a) Examples of the normalized tunnel rate  $\Gamma$  into the empty quantum dot for different detunings  $\Delta E$  and magnetic field strengths. Each trace exhibits two resonances, identified as the two spin states due to their behavior in magnetic field (black arrows). Fits are according to the model described by Eq. (5.1). In the trace taken at 4 T, the dashed line shows  $\Gamma_g(\Delta E)$ , the contribution of the spin ground state to the total tunnel rate. Further,  $\Delta$  indicates the Zeeman splitting and  $\xi$  the ratio of the tunnel rate into the spin ground and spin excited state. (b) Schematic of three distinct regime for different detunings from  $\mu$ . The corresponding detuning for each diagram is also marked in the 4T trace in (a): 1. the energy of the spin ground state  $|\uparrow\rangle$  is aligned with  $\mu$  and elastic tunneling of electrons with spin-up occurs. 2.  $|\downarrow\rangle$ -state is aligned with  $\mu$ . Now both spin species can tunnel. As the area of the potential barrier has increased (shaded region), the tunnel rate into  $|\uparrow\rangle$  has decreased. 3. Both states are below  $\mu$  and the tunnel rate into the dot is  $\Gamma = \Gamma_g + \Gamma_e$ , the sum of the tunnel rate into the spin ground state,  $\Gamma_g$ , and the spin excited state,  $\Gamma_e$ .

is a scaling parameter. For small energies  $\Delta E \ll V_0$ , this expression can be linearized such that  $\Gamma(\Delta E) \sim \Gamma_0 e^{-\beta \Delta E}$  where  $\Gamma_0$  and  $\beta$  depend on the details of the tunnel barrier potential [104].

For small detunings  $\Delta E$ , the tunnel rate then is

$$\begin{aligned} \Gamma(\Delta E) &= \Gamma_g(\Delta E) + \Gamma_e(\Delta E) \\ &= \Gamma_0 e^{-\beta \Delta E} [f(\Delta E, k_B T) + \chi f(\Delta E + \Delta, k_B T)], \end{aligned} \quad (5.1)$$

where  $\chi$  is an empirically introduced ratio between  $\Gamma_e$  and  $\Gamma_g$  [35]. From symmetry arguments it is expected that  $\Gamma_e = \Gamma_g$ : in a magnetic field, the ground state of the quantum dot and the conduction band both split by the Zeeman energy  $\Delta$ . As a consequence, the tunnel barrier for electrons of both spin species should be equal ( $\chi = 1$ ). This situation is depicted in the third schematic of Fig 5.2b. While not discussed in this article, in the experiment we often find spin dependent tunnel rates such that  $\chi < 1$  [149, 151]. The cause of this asymmetry is not understood conclusively yet [105].

## 5.4 g-factor corrections

Next, we look at the magnetic field dependence of the extracted  $\Delta$  to investigate the behavior of the g-factor. We take such data for magnetic fields applied along three distinct directions of the device:  $X, Y$  and  $XY$ , the angle in between (see Fig.5.1). The measured Zeeman splittings  $\Delta$  are plotted in Fig. 5.3 as a function of  $\mu_B B$ . We find that the data for all three directions shows a linear dependence which indicates a magnetic field-independent g-factor. Accordingly, we use a linear fit on these data sets to obtain  $g$ . The uncertainty obtained from the fits are on the range of a percent. Note that we can only extract the absolute values of the g-factor  $|g|$  with this method.

We find that  $g$  depends on the magnetic-field direction. With  $|g| \approx 0.41$ , the g-factor is maximal for a field along  $X$  and minimal along  $Y$  where  $|g| \approx 0.34$ . This is qualitatively in good agreement with the theory in Ref. [4]. In that model, the g-factor corrections to the bulk value are separated into an isotropic and an anisotropic part, such that

$$g \approx g_{bulk} + \delta g_i + \delta g_a \cos(2\phi + \pi/2), \quad (5.2)$$

where  $g_{bulk} = -0.44$  is GaAs bulk g-factor and  $\phi$  defines the in-plane angle with respect to the main crystal axis [100] (see inset in Fig. 5.3). We extract  $\delta g_i$  and  $\delta g_a$  experimentally and the quantification of these two parameters for our quantum dot is the main result of this article.

The magnitude of several g-factor corrections depend on  $\lambda_z$ , the effective width of the electron

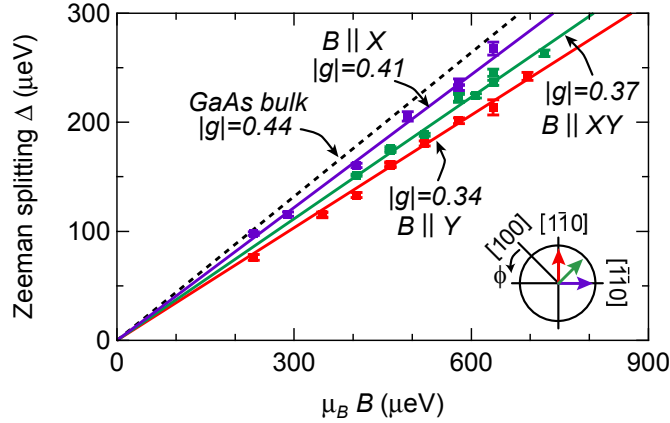


Figure 5.3: Zeeman splitting  $\Delta$  measured for different magnetic field strengths  $B$  and directions indicated by the labels. The slope is the absolute value of the  $g$ -factor  $|g| = \Delta/(\mu_B|B|)$  and differs from the GaAs bulk  $g$ -factor due to spin-orbit interaction induced corrections. A distinct  $g$ -factor anisotropy is observed in the data. The inset shows the direction of the applied magnetic fields with respect to the crystal axes.

wave function along the growth direction [4]. Here,  $\lambda_z$  is given by the triangular confinement potential formed by the GaAs/AlGaAs heterostructure. We fit it from excited orbital state data and find  $\lambda_z \approx 6.5$  nm (see Chap. 3 and Ref. [95]).

There are several directional-independent terms which contribute to the isotropic correction  $\delta g_i$  which originate either from the band structure or the heterostructure confinement. Fig. 5.4a shows the largest terms as estimated from the results of Ref. [4] for this specific quantum dot confinement and for a magnetic field along  $Y$ . In this Figure, the field direction only matters for the anisotropic Dresselhaus correction  $g_D$  which is discussed later. From these calculations, we conclude that the isotropic correction is dominated by  $g_R$ , a correction due to intrinsic Rashba SOI, and by  $g_{43}$ , a correction due to the generic SOI term  $H_{43}$  [4, 163]. The well known Rashba SOI term originates from the structural inversion asymmetry in the GaAs/AlGaAs heterostructure, while  $H_{43}$  is a bulk band structure term generated by a magnetic field. The next strongest isotropic correction is the penetration correction term  $g_p$  which arises from the overlap of the wave function with the AlGaAs bulk where  $g = +0.4$ . This term is negligible in our case but becomes substantial for smaller 2DEG widths ( $\lambda_z \lesssim 4$  nm). The model predicts  $\delta g_i \approx 0.1$  which leads to an average  $\bar{g} = g_{bulk} + \delta g_i \approx -0.34$  for an electron confined in such a quantum dot. The data presented

in Fig. 5.3 suggests an isotropic correction to  $|\bar{g}| \approx 0.37$  and therefore  $g_i \approx 0.07$ .

The anisotropic correction to the *g*-factor originates from the Dresselhaus SOI which is a consequence of bulk inversion asymmetry in the zinc blende crystal structure of GaAs. As shown in Fig. 5.4b, the largest correction to the bulk *g*-factor is observed along *Y*. This is a strong indication that the Dresselhaus constant  $\gamma_c$  is negative [4, 56, 164]. Our data suggests that  $\delta g_a \approx 0.035$  which is close to the predicted  $\delta g_a \approx 0.024$ . Further, for the relative correction to the *g*-factor, we find  $\delta g_a/|\bar{g}| \approx 10\%$  which is in good agreement with the model where this ratio is  $\approx 7\%$ .

We find a discrepancy of the *g*-factor corrections between the data and the prediction. One possible source for this is the lever arm: due to ambiguity of the electronic temperature during the calibration, this could lead to an uncertainty of the *g*-factor by at most 10%. Because we found a field independent lever arm, the scaling of the *g*-factors along all three directions would be equally. E.g. a smaller lever arm would result in a reduced  $|\bar{g}|$ , hence a larger  $g_i$  but a smaller  $g_a$ . Therefore, an uncertainty in the lever arm is not able explain the discrepancy in  $g_i$  and  $g_a$  at the same time. Another source of this deviation could be inaccuracies in the constants used for the k.p calculations in the model. From the data available, however, it is not possible to conclude which term leads to the overestimation of  $\delta g_i$  when compared to the experiment. Also strain effects could be a source of the discrepancy: in the theory, strain induced-SOI is not taken into account but will lead to additional *g*-factor corrections. Simplifications in the model of the heterointerface can also lead to a deviation from the observed *g*-factor: the model assumes a infinite linear slope of the triangular confinement potential and a step-like increase of the aluminum concentration at the AlGaAs/GaAs interface. In reality, the profile is different in both aspects: the linear slope levels off away from interface and there is a finite transition region from AlGaAs to GaAs. Again, this results in an adjustment of the corrections terms.

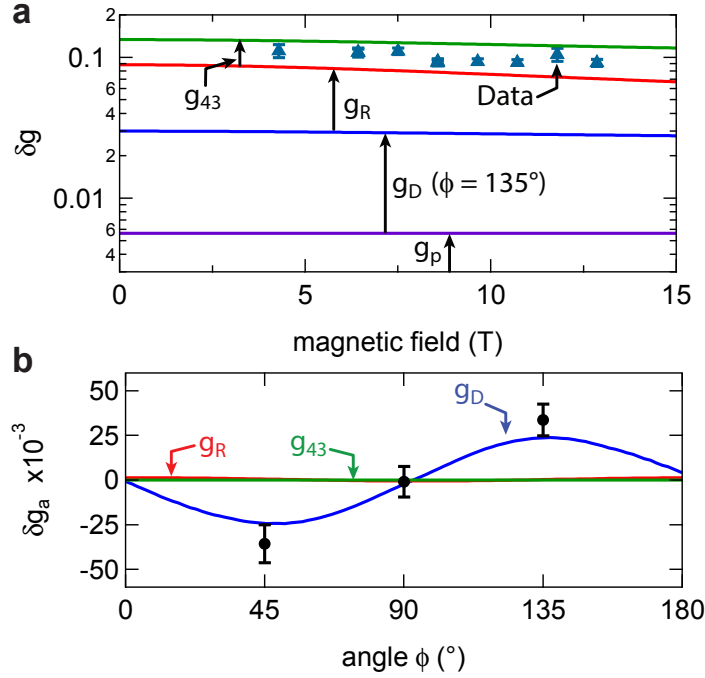


Figure 5.4: (a) Cumulative  $g$ -factor corrections to the GaAs bulk value. While  $g_p$ ,  $g_{43}$  and  $g_R$  are isotropic,  $g_D$  is anisotropic and shown for a field along  $Y$ , the same direction for which the data is shown (triangles). The green curve shows the total  $g$ -factor correction which is expected for this field direction. In agreement with the model, the experiment barely shows any dependence on the magnetic field strength. (b) The anisotropic correction to the  $g$ -factor is dominated by the Dresselhaus contribution  $g_D$ . The anisotropic contribution of the Rashba and  $H_{43}$  term,  $g_R$  and  $g_{43}$ , respectively, are insignificant.

## 5.5 Discussion

In summary, we find  $g$ -factors ranging from  $|g| \approx 0.34$  to  $0.41$  for a magnetic field applied along three main crystal axes in a lateral, gate defined quantum dot formed in a GaAs/AlGaAs heterostructure. Our results are in good agreement with recently proposed theory by *Stano et al.* [4] in which the  $g$ -factor corrections to the GaAs bulk value can be divided into a leading isotropic and a weaker anisotropic part. Here, the isotropic corrections arise from Rashba and  $H_{43}$ -type of spin-orbit interaction and the anisotropic correction originates in the Dresselhaus effect. Recently, in a silicon metal-oxide-semiconductor spin qubit, a  $g$ -factor anisotropy of only a few percent was reported. There, the corrections were found to originate from SOI terms which emerge due to surface roughness and lattice imperfections [75]. In contrast, here, the measured anisotropy is found to be substantial due to the sizable Dresselhaus SOI

present in GaAs.

Our findings substantiate the relevant  $g$ -factor corrections in GaAs spin qubits. This is a major step in probing band structure parameters using quantum dots. For example, extracting the  $k.p$  parameters from bulk measurements is often complicated by effects of the electron-electron interaction. Here, since the dot is singly occupied, such effects do not enter. This work demonstrates that a quantum dot can be used as well controlled probe in experiments aiming at the microscopic parameters of the semiconductor. Similar experiment could be performed for samples with different heterostructure confinement. From the dependence of the  $g$ -factor corrections on the width and symmetry of the heterostructure, the  $k.p$  parameters could be obtained with a new level of confidence [4].

And last, the identification of the dominant  $g$ -factor correction terms is also an important step towards the description of the processes which can give rise to an inhomogeneous  $g$ -factor. In presence of charge noise, such a spatially dependent  $g$ -factor leads to decoherence of the spin qubit but could, in principle, also be exploited for all-electrical spin manipulation.

## 5.6 Acknowledgments

We thank M. Steinacher and S. Martin for technical support. This work was supported by the Swiss Nanoscience Institute (SNI), NCCR QSIT, Swiss NSF, ERC starting grant (DMZ), and the European Microkelvin Platform (EMP). PS acknowledges support from CREST JST (JPMJCR1675), and JSPS Kakenhi Grant No. 16K05411.

## 6 Anisotropic Pauli spin blockade in a Ge/Si core-shell nanowire double quantum dot

Leon C. Camenzind, Florian N. M. Froning, Marko Rančić, Christoph Kloeffel,  
Daniel Loss, Dominik M. Zumbühl and Floris R. Braakman

*Department of Physics, University of Basel, Switzerland*

### Abstract

Spin qubits in semiconductors are among the leading candidates for the realization of a scalable quantum computer. Compared to electrons, spin qubits encoded in holes suffer less from hyper-fine interaction and allow all-electrical spin manipulation due to the presence of strong spin-orbit interaction. Here, we show lifting of the Pauli spin blockade in a Germanium-Silicon core-shell nanowire hole double quantum dot. In good agreement with nonspin-conserving interdot tunneling in the presence of strong spin-orbit coupling, we find a minimum of the leakage current at low magnetic fields. At higher fields, we then show an anisotropic behavior of the saturated leakage current due to an anisotropic spin relaxation rate. This observed anisotropy is explained by a strongly directional dependent g-factor in combination with the presence of a spin-orbit field.

## 6.1 Introduction

Recently, hole spin qubits have aroused attention because, in contrast to the s-type Bloch function for electrons, their p-type Bloch function prevents spin decoherence due to contact hyperfine interaction as the wave-function has no overlap with the nuclei. Additionally, spin-orbit interaction is strong for holes on an atomic level due to angular momentum  $L = 1$  which allows for fast all-electrical control of the spin qubit by means of electric dipole induced spin resonance (EDSR) [42, 43, 165, 166].

In semiconductors, the Rashba and Dresselhaus spin-orbit interaction (SOI), respectively, arise from structure inversion asymmetry (e.g., due to an applied electric field) and bulk inversion asymmetry (e.g., due to a zinc blende lattice) [67]. The standard terms for the Rashba and Dresselhaus SOI can be derived with multiband perturbation theory and are small for semiconductors with a large fundamental band gap [67]. Recently, a very strong and electric-field-induced SOI was predicted for holes confined in germanium or silicon nanowires (NWs) [5, 6]. Due to its similarities with the standard Rashba SOI, this mechanism was named direct Rashba SOI (DRSOI). However, in contrast to the standard Rashba SOI, the DRSOI is not suppressed by the fundamental band gap (see Sec. 2.2.2 in Chap. 2. DRSOI is one or two orders of magnitude stronger than conventional Rashba SOI such that spin-flip times of less than 100 ps are predicted when performing EDSR in presence of this strong type of SOI [50]. Because the presence of DRSOI is relying on an external electric field, it is highly tunable with gate electrodes [51, 53]. This tunability is very promising for numerous reasons: it allows to tune the qubit into a state of strong SOI for fast spin manipulation as well as into a state of weak SOI to mitigate decoherence e.g. for read-out or quantum information storage. It further allows for a tunable g-factor [54, 86, 161] which can be exploited by tuning the qubit in and out of resonance with a resonator by electrical control of the Zeeman energy. Here, we study Pauli spin blockade (PSB) in a Germanium-Silicon (Ge/Si) core-shell nanowire double quantum dot (DQD) – a system for which the emergence of DRSOI is predicted [5]. We find a lifting of the PSB with magnetic field and a saturation of the leakage current for large fields which is in good agreement with spin-orbit interaction mediated spin flips during



interdot tunneling. Upon rotations of the external magnetic field, we observe an anisotropy in the saturation of the leakage current that can be explained by a spin relaxation anisotropy induced by an anisotropic g-factor in combination with a spin-orbit field. We then speculate, that this observed spin-orbit field is of direct Rashba type and emerges due to coupling to the electric field of the confinement gates.

## 6.2 Device

A schematic of the device is presented in Fig. 6.1.  $p^{++}$  doped silicon with 290 nm of thermal oxide was used as a substrate of the device. Five lithographically defined Ti/Pd bottom gate electrodes serving as confinement gates and two large area pillars on the side were fabricated on top of the oxide. The bottom gates have a width of 20 nm and are equally spaced with a pitch of 50 nm. The pillars prevent bending of the NW. The gate electrodes and pillars are covered with a 20 nm thick  $\text{Al}_2\text{O}_3$  layer grown by atomic layer deposition (ALD). On top of the bottom gates, a Ge/Si core-shell NW with an estimated core radius of 10 nm and a shell thickness of 2.5 nm is transferred with a micro-manipulator such that the NW is mainly aligned with the  $\hat{x}$  direction. The exact angle of the NW with respect to  $\hat{x}$  is not known but assumed to be  $< 20^\circ$ . Electrical contact to the NW is established with two Ti/Pd pads which are lithographically defined and metallized after a HF dip to strip the native oxide of the NW. In a last step, two Ti/Pd side gates with a separation of  $2\ \mu\text{m}$  are lithographically defined parallel to the NW. These side gates allow to apply an electric field of up to  $2.5\ \text{V}/\mu\text{m}$  along the  $\hat{z}$  direction of the device, limited by the breakdown voltage of the  $\text{Al}_2\text{O}_3$  layer. Another source of electric fields are the confinement gates. We expect the field from the confinement gates to be predominantly oriented in the  $\hat{y}$  direction with a finite  $\hat{x}$  component. The device is bonded on a PCB (see Chap. 8) and cooled down to a base temperature of  $\sim 10\ \text{mK}$  in a dilution refrigerator. By applying positive voltages to the bottom gates, the hole density in the NW is locally controlled which allows to energize a double quantum dot. The corresponding charge stability diagram for a source-drain bias of  $V_{\text{SD}} = 2\ \text{mV}$  is presented in Fig. 6.1b. Here, transport through the double dot system occurs only inside the bias triangles when the electrochemical potentials of the two dots are

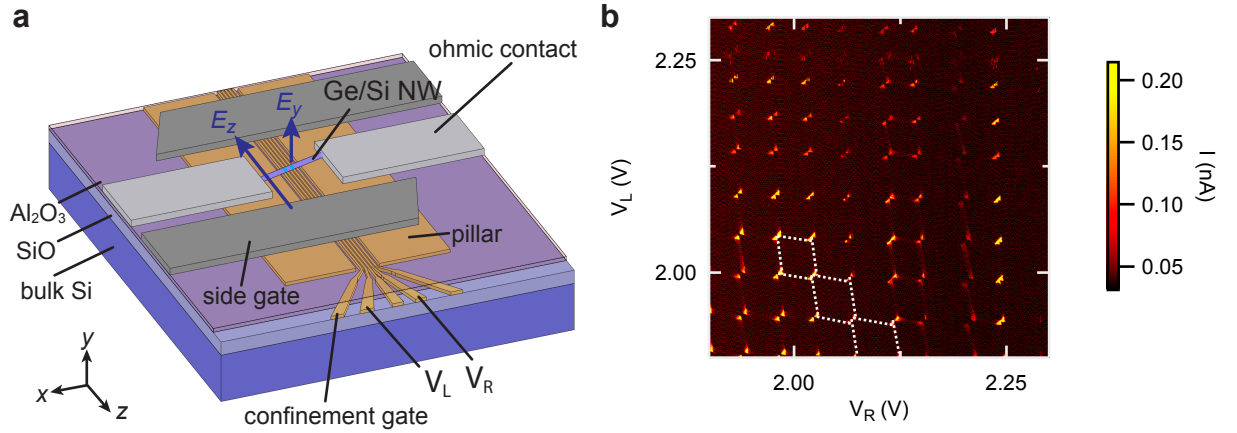


**Figure 6.1: Ge/Si NW double quantum dot device and charge stability diagram.** (a) A schematic of the device. The nanowire is aligned approximately along  $\hat{x}$ . Electric fields arise from the confinement gates ( $E_y$ ) and the side gate ( $E_z$ ). A 20 nm aluminum oxide film is grown on top of the confinement gates for electrical separation. (b) Charge stability diagram of the double quantum dot for a source-drain bias voltage of  $V_{SD} = +2$  mV. The voltage on the left ( $V_L$ ) and right ( $V_R$ ) plunger gates change the electrostatic potential inside the quantum dots. At zero-bias, a current flows only when the single particle energy levels of both dots are aligned with the chemical potential of the leads. Then, sequential tunneling occurs at triple points of a honey-comb shaped structure (white dashed lines). At finite bias, the triple points expand into bias triangles observed in the measurement.

both within the bias window. For some columns in the stability diagram, we find transport along the charging lines due to cotunneling effects with the lead reservoirs. This suggests a modulation of the coupling to the leads with voltage  $V_R$ .

### 6.3 Pauli spin blockade

Pauli spin blockade (PSB) is an important effect in spin based quantum information because it allows to study spin related effects using transport through a DQD. In the following, we therefore focus on a DQD interdot transition for which we find signatures of PSB. A zoom-in of the charge stability diagram at the triple points for such a transition is shown in Fig. 6.2. While transport through the DQD is unblocked for a positive bias  $V_{SD} = +4$  mV (Fig. 6.2a), it is prevalently blocked for a negative bias  $V_{SD} = -4$  mV (Fig. 6.2b) due to PSB. In Fig. 6.2c and d, the energy diagrams of the DQD for both bias directions is shown. These schematics show the electrochemical potential of the singlet (S) and triplet (T) states of the (2, 0) charge

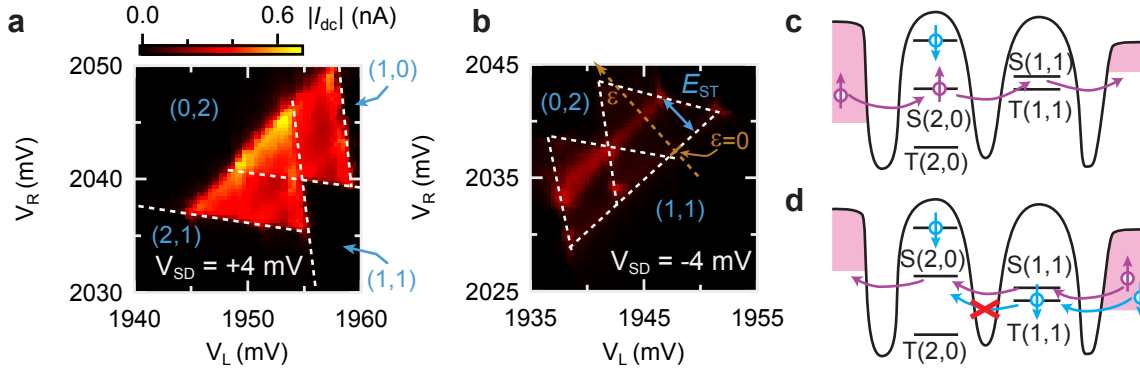


Figure 6.2: **Bias triangles and Pauli spin blockade.** For a positive bias  $V_{SD} = +4$  mV (a) transport is unblocked while Pauli spin blockade is observed for  $V_{SD} = -4$  mV (b). (a) and (b) are showing the absolute current  $|I_{DC}|$  on the same color scale revealing the high efficiency of the blockade. Along the detuning axis, indicated by the orange dashed arrow in (b), the detuning  $\epsilon$  of the charge states is defined.  $E_{ST}$  labels the singlet triplet splitting of the  $(2,0)$  charge state. (c),(b) Energy diagram for transport in the blocked (c) and unblocked (d) bias direction where the states in the right dot represent the  $(1,1)$  and the left dot represents the  $(2,0)$  charge states. When accessible, the triplet  $T(2,0)$  additionally contributes to the transport signal by opening another channel via  $T(1,1)$ . (c) A hole tunnels into the singlet  $S(2,0)$  and then to the accessible  $S(1,1)$  before leaving the right dot. (d) For the reversed bias, holes can still tunnel sequentially through the singlet states (purple). When the  $T(1,1)$  is occupied, the transport becomes blocked due to Pauli spin blockade when the  $T(2,0)$  is energetically not accessible.

state in the right dot and those of the  $(1,1)$  in the left dot<sup>9</sup>. In principle,  $n_L$  ( $n_R$ ) in the notation  $(n_L, n_R)$  stands for the number of holes in the left (right) dot. In the present system, it was not possible to deplete the quantum dot to the last hole. Here,  $(0,0)$  indicates that all the QD shells are filled and in  $(1,0)$  a hole with spin-down is additionally located on the left dot, occupying an unfilled shell (see Fig. 6.2c). We assign the  $(0,0)$  according to the charge states where we find the PSB (see Fig. 6.2a). The energy difference of the  $(2,0)$  singlet,  $S(2,0)$ , and triplet state,  $T(2,0)$ , is given by the single dot orbital energy minus the energy of the exchange interaction between electrons with parallel spins [58]: according to the Pauli principle, to fill the QD with two holes carrying the same spin, one of them has to occupy the next orbital. For the  $(1,1)$  charge state the situation is different. For a weakly coupled DQD at zero magnetic field, the  $(1,1)$  singlet and triplet states are only separated by the

<sup>9</sup>These schematics are not an accurate description in the sense that the  $(1,1)$  states are spatially expanded over both quantum dots.

Heisenberg exchange energy and are nearly degenerate for weak interdot tunneling [167].

For transport in positive bias direction as schematically depicted in Fig. 6.2c and shown in Fig. 6.2a, a spin-up hole contributes to the current by tunneling from the reservoir into  $S(2,0)$ , then it passes through the interdot barrier into  $S(1,1)$  before exiting the right dot by tunneling into the drain contact. The resulting  $(1,0)$  charge state is filled by a hole tunneling into the  $S(2,0)$ . Transitions from  $S(2,0)$  to  $T(1,1)$  are forbidden by conservation of spin. The picture changes for transport in the reversed bias direction. Transport via the singlet states is possible but as soon as a hole tunnels into the  $T(1,1)$  state, the transport is blocked due to PSB: the transition to  $T(2,0)$  is forbidden because of the Pauli exclusion principle which forces an asymmetric wave function for a triplet state such that one hole would need to occupy an energetically not accessible higher orbital level in the left quantum dot. Further, the transition to  $S(2,0)$  is not allowed because it would require a spin flip (see Fig. 6.2d). The system will remain in this blocked state until the PSB is lifted by e.g. spin relaxation [101, 168], spin-nonconservative interdot transitions [160] or spin-flip co-tunneling with the leads [161].

We define the detuning axis as indicated by the dashed arrow in Fig. 6.2b. Along this axis, the charge states,  $(1,1)$  and  $(2,0)$ , are detuned by  $\epsilon$ . At a detuning  $\epsilon \sim 4$  mV, indicated by  $E_{ST}$  in Fig. 6.2, the  $T(2,0)$  state becomes energetically accessible which opens an additional transport channel through the triplet states. Hence,  $E_{ST}$  is the singlet-triplet splitting of the left quantum dot. For  $\epsilon < E_{ST}$ , the transport is blocked due to PSB.

## 6.4 Pauli spin blockade in presence of spin-orbit interaction

For electrons in III-V semiconductor systems like InAs [44, 169] or InSb [46], the PSB is lifted at zero magnetic field by the hyperfine interaction between the hole spin and the nuclear spin bath which mixes the triplet and singlet states. Here, the lack of current along the baseline of the bias triangles ( $\epsilon = 0$ ) indicates that no such mixing is observed. One reason is the absence of the contact hyperfine interaction for holes. Due to the p-wave symmetry of their Bloch wave function and in contrast to the s-wave symmetry of electrons, the hole wave function

has minima at the position of the nuclei resulting in minimal overlap [2, 67, 169, 170] (see also Sec. 2.2 in Chap. 2). Notably, there are almost no nuclear spins in the host material of group IV semiconductors like Germanium and Silicon because most of the stable isotopes have zero nuclear spin. These materials can also be isotopically purified to further mitigate the effect of the hyperfine interaction [40].

At finite magnetic field, strong spin-orbit interaction couples some of the blocked  $(1, 1)$ -states to the  $S(2, 0)$  state via nonspin-conserving tunneling [171]. As a consequence, the PSB is lifted and transport through the DQD is enabled. We discuss this process by considering the energy diagram of the  $(1, 1)$  and  $(2, 0)$  states such as illustrated in Fig. 6.3. If an external magnetic field  $\mathbf{B}$  is applied, the  $(1, 1)$  triplet state splits into a  $T_-$ ,  $T_0$  and  $T_+$  state, separated by the Zeeman energy  $E_Z = g\mu_B|B|$  where  $g$  is the effective g-factor in the direction of  $\mathbf{B}$  and  $\mu_B$  the Bohr magneton. In presence of spin-orbit interaction, the  $(1, 1)$  singlet and triplet states start to mix.

At large magnetic fields the  $T_{\pm}(1, 1)$  triplet states are well separated, and  $T_0(1, 1)$  mixes with  $S(1, 1)$  such that a set of new, mixed basis states are defined:  $|M_{\alpha}\rangle$  is a  $T_0(1, 1)$ -like and  $|M_{\beta}\rangle$  is a  $S(1, 1)$ -like state [160, 171]. Consequently, transport through  $|M_{\alpha}\rangle$  is blocked due to the Pauli exclusion principle, but allowed through  $|M_{\beta}\rangle$ .

In absence of an external magnetic field, the hole spin is aligned with the spin-orbit field  $\mathbf{B}_{\text{SO}}$  because this field defines the quantization axis. When applying an external magnetic field  $\mathbf{B} < \mathbf{B}_{\text{SO}}$ , the hole spin starts to precess around the component of  $\mathbf{B}$  which is perpendicular to  $\mathbf{B}_{\text{SO}}$ . This precession enables nonspin-conservative spin-flip tunneling as indicated in Fig. 6.3a. Therefore, at finite field, transitions from  $|M_{\beta}\rangle$ ,  $T_-(1, 1)$  and  $T_+(1, 1)$  to  $S(2, 0)$  can contribute to the transport while at zero field only the singlet-like  $|M_{\beta}\rangle$  state contributes. Increasing the field strength  $|\mathbf{B}|$  leads to a faster precession of the spin which results in an increase of the spin-flip transition rates  $\Gamma_{\pm}^{\text{SO}}$  from  $T_{\pm}(1, 1)$  to  $S(2, 0)$  and consequently an increase of the leakage current. Because both states have a spin component of zero, the coupling  $\Gamma_{\beta}^{\text{SO}}$  of  $|M_{\beta}\rangle$  to  $S(2, 0)$  is field independent. Based upon the same argument, no transition which involves  $|M_{\alpha}\rangle$  is allowed. As a consequence, at high fields when  $\Gamma_{\pm}^{\text{SO}}$  is very fast, the transport becomes limited by the time the system spends in the state  $|M_{\alpha}\rangle$  and will

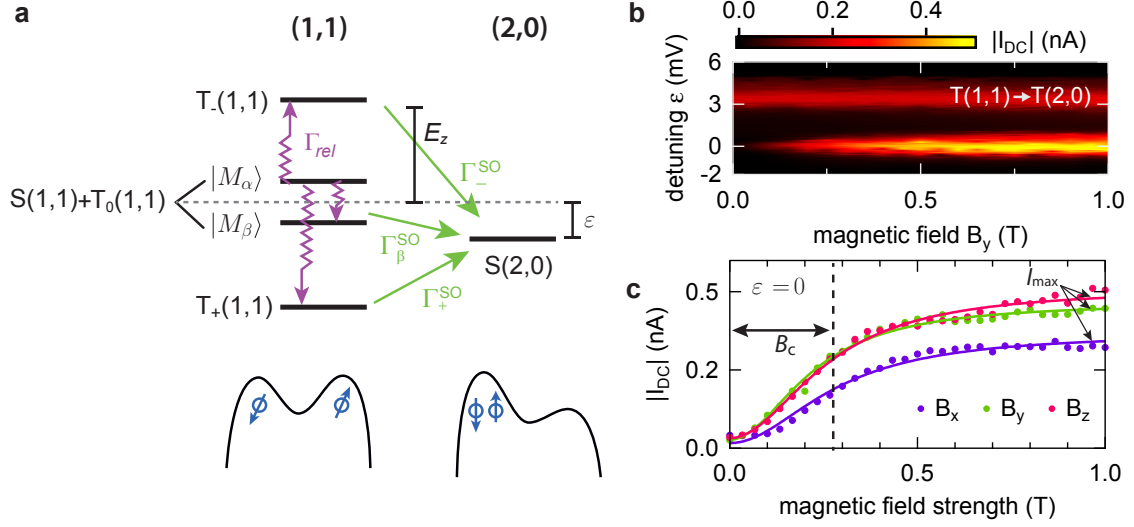


Figure 6.3: **Lifting of the Pauli spin blockade with magnetic field.** (a) Energy levels and transitions of the (1, 1) states into the  $S(2, 0)$  state. In presence of strong SOI,  $T_0(1, 1)$  and  $S(1, 1)$  are tunnel coupled and the mixed states  $|M_\alpha\rangle$  and  $|M_\beta\rangle$  become the new basic states. (b) Current through the double dot in PSB at  $V_{SD} = -2.5$  mV for varying detuning  $\epsilon$  and as a function of a magnetic field  $B_y$ , applied perpendicular to the NW. While the triplet transitions, labeled as  $T(1, 1) \rightarrow T(2, 0)$ , are not affected, the spin-blockade into the  $S(2, 0)$  at  $\epsilon = 0$  is lifted. The revealed low-field current minima is an indication of lifting of the PSB in presence of strong spin-orbit interaction. (c) Leakage current  $I_{DC}$  for magnetic field cuts along  $\epsilon = 0$  for different directions of the external magnetic field. Here, an anisotropic saturation current  $I_{max}$  is observed. The field dependence of  $I_{DC}$  is in good agreement with a Lorentzian shape (solid curves) predicted by the SOI model described by Eq. (6.2).

only become unblocked by relaxation into an unblocked state. Therefore, the relaxation rate out of the blocked state,  $\Gamma_{rel}$ , leads to a maximum current  $I_{max}$  which is given by

$$I_{max} = 4e\Gamma_{rel} \quad (6.1)$$

in the high field limit where  $\mu_B B \gg \hbar\sqrt{\Gamma_{\pm}^{SO}\Gamma_{rel}}$  [171]. And at  $\epsilon = 0$ , the field dependence of the SOI contribution to the leakage current is

$$I = I_{max} \left( 1 - \frac{8}{9} \frac{B_c^2}{B^2 + B_c^2} \right), \quad (6.2)$$

where  $B_c$  is related to the SOI field [171]. Hence, the current exhibits a Lorentzian shaped minimum at low field which is characteristic for the presence of strong SOI in the system and

scales with the SOI strength.

In Fig. 6.3b we show the current through the DQD in blocked bias direction, as a function of the strength of a magnetic field applied along  $\hat{y}$  and detuning  $\epsilon$ . In agreement with Eq. (6.2), a transition from low to a saturated current is observed with increasing magnetic field at  $\epsilon = 0$ . The transition rates  $\Gamma_{\pm}^{\text{SO}}$  as well as  $\Gamma_{\beta}^{\text{SO}}$  are suppressed by  $\epsilon^{-2}$  which is recognized in Fig. 6.3b as a energy window of blocked transport between the baseline and the triplet transitions. Further, the splitting of the triplet states with  $|\mathbf{B}|$  leads to a broadening of the baseline. The inter dot triplet transitions are unaffected by the magnetic field.

A cut at  $\epsilon = 0$  of the data presented in Fig. 6.3b is shown in Fig. 6.3c. We find good agreement to Eq. (6.2) with  $B_c \sim 270$  mT. Other experiments showed a  $B_c$  of the order of up to  $\sim 100$  mT [169] or of order 1 T [161]. These results cannot be directly compared because  $B_c$  scales with the interdot coupling. In Fig. 6.3c, we also show cuts at  $\epsilon = 0$  of the same type of measurements for the external magnetic field applied along  $\hat{x}$  and  $\hat{z}$ . While all directions show a comparable  $B_c$ , an anisotropy of the magnitude of the leakage current saturation  $I_{\text{max}}$  is revealed: For a magnetic field pointing along the double dot axis  $\hat{x}$ , the saturation current  $I_{\text{max}}$  is reduced. We speculate that this is due to an anisotropic spin relaxation rate  $\Gamma_{\text{rel}}$  which defines the magnitude of  $I_{\text{max}}$  according to Eq. (6.1).

## 6.5 Anisotropic Pauli spin blockade

We look into this saturation anisotropy in more detail by rotating a magnetic field of 1 T in the  $x$ - $z$ -,  $y$ - $z$  and  $x$ - $y$ -plane of the device. The observations are summarized in Fig. 6.4 where we labeled certain directions of particular interest of the magnetic field with marks  $A$  to  $D$ . Qualitatively, we understand our observation as a combination of two effects which modulate the spin relaxation rate  $\Gamma_{\text{rel}}$  and lead to an anisotropic saturation current: an anisotropic  $g$ -factor and a spin-orbit field  $\mathbf{B}_{\text{SO}}$ . The effect of the  $g$ -factor anisotropy is indirectly observed when rotating the magnetic field in the  $x$ - $z$ -plane as shown in Fig. 6.4a. The saturation current  $I_{\text{max}}$  becomes maximum (minimum) when the field is aligned perpendicular (parallel) to the wire oriented along the  $\hat{x}$  direction. We assign the small angle of the minima at label

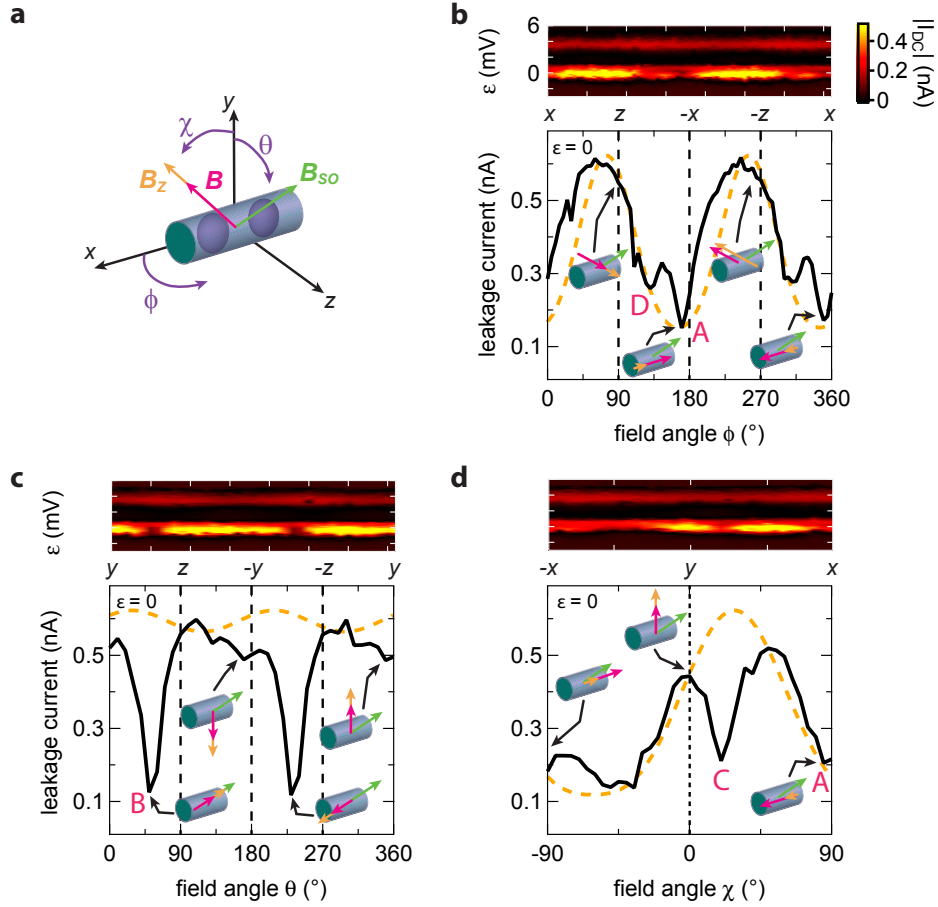


Figure 6.4: **Anisotropic Pauli spin blockade.** (a) Schematic of the directions, angles and fields involved to discuss the anisotropic PSB. Here,  $\mathbf{B}_Z \sim g\mathbf{B}$  is a resulting Zeeman field due to the external magnetic field  $\mathbf{B}$  and the corresponding  $g$ -factor  $g$ .  $\mathbf{B}_{SO}$  is the direction of the spin-orbit field identified in the measurements. (b) The upper panel shows  $|I_{DC}|$  for a 1 T field rotated in the  $x$ - $z$ -plane for different  $\epsilon$  exhibiting an anisotropic maximum current  $|I_{\max}|$  due to lifting the PSB through the double dot at  $\epsilon = 0$ . The triplet transition is unaffected. In the lower panel, a cut along  $\epsilon = 0$  is shown. The leakage current is minimum (maximum) when the magnetic field is aligned (perpendicular) with the wire. (c) and (d) show the same measurements as in (b) but for the field rotated in the  $y$ - $z$ - and  $x$ - $z$ -plane, respectively. Magnetic field directions emphasized with labels  $A$ - $D$  describe points of particular interest as discussed in the main text. The minima in leakage current are either due to  $g$ -factor anisotropy ( $A$ ) or an effective spin-orbit field  $\mathbf{B}_{SO}$  ( $B, C, D$ ). The orange dashed curve is a model of the contribution from the  $g$ -factor anisotropy as described in the text.

$A$  with respect to the  $\hat{x}$ -axis to a misalignment of the wire with respect to the coordinate system of the magnet. In a Ge/Si NW, the  $g$ -factor is maximum perpendicular to the wire while it almost vanishes along the wire [54, 86]. Because the  $g$ -factor is minimal along the



wire [54, 86], the Zeeman energy  $E_Z = g\mu_B B$  is minimal. SOI induced phonon mediated spin relaxation is known to show strong dependence on the Zeeman energy  $E_Z$  [90] (see also Chap. 4). For a Ge/Si NW in the field range considered here, the spin relaxation rate  $T_1^{-1}$  depends on  $E_z$  according to a power law  $T_1^{-1} \sim E_z^{7/2}$  [86]. As a consequence the relaxation rate  $\Gamma_{rel}$  is minimal along the wire.

A narrow minimum of the leakage current is observed, for an angle of the external field in the  $y$ - $z$ -plane when the field is applied in between the  $z$  and  $y$  direction (label  $B$ ). This observed leakage current anisotropy must be due to an effect which breaks the radial symmetry of the cylindrical NW. An effective spin-orbit field  $\mathbf{B}_{SO}$  breaks this symmetry and spin relaxation becomes inefficient if the external magnetic field is applied parallel to  $\mathbf{B}_{SO}$  because of the absence of a perpendicular magnetic field component which is necessary for a finite transition matrix element between the two spin states. Notably,  $\mathbf{B}_{SO}$  also shows a finite component in the  $x$ -direction, visible by the minima at the points labeled  $C$  and  $D$  in Fig. 6.4b and d, respectively, which are offset from the  $\hat{y}$ - and  $\hat{z}$ -axis by an angle  $\sim 20^\circ$  and  $\sim 40^\circ$ .

We introduce a phenomenological model which combines the contribution of the  $g$ -factor and  $\mathbf{B}_{SO}$  to the leakage current. We assume that the leakage current is

$$I_{leak} \sim \left( \left( |\mathbf{b}^T \tilde{g} \mathbf{b}| |B| \right)^p \cdot \mathbf{b} \right) \times \mathbf{B}_{SO}, \quad (6.3)$$

where  $\tilde{g}$  is the  $g$ -factor tensor,  $\mathbf{b} = \mathbf{B}/|B|$  is the unit vector along the magnetic field  $\mathbf{B}$  and  $p$  is a parameter to account for the dependence of the spin relaxation on the Zeeman energy  $E_Z = \mu_B |\mathbf{b}^T \tilde{g} \mathbf{b}| \cdot |B|$ . In Fig. 6.4 we show the expected anisotropy of the leakage current due to an anisotropic  $g$ -factor. Here, we used  $p = 3.5$ ,  $g_x = 0.1$ ,  $g_y = g_z = 2$  and found an offset of the wire  $\phi_0 \approx 15^\circ$  and  $\theta_0 \approx 30^\circ$ . Remarkably, because of anisotropic coupling to phonons, for the same  $E_Z$  the spin relaxation rate  $T_1^{-1}$  is predicted to be about two order of magnitude faster when the magnetic field is applied along compared to when it is applied perpendicular to the NW [86]. This effect might partially counter-act the anisotropic  $I_{leak}$  due to a  $g$ -factor anisotropy which modulates  $E_Z$ .

The experimentally found direction of  $\mathbf{B}_{SO}$  could point towards a direct Rashba type of

spin-orbit interaction. While we do not know the exact electric field profile arising from the voltages applied to the bottom gates, we expect the resulting electric field  $\mathbf{E}$  to have predominately  $y$ - and  $x$ -components and a rather small  $z$ -component. For direct Rashba SOI in a NW DQD with weakly coupled, elongated QDs,  $\mathbf{B}_{\text{SO}} \perp \mathbf{k}_{\text{x}} \perp \mathbf{E}$  where the momentum  $\mathbf{k}_{\text{x}}$  is given by the wire axis. For  $\mathbf{E} \parallel \hat{y}$ , this results in a  $\mathbf{B}_{\text{SO}} \parallel \hat{z}$  and a finite  $z$  component of  $\mathbf{E}$  leads to a finite angle of  $\mathbf{B}_{\text{SO}}$  in the  $y$ - $z$ -plane as observed in Fig. 6.4c. From the geometry of the device (see Fig. 6.1), the electric field component along  $z$  is expected to be small compared to the  $y$  component which contradicts the observed significant  $y$  component of  $\mathbf{B}_{\text{SO}}$ . Also, when assuming DRSOI, the surprisingly large  $\hat{x}$ -component of  $\mathbf{B}_{\text{SO}}$  is not yet understood. Partially, it might be explained by the orientation of the NW but this contradicts the  $g$ -factor anisotropy induced current minima at point  $A$  which suggests only a small misalignment with respect to the coordinate system of the device.

There are many possible explanations for these discrepancies. The effective electric field inside the NW might depend on local conditions and could therefore be rather chaotic. Further, the available predictions are based on low energy holes in the lowest subband of a NW. The effect of the confinement as well as larger energies has not yet been analyzed. The measurements shown here were performed in DQDs with  $\sim 10$  holes each. These residual holes also lead to electric fields which can give rise to a DRSOI.

## 6.6 Discussion and conclusions

In summary, we show transport experiments in a Ge/Si core-shell NW DQD device. We find a configuration of the DQD which exhibits very strong PSB. With a model based on spin-orbit interaction mediated spin-flip tunneling [172], we explain lifting of the PSB upon application of an external magnetic field and find the predicted saturation of the leakage current in the high field limit. While we do not find a dependence of  $B_c$ , the magnetic field scale required to lift the PSB, on the direction of the external magnetic field applied along the three major axes of our coordinate system, we observe a lower saturation current for the field applied along the wire. At high fields, this saturated leakage current is effectively limited by  $\Gamma_{\text{rel}}$ , the decay of the  $T_0$ -like  $(1, 1)$ -state  $|M_\alpha\rangle$  into the other  $(1, 1)$ -states. Data of

the leakage current as a function of different rotations of the external magnetic field suggests that a g-factor anisotropy and a  $\mathbf{B}_{\text{SO}}$  modulate the saturation of the leakage current.

The direction of  $\mathbf{B}_{\text{SO}}$  does not contradict the emergence of a direct Rashba spin-orbit interaction due to an electric field originating from confinement gates used to form the quantum dots. DRSOI is highly tunable with an external electric field [5, 50]. But here, the possible DRSOI emerges from the field stemming from the bottom gates which are used to create the quantum dot confinement potential. Therefore, it was not possible to study the electric field dependence in this device without changing the confinement potential of the DQD. In addition to the bottom gates, this device was fabricated with two side gates. These allow to create an electric field which is independent of the confinement potential. And indeed, along certain directions of the magnetic field, a dependence of the leakage current from the side gate voltages is observed. But from the data available (not shown), we can not yet state conclusively if this observed modulation is due to a tuning of DRSOI or an effect of the tunnel barriers. Further, these electric fields not only control the strength of the DRSOI field but also change the g-factor [86] which makes the interpretation of the observation difficult. Therefore, future experiments aim for a better understanding of the impact of these electric fields in order to conclusively demonstrate an electrically tuneable DRSOI.

# 7 Ambipolar quantum dots in undoped silicon fin field-effect transistors

Andreas V. Kuhlmann, Veeresh Deshpande

*IBM Research-Zürich, Rüschlikon, Switzerland*

Leon C. Camenzind, Dominik M. Zumbühl

*Department of Physics, University of Basel, Switzerland*

Andreas Fuhrer

*IBM Research-Zürich, Rüschlikon, Switzerland*

## Abstract

We integrate ambipolar quantum dots in silicon fin field-effect transistors using exclusively standard complementary metal-oxide-semiconductor fabrication techniques. We realize ambipolarity by replacing conventional highly-doped source and drain electrodes by a metallic nickel silicide with Fermi level close to the silicon mid-gap position. Such devices operate in a dual mode, either as classical field-effect or single-electron transistor. We implement a classical logic NOT gate at low temperature by tuning two interconnected transistors into opposite polarities. In the quantum regime, we demonstrate stable quantum dot operation in the few charge carrier Coulomb blockade regime for both electrons and holes.

This chapter is published in *Appl. Phys. Lett.* [173].

## 7.1 Introduction

Quantum information can be encoded in the spin state of a single electron or hole confined to a semiconductor quantum dot (QD) [1, 2, 60]. Several material systems have been explored in the search of a highly coherent spin quantum bit (qubit). Silicon (Si) is a particularly promising material platform for scalable spin-based quantum computing because of its fully developed, industrial manufacturing processes, which enable reliable and reproducible fabrication at the nanometer scale [40, 165, 174]. Furthermore, natural silicon consists of 95% non-magnetic nuclei (92%  $^{28}\text{Si}$ , 3%  $^{30}\text{Si}$ ), suppressing hyperfine-induced decoherence [31, 33, 34] (see also Chap. 4). A nearly nuclear-spin-free environment can additionally be engineered by means of isotopic purification [175]. Electron spins in silicon are also subject to a weak spin-orbit interaction (SOI) and can thus be almost completely isolated from environmental noise [176]. As a result, an excellent dephasing time  $T_2^*$  of  $120\ \mu\text{s}$  has been demonstrated for the electron spin qubit in isotopically enriched silicon ( $\geq 99.9\%$  of  $^{28}\text{Si}$ ) [40]. For scalable quantum circuits, qubit control via electric rather than magnetic fields is more promising in terms of speed and hardware implementation. In this regard, the hole spin represents an attractive alternative to its electron counterpart [69, 177, 178]. The asymmetry of the silicon band structure with respect to the conduction (CB) and valence bands (VB) manifests itself in different characteristics for electrons and holes. While the electron Bloch function has s-wave symmetry, the hole has p-wave symmetry (see also Sec. 2.2 in Chap 2). Consequently, hole spins experience a weaker hyperfine, yet stronger SOI, which enables fast, all-electrical spin manipulation [158–160, 179]. Despite these potential benefits, hole spin qubits in silicon are still largely unexplored. Recently, qubit functionality with fast, purely electrical, two-axis control was shown for a hole spin, yet with inferior coherence compared to the electron spin [165].

Usually, either electrons [180–183] or holes [115, 158, 165, 170, 184] are confined in silicon QDs. Ambipolar devices, by contrast, can be operated in both the electron and hole regime [185–192]. For planar silicon metal-oxide-semiconductor (MOS) QD structures, ambipolar behavior was demonstrated by integrating both  $n$ - and  $p$ -type reservoirs on the same device [193–197].

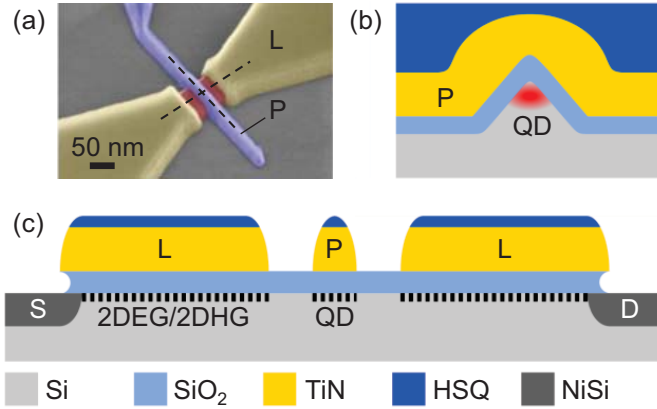


Figure 7.1: Device layout: (a) False-color scanning electron micrograph showing a FinFET structure before sealing it with a SiO<sub>2</sub> passivation layer. Devices consist of a single plunger (blueish color) and two lead gates (yellowish color) to silicided source and drain. The gate electrodes are operated in accumulation mode and are wrapped around the silicon fin (reddish color) defining the transistor channel. The dashed lines indicate the orientation of the schematic cross sections perpendicular to (b, sketched for a narrower fin than the one in (a)) and along (c) the fin. For a positive (negative) gate voltage electrons (holes) are accumulated at the Si-SiO<sub>2</sub> interface below the electrode. While the lead gates are designed to induce a two-dimensional electron (hole) gas opening low-resistance leads to source and drain, the plunger gate allows for local electrostatic control of the channel and to create a QD, which is located at the apex of the triangular shaped fin.

Ambipolar devices provide great flexibility for scalable spin-based quantum circuits, since both types of charge carriers can be manipulated in exactly the same crystalline environment, allowing for direct benchmarking of hole against electron spin qubits.

Here, we report on ambipolar silicon QD devices based on today's industry standard, non-planar fin field-effect transistors (FinFETs) [198–200]. In an overlapping-gate structure, ambipolarity is achieved by using a metallic nickel silicide (NiSi) with Fermi energy close to the silicon mid-gap for source (S) and drain (D) electrodes [187, 188, 201]. This approach allows for a highly compact device layout, is easy to integrate and fully compatible with complementary metal-oxide-semiconductor (CMOS) technology. We operate the devices both in a classical and quantum mode [202], demonstrating simple co-integration between silicon-based qubits and traditional CMOS control hardware.

## 7.2 Ambipolar fin field-effect transistor device

FinFETs can in principle be fabricated on either bulk silicon or silicon-on-insulator substrates. The latter have already been utilized to implement unipolar QDs with conventional highly-doped source and drain electrodes[158, 165, 203]. We, in contrast, build ambipolar devices on bulk silicon, which is more widely used in industry.

The layout of the home-built devices is shown in Fig. 7.1. First, the fin structures are defined on a near-intrinsic silicon substrate ( $\rho > 5000 \Omega\text{cm}$ , (100) surface) by means of electron-beam lithography (EBL) and dry etching, yielding a fin height of  $\simeq 25 \text{ nm}$ . A sacrificial thermally grown silicon dioxide ( $\text{SiO}_2$ ) layer, which is removed in buffered hydrofluoric acid, allows for narrowing of the fin width ( $\gtrsim 10 \text{ nm}$ ) and cleaning of etch-induced surface damage. This procedure leads to an almost triangular cross section for the narrowest fins. Subsequently, the gate stack is deposited, consisting of a high-quality, thermally grown  $\text{SiO}_2$  layer ( $\sim 10 \text{ nm}$ , breakdown voltage  $\sim 10 \text{ V}$ ), covered by  $40 \text{ nm}$  of titanium nitride (TiN). A uniform layer of TiN, which is wrapped around the silicon channel, is obtained by atomic layer deposition. The gate layer is patterned by means of EBL and dry etching of TiN, resulting in a gate length of  $\gtrsim 25 \text{ nm}$  at a gate-to-gate separation of  $\gtrsim 50 \text{ nm}$ . Conventional impurity-doped source and drain electrodes are replaced by a metallic, non-magnetic NiSi, forming a Schottky barrier at the S/D-to-substrate junction [201, 204]. By choosing a mid-gap silicide, ambipolar operation is realized in a simple, highly compact design, as no complementary charge reservoirs are required. So far, ambipolar silicon QDs have only been implemented by integrating separate  $n$ - and  $p$ -type contacts to the same channel, enlarging the device's footprint [193–197]. The NiSi electrodes are formed by EBL, Ni evaporation, lift-off and low-temperature silicidation annealing at  $475^\circ \text{C}$  for  $30 \text{ min}$  in an argon ambient. Lateral Ni diffusion below the gates allows for tuning of the Schottky barrier width, and ensures that source and drain contacts operate in an ohmic regime. After silicidation, unreacted Ni is selectively removed in order to avoid the presence of any magnetic impurities in the device. Finally, the devices are protected from contamination by a  $\text{SiO}_2$  passivation layer and are accessed via tungsten interconnects. The data presented here is obtained from direct current electrical transport measurements

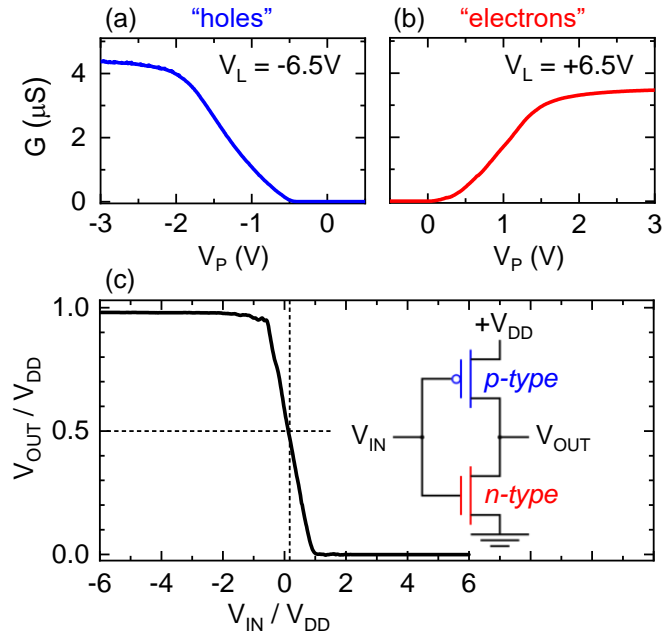


Figure 7.2: Ambipolar turn-on curves and CMOS logic at cryogenic temperatures: conductance  $G$  versus plunger gate voltage  $V_P$  for the hole (a) and electron (b) regime. The lead voltage  $V_L$  is kept fixed at a value well above threshold, and the source-drain voltage  $V_{\text{SD}}$  is  $-1\text{ V}$  for holes and  $+1\text{ V}$  for electrons, where the bias polarity is chosen such that electrical stress on the device is minimized. (c) Voltage transfer characteristics and the corresponding circuit diagram of a CMOS inverter, consisting of a p-type and a complementary n-type FinFET. For *low* input  $V_{\text{IN}} < 0\text{ V}$  the output  $V_{\text{OUT}}$  is *high* and vice versa. All the measurements are performed at  $T = 1.5\text{ K}$ .

with the sample cooled to  $T \simeq 1.5\text{ K}$ . The devices' gate layer consists of a central plunger (P) and individual lead (L) gates to source and drain electrodes, as shown in Fig. 7.1(c). The gates are operated in accumulation mode: for a negative (positive) applied voltage holes (electrons) are accumulated at the Si-SiO<sub>2</sub> interface. Therefore, a two-dimensional electron (2DEG) or hole gas (2DHG) forms beneath the lead gates, acting as electrostatically defined source and drain, while the plunger gate induces a Coulomb island that defines the QD. The gaps separating lead and plunger gates create tunnel barriers between them [203].

### 7.3 Classical field-effect transistor

First, the devices are operated in a classical field-effect transistor (FET)-like regime. Ambipolar transistor turn-on curves, revealing both *n*- and *p*-type conduction, are presented in



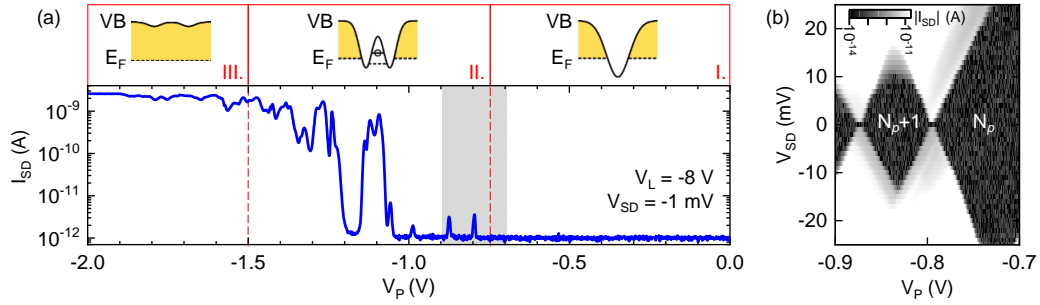


Figure 7.3: QD formation: (a) source-drain current  $I_{SD}$  versus plunger gate voltage  $V_P$  in the low-bias regime ( $V_{SD} = -1$  mV) on the hole side ( $V_L = -8$  V). Top panel: Sketches of the real space band alignment in the vicinity of the plunger gate for the observed three different conductance regimes. (b) Charge stability map of the first measurable Coulomb resonance. The corresponding plunger gate voltage range is indicated by the grey shaded area in (a). The Coulomb diamonds are labeled with the number of holes residing on the dot ( $N_p \gtrsim 0$ ). All the measurements are performed at  $T = 1.5$  K.

Figs. 7.2(a),(b). The linear conductance  $G$  is plotted versus plunger gate voltage  $V_P$  at a constant lead gate voltage  $V_L$  of  $\pm 6.5$  V, opening conducting channels beneath the lead gates and also ensuring close-to-ohmic operation by tuning the Schottky barrier width. A large source-drain voltage  $V_{SD}$  of  $\pm 1$  V ensures that the current is not dominated by charge carrier tunneling processes. The measurement reveals a slight asymmetry in current-onset voltages with respect to zero for electrons and holes: for  $V_P \gtrsim 0$  V  $n$ -type and for  $V_P \lesssim -0.35$  V  $p$ -type conduction occurs. In between, the Fermi level lies in the band gap of silicon and no states are available for transport. This asymmetry is not fully understood and most likely a combination of various effects, such as a residual wafer background doping, charge traps or the metal gate work function [194, 196, 197]. The lower saturation current for electrons may also be due to an asymmetry of the silicide Schottky barrier for electrons and holes.

Any CMOS circuit can in principle be constructed using ambipolar transistors as sole building blocks. In the inset of Fig. 7.2(c) the most basic logic circuit - the CMOS inverter - is shown schematically. It consists of two complementary transistors connected at the gate and drain terminals. The inverter output voltage  $V_{OUT}$  is taken from the common drain electrode and is limited to the supply voltage  $V_{DD}$ , which is applied to the  $p$ -type transistor's source contact. The voltage transfer curve of our home-built inverter is presented in Fig. 7.2(c). As the input voltage  $V_{IN}$  is varied from *low* to *high*, the inverted input signal is measured at the

output, going from *high* to *low*. The *high* output level gets with  $0.98 V_{DD}$  close to the ideal limit. The transition zone, however, is centered around  $V_{IN} \simeq 0.15 V_{DD}$  and not  $V_{DD}/2$  as the devices are not perfectly matched in threshold voltage and amplification. Nevertheless, the successful operation of an inverter at low-temperature proves that classical CMOS logic can be performed.

## 7.4 Single electron field-effect transistor

In the linear transport regime at  $V_{SD} = -1$  mV, quantum confinement in an island, which forms below the plunger gate, gives rise to pronounced Coulomb oscillations. The plunger gate-dependent source-drain current  $I_{SD}$  at  $V_L = -8$  V is shown in Fig. 7.3(a). In this regime the current is dominated by hole tunneling. The measurement is performed on a device with a fin width of  $\simeq 20$  nm, plunger gate length of  $\simeq 25$  nm and plunger-to-lead-gate separation of  $\simeq 25$  nm. Three different regimes of hole transport, which are depicted schematically in the top panel of Fig. 7.3(a), are observed: (i) for  $V_P \gtrsim -0.8$  V the barrier induced by the plunger gate prevents current flow. (ii) For  $V_P \lesssim -0.8$  V a series of Coulomb resonances indicates single-hole tunneling via a QD formed beneath the plunger gate. In the valleys between the peaks the device operates in Coulomb blockade, i.e. the QD contains a fixed number of holes [60, 174]. As this number increases with more negative  $V_P$ , the plunger gate's fringe fields lower the barriers and the QD starts to open ( $V_P \lesssim -1.05$  V). (iii) For  $V_P \lesssim -1.5$  V a conducting channel is opened and the current is limited by the series resistance of the device. Similar behavior is found for positive  $V_P$  on the electron side (see Fig. 7.4).

The first measurable Coulomb resonances are investigated in more detail by means of bias spectroscopy. In Fig. 7.3(b) the charge stability diagram is shown for a plunger gate voltage range highlighted by the gray shaded area in Fig. 7.3(a). Within this range, the tunnel barriers are still well defined. Clear Coulomb diamonds with a fixed number of holes  $N_p$  on the QD are observed. Outside the diamonds sequential tunneling of holes through the QD occurs. The small dimensions of the device and the closing of the Coulomb diamonds at zero bias suggest formation of a single QD. Moreover, similar coupling of the QD to both source and drain (from the shape of the diamond we determine that the source and drain

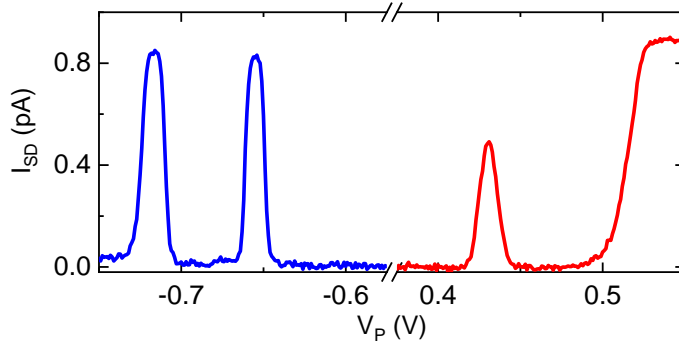


Figure 7.4: Ambipolar Coulomb blockade: source-drain current  $I_{SD}$  versus plunger gate voltage  $V_P$  for holes (blue,  $V_L = -4$  V,  $V_{SD} = +0.5$  mV) and electrons (red,  $V_L = +3.2$  V,  $V_{SD} = +2.5$  mV). The measurements are performed at  $T = 1.5$  K.

lever arms differ by just  $\sim 6\%$ ) dictates a central location of the charge island below the plunger gate. The charging energy is determined to be  $e^2/C_\Sigma \simeq 16$  meV that corresponds to a total capacitance  $C_\Sigma$  of 10 aF. The plunger gate voltage spacing of the Coulomb resonances yields a gate capacitance  $C_g$  of 2.1 aF. The latter is in good agreement with the calculated MOS plunger gate capacitance, which can be estimated by an equivalent planar capacitor  $C_g = \epsilon_0 \epsilon_{SiO_2} S / t_{SiO_2} \sim 3.5$  aF with  $\epsilon_{SiO_2} = 3.9$  the dielectric constant,  $t_{SiO_2}$  the oxide thickness and  $S$  the surface area of the gate-fin overlap. The gate voltage lever arm is  $\alpha = C_g / C_\Sigma \simeq 0.21$ . The large charging energy and the wide opening in  $V_{SD}$  of the last diamond could indicate that the device is operating in the single-hole regime. However, more sensitive charge detection methods and a device structure that offers more tunability are necessary to evaluate this [28, 60]. The lines of increased conductance that run parallel to the diamond edges in Fig. 7.3(b) can be attributed to resonant tunneling processes [61], for instance excited orbital states of the QD. Various devices have been measured, showing similar behavior and charging energies. However, instabilities and deviations from the ideal picture reveal that the device performance is affected by charge-trapping defects.

Ambipolar behavior in the low  $V_{SD}$  regime is demonstrated in Fig. 7.4 where  $I_{SD}$  is plotted versus  $V_P$  for both the electron and hole regime. The data was measured on a different device with the same physical dimensions as the one of Fig. 7.3 (the electron regime of this device suffers from charge traps). Both in the electron and hole transport regime Coulomb oscillations occur. However, the asymmetry in the band structure of silicon with respect to

the conduction and valence bands manifests itself in asymmetric electrical transport characteristics for holes and electrons. While for electrons a single current peak exists before the barriers vanish, the hole side exhibits a similar behavior to the previous device with several Coulomb oscillations.

## 7.5 Discussion and Conclusions

In conclusion, we have introduced ambipolar silicon QDs, integrated in today's industry standard, non-planar FinFETs. By making use of a mid-gap silicide, ambipolar devices are realized with the footprint of unipolar ones. In modern chips (with multiple layers added to the wafer surface and a multi-level metallization scheme) this will allow for the same high device density of unipolar and ambipolar devices. We operate these devices in a classical as well as quantum mode, thus demonstrate the compatibility of silicon-based quantum circuits with traditional CMOS control hardware. Future devices with even smaller physical dimensions, improved charge noise performance and a second gate layer for in-situ adjustment of the tunnel coupling will probably allow us to reliably access the single-electron (hole) regime. Such devices will enable direct benchmarking of electron against hole spin qubits. The FinFET architecture is also suitable to implement linear arrays of multiple tunnel-coupled QDs. In terms of fabrication, there is no significant additional process development work needed. Moreover, an interconnected array of ambipolar QDs will offer a blank canvas for building custom, on-the-fly reconfigurable "quantum CMOS" circuits, which in analogy to classical CMOS, utilize both  $n$ - and  $p$ -type devices.

## 7.6 Acknowledgement

We acknowledge technical support in device fabrication from Ute Drechsler, Antonis Olziersky and Ralph Heller. This work was supported by NCCR QSIT and the Georg H. Endress foundation.

# 8 A spin qubit setup in a cryofree dilution refrigerator

Leon C. Camenzind, Florian N. M. Froning,

Floris R. Braakman and Dominik M. Zumbühl

*Department of Physics, University of Basel, Switzerland*

## 8.1 Introduction

In general, to operate and read-out spin qubits, signals with high frequencies need to be applied to the qubit device. In this section, we discuss a radio frequency (RF)<sup>10</sup> setup capable of performing spin qubit operations, which we implement in a XLD400 cryofree dilution refrigerator from BlueFors Cryogenics Oy<sup>11</sup>. We first give a general overview on the hardware requirements for the different steps necessary to control spin qubits before the different components of the setup are explained in more detail.

Generally, the scheme to conduct a qubit operation can be separated into three major steps: Initialization, manipulation and read-out of the qubit. First, the qubit has to be initialized in to a well defined state. For a spin-1/2 qubit, this usually means preparing the spin in its ground state. There are various methods to achieve this initialization although the most obvious is to wait until the spin relaxes into the ground state as discussed in Chap. 4. However, depending on the spin relaxation time, this might severely limit the operation speed of the qubit. A more appropriate method is to apply a spin-to-charge conversion read-out as introduced in Chap. 4 in which at the end an electron tunnels into the spin ground state.

In a second step, the actual operations on the qubit are performed such that the initial state is changed. For spin-1/2 qubits, these operations are coherent spin rotations. Depending on

---

<sup>10</sup>According to convention by the International Telecommunications Union (ITU) only signals with frequency 3-30 MHz are defined as HF while the term radio-frequency (RF) covers a range from 20 kHz to 300 GHz. We therefore use the term radio frequency.

<sup>11</sup>[www.bluefors.com](http://www.bluefors.com)

which kind of spin qubit is operated, different operation schemes and exploitation of different physical effects are used to effectively perform the operation. But almost all of them rely on either exposing the spin qubit to an electrical or magnetic RF signal [43, 168] or on applying fast detuning pulses [34, 205].

In the future, we aim to operate spin-1/2 qubits using an electric dipole induced spin resonance (EDSR) scheme: By applying electrical RF signals to the gates confining the electron or hole which carries the qubit's spin, the charge carrier is coherently displaced due to dipole interaction with the oscillating electric field  $E(t)$ . Combined with spin-orbit interaction, this displacement is translated into an oscillating magnetic field  $B(t)$  which couples to the spin and facilitates coherent spin rotations [42–44, 46]. To achieve a maximal displacement with  $E(t)$ , it is beneficial to apply the RF signals to a gate electrode which is already involved in the confinement of the charge carrier. Because this confinement is defined with static voltages, we are required to couple the RF signal on a DC voltage offset using a bias tee. We divide the discussion of the setup and performance of this RF circuit into two parts: In Sec. 8.3, we show the performance of the coaxial lines installed in the refrigerator while in Sec. 8.4, the RF parts including the bias tee on our RF printed circuit board (PCB) are discussed.

In the third step, the state of the qubit after the operation is read-out in a projective measurement. In research environments and to benchmark the qubit fidelities, this means to measure the resulting  $\sigma_z$  component after the operation by averaging over a lot of initialization-manipulation cycles. An actual quantum computer however, must be designed to unambiguously return  $\sigma_z = 0$  or  $\sigma_z = 1$  after the operation has been performed [10]. For a spin-1/2 qubit, the spin is projected either into the "up" or "down" state. When the spin is in the "up" state, it can relax into the "down" state which leads to a complete loss of the initially stored quantum information. Therefore, the read-out has to be performed on a timescale much faster than the relaxation time of the qubit. Because the magnetic moment of the electron is tiny, it is currently not possible to read-out the  $\sigma_z$  component of a single spin with a magnetic field sensor. Therefore, it is often necessary to convert the spin information into charge information which can be read-out using an adjacent electrometer capacitively

coupled to the qubit.

For the different kind of spin qubits, there are different spin-to-charge conversion schemes. The spin-1/2 qubit is measured using the Elzerman read-out scheme [31]: if the chemical potential of a reservoir is located in between the energy levels of the two spin-states of the confined electron, the electron can only tunnel into the reservoir if its spin state is projected into the energetically higher state. For an electron in the lower spin state, there are no free states in the reservoir so elastic tunneling is prohibited. The change of the charge state if the electron tunnels out of the dot is observable with an adjacent electrometer. An other electron will tunnel into the energetically lower spin state once the dot is empty because this state lies below the chemical potential. Therefore, the electrometer must feature a large enough bandwidth to resolve such events, otherwise the tunnel event and therefore the conversion of the spin to a charge signal is missed.

There is a delicate trade-off for the Elzerman read-out: a larger Zeeman splitting leads to an increased read-out fidelity because the rates out of the states are more distinct in energy. Concurrently and as shown in Chap. 4, an increase in Zeeman energy leads to a shorter spin relaxation time  $T_1$  [36, 117, 149, 206] counteracting this gain in fidelity. The faster relaxation can be compensated with a faster read-out by increasing the tunnel-rate to the reservoir. But this will also increase the re-tunneling rate into the spin-ground state and therefore requires an even larger bandwidth of the charge sensor.

To achieve a read-out error rate of 1%, the tunneling rate out of the quantum dot must exceed the relaxation rate by a factor of 100. For spins hosted in an electron, the spin relaxation is usually relatively slow ( $T_1 \sim 1$  s) mitigating this problem — though there is a very strong magnetic field dependence as shown in Chap. 4. But for hole spin qubits  $T_1 \sim 100 \mu\text{s}$  or smaller and high-fidelity single-shot read-out requires fast charge detection using technologically challenging RF read-out schemes [206, 207].

Note, that the surface code, the state of the art error correction scheme for quantum computation, is much more robust against errors occurring during gate operation than read-out errors [2, 208]. Therefore the read-out stage will gain center stage for research in the future.

As elaborated above, a fast and reliable spin qubit read-out is essential for the realization of

a spin based quantum computer. Historically, the first realization of single electron charge sensing [28, 209, 210] and spin-to-charge conversion were performed by monitoring the DC current through a quantum point contact. Because of the poor performance of the DC lines at high frequencies, this technique has a rather low bandwidth. In Chap. 3 and Chap. 4 we used this method and showed data acquired with a comparatively fast DC charge sensor with a bandwidth of  $\sim 30$  kHz, limited by the electrical noise of the current amplifier. To increase the read-out speed, the charge sensor can be probed with a tank circuit connected to a cryogenic amplifier [30, 211–214]. Here, the quality factor of the tank circuit depends on the state of the charge sensor and therefore, by implication, also on the charge state of the quantum dot. The qubit is then read-out by measuring the amplitude or the phase of the reflected signal close to the resonance frequency of the tank circuit in a lock-in type of measurement. These reflectometry setups are currently the state of the art read-out method and allow to distinguish the  $(2, 0)$  from  $(1, 1)$  charge state of a double quantum dot (see Chap. 6) within a few  $\mu$ s [96].

It is usually difficult to match the impedance of the coaxial line  $Z_0 = 50 \Omega$  with the impedance of the tank-circuit. We therefore follow Ares et al. [215] and implement a varactor in parallel to the tank circuit. The varactor allows to tune the impedance of the tank circuit with a bias voltage such that almost perfect impedance matching is achieved. When compared to the intrinsic case, the matched condition increases the quality factor of the circuit remarkably. With a larger quality factor, the circuit is more sensitive to the state of the charge sensor and reduces the integration time needed to discriminate the states of the qubit. The performance of our two RF tank-circuits with implemented varactors is discussed in Sec. 8.5.

This electrometer based read-out is technologically rather difficult in terms of fabrication and implementation which makes this approach of read-out a limiting factor in regard to scalability. A tank circuit can also be used to directly measure the capacitance of a surface gate to the quantum dot. This so-called dispersive read-out has been introduced by Colless et al. [216] to semiconductor quantum dots and has since been widely used to measure the charge stability diagram of quantum dot devices [119, 206, 217]. This method is based on a dispersive shift of the tank circuit resonance frequency from the change of the quantum capacitance when



the charge carriers in the qubit undergo tunneling [216]. Because resonant tunneling occurs whenever a chemical potential of a lead and an energetically accessible level of a quantum dot are degenerate, dispersive read-out techniques are sensitive to charge transitions in the charge-stability diagram. The same argument is valid for interdot transitions in a double dot configuration.

Only very recently, the gate-based dispersive method has reached the sensitivity necessary to distinguish the charge states of a double quantum dot in a single-shot read-out [218–222]. Due to the rather simple implementation compared to the electrometer approach, dispersive single-shot read-out schemes are becoming the preferred approach when discussing concepts to scale-up spin qubit based quantum technologies [223, 224]. This chapter is structured as follows. First, in Sec. 8.2 a general overview of the setup is given while the transmission spectrum of the semi-rigid coaxial RF lines at room temperature is shown in Sec. 8.3. In Sec. 8.4 we focus on the design of the RF printed circuit board (RF-PCB) before discussing the performance of the two tank-circuits in Sec. 8.5.

## 8.2 From room temperature to the mixing chamber

The Bluefors XLD400 dilution refrigerator (XLD) with bottom loader allows fast sample exchange without the need to warm up the complete system. An exchangeable sample probe (PUCK) can be retracted from the XLD with a step motor to exchange the sample at room temperature. The XLD runs with a base temperature below 10 mK and is equipped with a 1-4-8 T vector magnet (American Magnetics Inc.). This vector magnet allows to study field direction dependent effects in spin qubits such as spin-orbit interaction (see Chap. 4 and Chap. 6) or anisotropic g-factor (see Chap. 5). Further, 8 semi-rigid coaxes with inner (outer) conductor out of silver-plated cupronickel (cupronickel) are installed in the XLD all the way down to the PUCK socket at the mixing chamber. The PUCK features an interface for 51 DC lines via a micro D-Sub connector (CINCH) and SMP connectors for the 8 RF lines whereas not all of these connections are currently used. A schematic of all electronic components from room temperature down to the sample is shown in Fig. 8.1.

Using this schematic, we first give an overview about the three sub-circuits of the setup: the DC lines, used to confine and control the spin qubit, a set of coaxial lines designated for manipulation by providing RF signals to gate electrodes and finally, the reflectometry circuits used for fast spin qubit read-out.

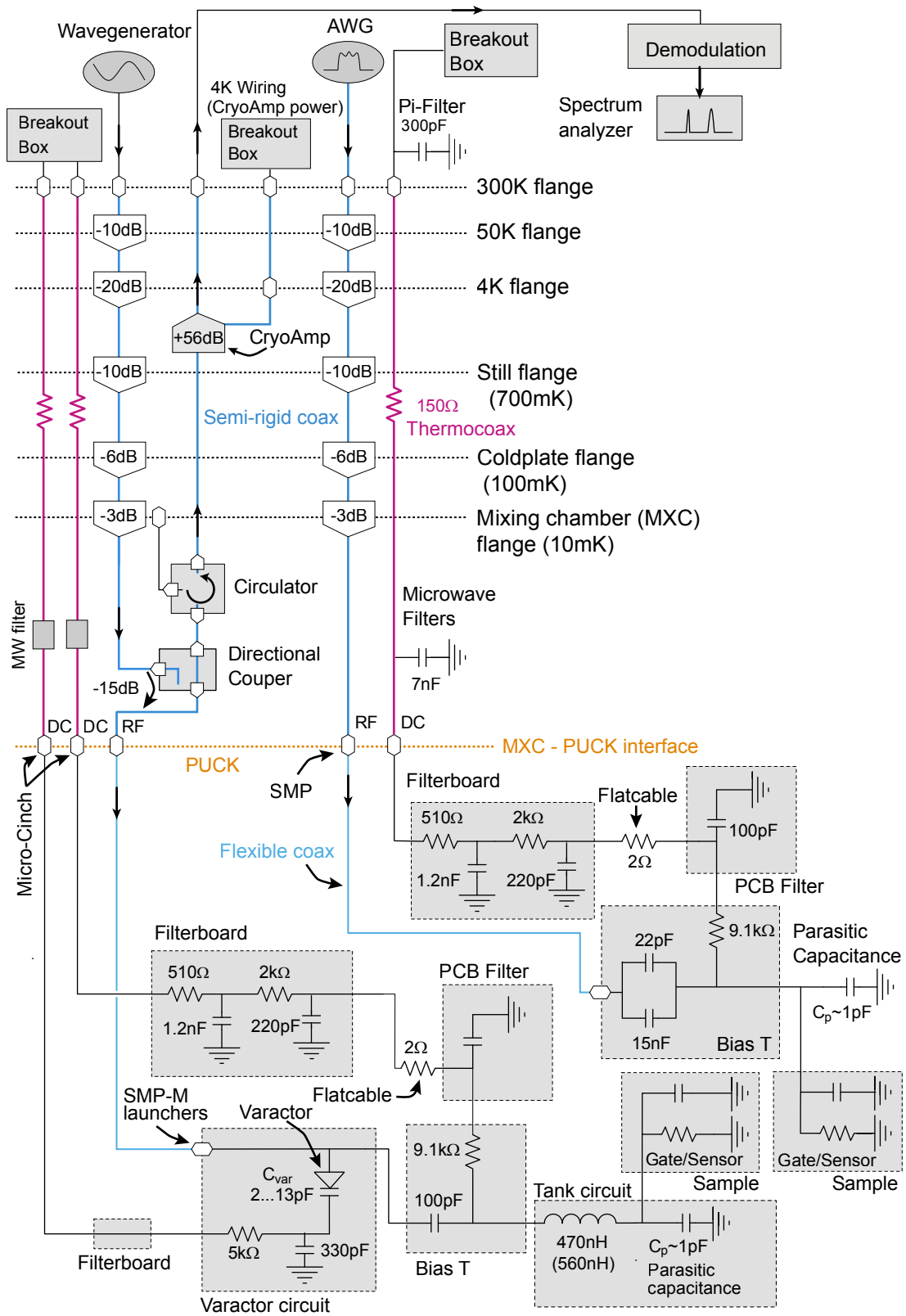


Figure 8.1: A schematic overview of the electronics built in the Bluefors XLD. The different components are explained in the text. The RF parts are marked in blue while the DC part is indicated in purple. The arrows give the intended forward direction of the RF signal. Inside the PUCK, all DC lines are first passing a filter board before feed into the RF PCB and routed towards the bonding pads and the sample.

## DC connections

For the DC connections from room-temperature down to the mixing chamber, we use 36 lossy thermocoaxes. These thermocoaxes are individually soldered to SMA connectors installed on three towers (A, B and C) on top of the XLD with 12 connectors each. Towers A and B are combined to a 24-pin D-Sub connector and connected to breakout box 1 (BoB 1) while tower C is connected to BoB 2 with another 24-pin D-Sub cable. Additionally, a Pi-filter (Spectrum Control) with 300 pF is mounted on top of the BoBs. Inside the fridge, the thermocoaxes are thermally anchored with bobbins at every temperature stage of the XLD all the way down to the mixing chamber flange. At room temperature, the resistance of the thermocoaxes was measured to be  $\sim 150\ \Omega$ . This resistance is not expected to change significantly at low temperature.

At the mixing chamber, each thermocoax is connected to a silver-epoxy microwave filter (MW) [97] which have a nominal capacitance between  $\sim 6\ \text{nF}$  and  $\sim 7.5\ \text{nF}$  and a resistance  $\sim 5\ \Omega$ . Such a large capacitance in front of the current-to-voltage (IV) converter (Basel Precision Instruments GmbH Low Noise High Stability IV-converter) severely limits the bandwidth of the line and consequently the speed of a possible DC charge sensor. We therefore installed four low-capacitance versions of the microwave filters with capacitances  $\sim 3.5\ \text{nF}$  to four lines of tower B. A comparison of the transmission spectrum  $S_{21}$  for the two kind of MW filters is given in Fig. 8.2. This transmission spectrum was obtained at room temperature with a vector network analyzer (Agilent N5230A PNA-L) and comprises the summed up attenuations of the thermocoaxes and the MW filters. As indicated in the schematic given in Fig. 8.2a,  $S_{21}$  is the forward two-port scattering parameter for a signal which is transmitted from port 1 to port 2.

The lines with conventional MW filters reach an attenuation of -120 dB, the noise floor of the vector network analyzer, at around 200 MHz while the lines with low capacitance MW filters reach this attenuation at  $\sim 1\ \text{GHz}$ , indicating the gain in bandwidth.

From the MW filters, phosphor bronze wires (California FineWire<sup>12</sup>) are used to connect

---

<sup>12</sup>[www.calfinewire.com](http://www.calfinewire.com)

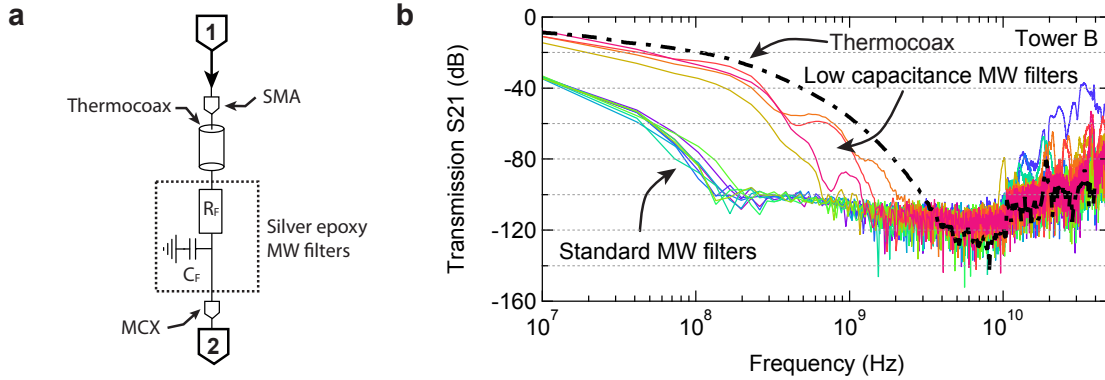


Figure 8.2: (a) Schematic of the setup to measure the transmission spectrum of the low-frequency lines from the SMA connectors on top of the XLD through the thermocoaxes and the silver epoxy MW filters to the MCX connectors installed at the end of the MW filters. Note that the lumped element schematic of the MW filters is simplified [97]. (b) Transmission spectrum  $S_{21}$  for all DC lines of tower B down to the mixing chamber flange measured at room temperature. The spectra of the low capacitance filters are clearly distinguishable from the standard MW filters. For comparison, also the transmission spectrum  $S_{21}$  for a thermocoax without any MW filter is shown (black dashed curve).

to straight Precidip<sup>13</sup> pin connectors. These connectors fit into a Precidip socket adapter soldered to the CINCH connector on the mixing chamber flange in which the counterpiece of the PUCK is plugged.

Inside the PUCK, individual phosphor bronze wires are used to link the DC lines from the CINCH to a custom-made filter board. From the filter board, a flexible flat cable (FFC) is used for the connection to a custom designed RF-PCB. On this PCB, conductive gold tracks route the lines to designated bond pads to which the sample is bonded. The PUCK with the filter board and the RF PCB explained in more detail in Sec. 8.4.

### RF frequency lines

The RF lines are accessible via SMA connectors on top of the XLD. Bulkhead feed-throughs thermalize the outer conductor of the semi-rigid coax cables at each temperature stage while the inner conductor is thermalized via cryogenic attenuators. The attenuators used at the different stage are indicated in Fig. 8.1 and add up to an attenuation of -49 dB.

Three RF lines are designated for spin qubit manipulation. These are directly connected

<sup>13</sup>www.precidip.com

to SMP connectors on the mixing chamber flange which make a connection to the SMP connectors located on top of the PUCK when the PUCK is inserted.

Inside the PUCK, formable coax cables (Pasternack<sup>14</sup> PE-SR405FL) are used to connect to SMP launchers (Amphenol<sup>15</sup> SMP-MSFD-PCE-1) soldered to the RF PCB. From the launcher, coplanar waveguides carry the RF signal to designated bond pads after passing through a bias tee. More details on the RF lines are given in Sec. 8.3.

### Reflectometry setup

Another two RF lines are used as input lines of the reflectometry setup. Each line is connected to the coupled port of a directional coupler (Mini-Circuits<sup>16</sup> ZEDC-15-2B). With an attenuation of -15 dB from the coupler, the signals are redirected to the tank circuits located on the RF-PCB via the SMP connectors and formable coax cables as described above. The circuitry of the tank circuits on the RF PCB as well as the performance is discussed in Sec. 8.5. The reflected signals from the two tank circuits pass to the input of the directional couplers (see Fig. 8.1). Then, the signal of each tank circuit is directed to a circulator (QuinStar<sup>17</sup> QCY-002) mounted at the mixing chamber flange before the signals are combined in a power combiner (Mini-Circuits ZESC-2-11+). Note that the power combiner is not shown in Fig.8.1. The circulators protect the sample from the noise created at the input of the cryogenic amplifier (CryoAmp) as follows: While the signal from the directional coupler gets redirected to the CryoAmp, noise radiating from the CryoAmp is shunted to a ground which is thermalized at the mixing chamber. The circulators serve as a band-pass filter and merely signals with frequencies around  $f_0$ , the resonance frequency of the tank circuit, are amplified. We use two circulators with distinguished band-pass windows (200 to 220 MHz and 220 to 240 MHz). Therefore the components (mainly the inductance) of the tank circuit have to be chosen carefully such that  $f_0$  is inside the respective frequency window. After passing the circulators, the signals of the two tank circuits are combined in a power combiner and then amplified by 56 dB with a cryogenic amplifier (QuinStar<sup>17</sup> QCA-U-219-33H) mounted at the

---

<sup>14</sup>[www.pasternack.com](http://www.pasternack.com)

<sup>15</sup>[www.amphenol.com](http://www.amphenol.com)

<sup>16</sup>[www.minicircuits.com](http://www.minicircuits.com)

<sup>17</sup>[www.quinstar.com](http://www.quinstar.com)

4 K flange. The CryoAmp is an active element and must be powered<sup>18</sup> as well as controlled by an external control unit placed at room temperature. Therefore, 12 additional twisted pair cables (phosphor-bronze) are fit from room temperature to the 4 K flange to supply the CryoAmp (see Fig. 8.1). Finally, the amplified signal is routed to room temperature and demodulated in an additional circuit before being measured with a spectrum analyzer. Currently, the demodulation circuit is still under development.

### 8.3 Characterisation of the coaxial lines

In spin resonance schemes, the spin rotation or Rabi frequency is controlled by the amplitude of the driving signal. To estimate the amplitude of the driving signal, it is essential to know the attenuation of the coaxial RF lines. In this section, we therefore show the attenuation spectrum of the semi-rigid coaxial lines installed in the XLD.

In Fig. 8.3a we show the transmission spectrum  $S_{21}$  of an installed coax line from the SMA connectors on top of the XLD to the SMP connectors on the PUCK flange. This measurement was performed with a vector network analyser at room temperature and the attenuation from the connecting cables was subtracted. Because the RF lines showed an identical transmission spectra, we only show it for one of the lines.

As expected, we find an attenuation offset of  $-49$  dB arising from the various cryogenic attenuators mounted at the different temperature stages of the XLD in order to thermalize the inner conductor of the coax (see Fig. 8.1). From the  $S_{21}$  spectra we extract an attenuation of 1 dB per GHz for frequencies  $f > 2$  GHz. The measured spectrum shows a very good agreement with the expected attenuation of a 1.6 m long cryogenic SC-086/50-SCN-CN (Coax CO.,LTD) coax. For this cryogenic coax the attenuation decreases at low temperatures. We therefore also show the expected spectrum of the coax at 4 K and find an attenuation of  $\sim 0.5$  dB per GHz.

The currently installed SMA interface is only specified for frequencies up to 18 GHz. But K-Type lines could be connected to two of the spare SMP connectors on the PUCK to increase

---

<sup>18</sup>The cryogenic amplifier consumes about 24 mW.

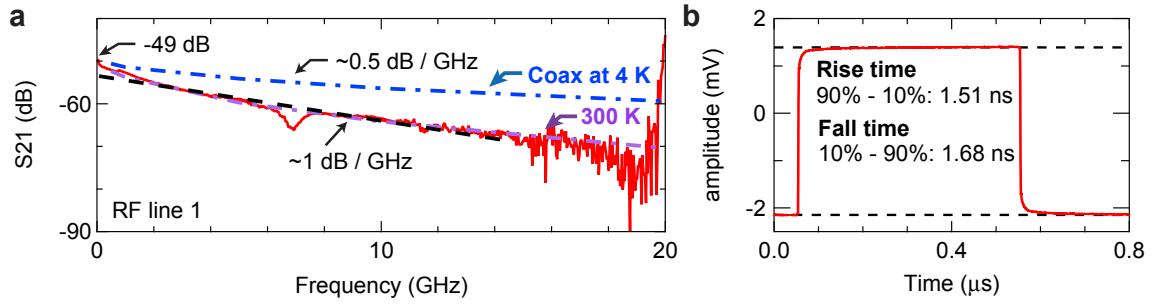


Figure 8.3: (a) The red data points show the transmission spectrum  $S_{21}$  of the XLD coax line 1 at room temperature. The attenuation offset of -49 dB matches the summed up attenuation of the cryogenic attenuators installed at the different temperature stages of the XLD. This data reflects the attenuation behavior of a 1.6 m semi-rigid cryogenic coax at room temperature (lower purple dashed curve). The blue dashed curve shows the predicted attenuation at 4 K. (b) Response to a step signal created with an arbitrary wave generator and measured with an oscilloscope from which the rise and fall time of a signal passing through the coaxial line is acquired.

the bandwidth up to 40 GHz.

To operate our spin qubits, we also need to apply fast rectangular voltage pulses. Therefore, we also measure the the rise and fall time of a rectangular voltage pulse signal created by an arbitrary waveform generator (Tektronix AWG7122C) using an oscilloscope. As presented in Fig. 8.3b, we obtain a signal rise time of 1.5 ns and a fall time of 1.7 ns respectively<sup>19</sup>.

## 8.4 Filterboard and RF PCB

From the CINCH connector on the PUCK, phosphor bronze wires are soldered to individual Precidip pin connectors. Compatible sockets are soldered at the input of the filter PCB. With this setup, the XLD DC lines connected to the BoB can be allocated to the PCB lines in the extracted PUCK without the need to open the cryostat.

In the present setup, the sample is not grounded when moving the probe into the XLD with the bottom loader. Only once the connection between the PUCK and mixing chamber CINCH connector is made, the sample becomes properly grounded. Therefore an additional filter board is mounted inside the PUCK to protect the sample from voltage spikes which can

<sup>19</sup>These numbers correspond to the rise (fall) time of the signal from 10% to 90% of the maximal (minimal) voltage of the trace.



occur while the floating PUCK is connected to the grounded lines of the fridge<sup>20</sup>.

The filter board is composed of two PCBs which are connected together with a pluggable Precidip pin-socket system. Each PCB has the capacity to filter 20 DC lines with two surface-mount component (SMC) based RC filters in series (see Fig. 8.1). After filtering, all 40 lines are combined in a 41-pin vertical FFC DC blade socket (JAE Electronics<sup>21</sup> FI-RE41S-HF) soldered to one of the two PCBs. The complete assembly of the two PCBs we call filter board. A FFC is used to connect the filter board with the main PCB (RF PCB) which hosts the sample. A computer model of the RF-PCB with the different electronic components and the housing is shown in Fig. 8.4a.

The RF-PCB is screwed to a copper back shield on which a sample holder has been screwed on beforehand. This sample holder is a rectangular copper cuboid with dimensions  $7 \times 2.9 \times 2.6$  mm such that it fits through a rectangular cutout in the RF-PCB. The sample is glued on the sample holder and then bonded. This systems allows to remove the sample holder when the sample is exchanged. To fully enclose the RF PCB, a copper RF shield is mounted on top of the back shield-RF PCB assembly. The complete unit is then screwed to the support rod structure of the PUCK. This enclosure serves as a Faraday cage shielding the sample from electromagnetic fields. It is also designed to limit the space close to the sample to shift possible cavity modes towards higher frequencies.

The RF PCB is fabricated on Rogers 3003, a laminate well-suited for RF applications due to its low dielectric loss and also eligible for low-temperature applications. A multilayer PCB with 4 individual layers was designed for which vertical interconnect access (via) technology was used to route the lines between the different layers as well as to interconnect the separated areas of the ground plane (white area in Fig. 8.4b).

This multilayer approach allows to assembly SMC capacitances serving as low pass filters for the DC lines and enables crossing of DC and RF lines which is necessary to evenly distribute the bond pads around the designated sample space. A schematic with all four

---

<sup>20</sup>Note that there is an alternative way to insert the PUCK with the sample grounded but this involves a second set of wires through the bottom loader inserting mechanism. But these connections are not physically removable and will lead to an excessive heat-load if not filtered properly.

<sup>21</sup>[www.jae.com](http://www.jae.com)

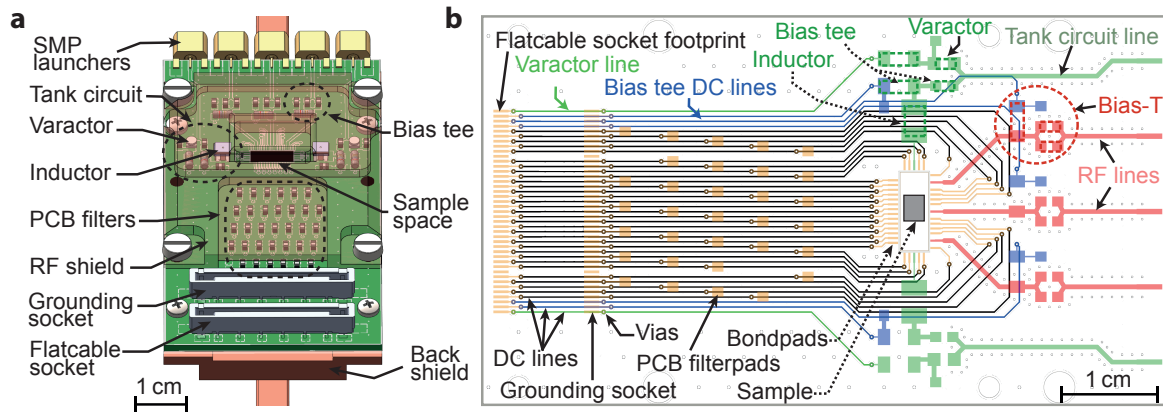


Figure 8.4: (a) Computer rendered model of the RF PCB mounted on a copper backshield enclosed by RF shield on the front side. In the render, the RF shield is made transparent. On top, SMP launchers are soldered to inject RF signals into the coplanar waveguides. The outer two RF lines are connected to tank circuits defined by a SMC inductor and the parasitic capacitance of the line together with the sample. A varactor is used to achieve impedance matching. Electrical pathways route the DC signals from the bottom flat cable socket to the bonding pads close to the sample. The grounding socket can be used to short all DC lines e.g. to ground the sample. (b) A schematic with superimposed layers of the multilayer PCB. From the left side the DC signals are routed from the flat cable socket and the RF signals are injected by SMP launchers (not shown) into coplanar waveguides shown on the right side. The RF lines are separated into tank circuit circuitry (green) and lines designated for the manipulation of spin qubits (red) when bonded to a sample gate electrode. The dashed rectangles at the upper RF lines, illustrate the position of SMCs for the bias-tees and tank circuits.

layers superimposed is shown in Fig. 8.4b.

On one side of the RF-PCB, a 41-pin vertical FFC DC blade socket (JAE Electronics FI-RE41S-HF) and a second, straight FFC DC blade socket (JAE Electronics FI-RE41S-VF) are mounted. The vertical socket is used to connect the FFC from the filter board while the second socket, marked as "grounding socket" in Fig. 8.4b, can be used to connect all DC lines to the ground by inserting a shorted FFC plug. It is convenient to short all lines to ground in order to protect the sample during bonding, transportation or storage.

On the opposite side of the board, SMP PCB launchers (Amphenol SMP-MSFD-PCE-1) are used to inject RF signals to the five coplanar wave guides. While the three launchers in the middle are designated to bring RF signals up to 18 GHz to the sample, the two launchers located at the side of the PCB are connected to the tank circuit and used for the reflectometry circuit operated at intermediate frequencies  $\sim 250$  MHz (Fig. 8.4b).

From here on, the discussion is separated into three parts: First the circuitry of the DC lines, then of the RF lines and at last the tank circuit is explained.

### **DC circuit on RF PCB**

Out of the 41 DC inputs at the FFC socket, 34 are directly routed to a bond-pad, five are coupled to the five RF lines over a bias tee and the remaining two are used to bias the two varactors. All DC lines are low-pass filtered on the PCB: For the 34 direct connections and the five bias tee DC input lines, a 100 pF capacitance to ground is added to not limit the bandwidth. The lines for biasing the varactors are filtered more ( $R \cdot C = 5 \text{ k}\Omega \cdot 330 \text{ pF}$ ). This additional filtering on the PCB is included to protect our sensitive samples from voltage spikes which might occur while handling the PCB without the filter board attached. Using a electrical circuit simulation software (OrCad P-Spice), we calculate the complete DC circuitry shown in Fig. 8.1 and estimate the characteristic frequency for an attenuation of 3 dB for the 34 direct connections to be  $f_{3dB} \sim 130 \text{ kHz}$ , limited by the bandwidth of the thermocoax and silver epoxy microwave filters. This bandwidth is sufficient to pulse quantum dot levels in a spin qubit operation by applying step pulses to the gate electrodes (see Chap. 3 and Chap. 4).

### **RF circuit on RF PCB**

Next, the RF circuit is explained. Bias tees are used to couple DC voltages to the high frequency circuits. To block DC signals from passing through the RF input of the bias tee, two capacitances of 22 pF and 15 nF are placed in parallel (see Fig. 8.1). To avoid RF signals on the DC lines, a resistor (9.1 k $\Omega$ ) is placed at the DC input of the bias tee. As the impedance of this resistor  $Z_R$  is different from the characteristic impedance  $Z_0 \sim 50 \Omega$  of the RF circuit the signals get reflected at the bias tee. We estimate the reflection coefficient to be  $\Gamma = (Z_R - Z_0) / (Z_R + Z_0) \sim 0.98$ . This reflection could be improved by increasing the resistor on the DC input but this would, unfortunately, also further limit the bandwidth of the DC line. Together with the resistance at DC input, the capacitance at the RF input also forms a low-pass filter for the DC signal passing to the sample. Therefore, and in contrast to  $f_{3dB} \sim 130 \text{ kHz}$  of the 34 DC lines, the DC lines coupled via a bias tee have a rather low

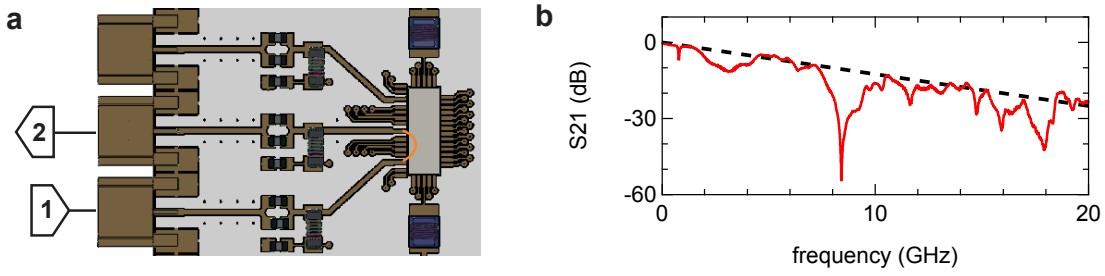


Figure 8.5: (a) Computer render graphic of the RF PCB showing the setup to measure the transmission spectrum  $S_{21}$  through two coplanar waveguides connected with a bonding wire at the bond pad as indicated by the orange curve. (b) The measured transmission spectrum  $S_{21}$ . The resonances most likely arise from the poor high frequency performance of the bonding wire. The black curve corresponds to  $\sim 1.25$  dB/GHz.

bandwidth of only  $f_{3dB} \sim 1$  kHz. To control spin qubits, it is often necessary to apply step pulses to the DC lines in addition to the RF signal. For example, it is preferred to pulse the spin qubit into Coulomb blockade to mitigate photon assisted tunneling of the electron out of the quantum dot when applying the RF signal to control the spin. Therefore, a larger bandwidth of the DC lines is generally preferred and the low bandwidth of the coupled lines has to be considered when designing an experiment. Here, we chose  $Z_R$  such that it gives a decent reflection while keeping a reasonable rise time.

We also measured the transmission spectrum through the coplanar waveguides of the PCB by connecting two RF lines together with a bonding wire at the bond pads as shown in Fig. 8.5. The measured data suggests an attenuation of  $\sim 1.25$  dB/GHz at room temperature. The resonances present in Fig. 8.5b are most likely stemming from the bonding wire. To mitigate such resonances, the bonding wire should be made short by placing the sample as close as possible to the bonding pads.

### Tank circuit on RF PCB

The two SMP launchers at the side of the RF-PCB are used for reflectometry in an intermediate frequency circuit. With a SMC wirewound ceramic chip inductor and the parasitic capacitance  $C_p$  on the order of pF, a tank circuit is formed. The resonance frequency is given by  $f_c = 1 / (2\pi\sqrt{C_p L})$  and thus the inductors are chosen such that the resonance frequencies of the tank circuits lie within the band-pass window of the two circulators. The exact value

of  $C_p$ , however, can vary between different samples such that the inductor must be adjusted. A varactor allows to tune the tank circuit impedance and match it to the characteristic impedance  $Z_0$  of the coaxial lines. The varactor or varicap (variable capacitance diode), is a type of diode whose capacitance is tunable with bias voltage, so a DC lines is needed for control (see Fig. 8.4b). A more detailed description of the tank circuit performance including the impedance matching with the varactors is given in Sec. 8.5.

## 8.5 Characterisation of tank circuits

In this section, we discuss and characterize the tank circuits which we use in our reflectometry setup (see Fig. 8.1). If the state of a qubit can be mapped to an impedance, such an electrical resonator setup can be used for fast read-out of a qubit state. For maximal sensitivity, it is essential to match the high impedance of the device to the impedance of connecting circuit. For spin qubit research, this matching is difficult because the parasitic capacitance is different for each sample due to different gate-layout, device architectures or materials. These effects can be mitigated by adding a matching capacitor and a decoupling capacitor [215]. In these scheme, for each parasitic capacitance there is a matching capacitance which leads to perfect matching. Here, we use the 100 pF capacitor from the bias tee as a decoupling capacitor and a voltage-tunable capacitor or varactor as a matching capacitor which allows *in situ* tuning to the matching condition for different parasitic capacitances.

We first focus on only one of the two tank circuits (Tank 1) without any sample attached. This tank circuit is defined by a SMC inductor with  $L = 470$  nH and the parasitic capacitance  $C_p$  of the RF-PCB.

We follow Ares et al. [215] and use a lumped element model to describe the circuit. A schematic is shown in Fig. 8.6a. Here, the inductor  $L$  is modeled as a network of elements to simulate self-resonances and losses. The network is composed out of an effective resistance through the coil  $R_L$  in front of the inductance  $L$ , both in parallel to a capacitance  $C_L$  and a resistor  $R_C$ . Other losses in the coil are modeled by the resistor  $R_{L2}$ . Due to the skin effect,  $R_L$  is frequency dependent and given by  $R_L = k \cdot \sqrt{f}$ , where  $k$  is a constant. For the

470 nH inductor (Coilcraft 1008CS-471) used, the values from the datasheet are  $L = 465$  nH,  $R_{L2} = 1.2 \Omega$ ,  $R_C = 31 \Omega$ ,  $C_L = 0.156$  pF and  $k = 4.27 \cdot 10^{-4} \Omega\text{Hz}^{-1/2}$ . In the model, we also include the resistance of  $9.1$  k $\Omega$  and capacitance of  $100$  pF of the bias tee. All other losses of the tank circuit are modeled with an effective resistance  $R$ . Further, the circuit includes the parasitic capacitance  $C_p$  and the tunable capacitance of the varactor  $C_{\text{var}}$ .

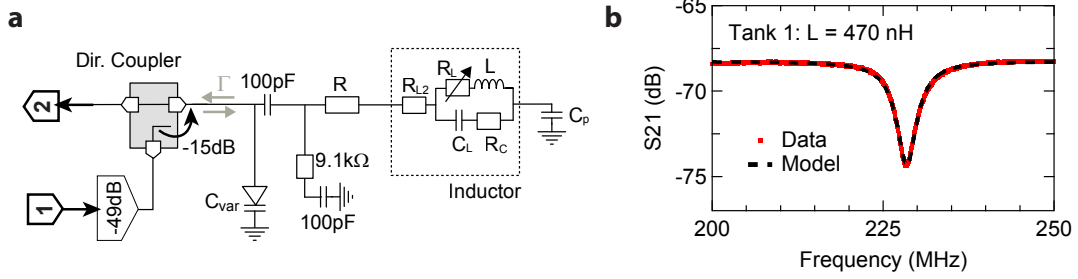


Figure 8.6: (a) Lumped element model of the tank circuit. Here, the inductor is divided into different impedance contributions specified in the main text. the capacitance  $C_{\text{var}}$  is tunable by biasing a varactor. To obtain the reflected signal of the tank circuit, a transmission measurement from port 1 through the directional coupler to port 2 is performed with a vector network analyzer. (b) Measurement of the transmission spectrum  $S_{21}$  (red dots) of the circuit described in (a) with  $L = 470$  nH without voltage bias applied to the varactor. At the resonance condition of the tank circuit ( $f_0 = 228.4$  MHz), a clear dip is recognized. A fit to the lumped element model described in (a) gives excellent agreement (black dashed curve).

In Fig. 8.6b we show a measurement probing the reflection of the tank circuit in a reflectometry setup using a directional coupler (see Fig. 8.6a). Here, no bias voltage is applied to the varactor such that its capacitance  $C_{\text{var}}$  is maximal<sup>22</sup>. We find a dip in the transmission spectrum at the resonance frequency of the tank circuit  $f_0 = 228.4$  MHz. At the resonance condition  $\omega L = 1/(\omega C)$  and therefore  $2\pi f_0 = 1/\sqrt{L \cdot C_p}$  from which we extract the parasitic capacitance  $C_p = 1.03$  pF.

To compare the model to our measurements we need to calculate the reflection coefficient  $\Gamma$  due to mismatch with the impedance of the transmission lines ( $Z_0 = 50 \Omega$ ) and the the total impedance  $Z_{\text{tot}}$  of the tank circuit [225]:

$$\Gamma(f) = \frac{Z_{\text{tot}}(f) - Z_0}{Z_{\text{tot}}(f) + Z_0}. \quad (8.1)$$

<sup>22</sup>In the datasheet, a maximal  $C_{\text{var}} \sim 30$  pF is specified.

The losses of the transmission lines and the directional coupler are taken into account by introducing an overall insertion loss constant  $A$  such that the transmission spectrum  $S_{21}$  is given by

$$|S_{21}(f)| = A |\Gamma(f)|. \quad (8.2)$$

In Fig. 8.6b, we show the fit of this model to the data and excellent agreement is found<sup>23</sup>.

We then change the impedance of the tank circuit  $Z_{tot}$  by biasing the varactors. In Fig. 8.7  $S_{21}$  for different bias voltages  $V_{var}$  applied to the varactors is shown for the tank circuit with  $L = 470$  nH (Fig. 8.7a) and  $L = 560$  nH (Fig. 8.7b), respectively.

Because of the higher inductance, the resonance frequency of the tank circuit with  $L = 560$  nH (Tank 2) is shifted to  $f_0 = 212.7$  Mhz for  $V_{var} = 0$ . For both tank circuits, the quality of the impedance match strongly depends on the bias voltage applied to the varactor. This rise in matching is recognized by the decrease of reflected signal due to increased energy absorption of the tank circuit at the resonance condition. The reflectometry measurements indicate a minimum of the reflected power for a varactor bias voltage near 1.8 V.

We fit the data of Fig. 8.7a,b to the circuitry model presented in Fig. 8.6b and find excellent agreement. From the fits we obtain a general loss  $A \sim -68.5$  dB, in good agreement with the -49 dB from the attenuators in addition to -15 dB from the directional coupler and some small, additional attenuation arising from the flexible coax cables used perform the measurement.

For the best matched situation, a lossy element of  $R \sim 12 \Omega$  and a parasitic capacitance  $C_p \sim 0.9$  pF is obtained for the tank circuit with  $L = 470$  nH. For the other tank circuit, the fit<sup>24</sup> results in  $C_p \sim 1.08$  pF and the same  $R \sim 12 \Omega$ .

We calculate the quality factor  $Q$  of the tank circuit according to  $Q = \frac{1}{R} \sqrt{\frac{L}{C}} \sim 60$ . This is in good agreement with the specified quality factor  $Q \sim 65$  of the inductors and indicates that the inductor is limiting the quality of the tank circuit.

In agreement with the model, we find that the parasitic capacitance  $C_p$  shows only a negligible

<sup>23</sup>Note that  $S_{21}$  signal which was measured by the vector network analyzer is the power attenuation  $P_{in}/P_{out} = (V_{in}/V_{out})^2$ .

<sup>24</sup>For Tank 2 with  $L = 560$  nH we used the lumped element network model parameters of the Coilcraft 1008CS-561 inductor.

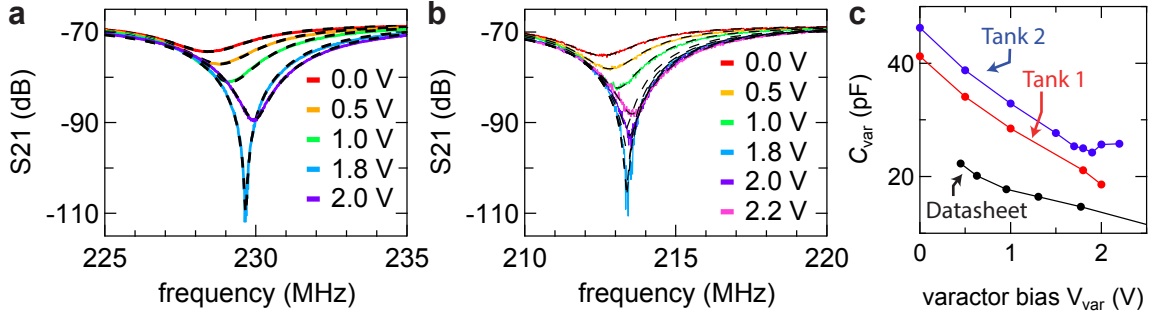


Figure 8.7: (a),(b) The reflected signal of the tank circuit with  $L = 470$  nH (a) and  $L = 560$  nH (b) for different bias voltages  $V_{\text{var}}$  applied to the varactor indicated by the color of the traces. The dashed lines show fits according to the lumped element network model presented in Fig. 8.6a. (c) Extracted varactor capacitance  $C_{\text{var}}$  of Tank 1 ( $L = 470$  nH) and Tank 2 ( $L = 560$  nH) from fits to the data shown in (a) and (b) for different  $V_{\text{var}}$ . The capacitance is off by a factor of two from the value specified in the datasheet (black curve).

dependence on the voltage applied to the varactor. Because only the impedance matching to the external circuitry and not the internal quality of the tank circuit is changed with the varactor, no significant dependence of the lossy element  $R$  on the varactor bias is noticed.

At last, a varactor capacitance of  $C_{\text{var}} = 21$  pF results from the fit for the tank circuit with  $L = 470$  nH. In the datasheet for the varactor (Macom MA46H204), at a bias voltage of 1.8 V where the best impedance matching is achieved and this data is taken, only half of the fitted capacitance ( $C_{\text{var}} \sim 14$  pF) is specified. However, using this capacitance leads to a very poor fit.

In Fig. 8.7c we show the extracted  $C_{\text{var}}$  as a function of  $V_{\text{var}}$  for both tank circuits. When compared to the capacitance-voltage behavior specified in the datasheet, the trend of  $C_{\text{var}}$  is reproduced but the measured values are off by a factor of about two. This discrepancy is subject to current investigations.

### 8.5.1 Parasitic capacitance with a Ge/Si core-shell nanowire sample

Up to now, the tank circuits were analysed without any sample connected. Next, we connect both tank circuits to gates of a Germanium-Silicon (Ge/Si) core-shell nanowire quantum dot device as described in Chap. 6 and Froning *et al.* [226]. A schematic of the device is shown



in Fig. 8.8a. This device was fabricated on top of heavily boron-doped ( $p^{++}$ ) silicon which serves as a back-gate. The back-gate is separated by  $290 \pm 15$  nm of dry, thermal silicon oxide ( $\text{SiO}_2$ ). Titanium palladium gates are put on top of the  $\text{SiO}_2$  by means of electron beam lithographic nanofabrication. Next, a 10 nm  $\text{Al}_2\text{O}_3$  layer is grown by atomic layer deposition. With a micromanipulator, a germanium-silicon core shell nanowire is placed on top of the gates and contacted. Two gates are bonded to the bonding pads of the tank circuits. As before, we used inductors with 470 nH and 560 nH for the tank circuits (see Sec. 8.5).

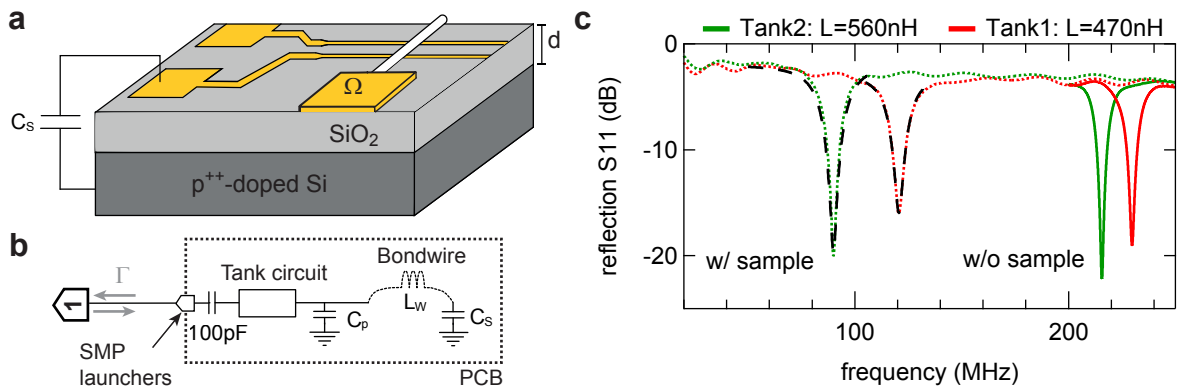


Figure 8.8: (a) Schematic of the Ge/Si nanowire double quantum dot sample used to study the influence of the sample on the tank circuit.  $C_S$  is the capacitance between the gate structure and the  $p^{++}$ -doped Silicon back gate and  $d$  is the height of the  $\text{SiO}_2$  layer. (b) Lumped element network model of the circuit. (c) Spectrum of the reflected signal  $S_{11}$  of both tank circuits with and without the sample bonded to bond pad connected to the tank circuits. Due to the additional parasitic capacitance stemming from the sample,  $C_S$ , a shift of the resonance frequencies is observed when the sample is connected.

The schematic of the circuit is presented in Fig. 8.8a. In contrast to the measurements in Sec. 8.5, no directional coupler was used here and the reflected signal  $S_{11}$  of the lines connected to the tank circuit is measured with a vector network analyzer (Agilent N5230A PNA-L). In these measurements, the varactors were not used. We find the resonance frequencies at 120.4 MHz and 90.0 MHz. Without the sample bonded the resonance frequencies for the tank circuits were at 215.61 and 229 MHz – slightly different than for the previous measurement presented in Fig. 8.7. We understand the decrease of the resonance frequency for the situation when the sample is bounded by a large increase of the total parasitic capacitance.

We estimate the self-inductance<sup>25</sup> of the  $\sim 2.5$  mm long bond wire with a diameter of  $32 \mu\text{m}$  to be  $L_W \sim 2.5$  nH. By expanding the model introduced in Sec. 8.5 by including the wire inductance  $L_w$  and the parasitic capacitance of the sample  $C_S$  (see Fig. 8.8a) we get decent fits to the data as shown in Fig. Fig. 8.8c. For the tank circuit with  $L = 470$  nH we obtain an additional capacitance  $C_S \sim 2.8$  pF while the tank circuit with  $L = 560$  nH gives an even larger  $C_S \sim 6.3$  pF. We assume that  $C_S$  is dominated by the capacitance of the titanium palladium gate structure to the  $\text{p}^{++}$  doped silicon back gate. By looking at geometric area of the gates, we estimate the area of a single gate to be between  $40'000$  and  $50'000 \mu\text{m}^2$ . Using a plate capacitor model we calculate a geometrical capacitance of  $\sim 5$  pF which is comparable to the values obtained in the measurement<sup>26</sup>. The same parasitic capacitance of the PCB  $C_p \sim 1$  pF as in Sec. 8.5 was obtained from fitting the expanded model (see Fig. 8.8a) to the reflected spectrum of the tank circuits with a bonded sample. When the tank circuits were designed, this large additional capacitance of samples with back-gates was not considered. We assumed that the parasitic capacitance would be completely dominated by the PCB ( $C_p \gg C_S$ ). The large shift due to  $C_S$ , however, shifted the resonance frequencies out of the band pass window of the circulators (200 to 220 MHz respectively 220 to 240 MHz) and the cryogenic amplifier (194 to 244 MHz). It was therefore not possible to test the tank circuits in the XLD at low temperature with a sample.

In the short term, we will replace the inductors such that the resonance frequency lies within the frequency window of the setup when the sample is connected. However, this might be a difficult task which requires a lot of fine tuning given the large difference of the two  $C_S$  measured. In the medium term, we plan to fabricate samples on undoped silicon substrates to mitigate the additional contribution to the parasitic capacitance. This might also be beneficial for the spin qubit coherence time because less charge noise is arising from the substrate.

<sup>25</sup>The self-inductance of a wire with length  $l$  and diameter  $d$  is  $L_w = 2l \left( \ln \left[ \left( \frac{2l}{d} \right) \left( 1 + \sqrt{1 + \left( \frac{d}{2l} \right)^2} \right) \right] - \sqrt{1 + \left( \frac{d}{2l} \right)^2} + \left( \frac{\mu}{4} \right) + \left( \frac{d}{2l} \right) \right)$  [227]. The permeability  $\mu$  is assumed to be 1.

<sup>26</sup>We ignore the  $\text{Al}_2\text{O}_3$  layer and use  $\epsilon_r = 3.9$  of  $\text{SiO}_2$

## 8.6 Discussion and Outlook

In this chapter, we presented the components and performance of the different parts of a low-temperature setup designated to operate spin qubits in the future. An overview of the circuitry is given in Fig. 8.1. On a RF-PCB a total of 39 pads are available to bond to a sample. Three of these pads are coupled RF lines which can provide signals up to 18 GHz. Another two pads are connected to a tank-circuit which is read-out with a reflectometry setup. The reflection of both tank circuits is probed by a directional coupler connected to a circulator before the signals are combined and passed to a cryogenic amplifier.

Low frequency (DC) signals are provided to the sample mounted and bonded to the RF-PCB via thermocoaxes, additionally filtered by silver epoxy MW filters [97]. Measurements of a Coulomb blockade thermometer [135] in another PUCK suggest an electron temperature of  $\sim 18$  mK at a base temperature  $\sim 10$  mK when only DC lines are connected to the sample. We assume that this temperature will increase when RF lines are connected to the sample. Nevertheless, such a low electron temperature is impressive when considering that only one stage of silver epoxy MW filters is used for cooling the charge carriers. Using the DC circuitry of this setup, we were able to perform the experiment presented in Chap. 6 on a Ge/Si core-shell nanowire quantum dot sample installed on the RF-PCB at base temperature.

In the experiment mentioned, we also tried to apply RF signals to the confinement gates to perform electric dipole induced spin resonance (EDSR) in order to lift the Pauli spin blockade in the double dot system [42, 43]. During this experiment, we realized that only RF signals with frequencies up to  $\sim 2$  GHz could be delivered to the sample but higher frequencies would be attenuated too much. And, as a consequence, we were not able to measure the EDSR response. We first suspected a problem with one of the connectors. But poor electrical connection usually leads to a capacitance for which, in contrast to our observation, the impedance decreases with frequency. Further, the same behavior was observed when applying the RF signal to other gate electrodes connected to different RF lines. Therefore, we concluded that the failure of a single connector is a very unlikely source of this problem. Later, we tested all RF components of the PUCK but could not yet find any issue there. At the moment,

we suspect that the additional attenuation from the flexible coax cables used to connect the setup and from the PCB results lead to such a large attenuation that barely any signal can be delivered above 2 GHz. We therefore removed 20 dB of attenuation and will also use shorter flexible coax cables in the future.

In another cooldown, using a different Ge/Si sample, we tried to achieve dispersive read-out using the reflectometry setup but we could not find the tank circuit resonance with the spectrum analyzer. Later and as discussed in Sec. 8.5.1, tests at room temperature showed that the resonance frequencies of the tank circuits shift outside of the band-pass windows of the circulators when a sample is connected. We suspect that a large additional parasitic capacitance arises from the mutual capacitance between the gate structure of the sample and the  $p^{++}$  doped silicon back gate embedded in the substrate. To avoid this frequency shift, we plan to fabricate devices on substrates without any doping.

In short term and in order to use the reflectometry setup for Ge/Si samples already fabricated, we will change the inductors to adjust the resonance frequency accordingly. On the positive side, we were able to match the impedance of the tank circuit with the external circuit using a varactor. While the measurements presented in this chapter were performed at room temperature, we obtained comparable results when the RF PCB was cooled down to 4 K. Therefore, we assume that the reflectometry setup is working once the problem with the parasitic capacitance of the sample is solved.

At last, we give some ideas to improve the next generation of the RF PCB. In the current design, the SMP launchers are soldered to the RF PCB at a very small extension of the adapter (see Fig. 8.4). To match the mounting instructions, the PCB should be cut such that the launchers can be embedded into the board. In the current design, the SMP connectors are mechanically unstable and can detach due to the force applied a coaxial cable is plugged. To increase stability, we glued all five SMP launchers to the RF PCB using Stycast 2850 epoxy. Most likely, the improper installation is also negatively affecting the general RF performance of the SMP launchers.

An conceptional improvement of a new board is to start using a daughter board. Currently, the sample is removed from the RF PCB by cutting the bonding wire before the copper

sample holder can be unscrewed. Because this increases the chance of damaging the sensitive sample, it would be beneficial bond the sample on a exchangeable, cheap daughterboard which is then mounted on a more complex, expensive motherboard which carries all the exhaustive electronics. Such a system was proposed and realised in Ref. [228] and will become convenient when the sample is often exchanged.

## 9 Summary and Outlook

In this thesis, the physics of three different quantum dot systems was investigated: lateral GaAs quantum dots, quantum dots in germanium-silicon core-shell nanowires (Ge/Si NW), and quantum dots in a silicon fin field-effect transistor (FinFET). In this section, the findings of the individual projects are shortly summarized, and an outlook on the different projects is presented.

### 9.1 Lateral GaAs quantum dots

For the experiments in GaAs quantum dots discussed here, it was essential to understand the confinement of the quantum dot. Therefore, a new spectroscopy tool was developed to obtain the three dimensional confinement potential landscape of a lateral GaAs single electron quantum dot. With this method, the confinement of the electron wave function in the quantum dot is measured indirectly by probing the mixing of the quantum dot orbitals, which is recognized through the dependence of the orbital energies on the strength and direction of an in-plane magnetic field. In this device, the layout of the fabricated surface gates was optimized to control the shape of the quantum dot. This enabled tuning of the confinement potential, such that a rotationally symmetric, circular confinement of the quantum dot in the plane of the 2DEG could be achieved.

In such a symmetric quantum dot, the effect of the orbitals on the spin relaxation is mitigated, such that the experimentally observed spin relaxation anisotropy could be attributed to the interplay of Rashba and Dresselhaus spin-orbit interaction (SOI) known to be present in GaAs 2DEGs. Because of the comprehensive understanding of the investigated system, the strengths of those two types of SOI are the only free parameters of the theoretical model, which was fit to the spin relaxation data. As a result, the absolute magnitudes and relative signs of the Rashba and Dresselhaus SOI were obtained in a GaAs quantum dot for the first time.

At lower magnetic field strengths, the spin relaxation rate was found to be larger than ex-

pected from a SOI model, which indicates the opening of an additional relaxation process. This process was found to be isotropic and showed an appropriate field scaling of the spin relaxation rate, such that it was concluded that hyperfine induced phonon mediated spin relaxation was demonstrated for the first time. In this process, the hyperfine replaces spin-orbit as the interaction which mixes the orbital and spin degrees of freedom to facilitate spin relaxation. Experimentally limited by the magnetic field necessary for reliable spin-to-charge conversion, a maximal spin relaxation time of  $57 \pm 15$  s was measured – hence reclaiming the record of the spin lifetime in a nanostructure device from phosphorus atom quantum dots embedded in silicon [36] .

The knowledge gained on the quantum dot orbitals and SOI in our devices from the previous experiments encouraged the development of a theoretical framework to describe isotropic and anisotropic corrections to the GaAs bulk g-factor due to different types of SOI [4]. In a subsequent experiment, the corrections of the g-factor were found to be in good agreement with the theoretical predictions. While exciting results on the g-factor anisotropy in GaAs are already presented in this thesis, this project is still ongoing. Additionally, it would be interesting to investigate the g-factor of the excited orbital states, which are predicted to show a shape-dependent directional dependence that is qualitatively different from the ground state [4].

For a long time, GaAs was the workhorse of the spin qubit community. Due to short coherence times limited by the nuclear spins in group III-V compound semiconductors [33, 34, 43], however, the main focus of spin qubit research shifted towards group V systems, such as silicon and germanium [40, 165, 174].

Given the still unmatched mobilities in GaAs 2DEGs, and due to the decade long experience in the nanofabrication of lateral GaAs devices, GaAs could still become the material of choice to investigate fundamental physics in quantum simulation-type experiments. As a recent example, a linear quantum dot array device fabricated on GaAs was used to investigate the Fermi-Hubbard model [229]. Further, individual control of the inter-dot coupling was demonstrated in a  $2 \times 2$  quantum dot array device [230]. This is an important step towards coupling quantum dots in a two-dimensional arrangement, which is necessary for implementation of

the surface code. Systems of a few coupled quantum dots are already interesting because they can be used to form artificial molecules. The aforementioned excited state spectroscopy could be extended to such coupled, non-linear, multi-dot arrays to investigate the orbital physics of these artificial molecules. In analogue to 'electronics' and 'spintronics', experiments focused on the orbital degrees of freedom of coupled quantum dots could potentially open the door to a new 'orbitronics' field of research.

While experiments in other materials struggle to obtain stable spin qubits, GaAs devices are usually very reliable. Therefore, they can be used to prove general concepts, which can later be transferred to other systems. In Ref. [231] for example, we showed that a machine learning algorithm can be used to train computers how to automatically form quantum dots in a GaAs device. This technique might be very beneficial to tune large quantum dot arrays when scaling up spin qubit processors. While in this experiment, the data which was fed to the algorithms was obtained by measuring the transport through the quantum dot, extending this procedure to tuning the quantum dot from a charge-sensing signal is currently being worked on.

## **9.2 Ge/Si NW quantum dots and towards a direct Rashba spin-orbit interaction driven hole spin qubit**

One of the main results obtained in the aforementioned experiments in GaAs quantum dots is that at low magnetic field strengths not only the spin coherence time  $T_2$  but also the spin relaxation time  $T_1$  is limited by hyperfine interaction. However, it is mostly the rather short  $T_2$  time found in these system, which shifted the focus of the spin qubit research from GaAs towards other materials, in which longer spin coherence times are possible. In contrast to group III-V compounds such as GaAs, group V semiconductors such as silicon or germanium are intrinsically almost free of nuclear spins and can be isotopically purified to achieve a nuclear spin free host substrate for the spin qubits. Another way to increase coherence is to encode spin qubits into holes because those are much less susceptible to the contact hyperfine interaction with the nuclear spins, due to minima of the wave function at the position of the



nuclei. An additional benefit of using holes is that they experience strong SOI, which allows for fast, all-electrical spin manipulation by electric dipole-induced spin resonance (EDSR).

In the project presented in this thesis, both approaches are combined by forming hole quantum dots in a Ge/Si NW [226]. Here, an anisotropic leakage current through such a hole quantum dot system in Pauli spin blockade (PSB) was observed. This observation is explained with a phenomenological model, which uses an anisotropic g-factor [54, 86] in combination with a spin-orbit field [160]. Currently, it is not clear if the observed spin-orbit field is of direct Rashba type. While conventional Rashba SOI is also tunable with electric fields [56], the direct Rashba SOI (DRSOI) is predicted to show a much larger tunability. The investigated device featured two side gates, which allowed the control of an additional external electric field without changing the potential of the QD. While an effect of the side gate voltage on the leakage current was observed for certain directions, it was not possible to show if this effect was attributed to control of DRSOI or an inadvertent tuning of the tunnel barriers. Given the geometry of the device, it is speculated that the electric field which could lead to DRSOI predominately arises from the confinement gates and the electric field from the side gates would only lead to a slight tilt of the DRSOI field direction. Hence, a strong dependence of the leakage current on the voltages applied on the confinement gates would be an indication of the emergence of DRSOI. Unfortunately, it was not possible to significantly change the voltages on those confinement gates without changing the confinement of the double quantum dot.

Currently, the next milestone of this project remains to prove and study the predicted emergence of DRSOI in those Ge/Si NW devices. In the near future, it is planned to implement charge sensing for single-shot readout either by gate rf-reflectometry [218–222] or by an adjacent a charge sensor [207, 232]. Further, it would be interesting to couple the hole-spin qubit to a cavity resonator for circuit quantum electrodynamics experiments [50, 233].

The most promising way to show the presence of DRSOI is to show a dependence of the spin-flip or Rabi frequency on the side-gate voltage in an EDSR scheme. In such a setup, spin-flip times as short as  $\sim 100$  ps are predicted due to the large strength of the DRSOI [2]. As a comparison, recently a spin-flip time of  $\sim 7$  ns was demonstrated in a germanium hole

spin qubit without DRSOI [166]. For electrons, a spin-flip time of 10 ns was reported in a spin qubit hosted in an InSb nanowire – a system which is well known for its strong SOI [47]. An alternative way to demonstrate DRSOI is to investigate the external electric field dependence of the singlet-triplet anti-crossing in a magnetic field of a two-hole single quantum dot [234]. This anti-crossing is a consequence of the SOI-induced mixing of the singlet and  $T^+$  state<sup>27</sup>.

A third possibility to experimentally establish DRSOI is by measuring the magnetoconductance corrections in a Ge/Si NW. In this experiment, the weak anti-localization signature is expected to be dominated by DRSOI and, therefore, to depend on the electric field created by the side gates. In a similar experiment, a large SOI energy and an electrostatic controllability of the SOI strengths was found in a Ge/Si NW, which indicates the presence of DRSOI [53]. Therefore, Ge/Si NWs remain among the most promising platforms for fast spin-orbit qubits.

### 9.3 Towards a scalable, all-electrically controllable hole spin-orbit qubit

Our Ge/Si NW devices already allow for the formation of stable single, double, and triple quantum dots [226], and investigate spin related effects. While a considerable amount of fundamental physics and proof of principles can be shown in this system, such a qubit is currently not conceived to be scalable because each NW has to be placed manually. The ambipolar silicon FinFET project, conversely, is still at the very beginning but has the potential to result in a fast and industrially scalable hole spin qubit. Up to now it was shown that these devices can be operated in the hole and electron regime either as a classical field-effect transistor or as a single-electron transistor.

More than fifty percent of the devices such as the one measured in Chap. 7 showed severe leakage from the TiN lead gates to the NiSi contacts because the insulating SiO<sub>2</sub> separating these structures was inadvertently etched during fabrication (see Fig. 7.1). This problem

---

<sup>27</sup>Here,  $T_+$  describes the triplet state, which is energetically lowered with applied magnetic field and eventually becomes the two-electron ground state.

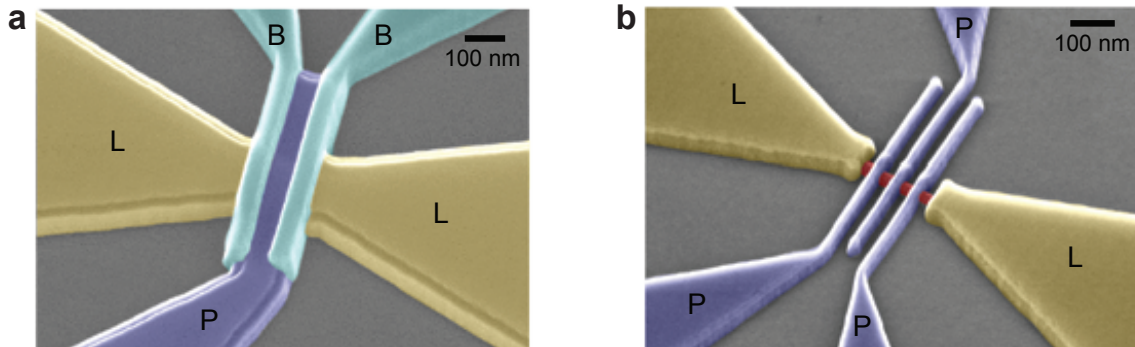


Figure 9.1: False colored SEM image of a prototype device with a single plunger gate P (dark blue) and two barrier gates B (light blue) that allow to adjust the tunnel coupling to the leads L (yellow). (b) A device with three plunger gates for formation of a triple quantum dot along the fin (reddish color)

can be mitigated by replacing the wet etch with a dry etch process and by reducing the thickness of the oxide such that less applied voltage on the lead gates is required. With these fabrication optimization measures, the yield of the new generation of FinFET spin qubit devices is expected to be significantly better.

At the moment, additional adjustments in the design and fabrication procedure of these devices are being implemented and examined. The next milestone of this project, will be to fabricate and measure a double quantum dot device with an additional gate layer which allows independent control of the tunnel barriers. A scanning electron microscope (SEM) image of a single quantum dot prototype device fabricated with a multi-layer gate stack is presented in Fig. 9.1a. Also, devices with multiple plunger gates were already successfully fabricated. In Fig. 9.1b, an SEM image of such a triple quantum dot array prototype device is shown.

The fin of the next generation of devices will be fabricated along the [110] crystal direction for which a much stronger SOI of direct Rashba type was recently predicted [6]. In a first step, the external electric field, which will introduce DRSOI is provided by the plunger gate. However, for the future, the implementation of side-gates is conceivable and would allow to electrically switch the qubit between an 'idle', 'EDSR' and 'cavity' state by controlling the DRSOI strength as proposed in Ref. [2]. From the Ge/Si project it is known that such side gates can be fabricated close to the fin or NW, such that sizable electric field strengths of a

few  $V/\mu\text{m}$  can be induced.

Future devices will be fabricated with a buried oxide layer (BOX) produced by silicon-on-insulator technology, which will result in a better confinement of the wave function in the vertical direction [158, 165]. This BOX also allows for the implementation of a back gate, which can be used as a global plunger gate or to accumulate charge carriers, such that the devices can be operated in depletion mode. Additionally, the BOX will facilitate fabrication because it serves as an edge stop when defining the fin. It will also lead to a better electrical insulation of individual devices on the same chip.

Because the goals are very similar, at this stage the rough research plan of the FinFET project is very similar to the Ge/Si project. Once stable few-electron/hole spin qubit devices are achieved, characterizing the spin-orbit interaction by lifting the Pauli spin blockade of a double quantum dot with electric dipole-induced spin resonance is planned [33]. With the same technique, the g-factor tensor and charge noise-induced spin decoherence will be investigated [75, 158].

In the next step of the project, charge sensing via gate-based rf-reflectometry will be implemented [216, 218–222, 235], and the devices will be coupled to a microwave cavity, where the strong coupling between the hole spin qubit and the cavity as well as strong coupling between multiple spin qubits via the cavity is planned for investigation [2]. In regards to coupling the spin qubits, it might be advantageous to implement coupling via floating gates technology [236] instead of a cavity. So far, this theoretical proposal has not been demonstrated experimentally but could, in principle, lead to a better scalability.

## Bibliography

- [1] D. Loss and D. P. DiVincenzo. *Quantum computation with quantum dots*. Phys. Rev. A **57**, 120 (1998).
- [2] C. Kloeffel and D. Loss. *Prospects for Spin-Based Quantum Computing in Quantum Dots*. Annu. Rev. Condens. Matter Phys. **4**, 51 (2013).
- [3] S. I. Erlingsson and Y. V. Nazarov. *Hyperfine-mediated transitions between a Zeeman split doublet in GaAs quantum dots: The role of the internal field*. Phys. Rev. B **66**, 155327 (2002).
- [4] P. Stano, C.-H. Hsu, M. Serina, L. C. Camenzind, D. M. Zumbühl, and D. Loss.  *$g$ -factor of electrons in gate-defined quantum dots in a strong in-plane magnetic field*. Phys. Rev. B **98**, 195314 (2018).
- [5] C. Kloeffel, M. Trif, and D. Loss. *Strong spin-orbit interaction and helical hole states in Ge/Si nanowires*. Phys. Rev. B **84**, 195314 (2011).
- [6] C. Kloeffel, M. J. Rančić, and D. Loss. *Direct Rashba spin-orbit interaction in Si and Ge nanowires with different growth directions*. Phys. Rev. B **97**, 235422 (2018).
- [7] G. E. Moore. *Cramming more components onto integrated circuits*. Electronics **38** (1965).
- [8] R. P. Feynman. *Simulating physics with computers*. International Journal of Theoretical Physics **21**, 467 (1982).
- [9] D. Deutsch. *Quantum Theory, the Church-Turing Principle and the Universal Quantum Computer*. Proceedings of the Royal Society A: Mathematical, Physical and Engineering Sciences **400**, 97 (1985).
- [10] D. P. DiVincenzo. *The physical implementation of quantum computation*. Fortschritte der Physik **48**, 771 (2000).

- [11] T. D. Ladd, F. Jelezko, R. Laflamme, Y. Nakamura, C. Monroe, and J. L. O'Brien. *Quantum computers*. Nature **464**, 45 (2010).
- [12] D. Wineland, C. Monroe, W. Itano, D. Leibfried, B. King, and D. Meekhof. *Experimental issues in coherent quantum-state manipulation of trapped atomic ions*. J. Res. Natl. Inst. Stan. **103**, 259 (1998).
- [13] R. Blatt and D. Wineland. *Entangled states of trapped atomic ions*. Nature **453**, 1008 (2008).
- [14] C. Nayak, S. H. Simon, A. Stern, M. Freedman, and S. Das Sarma. *Non-Abelian anyons and topological quantum computation*. Rev. Mod. Phys. **80**, 1083 (2008).
- [15] F. Wilczek. *Majorana returns*. Nat. Phys. **5**, 614 (2009).
- [16] V. Mourik, K. Zuo, S. M. Frolov, S. R. Plissard, E. P. A. M. Bakkers, and L. P. Kouwenhoven. *Signatures of majorana fermions in hybrid superconductor-semiconductor nanowire devices*. Science **336**, 1003 (2012).
- [17] E. J. Lee, X. Jiang, M. Houzet, R. Aguado, C. M. Lieber, and S. De Franceschi. *Spin-resolved Andreev levels and parity crossings in hybrid superconductor-semiconductor nanostructures*. Nat. Nanotechnol. **9**, 79 (2014).
- [18] M. T. Deng, S. Vaitiekenas, E. B. Hansen, J. Danon, M. Leijnse, K. Flensberg, J. Nygård, P. Krogstrup, and C. M. Marcus. *Majorana bound state in a coupled quantum-dot hybrid-nanowire system*. Science **354**, 1557 (2016).
- [19] J. Klinovaja and D. Loss. *Parafermions in an Interacting Nanowire Bundle*. Phys. Rev. Lett. **112**, 246403 (2014).
- [20] A. Hutter and D. Loss. *Quantum computing with parafermions*. Phys. Rev. B **93**, 125105 (2016).
- [21] F. Hassler. *Majorana Qubits*. Available at <http://arxiv.org/abs/1404.0897> (2014).

- 
- [22] Y. Nakamura, Y. A. Pashkin, and J. S. Tsai. *Coherent control of macroscopic quantum states in a single cooper pair box*. Nature **398**, 786 (1999).
- [23] J. Clarke and F. K. Wilhelm. *Superconducting quantum bits*. Nature **453**, 1031 (2008).
- [24] M. H. Devoret and R. J. Schoelkopf. *Superconducting circuits for quantum information: An outlook*. Science **339**, 1169 (2013).
- [25] The performance of all running IBM Q quantum devices is available at <https://www.research.ibm.com/ibm-q/technology/devices/>. Accessed January 2019.
- [26] B. E. Kane. *A silicon-based nuclear spin quantum computer*. Nature **393**, 133 (1998).
- [27] M. Ciorga, A. S. Sachrajda, P. Hawrylak, C. Gould, P. Zawadzki, S. Jullian, Y. Feng, and Z. Wasilewski. *Addition spectrum of a lateral dot from Coulomb and spin-blockade spectroscopy*. Phys. Rev. B **61**, R16315 (2000).
- [28] M. Field, C. G. Smith, M. Pepper, D. A. Ritchie, J. E. F. Frost, G. A. C. Jones, and D. G. Hasko. *Measurements of Coulomb blockade with a noninvasive voltage probe*. Phys. Rev. Lett. **70**, 1311 (1993).
- [29] J. M. Elzerman, R. Hanson, J. S. Greidanus, L. H. Willems van Beveren, S. De Franceschi, L. M. K. Vandersypen, S. Tarucha, and L. P. Kouwenhoven. *Few-electron quantum dot circuit with integrated charge read out*. Phys. Rev. B **67**, 161308 (2003).
- [30] W. Lu, Z. Ji, L. Pfeiffer, K. W. West, and A. J. Rimberg. *Real-time detection of electron tunnelling in a quantum dot*. Nature **423**, 422 (2003).
- [31] J. M. Elzerman, R. Hanson, L. H. W. van Beveren, B. Witkamp, L. M. K. Vandersypen, and L. P. Kouwenhoven. *Single-shot read-out of an individual electron spin in a quantum dot*. Nature **430**, 431 (2004).
- [32] R. Hanson, L. H. W. van Beveren, I. T. Vink, J. M. Elzerman, W. J. M. Naber, F. H. L. Koppens, L. P. Kouwenhoven, and L. M. K. Vandersypen. *Single-shot readout of electron spin states in a quantum dot using spin-dependent tunnel rates*. Phys. Rev. Lett. **94**, 196802 (2005).

- [33] F. H. L. Koppens, C. Buizert, K. J. Tielrooij, I. T. Vink, K. C. Nowack, T. Meunier, L. P. Kouwenhoven, and L. M. K. Vandersypen. *Driven coherent oscillations of a single electron spin in a quantum dot*. Nature **442**, 766 (2006).
- [34] J. R. Petta, A. C. Johnson, J. M. Taylor, E. A. Laird, A. Yacoby, M. D. Lukin, C. M. Marcus, M. P. Hanson, and A. C. Gossard. *Coherent manipulation of coupled electron spins in semiconductor quantum dots*. Science **309**, 2180 (2005).
- [35] S. Amasha, K. MacLean, I. P. Radu, D. M. Zumbühl, M. A. Kastner, M. P. Hanson, and A. C. Gossard. *Electrical control of spin relaxation in a quantum dot*. Phys. Rev. Lett. **100**, 046803 (2008).
- [36] T. F. Watson, B. Weber, Y.-L. Hsueh, L. C. L. Hollenberg, R. Rahman, and M. Y. Simmons. *Atomically engineered electron spin lifetimes of 30 s in silicon*. Sci. Adv. **3**, e1602811 (2017).
- [37] F. H. L. Koppens, K. C. Nowack, and L. M. K. Vandersypen. *Spin echo of a single electron spin in a quantum dot*. Phys. Rev. Lett. **100**, 236802 (2008).
- [38] F. K. Malinowski, F. Martins, P. D. Nissen, E. Barnes, Ł. Cywiński, M. S. Rudner, S. Fallahi, G. C. Gardner, M. J. Manfra, C. M. Marcus, and F. Kuemmeth. *Notch filtering the nuclear environment of a spin qubit*. Nat. Nanotechnol. **12**, 16 (2016).
- [39] E. Kawakami, P. Scarlino, D. R. Ward, F. R. Braakman, D. E. Savage, M. G. Lagally, M. Friesen, S. N. Coppersmith, M. A. Eriksson, and L. M. K. Vandersypen. *Electrical control of a long-lived spin qubit in a Si/SiGe quantum dot*. Nat. Nanotechnol. **9**, 666 (2014).
- [40] M. Veldhorst, J. C. C. Hwang, C. H. Yang, A. W. Leenstra, B. de Ronde, J. P. Dehollain, J. T. Muhonen, F. E. Hudson, K. M. Itoh, A. Morello, and A. S. Dzurak. *An addressable quantum dot qubit with fault-tolerant control-fidelity*. Nat. Nanotechnol. **9**, 981 (2014).
- [41] M. Veldhorst, C. H. Yang, J. C. C. Hwang, W. Huang, J. P. Dehollain, J. T. Muhonen, S. Simmons, A. Laucht, F. E. Hudson, K. M. Itoh, A. Morello, and A. S. Dzurak. *A two-qubit logic gate in silicon*. Nature **526**, 410 (2015).



- 
- [42] V. N. Golovach, M. Borhani, and D. Loss. *Electric-dipole-induced spin resonance in quantum dots*. Phys. Rev. B **74**, 165319 (2006).
- [43] K. C. Nowack, F. H. L. Koppens, Y. V. Nazarov, and L. M. K. Vandersypen. *Coherent control of a single electron spin with electric fields*. Science **318**, 1430 (2007).
- [44] S. Nadj-Perge, S. M. Frolov, E. P. Bakkers, and L. P. Kouwenhoven. *Spin-orbit qubit in a semiconductor nanowire*. Nature **468**, 1084 (2010).
- [45] M. D. Schroer, K. D. Petersson, M. Jung, and J. R. Petta. *Field tuning the  $g$  factor in InAs nanowire double quantum dots*. Phys. Rev. Lett. **107**, 176811 (2011).
- [46] S. Nadj-Perge, V. S. Pribiag, J. W. G. Van Den Berg, K. Zuo, S. R. Plissard, E. P. A. M. Bakkers, S. M. Frolov, and L. P. Kouwenhoven. *Spectroscopy of spin-orbit quantum bits in indium antimonide nanowires*. Phys. Rev. Lett. **108**, 166801 (2012).
- [47] J. W. Van Den Berg, S. Nadj-Perge, V. S. Pribiag, S. R. Plissard, E. P. Bakkers, S. M. Frolov, and L. P. Kouwenhoven. *Fast spin-orbit qubit in an indium antimonide nanowire*. Phys. Rev. Lett. **110**, 066806 (2013).
- [48] K. Takeda, J. Kamioka, T. Otsuka, J. Yoneda, T. Nakajima, M. R. Delbecq, S. Amaha, G. Allison, T. Kodera, S. Oda, and S. Tarucha. *A fault-tolerant addressable spin qubit in a natural silicon quantum dot*. Sci. Adv. **2**, e1600694 (2016).
- [49] J. Yoneda, T. Otsuka, T. Takakura, M. Pioro-Ladrière, R. Brunner, H. Lu, T. Nakajima, T. Obata, A. Noiri, C. J. Palmstrøm, A. C. Gossard, and S. Tarucha. *Robust micro-magnet design for fast electrical manipulations of single spins in quantum dots*. Appl. Phys. Express **8**, 084401 (2015).
- [50] C. Kloeffel, M. Trif, P. Stano, and D. Loss. *Circuit QED with hole-spin qubits in Ge/Si nanowire quantum dots*. Phys. Rev. B **88**, 241405 (2013).
- [51] X.-J. Hao, T. Tu, G. Cao, C. Zhou, H.-O. Li, G.-C. Guo, W. Y. Fung, Z. Ji, G.-P. Guo, and W. Lu. *Strong and tunable spin-orbit coupling of one-dimensional holes in Ge/Si core/shell nanowires*. Nano Lett. **10**, 2956 (2010).

- [52] A. P. Higginbotham, F. Kuemmeth, T. W. Larsen, M. Fitzpatrick, J. Yao, H. Yan, C. M. Lieber, and C. M. Marcus. *Antilocalization of Coulomb Blockade in a Ge/Si Nanowire*. Phys. Rev. Lett. **112**, 216806 (2014).
- [53] R. Wang, R. S. Deacon, J. Yao, C. M. Lieber, and K. Ishibashi. *Electrical modulation of weak-antilocalization and spin-orbit interaction in dual gated Ge/Si core/shell nanowires*. Semicond. Sci. Technol. **32**, 094002 (2017).
- [54] M. Brauns, J. Ridderbos, A. Li, E. P. A. M. Bakkers, and F. A. Zwanenburg. *Electric-field dependent g-factor anisotropy in Ge-Si core-shell nanowire quantum dots*. Phys. Rev. B **93**, 121408 (2016).
- [55] T. Heinzl. *Mesoscopic Electronics in Solid State Nanostructures* (Wiley-VCH Verlag GmbH, Weinheim, Germany, 2006).
- [56] F. Dettwiler, J. Fu, S. Mack, P. J. Weigele, J. C. Egues, D. D. Awschalom, and D. M. Zumbühl. *Stretchable persistent spin helices in GaAs quantum wells*. Phys. Rev. X **7**, 031010 (2017).
- [57] L. P. Kouwenhoven, T. H. Oosterkamp, M. W. S. Danoesastro, M. Eto, D. G. Austing, T. Honda, and S. Tarucha. *Excitation spectra of circular, few-electron quantum dots*. Science **278**, 1788 (1997).
- [58] L. P. Kouwenhoven, D. G. Austing, and S. Tarucha. *Few-electron quantum dots*. Reports on Progress in Physics **64**, 701 (2001).
- [59] J. D. Jackson. *Classical electrodynamics* (Wiley, New York, NY, 1999).
- [60] R. Hanson, L. P. Kouwenhoven, J. R. Petta, S. Tarucha, and L. M. K. Vandersypen. *Spins in few-electron quantum dots*. Rev. Mod. Phys. **79**, 1217 (2007).
- [61] C. C. Escott, F. A. Zwanenburg, and A. Morello. *Resonant tunnelling features in quantum dots*. Nanotechnology **21**, 274018 (2010).
- [62] D. E. F. Biesinger. *Thermally activated charge fluctuations in GaAs double quantum dots*. Ph.D. thesis, University of Basel (2014).

- [63] S. M. Reimann and M. Manninen. *Electronic structure of quantum dots*. Rev. Mod. Phys. **74**, 1283 (2002).
- [64] J. H. Davies, I. A. Larkin, and E. V. Sukhorukov. *Modeling the patterned two-dimensional electron gas: Electrostatics*. Journal of Applied Physics **77**, 4504 (1995).
- [65] J. J. Sakurai. *Advanced quantum mechanics* (Pearson Education, Incorporated, 1967).
- [66] J. J. Sakurai and J. Napolitano. *Modern Quantum Mechanics* (Addison-Wesley, 2011).
- [67] R. Winkler. *Spin-orbit coupling effects in two-dimensional electron and hole systems*, volume 191 of *Springer Tracts in Modern Physics* (Springer, 2003).
- [68] T. Schäpers. *Semiconductor Spintronics* (De Gruyter, 2016).
- [69] J. H. Prechtel, A. V. Kuhlmann, J. Houel, A. Ludwig, S. R. Valentin, A. D. Wieck, and R. J. Warburton. *Decoupling a hole spin qubit from the nuclear spins*. Nat. Mater. **15**, 981 (2016).
- [70] P. Fallahi, S. T. Yılmaz, and A. Imamoğlu. *Measurement of a Heavy-Hole Hyperfine Interaction in InGaAs Quantum Dots Using Resonance Fluorescence*. Phys. Rev. Lett. **105**, 257402 (2010).
- [71] M. I. Dyakonov. *Spin physics in semiconductors*, volume 157 of *Springer series in Solid-State Sciences* (Springer, 2008).
- [72] J. Phillips. *Bonds and bands in semiconductors* (Academic Press, 1973).
- [73] G. Dresselhaus. *Spin-Orbit Coupling Effects in Zinc Blende Structures*. Phys. Rev. **100**, 580 (1955).
- [74] R. Ferdous, K. W. Chan, M. Veldhorst, J. C. Hwang, C. H. Yang, H. Sahasrabudhe, G. Klimeck, A. Morello, A. S. Dzurak, and R. Rahman. *Interface-induced spin-orbit interaction in silicon quantum dots and prospects for scalability*. Phys. Rev. B **97**, 241401 (2018).

- [75] T. Tantt, B. Hensen, K. W. Chan, C. H. Yang, W. W. Huang, M. Fogarty, F. Hudson, K. Itoh, D. Culcer, A. Laucht, A. Morello, and A. Dzurak. *Controlling Spin-Orbit Interactions in Silicon Quantum Dots Using Magnetic Field Direction*. Phys. Rev. X **9**, 021028 (2019).
- [76] Y. A. Bychkov and E. I. Rashba. *Oscillatory effects and the magnetic susceptibility of carriers in inversion layers*. J. Phys. C **17**, 6039 (1984).
- [77] G. Bihlmayer, O. Rader, and R. Winkler. *Focus on the Rashba effect*. New J. Phys. **17**, 050202 (2015).
- [78] E. I. Rashba. *Symmetry of energy bands in crystals of Wurtzite type*. Sov. Phys.-Solid State **1**, 368 (1959).
- [79] J. M. Luttinger. *Quantum theory of cyclotron resonance in semiconductors: General theory*. Phys. Rev. **102**, 1030 (1956).
- [80] J. M. Luttinger and W. Kohn. *Motion of Electrons and Holes in Perturbed Periodic Fields*. Phys. Rev. **97**, 869 (1955).
- [81] N. O. Lipari and A. Baldereschi. *Angular momentum theory and localized states in solids. Investigation of shallow acceptor states in semiconductors*. Phys. Rev. Lett. **25**, 1660 (1970).
- [82] D. Csontos and U. Zülicke. *Large variations in the hole spin splitting of quantum-wire subband edges*. Phys. Rev. B **76**, 073313 (2007).
- [83] D. Csontos, P. Brusheim, U. Zülicke, and H. Q. Xu. *Spin-3/2 physics of semiconductor hole nanowires: Valence-band mixing and tunable interplay between bulk-material and orbital bound-state spin splittings*. Phys. Rev. B **79**, 155323 (2009).
- [84] W. Lu, J. Xiang, B. P. Timko, Y. Wu, and C. M. Lieber. *One-dimensional hole gas in germanium/silicon nanowire heterostructures*. Proc. Natl. Acad. Sci. USA **102**, 10046 (2005).

- 
- [85] P. Chuang, S. C. Ho, L. W. Smith, F. Sfigakis, M. Pepper, C. H. Chen, J. C. Fan, J. P. Griffiths, I. Farrer, H. E. Beere, G. A. Jones, D. A. Ritchie, and T. M. Chen. *All-electric all-semiconductor spin field-effect transistors*. Nat. Nanotechnol. **10**, 35 (2015).
- [86] F. Maier, C. Kloeffel, and D. Loss. *Tunable  $g$  factor and phonon-mediated hole spin relaxation in Ge/Si nanowire quantum dots*. Phys. Rev. B **87**, 161305 (2013).
- [87] L. C. Camenzind, L. Yu, P. Stano, J. D. Zimmerman, A. C. Gossard, D. Loss, and D. M. Zumbühl. *Spectroscopy of quantum dot orbitals with in-plane magnetic fields*. Phys. Rev. Lett. **122**, 207701 (2019).
- [88] O. Malkoc, P. Stano, and D. Loss. *Optimal geometry of lateral GaAs and Si/SiGe quantum dots for electrical control of spin qubits*. Phys. Rev. B **93**, 235413 (2016).
- [89] P. Scarlino, E. Kawakami, P. Stano, M. Shafiei, C. Reichl, W. Wegscheider, and L. M. K. Vandersypen. *Spin-relaxation anisotropy in a GaAs quantum dot*. Phys. Rev. Lett. **113**, 256802 (2014).
- [90] V. N. Golovach, A. Khaetskii, and D. Loss. *Phonon-induced decay of the electron spin in quantum dots*. Phys. Rev. Lett. **93**, 016601 (2004).
- [91] M. Pioro-Ladrière, T. Obata, Y. Tokura, Y.-S. Shin, T. Kubo, K. Yoshida, T. Taniguchi, and S. Tarucha. *Electrically driven single-electron spin resonance in a slanting Zeeman field*. Nat. Phys. **4**, 776 (2008).
- [92] M. A. Topinka, B. J. LeRoy, R. M. Westervelt, S. E. J. Shaw, R. Fleischmann, E. J. Heller, K. D. Maranowski, and A. C. Gossard. *Coherent branched flow in a two-dimensional electron gas*. Nature **410**, 183 (2001).
- [93] A. Pioda, S. Kičičin, T. Ihn, M. Sigrist, A. Fuhrer, K. Ensslin, A. Weichselbaum, S. E. Ulloa, M. Reinwald, and W. Wegscheider. *Spatially resolved manipulation of single electrons in quantum dots using a scanned probe*. Phys. Rev. Lett. **93**, 216801 (2004).
- [94] M. Stopa. *Quantum dot self-consistent electronic structure and the Coulomb blockade*. Phys. Rev. B **54**, 13767 (1996).

- [95] P. Stano, C.-H. Hsu, L. C. Camenzind, L. Yu, D. Zumbühl, and D. Loss. *Orbital effects of a strong in-plane magnetic field on a gate-defined quantum dot*. Phys. Rev. B **99**, 085308 (2019).
- [96] C. Barthel, M. Kjærgaard, J. Medford, M. Stopa, C. M. Marcus, M. P. Hanson, and A. C. Gossard. *Fast sensing of double-dot charge arrangement and spin state with a radio-frequency sensor quantum dot*. Phys. Rev. B **81**, 161308 (2010).
- [97] C. P. Scheller, S. Heizmann, K. Bedner, D. Giss, M. Meschke, , D. M. Zumbühl, J. D. Zimmerman, and A. C. Gossard. *Silver-epoxy microwave filters and thermalizers for millikelvin experiments*. Appl. Phys. Lett. **104**, 211106 (2014).
- [98] D. Maradan, L. Casparis, T.-M. Liu, D. E. F. Biesinger, C. P. Scheller, D. M. Zumbühl, J. D. Zimmerman, and A. C. Gossard. *GaAs quantum dot thermometry using direct transport and charge sensing*. J. Low Temp. Phys. **175**, 784 (2014).
- [99] D. E. F. Biesinger, C. P. Scheller, B. Braunecker, J. Zimmerman, A. C. Gossard, and D. M. Zumbühl. *Intrinsic metastabilities in the charge configuration of a double quantum dot*. Phys. Rev. Lett. **115**, 106804 (2015).
- [100] J. M. Elzerman, R. Hanson, L. H. Willems Van Beveren, L. M. K. Vandersypen, and L. P. Kouwenhoven. *Excited-state spectroscopy on a nearly closed quantum dot via charge detection*. Appl. Phys. Lett. **84**, 4617 (2004).
- [101] A. C. Johnson, J. R. Petta, J. M. Taylor, A. Yacoby, M. D. Lukin, C. M. Marcus, M. P. Hanson, and A. C. Gossard. *Triplet-singlet spin relaxation via nuclei in a double quantum dot*. Nature **435**, 925 (2005).
- [102] T. Fujisawa, Y. Tokura, and Y. Hirayama. *Transient current spectroscopy of a quantum dot in the Coulomb blockade regime*. Phys. Rev. B **63**, 081304 (2001).
- [103] R. Hanson, B. Witkamp, L. M. K. Vandersypen, L. H. W. van Beveren, J. M. Elzerman, and L. P. Kouwenhoven. *Zeeman energy and spin relaxation in a one-electron quantum dot*. Phys. Rev. Lett. **91**, 196802 (2003).

- [104] K. MacLean, S. Amasha, I. P. Radu, D. M. Zumbühl, M. A. Kastner, M. P. Hanson, and A. C. Gossard. *Energy-dependent tunneling in a quantum dot*. Phys. Rev. Lett. **98**, 036802 (2007).
- [105] P. Stano and P. Jacquod. *Spin-dependent tunneling into an empty lateral quantum dot*. Phys. Rev. B **82**, 125309 (2010).
- [106] F. Stern. *Transverse Hall effect in the electric quantum limit*. Phys. Rev. Lett. **21**, 1687 (1968).
- [107] V. I. Fal'ko and T. Jungwirth. *Orbital effect of an in-plane magnetic field on quantum transport in chaotic lateral dots*. Phys. Rev. B **65**, 081306 (2002).
- [108] D. M. Zumbühl, J. B. Miller, C. M. Marcus, V. I. Fal'ko, T. Jungwirth, and J. S. Harris. *Orbital effects of in-plane magnetic fields probed by mesoscopic conductance fluctuations*. Phys. Rev. B **69**, 121305 (2004).
- [109] D. M. Zumbühl, J. B. Miller, C. M. Marcus, D. Goldhaber-Gordon, J. S. Harris, K. Campman, and A. C. Gossard. *Conductance fluctuations and partially broken spin symmetries in quantum dots*. Phys. Rev. B **72**, 081305 (2005).
- [110] B. Schuh. *Algebraic solution of a non-trivial oscillator problem*. J. Phys. A **18**, 803 (1985).
- [111] I. M. Davies. *The propagator for a charged particle in a constant magnetic field and with a quadratic potential*. J. Phys. A **18**, 2737 (1985).
- [112] T. K. Rebane. *The anisotropic harmonic oscillator in a magnetic field*. Theor. Exp. Chem. **5**, 1 (1972).
- [113] S. Gustavsson, R. Leturcq, B. Simovič, R. Schleser, T. Ihn, P. Studerus, K. Ensslin, D. C. Driscoll, and A. C. Gossard. *Counting statistics of single electron transport in a quantum dot*. Phys. Rev. Lett. **96**, 076605 (2006).

- [114] L. Casparis, M. Meschke, D. Maradan, A. C. Clark, C. P. Scheller, K. K. Schwarzwalder, J. P. Pekola, , and D. M. Zumbuhl. *Metallic Coulomb blockade thermometry down to 10 mK and below*. Rev. Sci. Instrum. **83**, 083903 (2012).
- [115] S. D. Liles, R. Li, C. H. Yang, F. E. Hudson, M. Veldhorst, A. S. Dzurak, and A. R. Hamilton. *Spin filling and orbital structure of the first six holes in a silicon metal-oxide-semiconductor quantum dot*. Nat. Commun. **9**, 3255 (2018).
- [116] P. Stano and J. Fabian. *Orbital and spin relaxation in single and coupled quantum dots*. Phys. Rev. B **74**, 045320 (2006).
- [117] L. C. Camenzind, L. Yu, P. Stano, J. D. Zimmerman, A. C. Gossard, D. Loss, and D. M. Zumbuhl. *Hyperfine-phonon spin relaxation in a single-electron GaAs quantum dot*. Nat. Commun. **9**, 3454 (2018).
- [118] A. V. Khaetskii and Y. V. Nazarov. *Spin-flip transitions between Zeeman sublevels in semiconductor quantum dots*. Phys. Rev. B **64**, 125316 (2001).
- [119] T. A. Baart, M. Shafiei, T. Fujita, C. Reichl, W. Wegscheider, and L. M. K. Vandersypen. *Single-spin CCD*. Nat. Nanotechnol. **11**, 330 (2016).
- [120] T. Nakajima, M. R. Delbecq, T. Otsuka, P. Stano, S. Amaha, J. Yoneda, A. Noiri, K. Kawasaki, K. Takeda, G. Allison, A. Ludwig, A. D. Wieck, D. Loss, and S. Tarucha. *Robust single-shot spin measurement with 99.5% fidelity in a quantum dot array*. Phys. Rev. Lett. **119**, 017701 (2017).
- [121] P. Stano and J. Fabian. *Theory of phonon-induced spin relaxation in laterally coupled quantum dots*. Phys. Rev. Lett. **96**, 186602 (2006).
- [122] E. A. Chekhovich, M. N. Makhonin, A. I. Tartakovskii, A. Yacoby, H. Bluhm, K. C. Nowack, and L. M. K. Vandersypen. *Nuclear spin effects in semiconductor quantum dots*. Nat. Mater. **12**, 494 (2013).
- [123] D. M. Zumbuhl, C. M. Marcus, M. P. Hanson, and A. C. Gossard. *Cotunneling spectroscopy in few-electron quantum dots*. Phys. Rev. Lett. **93**, 256801 (2004).



- 
- [124] D. M. Zumbühl, J. B. Miller, C. M. Marcus, K. Campman, and A. C. Gossard. *Spin-orbit coupling, antilocalization, and parallel magnetic fields in quantum dots*. Phys. Rev. Lett. **89**, 276803 (2002).
- [125] T. Fujita, P. Stano, G. Allison, K. Morimoto, Y. Sato, M. Larsson, J. H. Park, A. Ludwig, A. D. Wieck, A. Oiwa, and S. Tarucha. *Signatures of hyperfine, spin-orbit, and decoherence effects in a Pauli spin blockade*. Phys. Rev. Lett. **117**, 206802 (2016).
- [126] A. Hofmann, V. F. Maisi, T. Krähenmann, C. Reichl, W. Wegscheider, K. Ensslin, and T. Ihn. *Anisotropy and suppression of spin-orbit interaction in a GaAs double quantum dot*. Phys. Rev. Lett. **119**, 176807 (2017).
- [127] D. V. Bulaev and D. Loss. *Spin relaxation and anticrossing in quantum dots: Rashba versus Dresselhaus spin-orbit coupling*. Phys. Rev. B **71**, 205324 (2005).
- [128] J. I. Climente, A. Bertoni, M. Rontani, G. Goldoni, and E. Molinari. *Phonon-induced electron relaxation in correlated quantum dots*. Phys. status solidi (c) **3**, 3660 (2006).
- [129] P. San-Jose, G. Zarand, A. Shnirman, and G. Schön. *Geometrical spin dephasing in quantum dots*. Phys. Rev. Lett. **97**, 076803 (2006).
- [130] P. Huang and X. Hu. *Electron spin relaxation due to charge noise*. Phys. Rev. B **89**, 195302 (2014).
- [131] F. Marquardt and V. A. Abalmassov. *Spin relaxation in a quantum dot due to Nyquist noise*. Phys. Rev. B **71**, 165325 (2005).
- [132] A. C. Clark, K. K. Schwarzwälder, T. Bandi, D. Maradan, and D. M. Zumbühl. *Method for cooling nanostructures to microkelvin temperatures*. Rev. Sci. Instrum. **81**, 103904 (2010).
- [133] A. V. Feshchenko, L. Casparis, I. M. Khaymovich, D. Maradan, O.-P. Saira, M. Palma, M. Meschke, J. P. Pekola, and D. M. Zumbühl. *Tunnel-junction thermometry down to millikelvin temperatures*. Phys. Rev. Applied **4**, 034001 (2015).

- [134] M. Palma, D. Maradan, L. Casparis, T.-M. Liu, F. N. M. Froning, and D. M. Zumbühl. *Magnetic cooling for microkelvin nanoelectronics on a cryofree platform*. Rev. Sci. Instrum. **88**, 043902 (2017).
- [135] M. Palma, C. P. Scheller, D. Maradan, A. V. Feshchenko, M. Meschke, and D. M. Zumbühl. *On-and-off chip cooling of a Coulomb blockade thermometer down to 2.8 mK*. Appl. Phys. Lett. **111**, 253105 (2017).
- [136] A. G. Huibers, J. A. Folk, S. R. Patel, C. M. Marcus, C. I. Duruöz, and J. S. Harris. *Low-temperature saturation of the dephasing time and effects of microwave radiation on open quantum dots*. Phys. Rev. Lett. **83**, 5090 (1999).
- [137] I. Karakurt, V. J. Goldman, J. Liu, and A. Zaslavsky. *Absence of Compressible Edge Channel Rings in Quantum Antidots*. Phys. Rev. Lett. **87**, 146801 (2001).
- [138] R. M. Potok, I. G. Rau, H. Shtrikman, Y. Oreg, and D. Goldhaber-Gordon. *Observation of the two-channel Kondo effect*. Nature **446**, 167 (2007).
- [139] C. Altimiras, H. le Sueur, U. Gennser, A. Cavanna, D. Mailly, and F. Pierre. *Non-equilibrium edge-channel spectroscopy in the integer quantum Hall regime*. Nat. Phys. **6**, 34 (2010).
- [140] O. E. Dial, M. D. Shulman, S. P. Harvey, H. Bluhm, V. Umansky, and A. Yacoby. *Charge noise spectroscopy using coherent exchange oscillations in a singlet-triplet qubit*. Phys. Rev. Lett. **110**, 146804 (2013).
- [141] G. Granger, D. Taubert, C. E. Young, L. Gaudreau, A. Kam, S. A. Studenikin, P. Zawadzki, D. Harbusch, D. Schuh, W. Wegscheider, Z. R. Wasilewski, A. A. Clerk, S. Ludwig, and A. S. Sachrajda. *Quantum interference and phonon-mediated back-action in lateral quantum-dot circuits*. Nat. Phys. **8**, 522 (2012).
- [142] L. A. Yeoh, A. Srinivasan, T. P. Martin, O. Klochan, A. P. Micolich, and A. R. Hamilton. *Piezoelectric rotator for studying quantum effects in semiconductor nanostructures at high magnetic fields and low temperatures*. Rev. Sci. Instrum. **81**, 113905 (2010).

- 
- [143] W. H. Press, S. A. Teukolsky, W. T. Vetterling, and B. P. Flannery. *Numerical Recipes 3rd Edition: The Art of Scientific Computing* (Cambridge University Press, New York, NY, USA, 2007).
- [144] P. Stano and J. Fabian. *Spin-orbit effects in single-electron states in coupled quantum dots*. Phys. Rev. B **72**, 155410 (2005).
- [145] F. Baruffa, P. Stano, and J. Fabian. *Theory of anisotropic exchange in laterally coupled quantum dots*. Phys. Rev. Lett. **104**, 126401 (2010).
- [146] L. C. Camenzind, L. Yu, P. Stano, J. Zimmerman, A. C. Gossard, D. Loss, and D. M. Zumbühl. *Supporting data for "Hyperfine-phonon spin relaxation in a single-electron GaAs quantum dot"*. Zenodo, <https://doi.org/10.5281/zenodo.1241104>, (2018).
- [147] S. Amasha, K. Maclean, I. P. Radu, D. M. Zumbühl, M. A. Kastner, M. P. Hanson, and A. C. Gossard. *Measurements of the spin relaxation rate at low magnetic fields in a quantum dot*. Preprint available at <http://arxiv.org/abs/cond-mat/0607110> (2006).
- [148] Y. V. Nazarov and Y. M. Blanter. *Quantum Transport* (Cambridge University Press, Cambridge, 2009).
- [149] S. Amasha, K. MacLean, I. P. Radu, D. M. Zumbühl, M. A. Kastner, M. P. Hanson, and A. C. Gossard. *Spin-dependent tunneling of single electrons into an empty quantum dot*. Phys. Rev. B **78**, 041306 (2008).
- [150] M. G. House, M. Xiao, G. Guo, H. Li, G. Cao, M. M. Rosenthal, and H. Jiang. *Detection and measurement of spin-dependent dynamics in random telegraph signals*. Phys. Rev. Lett. **111**, 126803 (2013).
- [151] M. Yamagishi, N. Watase, M. Hashisaka, K. Muraki, and T. Fujisawa. *Spin-dependent tunneling rates for electrostatically defined GaAs quantum dots*. Phys. Rev. B **90**, 035306 (2014).

- [152] A. Morello, J. J. Pla, F. A. Zwanenburg, K. W. Chan, K. Y. Tan, H. Huebl, M. Möttönen, C. D. Nugroho, C. Yang, J. A. van Donkelaar, A. D. C. Alves, D. N. Jamieson, C. C. Escott, L. C. L. Hollenberg, R. G. Clark, and A. S. Dzurak. *Single-shot readout of an electron spin in silicon*. Nature **467**, 687 (2010).
- [153] I. A. Merkulov, A. L. Efros, and M. Rosen. *Electron spin relaxation by nuclei in semiconductor quantum dots*. Phys. Rev. B **65**, 205309 (2002).
- [154] M. R. Delbecq, T. Nakajima, P. Stano, T. Otsuka, S. Amaha, J. Yoneda, K. Takeda, G. Allison, A. Ludwig, A. D. Wieck, and S. Tarucha. *Quantum dephasing in a Gated GaAs triple quantum dot due to nonergodic noise*. Phys. Rev. Lett. **116**, 046802 (2016).
- [155] L. Cywiński, W. M. Witzel, and S. Das Sarma. *Electron spin dephasing due to hyperfine interactions with a nuclear spin bath*. Phys. Rev. Lett. **102**, 057601 (2009).
- [156] H. Bluhm, S. Foletti, I. Neder, M. Rudner, D. Mahalu, V. Umansky, and A. Yacoby. *Dephasing time of GaAs electron-spin qubits coupled to a nuclear bath exceeding 200 $\mu$ s*. Nat. Phys **7**, 109 (2011).
- [157] J. Yoneda, K. Takeda, T. Otsuka, T. Nakajima, M. R. Delbecq, G. Allison, T. Honda, T. Kodera, S. Oda, Y. Hoshi, N. Usami, K. M. Itoh, and S. Tarucha. *A quantum-dot spin qubit with coherence limited by charge noise and fidelity higher than 99.9%*. Nat. Nanotechnol. **13**, 102 (2018).
- [158] B. Voisin, R. Maurand, S. Barraud, M. Vinet, X. Jehl, M. Sanquer, J. Renard, and S. De Franceschi. *Electrical Control of g-factor in a few-hole silicon nanowire MOSFET*. Nano Lett. **16**, 88 (2016).
- [159] A. Crippa, R. Maurand, L. Bourdet, D. Kotekar-Patil, A. Amisse, X. Jehl, M. Sanquer, R. Laviéville, H. Bohuslavskyi, L. Hutin, S. Barraud, M. Vinet, Y.-M. Niquet, and S. D. Franceschi. *Electrical spin driving by g-matrix modulation in spin-orbit qubits*. Phys. Rev. Lett. **120**, 137702 (2018).

- 
- [160] D. Q. Wang, O. Klochan, J.-T. Hung, D. Culcer, I. Farrer, D. A. Ritchie, and A. R. Hamilton. *Anisotropic Pauli spin blockade of holes in a GaAs double quantum dot*. Nano Lett. **16**, 7685 (2016).
- [161] M. Brauns, J. Ridderbos, A. Li, E. P. Bakkers, W. G. Van Der Wiel, and F. A. Zwanenburg. *Anisotropic Pauli spin blockade in hole quantum dots*. Phys. Rev. B **94**, 041411 (2016).
- [162] C. B. Simmons, J. R. Prance, B. J. Van Bael, T. S. Koh, Z. Shi, D. E. Savage, M. G. Lagally, R. Joynt, M. Friesen, S. N. Coppersmith, and M. A. Eriksson. *Tunable spin loading and  $T1$  of a silicon spin qubit measured by single-shot readout*. Phys. Rev. Lett. **106**, 156804 (2011).
- [163] M. Braun and U. Rössler. *Magneto-optic transitions and non-parabolicity parameters in the conduction band of semiconductors*. Journal of Physics C: Solid State Physics **18**, 3365 (1985).
- [164] G. Salis, Y. Kato, K. Ensslin, D. C. Driscoll, A. C. Gossard, and D. D. Awschalom. *Electrical control of spin coherence in semiconductor nanostructures*. Nature **414**, 619 (2001).
- [165] R. Maurand, X. Jehl, D. Kotekar-Patil, A. Corna, H. Bohuslavskyi, R. Laviéville, L. Hutin, S. Barraud, M. Vinet, M. Sanquer, and S. De Franceschi. *A CMOS silicon spin qubit*. Nat. Commun. **7**, 13575 (2016).
- [166] H. Watzinger, J. Kukučka, L. Vukušić, F. Gao, T. Wang, F. Schäffler, J. J. Zhang, and G. Katsaros. *A germanium hole spin qubit*. Nat. Commun. **9**, 3902 (2018).
- [167] K. Ono, D. G. Austing, Y. Tokura, and S. Tarucha. *Current rectification by Pauli exclusion in a weakly coupled double quantum dot system*. Science **297**, 1313 (2002).
- [168] F. H. L. Koppens, J. A. Folk, J. M. Elzerman, R. Hanson, L. H. W. van Beveren, I. T. Vink, H. P. Tranitz, W. Wegscheider, L. P. Kouwenhoven, and L. M. K. Vandersypen. *Control and detection of singlet-triplet mixing in a random nuclear field*. Science **309**, 1346 (2005).

- [169] J. Y. Wang, G. Y. Huang, S. Huang, J. Xue, D. Pan, J. Zhao, and H. Xu. *Anisotropic Pauli spin-blockade effect and spin-orbit interaction field in an InAs nanowire double quantum dot*. Nano Lett. **18**, 4741 (2018).
- [170] R. Li, F. E. Hudson, A. S. Dzurak, and A. R. Hamilton. *Pauli spin blockade of heavy holes in a silicon double quantum dot*. Nano Lett. **15**, 7314 (2015).
- [171] J. Danon and Y. V. Nazarov. *Pauli spin blockade in the presence of strong spin-orbit coupling*. Phys. Rev. B **80**, 041301 (2009).
- [172] J. Danon, I. T. Vink, F. H. L. Koppens, K. C. Nowack, L. M. K. Vandersypen, and Y. V. Nazarov. *Multiple nuclear polarization states in a double quantum dot*. Phys. Rev. Lett. **103**, 046601 (2009).
- [173] A. V. Kuhlmann, V. Deshpande, L. C. Camenzind, D. M. Zumbühl, and A. Fuhrer. *Ambipolar quantum dots in undoped silicon fin field-effect transistors*. Appl. Phys. Lett. **113**, 122107 (2018).
- [174] F. A. Zwanenburg, A. S. Dzurak, A. Morello, M. Y. Simmons, L. C. L. Hollenberg, G. Klimeck, S. Rogge, S. N. Coppersmith, and M. A. Eriksson. *Silicon quantum electronics*. Rev. Mod. Phys. **85**, 961 (2013).
- [175] K. M. Itoh, J. Kato, M. Uemura, A. K. Kaliteevskii, O. N. Godisov, G. G. Devyatych, A. D. Bulanov, A. V. Gusev, I. D. Kovalev, P. G. Sennikov, H.-J. Pohl, N. V. Abrosimov, and H. Riemann. *High purity isotopically enriched  $^{29}\text{Si}$  and  $^{30}\text{Si}$  single crystals: Isotope separation, purification, and growth*. Jpn. J. Appl. Phys **42**, 6248 (2003).
- [176] A. V. Kuhlmann, J. Houel, A. Ludwig, L. Greuter, D. Reuter, A. D. Wieck, M. Poggio, and R. J. Warburton. *Charge noise and spin noise in a semiconductor quantum device*. Nat. Phys. **9**, 570 (2013).
- [177] J. Fischer, W. A. Coish, D. V. Bulaev, and D. Loss. *Spin decoherence of a heavy hole coupled to nuclear spins in a quantum dot*. Phys. Rev. B **78**, 155329 (2008).

- 
- [178] D. Brunner, B. D. Gerardot, P. A. Dalgarno, G. Wüst, K. Karrai, N. G. Stoltz, P. M. Petroff, and R. J. Warburton. *A coherent single-hole spin in a semiconductor*. *Science* **325**, 70 (2009).
- [179] J. H. Prechtel, F. Maier, J. Houel, A. V. Kuhlmann, A. Ludwig, A. D. Wieck, D. Loss, and R. J. Warburton. *Electrically tunable hole  $g$  factor of an optically active quantum dot for fast spin rotations*. *Phys. Rev. B* **91**, 165304 (2015).
- [180] S. J. Angus, A. J. Ferguson, A. S. Dzurak, and R. G. Clark. *Gate-defined quantum dots in intrinsic silicon*. *Nano Lett.* **7**, 2051 (2007).
- [181] W. H. Lim, H. Huebl, L. H. Willems Van Beveren, S. Rubanov, P. G. Spizzirri, S. J. Angus, R. G. Clark, and A. S. Dzurak. *Electrostatically defined few-electron double quantum dot in silicon*. *Appl. Phys. Lett.* **94**, 173502 (2009).
- [182] W. H. Lim, F. A. Zwanenburg, H. Huebl, M. Möttönen, K. W. Chan, A. Morello, and A. S. Dzurak. *Observation of the single-electron regime in a highly tunable silicon quantum dot*. *Appl. Phys. Lett.* **95**, 242102 (2009).
- [183] E. Prati, M. De Michielis, M. Belli, S. Cocco, M. Fanciulli, D. Kotekar-Patil, M. Ruff, D. P. Kern, D. A. Wharam, J. Verduijn, G. C. Tettamanzi, S. Rogge, B. Roche, R. Wacquez, X. Jehl, M. Vinet, and M. Sanquer. *Few electron limit of  $n$ -type metal oxide semiconductor single electron transistors*. *Nanotechnology* **23**, 215204 (2012).
- [184] R. Li, F. E. Hudson, A. S. Dzurak, and A. R. Hamilton. *Single hole transport in a silicon metal-oxide-semiconductor quantum dot*. *Appl. Phys. Lett.* **103**, 163508 (2013).
- [185] R. Martel, V. Derycke, C. Lavoie, J. Appenzeller, K. K. Chan, J. Tersoff, and P. Avouris. *Ambipolar electrical transport in semiconducting single-wall carbon nanotubes*. *Phys. Rev. Lett.* **87**, 256805 (2001).
- [186] P. Jarillo-Herrero, S. Sapmaz, C. Dekker, L. P. Kouwenhoven, and H. S. J. van der Zant. *Electron-hole symmetry in a semiconducting carbon nanotube quantum dot*. *Nature* **429**, 389 (2004).

- [187] K. Byon, D. Tham, J. E. Fischer, and A. T. Johnson. *Systematic study of contact annealing: Ambipolar silicon nanowire transistor with improved performance*. Appl. Phys. Lett. **90**, 143513 (2007).
- [188] A. Colli, S. Pisana, A. Fasoli, J. Robertson, and A. C. Ferrari. *Electronic transport in ambipolar silicon nanowires*. Physica Status Solidi (B) **244**, 4161 (2007).
- [189] J. Güttinger, C. Stampfer, F. Libisch, T. Frey, J. Burgdörfer, T. Ihn, and K. Ensslin. *Electron-hole crossover in graphene quantum dots*. Phys. Rev. Lett. **103**, 046810 (2009).
- [190] J. C. H. Chen, D. Q. Wang, O. Klochan, A. P. Micolich, K. Das Gupta, F. Sfigakis, D. A. Ritchie, D. Reuter, A. D. Wieck, and A. R. Hamilton. *Fabrication and characterization of ambipolar devices on an undoped AlGaAs/GaAs heterostructure*. Appl. Phys. Lett. **100**, 052101 (2012).
- [191] P. W. Li, D. M. T. Kuo, W. M. Liao, and W. T. Lai. *Study of tunneling currents through germanium quantum-dot single-hole and -electron transistors*. Appl. Phys. Lett. **88**, 213117 (2006).
- [192] H. Ishikuro and T. Hiramoto. *On the origin of tunneling barriers in silicon single electron and single hole transistors*. Appl. Phys. Lett. **74**, 1126 (1999).
- [193] A. C. Betz, M. F. Gonzalez-Zalba, G. Podd, and A. J. Ferguson. *Ambipolar quantum dots in intrinsic silicon*. Appl. Phys. Lett. **105**, 153113 (2014).
- [194] F. Mueller, G. Konstantaras, W. G. van der Wiel, and F. A. Zwanenburg. *Single-charge transport in ambipolar silicon nanoscale field-effect transistors*. Appl. Phys. Lett. **106**, 172101 (2015).
- [195] F. Mueller, G. Konstantaras, P. C. Spruijtenburg, W. G. van der Wiel, and F. A. Zwanenburg. *Electron-hole confinement symmetry in silicon quantum dots*. Nano Lett. **15**, 5336 (2015).
- [196] P. C. Spruijtenburg, S. V. Amitonov, F. Mueller, W. G. van der Wiel, and F. A.



- 
- Zwanenburg. *Passivation and characterization of charge defects in ambipolar silicon quantum dots*. *Sci. Rep.* **6**, 38127 (2016).
- [197] P. C. Spruijtenburg, S. V. Amitonov, W. G. van der Wiel, and F. A. Zwanenburg. *A fabrication guide for planar silicon quantum dot heterostructures*. *Nanotechnology* **29**, 143001 (2018).
- [198] Intel, <https://newsroom.intel.com/press-kits/intel-22nm-3-d-tri-gate-transistor-technology/> for Intel 22nm 3-D tri-gate transistor technology (2011).
- [199] C. Auth *et al.* *A 22nm high performance and low-power CMOS technology featuring fully-depleted tri-gate transistors, self-aligned contacts and high density MIM capacitors*. In *2012 Symposium on VLSI Technology (VLSIT)*, 2003 (IEEE, 2012).
- [200] C. Auth *et al.* *A 10nm high performance and low-power CMOS technology featuring 3rd generation FinFET transistors, Self-Aligned Quad Patterning, contact over active gate and cobalt local interconnects*. In *2017 IEEE International Electron Devices Meeting (IEDM)* (IEEE, 2017).
- [201] J. Larson and J. Snyder. *Overview and status of metal S/D Schottky-barrier MOSFET technology*. *IEEE Transactions on Electron Devices* **53**, 1048 (2006).
- [202] B. Roche, B. Voisin, X. Jehl, R. Wacquez, M. Sanquer, M. Vinet, V. Deshpande, and B. Previtali. *A tunable, dual mode field-effect or single electron transistor*. *Appl. Phys. Lett.* **100**, 032107 (2012).
- [203] M. Hofheinz, X. Jehl, M. Sanquer, G. Molas, M. Vinet, and S. Deleonibus. *Simple and controlled single electron transistor based on doping modulation in silicon nanowires*. *Appl. Phys. Lett.* **89**, 143504 (2006).
- [204] F. A. Zwanenburg, C. E. W. M. van Rijmenam, Y. Fang, C. M. Lieber, and L. P. Kouwenhoven. *Spin states of the first four holes in a silicon nanowire quantum dot*. *Nano Letters* **9**, 1071 (2009).

- [205] E. A. Laird, J. M. Taylor, D. P. DiVincenzo, C. M. Marcus, M. P. Hanson, and A. C. Gossard. *Coherent spin manipulation in an exchange-only qubit*. Phys. Rev. B **82**, 075403 (2010).
- [206] L. Vukušić, J. Kukučka, H. Watzinger, J. M. Milem, F. Schäffler, and G. Katsaros. *Single-shot readout of hole spins in Ge*. Nano Lett. **18**, 7141 (2018).
- [207] Y. Hu, F. Kuemmeth, C. M. Lieber, and C. M. Marcus. *Hole spin relaxation in Ge-Si core-shell nanowire qubits*. Nat. Nanotechnol. **7**, 47 (2012).
- [208] J. R. Wootton and D. Loss. *High threshold error correction for the surface code*. Phys. Rev. Lett. **109**, 160503 (2012).
- [209] R. Schleser, E. Ruh, T. Ihn, K. Ensslin, D. C. Driscoll, and A. C. Gossard. *Time-resolved detection of individual electrons in a quantum dot*. Appl. Phys. Lett. **85**, 2005 (2004).
- [210] L. M. K. Vandersypen, J. M. Elzerman, R. N. Schouten, L. H. Willems van Beveren, R. Hanson, and L. P. Kouwenhoven. *Real-time detection of single-electron tunneling using a quantum point contact*. Appl. Phys. Lett. **85**, 4394 (2004).
- [211] H. Qin and D. A. Williams. *Radio-frequency point-contact electrometer*. Appl. Phys. Lett. **88**, 203506 (2006).
- [212] D. J. Reilly, C. M. Marcus, M. P. Hanson, and A. C. Gossard. *Fast single-charge sensing with a rf quantum point contact*. Appl. Phys. Lett. **91**, 162101 (2007).
- [213] M. C. Cassidy, A. S. Dzurak, R. G. Clark, K. D. Petersson, I. Farrer, D. A. Ritchie, and C. G. Smith. *Single shot charge detection using a radio-frequency quantum point contact*. Appl. Phys. Lett. **91**, 222104 (2007).
- [214] C. Barthel, M. Kjargaard, J. Medford, M. Stopa, C. M. Marcus, M. P. Hanson, and A. C. Gossard. *Fast sensing of double-dot charge arrangement and spin state with a radio-frequency sensor quantum dot*. Phys. Rev. B **81**, 161308 (2010).

- 
- [215] N. Ares, F. J. Schupp, A. Mavalankar, G. Rogers, J. Griffiths, G. A. C. Jones, I. Farrer, D. A. Ritchie, C. G. Smith, A. Cottet, G. A. D. Briggs, and E. A. Laird. *Sensitive radio-frequency measurements of a quantum dot by tuning to perfect impedance matching*. Phys. Rev. Appl. **5**, 034011 (2016).
- [216] J. I. Colless, A. C. Mahoney, J. M. Hornibrook, A. C. Doherty, H. Lu, A. C. Gossard, and D. J. Reilly. *Dispersive readout of a few-electron double quantum dot with fast rf gate sensors*. Phys. Rev. Lett. **110**, 046805 (2013).
- [217] A. Rossi, R. Zhao, A. S. Dzurak, and M. F. Gonzalez-Zalba. *Dispersive readout of a silicon quantum dot with an accumulation-mode gate sensor*. Appl. Phys. Lett. **110**, 212101 (2017).
- [218] A. West, B. Hensen, A. Jouan, T. Tantt, C.-H. Yang, A. Rossi, M. F. Gonzalez-Zalba, F. Hudson, A. Morello, D. J. Reilly, and A. S. Dzurak. *Gate-based single-shot readout of spins in silicon*. Nat. Nanotechnol. **14**, 437 (2019).
- [219] P. Pakkiam, A. V. Timofeev, M. G. House, M. R. Hogg, T. Kobayashi, M. Koch, S. Rogge, and M. Y. Simmons. *Single-shot single-gate rf spin readout in silicon*. Phys. Rev. X **8**, 041032 (2018).
- [220] M. Urdampilleta, D. J. Niegemann, E. Chanrion, B. Jadot, C. Spence, P.-A. Mortemousque, C. Bäuerle, L. Hutin, B. Bertrand, S. Barraud, R. Maurand, M. Sanquer, X. Jehl, S. D. Franceschi, M. Vinet, and T. Meunier. *Gate-based high fidelity spin readout in a CMOS device*. Nat. Nanotechnol. (2019).
- [221] M. J. Curry, M. Rudolph, T. D. England, A. M. Mounce, R. M. Jock, C. Bureau-Oxton, P. Harvey-Collard, P. A. Sharma, J. M. Anderson, D. M. Campbell, J. R. Wendt, D. R. Ward, S. M. Carr, M. P. Lilly, and M. S. Carroll. *Single-shot readout performance of two heterojunction-bipolar-transistor amplification circuits at millikelvin temperatures*. Preprint available at <http://arxiv.org/abs/1901.04570> (2019).
- [222] G. Zheng, N. Samkharadze, M. L. Noordam, N. Kalhor, D. Brousse, A. Sammak,

- G. Scappucci, and L. M. K. Vandersypen. *Rapid high-fidelity gate-based spin read-out in silicon*. Preprint available at <http://arxiv.org/abs/1901.00687> (2019).
- [223] L. M. K. Vandersypen, H. Bluhm, J. S. Clarke, A. S. Dzurak, R. Ishihara, A. Morello, D. J. Reilly, L. R. Schreiber, and M. Veldhorst. *Interfacing spin qubits in quantum dots and donors - hot, dense, and coherent*. npj Quantum Inf. **3**, 34 (2017).
- [224] M. Veldhorst, H. G. J. Eenink, C. H. Yang, and A. S. Dzurak. *Silicon CMOS architecture for a spin-based quantum computer*. Nat. Commun. **8**, 1766 (2016).
- [225] D. M. Pozar. *Microwave engineering* (Wiley, 2005).
- [226] F. N. M. Froning, M. K. Rehmann, J. Ridderbos, M. Brauns, F. A. Zwanenburg, A. Li, E. P. A. M. Bakkers, D. M. Zumbühl, and F. R. Braakman. *Single, double, and triple quantum dots in Ge/Si nanowires*. Appl. Phys. Lett. **113**, 073102 (2018).
- [227] F. W. Grover and I. S. of America. *Inductance calculations: working formulas and tables* (Instrument Society of America, 1981).
- [228] J. I. Colless and D. J. Reilly. *Modular cryogenic interconnects for multi-qubit devices*. Rev. Sci. Instrum. **85**, 114706 (2014).
- [229] T. Hensgens, T. Fujita, L. Janssen, X. Li, C. J. Van Diepen, C. Reichl, W. Wegscheider, S. Das Sarma, and L. M. K. Vandersypen. *Quantum simulation of a Fermi–Hubbard model using a semiconductor quantum dot array*. Nature **548**, 70 (2017).
- [230] U. Mukhopadhyay, J. P. Dehollain, C. Reichl, W. Wegscheider, and L. M. Vandersypen. *A 2x2 quantum dot array with controllable inter-dot tunnel couplings*. Appl. Phys. Lett. **112**, 183505 (2018).
- [231] D. T. Lennon, H. Moon, L. C. Camenzind, L. Yu, D. M. Zumbühl, G. A. D. Briggs, M. A. Osborne, E. A. Laird, and N. Ares. *Efficiently measuring a quantum device using machine learning*. Preprint available at <http://arxiv.org/abs/1810.10042> (2018).

- [232] Y. Hu, H. O. H. Churchill, D. J. Reilly, J. Xiang, C. M. Lieber, and C. M. Marcus. *A Ge/Si heterostructure nanowire-based double quantum dot with integrated charge sensor*. Nat. Nanotechnol. **2**, 622 (2007).
- [233] K. D. Petersson, L. W. McFaul, M. D. Schroer, M. Jung, J. M. Taylor, A. A. Houck, and J. R. Petta. *Circuit quantum electrodynamics with a spin qubit*. Nature **490**, 380 (2012).
- [234] C. Fasth, A. Fuhrer, L. Samuelson, V. N. Golovach, and D. Loss. *Direct measurement of the spin-orbit interaction in a two-electron InAs nanowire quantum dot*. Phys. Rev. Lett. **98**, 266801 (2007).
- [235] A. J. Landig, J. V. Koski, P. Scarlino, C. Reichl, W. Wegscheider, A. Wallraff, K. Enslin, and T. Ihn. *Microwave cavity detected spin blockade in a few electron double quantum dot*. Preprint available at <https://arxiv.org/abs/1811.03907> (2018).
- [236] L. Trifunovic, O. Dial, M. Trif, J. R. Wootton, R. Abebe, A. Yacoby, and D. Loss. *Long-distance spin-spin coupling via floating gates*. Physical Review X **2**, 011006 (2012).

## Acknowledgment

I want to thank Prof. Dominik Zumbühl for giving me the opportunity to be a part of his research group and for supervising my PhD. There was so much which I learned in these years and I am very grateful for Dominik's support and patience during all this time.

All this research was only possible due to collaborations with very motivated and talented scientists. Especially, I would like to thank Liuqi Yu with whom I collaborated very closely and we complemented each other very well. Together we produced the GaAs samples, measured and analyzed the data and wrote most of the manuscripts. Also, we had a good time in- as well as outside of the lab. I would also like to give special thanks to Peter Stano from RIKEN (Japan). Peter's help was essential for the understanding of the spin relaxation experiment. From this point on, we had a very fruitful collaboration which lead to investigations on orbital an spin effects of quantum dots in in-plane magnetic fields.

I started to work on the Ge/Si project because I was particularly interested in spin qubit manipulations and wanted to participate in the set-up of the new Bluefors refrigerator which was designated for these kind of experiments. Due to the very interesting physics predicted in this Ge/Si system, I was very motivated when I got the chance to be a part of this research project. In this intense time, I very much appreciated the collaboration with Floris Braakman and Florian Froning. It was fast-paced and challenging and still, I had a very good time. From the theory side, we enjoyed a very close collaborations with Marko Rančić and Christoph Kloeffel from the Condensed Matter Theory & Quantum Computing group (Loss group). At this point, I would also like to thank Prof. Daniel Loss for his active support of the Ge/Si as well as the GaAs project.

Obviously, I was excited when I got the chance to be a part of the ambipolar FinFET project by helping Andreas Kuhlmann measuring these promising devices which he fabricated in the group of Andreas Fuhrer at IBM Research Zurich. I enjoyed this collaboration, especially because I could get some insight on approaches and processes of the semiconductor industry. I sincerely hope that this project can fulfill its high ambitions in the future.

Also, I very much appreciate all the time spend, the numerous discussions and collaborations with Christian Scheller, Daniel Biesinger, Pirmin Weigele, Mario Palma, Taras Patlatiuk, Bilal Kalyoncu and Mirko Rehmann. Thanks for the help and the good time! I also want to thank all current and former member of the Zumbühl group: Florian Dettwiler, Dario Maradan, Lucas Casparis, Dorothee Hug, Myrsini Lafkioti, Philip Häner, Simon Svab, Oliver Bärenbold, Tim Camenzind, Kristopher Ceverny and Miquel Carballido.

In the Department of Physics at the University of Basel we are blessed with an electrical and a mechanical workshop which were immensely crucial for the success of my projects. I would like to thank Michael Steinacher, Sascha Lindner and Roberto Maffiolini for your help with our electronics – especially for the help designing the PCBs for the high-frequency setup. From the mechanical workshop I appreciated the collaboration with Sascha Martin, Patrick Stöcklin and Dominik Sifrig. Also, I want to thank the administrative assistants, especially Barbara Kammermann and Astrid Kalt. Thank you for always being so helpful!

Last, I would like to thank my family, my friends and my girlfriend Ilona Birrer for their support in times of stress and frustration and for sharing my happiness in times of success.

# Curriculum Vitae and Publications

Leon Luca Caspar Camenzind

2014 - 2019	PhD at University of Basel
2012 - 2014	Research & Development at ARTIDIS AG, Basel
2010 - 2012	MSc. of Science in Nanoscience at University of Basel
2007 - 2010	BSc. of Science in Nanoscience at University of Basel
2006	Military service
2002 - 2006	Gymnasium Kirchenfeld, Bern

## Publications

1. **Camenzind, L. C.**, Yu, L., Stano, P., Zimmerman, J., Gossard, A. C., Loss, D., and Zumbühl, D. M. Spectroscopy of quantum-dot orbitals with in-plane magnetic fields. *Phys. Rev. Lett.* **122**, 207701 (2019).
2. **Camenzind, L. C.**, Yu, L., Stano, P., Zimmerman, J. D., Gossard, A. C., Loss, D., and Zumbühl, D. M. Hyperfine-phonon spin relaxation in a single-electron GaAs quantum dot. *Nat. Commun.* **9**, 3454 (2018).
3. Kuhlmann, A. V., Deshpande, V., **Camenzind, L. C.**, Zumbühl, D. M., and Fuhrer, A. Ambipolar quantum dots in undoped silicon fin field-effect transistors. *Appl. Phys. Lett.* **113**, 122107 (2018).
4. Stano, P., Hsu, C.-H., **Camenzind, L. C.**, Yu, L., Zumbühl, D., and Loss, D., Orbital effects of a strong in-plane magnetic field on a gate-defined quantum dot. *Phys. Rev. B* **99**, 085308 (2019).
5. Stano, P., Hsu, C.-h., Serina, M., **Camenzind, L. C.**, Zumbühl, D. M., and Loss, D. g-factor of electrons in gate-defined quantum dots in a strong in-plane magnetic field. *Phys. Rev. B* **98**, 195314 (2018).



6. Lennon, D. T., Moon, H., **Camenzind, L. C.**, Yu, L., Zumbühl, D. M., Briggs, G. A. D., Osborne, M. A., Laird, E. A., and Ares, N. Efficiently measuring a quantum device using machine learning. *ArXiv*, 1810.10042 (2018).
7. Lua, M., Oertle, P., **Camenzind, L.**, Goz, A., Meyer, C., Konieczka, K., Loparic, M., Halfter, W., and Henrich, P. Superior rim stability of the lens capsule following manual over femtosecond laser capsulotomy. *Investig. Ophthalmol. Vis. Sci.* **57**, 2839 (2016).
8. Halfter, W., Oertle, P., Monnier, C., **Camenzind, L.**, Reyes-Lua, M., Hu, H., Candiello, J., Labilloy, A., Balasubramani, M., Henrich, P., and Plodinec, M. New concepts in basement membrane biology. *FEBS J.* **282**, 4466 (2015).
9. To, M., Goz, A., **Camenzind, L.**, Oertle, P., Candiello, J., Sullivan, M., Henrich, P., Loparic, M., Safi, F., Eller, A., and Halfter, W. Diabetes-induced morphological, biomechanical, and compositional changes in ocular basement membranes. *Exp. Eye Res.* **116**, 298 (2013).